PHASE DISTRIBUTION AND PRESSURE DROP OF TWO-PHASE FLOWS IN A HORIZONTAL IMPACTING TEE JUNCTION

by

Ahmed M. F. El-Shaboury

A Thesis
Submitted to the Faculty of Graduate Studies
in Partial Fulfillment of the
Requirements for the Degree of

DOCTOR OF PHILOSOPHY

Department of Mechanical and Manufacturing Engineering
University of Manitoba
Winnipeg, Manitoba

THE UNIVERSITY OF MANITOBA

FACULTY OF GRADUATE STUDIES
*****
COPYRIGHT PERMISSION

PHASE DISTRIBUTION AND PRESSURE DROP OF TWO-PHASE FLOWS IN A HORIZONTAL IMPACTING TEE JUNCTION

BY

Ahmed M.F. El-Shaboury

A Thesis/Practicum submitted to the Faculty of Graduate Studies of The University of Manitoba in partial fulfillment of the requirement of the degree

Of

Doctor of Philosophy

ABSTRACT

In the present investigation, phase-distribution and pressure-drop data were generated for air-water flows in a horizontal impacting tee junction. The junction was machined in an acrylic block with the three sides, all horizontal, having a diameter of 0.0378 m. The operating conditions were as follows: a junction pressure of 1.5 bar, an inlet temperature near the ambient, inlet superficial gas velocity in the range of $0.5 \leq J_{G1} \leq 40$ m/s, inlet superficial liquid velocity in the range of $0.0026 \leq J_{L1} \leq 0.18$ m/s, and an extraction ratio in the range of $0.0 \leq W_3/W_1 \leq 1.0$. These inlet conditions lead to the observation of the following flow regimes in the inlet pipe: stratified, stratified-wavy, wavy, and annular.

It was found that the phases did not distribute themselves evenly between the two outlets unless the extraction ratio was 0.5. For a fixed J_{G1}, as J_{L1} increases, the line, or curve that represents the data rotates in a clockwise direction around the point of (0.5,0.5) on coordinates of F_{BL} vs. F_{BG}. For a fixed J_{L1}, as J_{G1} increases, the line, or curve that represents the data rotates in an anti-clockwise direction around the point of (0.5,0.5) on coordinates of F_{BL} vs. F_{BG}. The previously-mentioned effects of J_{L1} and J_{G1} are consistent with the observations of El-Shaboury et al. (2001) for others' data. These effects of J_{L1} and J_{G1} on the phase distribution are valid within each inlet flow regime; however, these effects may not hold near the flow-regime boundaries.

Comparisons of the present phase-distribution data and the data of other researchers under similar conditions were made. These comparisons showed good agreement in general. Some present phase-distribution data were compared against the

data of Azzopardi et al. (1986a) for a vertical inlet and annular flow. That comparison also showed a good agreement even though the inlet orientation was different.

The phase-distribution data were compared against the models of Ottens et al. (1995) and Hwang (1986). These two models were found to be the best available models for predicting phase distribution in horizontal impacting tee junctions (El-Shaboury et al. (2001)). For annular and wavy flows, the model of Ottens et al. gave better overall predictions of the present data. For stratified flows, none of the two models gave good predictions.

For the present data, the pressure drops ΔP_{12} and ΔP_{13} were found to depend on the inlet conditions (J_{G1} and J_{L1}) and the extraction ratio (W_3/W_1). In general, the absolute values of the pressure drops increased with the increase in the inlet mass flow rate. Also, the absolute value of ΔP_{13} increased as the extraction ratio increased. For stratified flows, the current pressure-distribution data are given in Appendix C but values of ΔP_{12} and ΔP_{13} were not reported for reasons explained in the text.

To the best of the author's knowledge, the only available pressure-drop data in the literature are those of Hwang (1986) for bubbly flows. Also, there are no available models or correlations for predicting pressure drops in impacting tee junctions. As a result, the present data could not be compared against other data or models.

A model capable of predicting the phase distribution and the pressure drop was developed. The model is limited to horizontal equal-diameter impacting tee junctions and is applicable to three inlet flow regimes: stratified, wavy, and annular. The model is based on five equations: two mass-conservation equations written for the gas phase and the total inlet mass, one energy-conservation equation written for the inlet-to-outlet 3

gas phase, one momentum-conservation equation written in the direction of the outlets, and the symmetry equation; $\Delta P_{12}\big|_{W_2/W_1=\delta} = \Delta P_{13}\big|_{W_3/W_1=\delta}$. The term representing the irreversible mechanical-energy loss in the energy-conservation equation and the terms in the momentum-conservation equation that accounts for the deviations of the flows from the main directions and the wall friction at the junction centre were correlated empirically in a flow-regime-dependent way.

Comparison of the proposed model predictions with the current phase-distribution and pressure-drop data showed good agreement in general. The model predictions were also compared against the phase-distribution data of other researchers including the data of Azzopardi et al. (1986a) for annular flow in a vertical inlet. Reasonable agreement was obtained particularly for the data of stratified and wavy flows. Overall, the present model has been successfully tested for air-water mixtures (stratified, wavy, and annular flow regimes) over the following conditions: junction diameter between 19 and 37.8 mm, and system pressure between 1.0 and 1.7 bar.

ACKNOWLEDGEMENTS

I would like to sincerely thank Dr. Hassan Soliman and Dr. Grant Sims for their great insight, encouragement, and guidance. Their support was extremely helpful in completing my thesis.

Mr. John Finken and Mr. Irwin Penner were very important and helpful in constructing the test facility.

The Post Graduate Fellowship awarded by the Natural Sciences and Engineering Research Council of Canada (NSERC), the Graduate Fellowship awarded by the Faculty of Graduate Studies at the University of Manitoba, and the Teaching Assistantships/Lectureships awarded by the Department of Mechanical and Manufacturing Engineering at the University of Manitoba are gratefully acknowledged.

TABLE OF CONTENTS

LIST OF FIGURES

LIST OF TABLES

NOMENCLATURE

Symbol	Description	Units
a	Constant relating the surface area A_{co} and the cross-sectional area of the pipe A, see Equation (5.10b)	-
A	Cross-sectional area of the pipe	m^2
A_{CO}	Surface area cut out of the control volume located at the junction, Equation (5.10b)	
$\tilde{A}_L$	Area multiplier for the hydrostatic pressure, see Equation (C.1)	m^2
A_w	Wall surface area of the control volume located at the junction, Equation (5.10c)	m^2
b_G	Parameter defining the location of the gas dividing streamline from the point of impact (Hwang (1986) model, Figure2.1)	m
b_L	Parameter defining the location of the liquid dividing streamline from the point of impact (Hwang (1986) model, Figure2.1)	m
C_i	Constant in the current model, i = 1,2, and 3 (Equations (5.18) to (5.23))	-
C_f	Friction coefficient	-
D	Diameter	m
f	Friction factor, Equations (4.7) and (4.8)	-
F_{BG}	Fraction of inlet gas exiting through outlet 3, = W_{G3}/W_{G1}	-
F_{BL}	Fraction of inlet liquid exiting through outlet 3, = W_{L3}/W_{L1}	-
F_D	Net drag force acting on the control volume located at the junction, Equation (5.9)	N
F_{DG}	Drag force acting on gas (Hwang (1986) model, Figure2.2)	N
F_{DL}	Drag force acting on liquid (Hwang (1986) model, Figure2.2)	N

g	Gravitational acceleration	m/s^2
G	Mass flux	$kg/m^2.s$
h	Vertical height of the gas-liquid interface above the pressure transducer compartment, Equation (4.10)	m
h_L	Liquid height in the tube	m
$(h_L)_r$	Liquid height in the tube at tap 1	m
J_G	Superficial gas velocity	m/s
J_L	Superficial liquid velocity	m/s
K	Single-phase friction loss coefficient	-
K_G	Mechanical-energy loss coefficient for the gas phase	-
L	Vertical height of the bottom of the tube above the pressure transducer compartment	m
m_G	Coefficient related to the shape of the gas dividing streamline (Hwang (1986) model)	-
m_L	Coefficient related to the shape of the liquid dividing streamline (Hwang (1986) model)	-
$M_{in,x}$	Inlet momentum in the x-direction, see Equation (C.1)	N
$\dot{M}_R$	Inlet-momentum-flux ratio, Equation (4.2)	-
N	Empirical coefficient (Hwang (1986) model)	-
P	Average junction pressure	Pa
P_s	Test-section pressure	Pa
P_{st}	Static pressure of the gas phase	Pa
$(P_{st})_r$	Static pressure of the gas phase at tap 1	Pa

P_r	Absolute pressure at tap 1	Pa
Re_l	Inlet Reynolds number, Equation (4.1)	-
Re_{Gl}	Inlet-gas Reynolds number (Ottens et al. (1995) model, Equation (2.21))	-
Re_{Ll}	Inlet-liquid Reynolds number (Ottens et al. (1995) model, Equation (2.20))	-
Re_{SLl}	Inlet-liquid superficial Reynolds number (Ottens et al. (1995) model, Equation (2.14))	-
R_G	Radius of curvature of a gas streamline (Hwang (1986) model, Figure 2.2)	m
R_L	Radius of curvature of a liquid streamline (Hwang (1986) model, Figure 2.2)	m
S_G	Gas perimeter, see Equation (C.1)	m
S_L	Liquid perimeter, see Equation (C.1)	m
T_l	Temperature at the tee junction inlet	°C
V	Average velocity	m/s
V_G	Average gas velocity, Equation (4.4)	m/s
V_L	Average liquid velocity, Equation (4.5)	m/s
V_m	Momentum velocity of the mixture, Equation (5.7)	m/s
W	Total mass flow rate	kg/s
W_G	Gas mass flow rate	kg/s
W_L	Liquid mass flow rate	kg/s
x	Cartesian co-ordinate	m
x_i	Quality, i = 1,2, and 3	-
y	Cartesian co-ordinate	m

Y	Slope of the straight line describing the relation between β' and W_3/W_1, See Equations (5.24) to (5.27)	-

Greek Symbols

α	Void fraction, Equation (4.3)	-
β	Hypothetical angle between the inlet flow and the positive x-direction, Figure 5.7	rad
β'	Parameter in the current model, see Equation (5.14)	-
β_G	Constant in Ottens et al.(1995) model, Equation (2.22)	-
β_L	Constant in Ottens et al.(1995) model, Equation (2.22)	-
ΔP_{12}	Inlet-to-outlet-2 pressure difference ($= P_1 - P_2$)	Pa
ΔP_{13}	Inlet-to-outlet-3 pressure difference ($= P_1 - P_3$)	Pa
δ_G	Parameter defining the location of the gas dividing streamline in the inlet pipe (Hwang (1986) model, Figure 2.1)	m
δ_L	Parameter defining the location of the liquid dividing streamline in the inlet pipe (Hwang (1986) model, Figure 2.1)	m
ε_{L1}	Liquid hold-up in the inlet (Ottens et al.(1995) model, Equation (2.15))	-
ϕ	Angle between gas and liquid streamlines when crossing (Hwang (1986) model, (Figure 2.2))	rad
γ	Angle between the centrifugal and drag forces acting on gas (Hwang (1986) model, (Figure 2.2))	rad
η	Cartesian co-ordinate (Hwang (1986) model, Figure 2.1)	m
κ	Ratio of kinetic energies per unit volume of gas and liquid in the inlet (Ottens et al.(1995) model, Equation (2.23))	-

λ_0	Junction energy dissipation factor (Ottens et al. (1995) model, Equation (2.24))	-
μ_G	Gas viscosity	Pa.s
μ_L	Liquid viscosity	Pa.s
ρ	Density	kg/m^3
ρ_G	Gas density	kg/m^3
ρ_L	Liquid density	kg/m^3
ρ_m	Momentum-weighted density, Equation (5.8)	kg/m^3
θ_{L1}	Fraction of the inlet pipe wetted by the liquid (Ottens et al. (1995) model, Equation (2.19))	-
$\tau_{w,G}$	Gas wall shear stress, see Equation (C.1) and Figure C.1	Pa
$\tau_{w,L}$	Liquid wall shear stress, see Equation (C.1) and Figure C.1	Pa

Subscripts

1	Inlet
2	Outlet 2
3	Outlet 3
12	Inlet to outlet 2
13	Inlet to outlet 3

Chapter 1

INTRODUCTION

Two-phase flow commonly occurs in many systems in the power and process industries, such as conventional steam power plants, evaporators and condensers, boiling-water and pressurized-water nuclear reactors, and a wide variety of chemical and petroleum applications. Quite often, the complex piping networks in these systems require the two-phase flow to pass through tee junctions. Tee junctions may be used to combine two inlet streams into one outlet stream (combining tees) or to divide one inlet stream into two outlet streams (dividing tees). For the case of dividing tees, a junction may have one of two different configurations: branching or impacting. For the case of branching tees, one of the two outlet streams is in the same direction as the inlet and the other outlet is perpendicular to the inlet. For the case of impacting tees, the two outlet streams have opposite directions and both are perpendicular to the inlet. The three sides of an impacting tee junction may have different orientations between two limiting positions; vertically upward and vertically downward. In this study, the focus is on impacting tee junctions with three horizontal sides.

When two-phase flow passes through an impacting tee, maldistribution of the phases may occur; i.e., the qualities of the mixtures in both outlets downstream from the junction are not equal to the inlet quality. Certain mass split ratios can lead to single-phase gas flowing in one of the outlets, while other split ratios can lead to single-phase liquid flowing in one of the outlets. This severe maldistribution of the phases can have a significant effect on the operation and efficiency of components downstream from the junction. However, this maldistribution may be desirable in some cases where

the tee is used as a separator. Therefore, it is very important to be able to predict the manner by which the two phases distribute themselves at impacting tees for different operating conditions. Another consideration is the pressure drop that occurs at the junction. Experimental evidence has shown that the pressure drop during two-phase flow can be much greater than that during a single-phase flow with the same inlet mass flow rate.

Figure 1.1 shows a schematic diagram of an impacting tee junction. The relevant flow parameters are as follows: the inlet, and the two outlet mass flow rates (W_1, W_2, and W_3, respectively); the inlet, and the two outlet average pressures (P_1, P_2, and P_3, respectively); and the inlet, and the two outlet qualities (x_1, x_2, and x_3, respectively). Relevant geometric parameters are the inlet, and the two outlets diameters (D_1, D_2, and

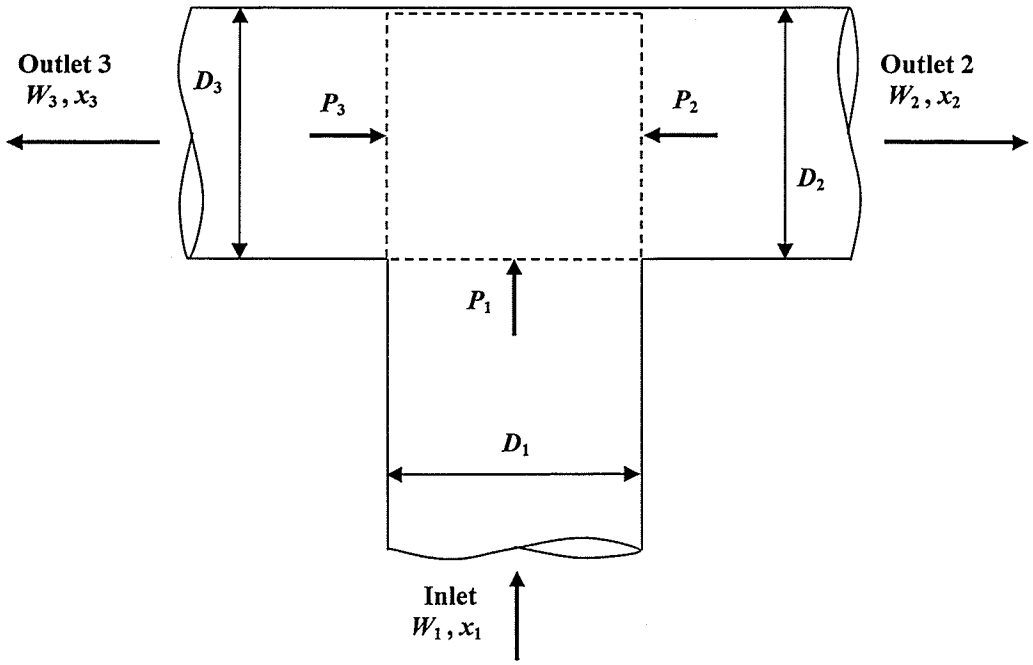

Figure 1.1 Relevant parameters for two-phase flow in an impacting tee junction

D_3, respectively). Other important parameters are the thermophysical and transport properties of the two-phase mixture. The two phases may belong to the same fluid component, such as steam and water, or two distinct components, such as air and water. The extraction ratio, given by W_3/W_1, is the fraction of the total inlet flow that is withdrawn through outlet 3. In a typical application, the geometrical parameters (D_1, D_2, and D_3), the inlet conditions (W_1, P_1, and x_1), one outlet flow rate (e.g., W_3), and the fluid properties will be known. For these given parameters, it will be required to determine W_2, x_2, x_3, P_2, and P_3.

Figure 1.2(a) illustrates one method that has been used to present the phase-distribution data for a horizontal impacting tee. In this figure, the ordinate F_{BL} is the fraction of inlet liquid flowing in outlet 3 ($F_{BL} = W_{L3}/W_{L1}$) and the abscissa F_{BG} is the fraction of inlet gas flowing in the same outlet ($F_{BG} = W_{G3}/W_{G1}$). Because of the geometric symmetry of the outlets of an equal-sided horizontal impacting tee, all the curves representing the phase-distribution data should pass through point **E** that has an F_{BG} of 0.5 and an F_{BL} of 0.5. Also, in order to satisfy mass balance, the two parts of the curve before and after point **E** should be the inverted mirror image of each other. Therefore, F_{BL} at a given value of F_{BG} should be equal to (1- F_{BL}) at (1-F_{BG}). An example of data that satisfy mass balance is shown in Figure 1.2(b) with two selected values of F_{BG} and F_{BL}.

On Figure 1.2(a), all the data must start at point **A** (0,0) and as the extraction ratio W_3/W_1 increases, there are two limiting conditions represented by lines **AC** and **AD**. For line **AC**, only gas is diverted into outlet 3 while for line **AD**, only liquid is diverted into outlet 3. Lines **AC** and **AD** are limiting lines, i.e., data may fall anywhere between these two lines. When the data reach point **C** or **D**, the data automatically have to go

through point **E**. This is due to the fact that for $F_{BG} = 0.5$, F_{BL} has to be 0.5 as well. As the data go past point **E**, and to satisfy mass balance, the data have to go through the inverted mirror images of the curves (or lines) before point **E**. The inverted mirror images of lines **ACE** and **ADE** are lines **EGH** and **EFH**, respectively. Considering the

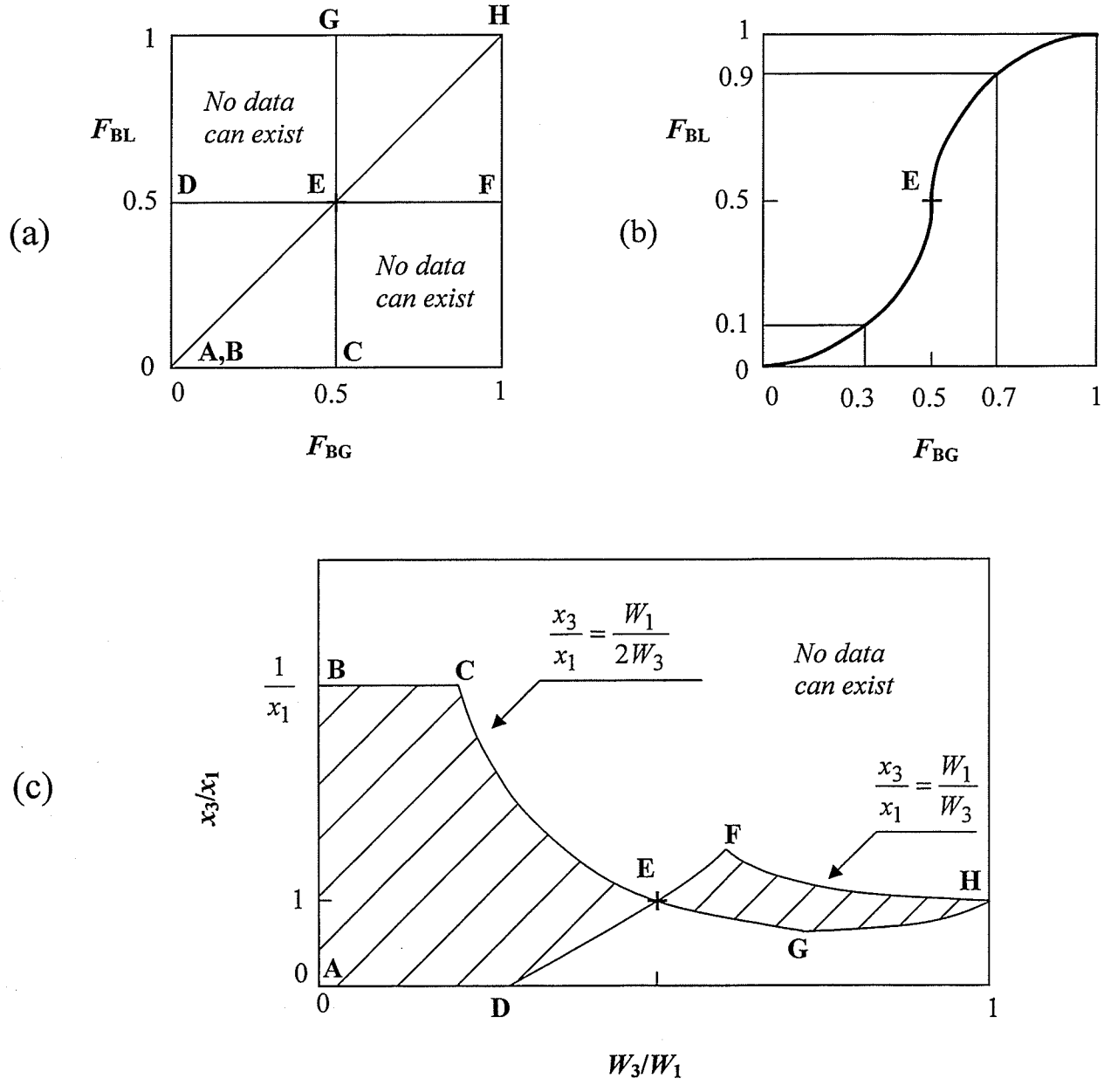

Figure 1.2 Schematic representation of two different ways to present phase-distribution data

limiting lines before and after point **E**, it can be said that data may exist only in the two squares **ADEC** and **EGHF**. No data can exist in the other two squares. For gas-liquid two-phase flow, there are two limiting cases: single-phase gas flow ($x_1 = 1$) and single-phase liquid flow ($x_1 = 0$). As x_1 approaches zero, as will be seen later, the data in Figure 1.2(a) approach the line $F_{BL} = 0.5$ and as x_1 approaches 1, again as will be seen later, the data approach the line $F_{BG} = 0.5$. Thus the two limiting cases for the two-phase flow bound that data within the squares **ADEC** and **EGHF.** Furthermore, if data existed in the square **DEG1**, this would mean that for a single value of F_{BL}, there are more than one corresponding value of F_{BG}, which is physically impossible. The 45° line passing through point **E** represents even phase split, i.e., the mixtures in the three sides of the junction have the same qualities. For simplicity, the term "point of 0.5" will be used to refer to point **E** in the three parts of Figure 1.2. Also, the term "symmetry of the data" (or "symmetry of prediction" in case of model and correlation predictions) will be used to refer to a data curve of two parts that are the inverted mirror image of each other and pass through the "point of 0.5", or in other words to indicate that the data satisfy mass balance. In the present study, the phase-distribution data and the predictions will be presented on coordinates of F_{BL} vs. F_{BG}.

Another method used to present the phase-distribution data for a horizontal impacting tee is shown in Figure 1.2(c). The ordinate in this figure is the ratio of one of the outlet qualities to the inlet quality (x_3/x_1), and the abscissa is the extraction ratio W_3/W_1. The points labeled **A**, **B**, **C**, **D**, **E**, **F**, **G**, and **H** correspond to the same points given in Figure 1.2(a). The curve **DF** is given by the equation $F_{BL} = 0.5$, or $\frac{x_3}{x_1} = \frac{1}{x_1} - \frac{(1-x_1)}{2x_1(W_3/W_1)}$, while the curve **GH** is given by the equation $F_{BL} = 1.0$, or

$\frac{x_3}{x_1} = \frac{1}{x_1} - \frac{(1-x_1)}{x_1(W_3/W_1)}$. Lines **BC**, **CG**, and **FH** are given by $\frac{x_3}{x_1} = \frac{1}{x_1}$, $\frac{x_3}{x_1} = \frac{W_1}{2W_3}$, and $\frac{x_3}{x_1} = \frac{W_1}{W_3}$, respectively. Points **C**, **D**, **F**, and **G** have the coordinates of $(\frac{x_1}{2}, \frac{1}{x_1})$, $(\frac{(1-x_1)}{2}, 0)$, $(\frac{(x_1+1)}{2}, \frac{2}{(x_1+1)})$, and $(\frac{(2-x_1)}{2}, \frac{1}{(2-x_1)})$, respectively. Data may exist in the hatched areas only. No data can exist outside these two areas. Point **E** has a quality ratio of 1 and an extraction ratio of 0.5. Again, due to geometric symmetry, all the curves representing the data should pass through point **E**.

A review of the currently existing data indicated that limited work has been done on horizontal impacting tee junctions. Few phase-distribution data sets and even fewer pressure-drop data sets have been published. The phase-distribution data cover small ranges of the inlet mass flow rates and qualities. Some models have been developed to predict the phase-distribution over a limited range of inlet conditions. It is therefore desirable to develop models to predict phase distribution and pressure drop for inlet conditions not covered so far.

A fundamental prerequisite to the development of a mathematical model capable of predicting the phase distribution and pressure drop, is a full understanding of the physical phenomena associated with the existing data. Also, the availability of a wide range of experimental data against which any proposed model can be tested will help significantly in the development of a successful model. The purpose of this study, therefore, is to enhance the current state of knowledge on two-phase flow in horizontal impacting tee junctions.

The following is a list of the specific objectives of the present study:

1- To carry out preliminary numerical studies on the hydrodynamic and heat-transfer characteristics of a single-phase flow in impacting and branching junctions with a simplified two-dimensional geometry.

2- To generate experimental data on the phase distribution and pressure drop for air-water mixtures through a horizontal impacting tee junction.

3- To develop new models/correlations for predicting the phase split and pressure drop during two-phase flow in horizontal impacting tees. These models should be capable of predicting the present data, as well as others reported in the literature.

Chapter 2

LITERATURE REVIEW

2.1 Overview

A considerable amount of research has been done on two-phase flow in dividing tee junctions. Most of this research was directed to the geometry of branching tees and excellent reviews of this segment of the literature can be found in Lahey (1986), Azzopardi and Hervieu (1994), and Azzopardi (1999). By contrast, a much smaller number of studies have been reported in the literature on the geometry of impacting tees. As a consequence, serious gaps in knowledge currently exist for this type of junction, particularly on the issue of two-phase pressure drop. The focus in this literature review will be on two-phase flow in impacting tee junctions.

Table 2.1 gives a summary of previously published experimental work on two-phase flow through impacting junctions. Most of the previous work correspond to air-water flows at low pressure; however, some work has been done for wet-steam and R-11 two-phase flows. Table 2.1 includes the previous work for all the inlet orientations and junction geometries. This table indicates a serious lack in pressure-drop data for two-phase flow in impacting junctions with only one reference (Hwang, 1986) reporting such data for bubbly and bubbly-stratified inlet flow regimes. Both the phase distribution and pressure drop are expected to be dependent on the inlet flow regime and therefore, it is mandatory to cover as wide a region as possible of the flow-regime map. The rest of this chapter has as its primary focus two-phase flow through horizontal impacting tee junctions.

Table 2.1 Summary of the previous experimental work on impacting junctions

Author(s)	Junction Geometry and Orientation				D_1 (mm)	$D_2 = D_3$ (mm)	Test Fluids	P_s (bar)	J_{G1} (m/s)	J_{L1} (m/s)	x_1	W_3/W_1	Inlet Flow Regime	Inlet flow regimes are specified based on	Phase Dist.	Press. Drop
	Angle Between Inlet and Outlet 2	Angle Between Inlet and Outlet 3	Inlet Orientation	Outlets Orientation												
Hong (1978)	90°	90°	Horizontal	Horizontal	9.5	9.5	Air - Water	1.22	27.4	0.024	0.62	0.0 - 1.0	An	Barnea et al. (1983)	Yes	No
Hwang (1986)	135° 90°	45° 90°	Horizontal	Horizontal	38	38	Air - Water	1.3 - 2.0	0.9 - 6.3	1.35 - 2.6	0.002 - 0.004	0.02 - 0.96	St Bub-St	Visual observation	Yes	Yes
Lightstone et al. (1991)	90° 120° 135° 150°	90° 120° 135° 150°	Horizontal	Horizontal	20	20	Air - Water	1	0.1 - 2.65	0.01 - 0.18	0.0007 - 0.24	0.5	An , Pl Sl , St St-W	Visual observation	*	**
Chien and Rubel (1992)	90°	90°	Horizontal	Horizontal	49.3	49.3	Steam - Water	28.6 - 42.4	12 - 40	0.052 - 4.17	0.2 - 0.8	F_{BG} = 0.2 - 0.5	An An-Mt	Chien, S.-F (1990)	Yes	No
Ottens et al. (1995)	90°	90°	Horizontal	Horizontal	29.5	29.5	Air - Water	1	15.8	0.00063 - 0.03	0.38 - 0.97	0.0 - 1.0	St-W	Visual observation	Yes	No
Hong and Griston (1995)	90°	90°	Horizontal	Horizontal	19	19	Air - Water	1	4.6 - 22.86	0.023-1.46	0.018 – 0.19	F_{BG} = 0.05 - 0.95	An-Mt St	Visual observation	Yes	No
Fujii et al. (1995)	90°	90°	Horizontal	Horizontal	10	10	Nitrogen - Water	1	0.03 - 12	0.05 - 0.5	0.00007 – 0.22	0.0 - 1.0	An , Pl Sl , St , W	Visual observation	Yes	No
Fujii et al. (1996)	150° 120° 90°	30° 60° 90°	Horizontal	Horizontal	10.5	10.5	Air - Water	1	0.1 - 7	0.05 - 0.5	0.0002 – 0.14	0.0 - 1.0	An , Pl	Visual observation	Yes	***
Asano et al. (1997)	150° 120° 90°	30° 60° 90°	Horizontal	Horizontal	10	10	R-11 (Saturated mixture)	1	0.07 - 19	0.03 - 0.55	0.001 – 0.3	0.0 - 1.0	Pl , Sl	Visual observation	Yes	No
Azzopardi et al. (1986a)	90°	90°	Vertical (Upward)	Horizontal	31.8	31.8	Air - Water	1.7	10.4 - 21.9	0.032 - 0.079	0.21 - 0.58	0.0 - 1.0	An	Visual observation	Yes	No
Azzopardi et al. (1986b)	90°	90°	Vertical (Upward)	Horizontal	31.8	31.8	Air - Water	1.7	1.61 - 4.02	0.08 - 0.8	0.004 - 0.1	0.0 - 1.0	Ch	Visual observation	Yes	No
Wang and Shoji (2002)	90°	90°	Vertical (Upward)	Horizontal	15	15	Air - Water	1	0.09 - 7.08	0.09 - 0.19	0.0006 – 0.084	0.0 - 1.0	Ch	Visual observation	****	****
Wang et al. (2003)	90°	90°	Vertical (Upward)	Horizontal	15	15	Air - Water	1	0.03 - 9.4	0.09 - 0.47	0.00008 – 0.11	0.0 - 1.0	An , Bub Ch	Visual observation	****	****

An = Annular, **An-Mt** = Annular-Mist, **Bub** = Bubbly, **Bub-St** = Bubbly-Stratified, **Ch** = Churn, **Pl** = Plug, **Sl** = Slug, **St** = Stratified, **St-W** = Stratified-Wavy, **W** = Wavy.

* They provided data on the distribution of void fraction upstream and downstream of the junction.

** They reported limited data on the pressure distribution including two locations both upstream and downstream of the junction.

*** They provided data on the total rate of mechanical energy loss due to the junction.

**** They provided data on the root mean square of the fluctuation in the pressure drop and the outlet gas flow rate.

2.2 Phase-Distribution and Pressure-Drop Data

Hong (1978) presented data for phase distribution through a horizontal impacting tee junction. The experiment was conducted with air-water flow in a 9.5-mm I.D. tee with an inlet mass flux of 63.1 (kg/m^2.s) and an inlet quality of 0.62. The data indicated that over a wide range of W_3/W_1 (0.15 to 0.85), even phase split was obtained; i.e. the outlet flows had the same quality as the inlet flow. Data were obtained for one set of inlet conditions only. The trend of Hong's data is quite different from that obtained by later researchers. It was suggested by other researchers that Hong's data may have been affected by strong surface-tension forces due to the small tube diameter and the hydrostatic head of the fluid in the pipes leading to the phase separators (Hwang et al., 1989).

Hwang (1986) and Hwang et al. (1989) presented data for phase distribution and pressure drop through horizontal impacting junctions. Measurements were taken for air-water flows through a 38-mm I.D. tee and a wye at various inlet conditions. The system pressure ranged between 0.13 and 0.2 MPa. Three inlet mass fluxes (1350, 2050, and 2700 kg/m^2.s) were considered with an inlet quality range of 0.1-0.4 %. These inlet conditions resulted in stratified and bubbly-stratified inlet flow regimes. The extraction ratio was varied over a range of 0.02 to 0.96. For the impacting tee, the data indicated that over the whole range of the extraction ratio, there were three distinct zones. The first one started from $W_3/W_1 \approx 0.02$ up to a value between 0.3 and 0.4 in which only liquid was diverted into outlet 3. The second went up to a value of W_3/W_1 between 0.6 and 0.7 in which mixtures of gas and liquid were diverted into both outlets. The last one went to the end of the extraction-ratio range in which all the gas was diverted into

outlet 3. For the impacting wye, the data had the same trend as those of the impacting tee. The only difference was that the zone over which mixtures of gas and liquid were diverted into both outlets started at $W_3/W_1 \approx 0.03$ and ended at $W_3/W_1 \approx 0.3$. Using seven pressure taps on the inlet and eight taps on each of the outlets, Hwang (1986) obtained pressure-distribution data for the above operating conditions. These data were used to obtain the three average junction pressures, P_1, P_2, and P_3 (Figure 1.1).

Lightstone et al. (1991) reported data for the average void fraction and pressure drop for air-water two-phase flow. Four different test sections were used; an impacting tee, and 120°, 90°, and 60° (total angle between the outlets) wyes all positioned horizontally. The experiments were conducted using 20-mm I.D. tubes and results were obtained for equal mass split at the junction, i.e., $W_3/W_1 = 0.5$. Observations of the flow-regime transitions were also reported. Flow-regime maps were developed at four different locations along the test tubes. Two of these locations were upstream of the junction at 37 and 14 pipe diameters. The other two were downstream at 2 and 25 pipe diameters. Void fraction measurements were also taken at these locations. These measurements indicated that a large increase in void fraction occurs just downstream of the junction due to the splitting of the fluid mass flow rate. Two pressure taps on the inlet and another two on each of the outlets were used to obtain pressure measurements. It was reported that an impacting tee junction always produces pressure loss contrary to impacting wyes which may produce pressure recovery. The momentum equations (one-dimensional and separated-flow model) for both phases were developed and used to predict the pressure distribution around the junctions. The model included empirically-determined quantities. The model predictions were compared against the pressure

measurements taken at the above-mentioned locations. The model did not converge for some cases and appeared to predict results inconsistent with the experimental measurements. The model was not presented in enough details to make it executable.

Chien and Rubel (1992) investigated the phase distribution of wet steam through horizontal impacting tee junctions. The tee junction diameter was 49.3 mm. The inlet-pressure range was 28.6 to 42.4 bars, inlet-steam-quality range was 0.2 to 0.8, and the vapour extraction ratio ranged from 0.2 to 0.5. The inlet superficial vapour velocity ranged from 12 to 40 m/s, which gave annular and annular-mist inlet flow regimes. The data showed that the outlet steam qualities were always different from the inlet quality if the vapour extraction ratio was not equal to 0.5. The difference between the inlet and outlet-3 qualities increased as the vapour extraction ratio deviated from 0.5. This difference decreased as the inlet quality increased. For a given inlet quality, outlet-3 quality decreased slightly with increasing inlet vapour velocity. Inlet steam pressure was not found to have a significant effect on the data.

Ottens et al. (1995) reported an experimental and analytical investigation of two-phase flow through impacting tee junctions. Phase-distribution data of air-water flow for four sets of inlet conditions were reported. A superficial gas velocity of 15.8 m/s with four superficial liquid velocities of 0.00063, 0.00302, 0.012, and 0.03 m/s represent the four sets. The inlet-quality range was approximately 0.38 to 0.97. The data indicated that at high qualities, no liquid was diverted into outlet 3 up to a certain gas extraction ratio (F_{BG} of around 0.4). At $F_{BG} = 0.5$ the qualities at the inlet and both outlets were equal, as expected. For gas extraction ratios above a certain value (around 0.6), all the liquid was diverted into outlet 3. At low qualities, no gas was diverted into

outlet 3 up to a certain liquid extraction ratio (F_{BL} of around 0.2). Again, the three qualities were equal at the point of $F_{BL} = 0.5$. For liquid extraction ratios above a certain value (around 0.8), all the gas was diverted into outlet 3. This trend of data at low qualities agrees with the trend obtained by Hwang et al. (1989).

Hong and Griston (1995) reported phase-distribution data for laboratory air-water and field wet-steam flows through horizontal impacting junctions. They also developed an empirical method for predicting phase splitting. They also tested different types of insert devices in order to determine the one that increases the extraction-ratio range over which even phase splitting can be obtained. Laboratory experiments were conducted using a 19-mm I.D. tee with inlet superficial gas velocities between 4.6 and 22.86 m/s and liquid volume fractions ranged from 0.005 to 0.06. The pressure at the junction was near atmospheric. The liquid volume fractions tested corresponded to inlet qualities between 0.19 and 0.018. These are low qualities and one would expect the trend of the data to be similar to that obtained by Hwang (1986) and Ottens et al. (1995). Indeed, this was the case and the only differences were the values of F_{BL} up to which F_{BG} was equal to zero and the value of F_{BL} beyond which F_{BG} reaches 1. The data showed that, at low gas superficial velocity (e.g., 4.6 m/s) and low liquid volume fraction (e.g., 0.01), equal phase splitting occurred over the entire range of the extraction ratio. Also, as the liquid volume fraction increased (or the inlet quality decreased) the data points approach a horizontal line passing through the "point of 0.5" on an F_{BL} vs. F_{BG} plot. It may be noted that the data obtained by Ottens et al. (1995) showed that as the inlet quality increased the data points approached a vertical line passing through the "point of 0.5" on an F_{BL} vs. F_{BG} plot. Data for tees modified with

insert devices showed that the greatest improvements for equal-quality splits were obtained with the preseparator vane, downstream nozzles, and vane/nozzles combination. These devices were tested in the field with wet steam to verify their effects. Field wet-steam tests were done with pipe tees that had diameters of 50 and 100 mm. The inlet steam velocity and the liquid volume fraction ranged from 1.5 to 21.3 m/s and from 0.01 to 0.1, respectively. The data for the 50-mm diameter tee showed that the outlet with the lower vapour flow received a disproportionately higher liquid flow. For the 100-mm diameter tee, the data showed that the liquid and vapour phases split proportionately to each outlet for nearly the entire range of test conditions. The data obtained with the modified tee designs showed that the mixer stratifier did not improve phase separation, the preseparator vane slightly improved phase separation, and the nozzle reducer greatly improved phase separation so that liquid and gas phases split evenly over the entire range of extraction ratio.

Fujii et al. (1995) investigated the effect of the inlet flow regime on phase splitting of nitrogen-water flow through horizontal impacting junctions. The possibility of using the junction as a separator was the main objective. A 10-mm I.D. tee was used with liquid superficial velocities of 0.05 to 0.5 m/s and gas superficial velocities of 0.03 to 12 m/s. These inlet flow conditions corresponded to plug, slug, annular, stratified, and wavy flow regimes. For plug, slug, and annular flows, the data followed the same trend obtained by Hwang (1986), Ottens et al. (1995), and Hong and Griston (1995). No gas was diverted into outlet 3 up to a certain value of the extraction ratio W_3/W_1. This value was called the "gas take-off point". On increasing the extraction ratio, gas started to divert into outlet 3 and data points passed through the "point of 0.5" up to a certain

value where all the gas was diverted into outlet 3. The only exception to the above-mentioned trend was for liquid superficial velocities less than 0.15 m/s with annular flow, where gas and liquid always appeared in outlet 3 no matter what was the value of the extraction ratio. For stratified and wavy flows, the data did not follow the same trend. Instead, gas and liquid were diverted into the two outlets for all values of the extraction ratio. The conclusion was that the phase separation is strongly affected by the inlet flow regime and somewhat affected by the liquid superficial velocity. Experiments were also conducted under microgravity in order to investigate the reliability of an impacting tee junction as a phase separator for two-phase flow thermal control systems in space applications. These two-phase systems have been proposed to replace the single-phase systems used already in space ships because of their compactness and reduced weight.

Fujii et al. (1996) reported phase-distribution and pressure-drop data for air-water flow through horizontal impacting junctions. Experiments were conducted using a tee and wyes of 10.5-mm I.D. with liquid superficial velocities of 0.05 to 0.5 m/s and gas superficial velocities of 0.1 to 7.0 m/s. It was reported that these flow conditions correspond to annular and plug flow regimes. For the impacting tee, the data obtained follow the same trend obtained by Hwang (1986), Ottens et al. (1995), Hong and Griston (1995), and Fujii et al. (1995). No gas was diverted into outlet 3 up to a certain extraction ratio (below 0.5). Increasing the extraction ratio, the data points passed through the "point of 0.5". For extraction ratios above a certain value (higher than 0.5), all the gas was diverted into outlet 3. For the impacting wyes, the data have the same trend as those of the impacting tee. It was found that as the angle between outlet 3 and

the inlet decreased from 90°, the extraction-ratio range over which all the inlet gas was diverted to outlet 3 increased. This is consistent with the impacting wye results of Hwang (1986). The pressure-drop data were reported in terms of the energy loss due to the presence of the junction. For impacting tees, the energy loss was minimum at $W_3/W_1 = 0.5$ and 1.0 while for impacting wyes the minimum occurred at W_3/W_1 between 0.0 and 0.2.

Asano et al. (1997) reported phase distribution data for two-phase one-component flow through horizontal impacting junctions. The inlet mass flux ranged from 63.7 to 828 kg/m^2.s and the inlet quality ranged from 0.001 to 0.3. Refrigerant R-11 was used as the working fluid through a tee and wyes of 10-mm I.D. For the impacting tee, at low qualities, the results followed the same trend obtained by Hwang (1986), Ottens et al. (1995), Hong and Griston (1995), and Fujii et al. (1995). This was the case with differences in values of the "gas take-off point" which is the value of W_3/W_1 at which gas starts to be diverted into outlet 3. For the same inlet conditions, the value of the "gas take-off point" for R-11 was higher than that for air-water. Also, values of the "gas take-off point" for impacting wyes were lower then that of the impacting tee.

Azzopardi et al. (1986a) reported phase-distribution data for air-water flow through an impacting tee with a vertical inlet and horizontal outlets. The flow regime in the vertical inlet was annular. Experiments were conducted using a 31.8-mm I.D. tee with liquid superficial velocities of 0.032 to 0.079 m/s and gas superficial velocities of 10.4 to 21.9 m/s. The pressure at the junction was maintained at 1.7 bar. The results showed that for extraction ratio less than 0.5, the outlet with the lower air flow has proportionately more liquid. For extraction ratios higher than 0.5, the data were mirror

image of the low-extraction-ratio data. Azzopardi et al. (1986a) presented a phase-distribution model and compared the model predictions against the experimental data. The predictions followed the data accurately at the low inlet liquid velocity while they deviated from the data at the high inlet liquid velocity. The model can be used for horizontal inlets if the circumferential variation of the film flow rate is known.

Azzopardi et al. (1986b) reported phase-distribution data for air-water flow through an impacting tee with a vertical inlet and horizontal outlets. The flow regime in the vertical inlet was churn. The tee junction used was the same as the one used for annular flow. The liquid superficial velocities varied from 0.08 to 0.8 m/s and the gas superficial velocities varied from 1.61 to 4.02 m/s. The pressure at the junction was maintained at 1.7 bar. The trend in the results was very similar to those obtained by Azzopardi et al. (1986a) for annular flow. The model used in Azzopardi et al. (1986a) for annular flow was modified and its predictions were compared against the data for churn flow. There was a good agreement between the data and the predictions.

Wang and Shoji (2002) investigated the fluctuation characteristics of two-phase churn flow splitting in an equal-sided impacting tee junction (15 mm I.D.) with a vertical inlet and horizontal outlets. Air-water mixtures at atmospheric pressure and temperature were used with various combinations of inlet gas superficial velocity, inlet liquid superficial velocity, and extraction ratio. The fluctuating nature of the churn flow in the inlet pipe caused fluctuations in the differential pressure ΔP_{13} and the outlet gas flow rate W_{G3}. The root-mean-square amplitude of the fluctuations in ΔP_{13} and W_{G3} were calculated from measured signals. It was found that the root-mean-square amplitude of these fluctuations increased with increases in inlet gas superficial velocity,

inlet liquid superficial velocity, or extraction ratio. Later, Wang et al. (2003) used the same flow loop and extended the test conditions to include bubbly, churn, and annular flows of air-water at atmospheric pressure and temperature. Several measurement methods of chaos dynamics were employed to analyse the fluctuations in the ΔP_{13} signal. Their results suggest that chaotic behaviour exists and that two-phase flow splitting at impacting tees is a complicated nonlinear dynamic system. The averaged data for phase separation and pressure drop were not reported in these two investigations.

Hatziavramidis et al. (1997) analysed the phase separation in branching and impacting tees using conformal mapping and Computational Fluid Dynamics (CFD) modelling. The conformal-mapping approach assumed inviscid, incompressible, and irrotational flow, which limits the results to conditions of high gas flow rate and low volumetric fraction of liquid (where inertia forces dominate). The CFD model assumed two-dimensional flow with a specific formation for the interfacial drag. A commercial code called K-FIX was used in the simulations and the resulting system of algebraic equations was found to be ill-posed in most conditions. A few comparisons were presented between these predictions (whenever the numerical results were reasonable) and experimental results from the literature showing reasonable agreement.

2.3 Phase-Distribution Models

2.3.1 Hwang (1986) Model

Hwang (1986) developed an analytical model for predicting the phase distribution at horizontal impacting tees (the model is also reported in Hwang et al., 1989). The model is claimed to work for all the flow regimes and is based on the

dividing-streamline approach. That is, a " zone of influence" exists for each phase and that each "zone of influence" is bounded by a dividing streamline, as shown in Figure 2.1. In Figure 2.1, all liquid entering the inlet of the junction on the left hand side of the liquid dividing streamline, line (**b**) in Figure 2.1, will exit through outlet 3 of the junction and the remaining liquid will exit through outlet 2. The gas phase behaves in a similar manner with its split between outlets 2 and 3 defined by the gas dividing

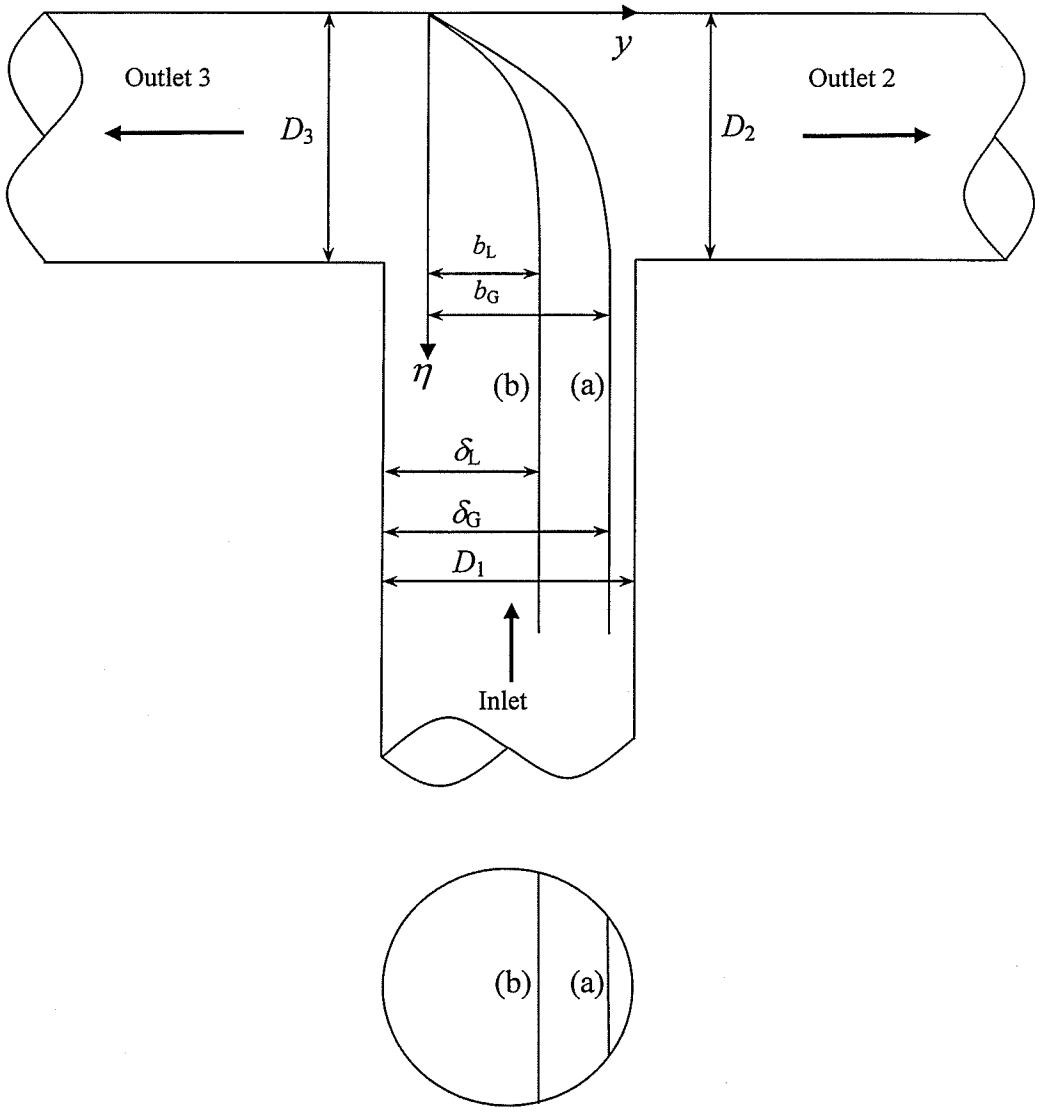

Figure 2.1 Zone of influence and the dividing streamline for the Hwang (1986) model

streamline, line (**a**) in Figure 2.1. Figure 2.2 shows the dominant forces acting on the gas and liquid for a typical junction with streamlines crossing with an angle ϕ. In Figure 2.2, V_{G1} and V_{L1} are the average velocities of the gas and liquid phases, respectively, F_{DG} and F_{DL} are the drag forces generated due to the phasic slip and acting on the gas and liquid, respectively, R_G and R_L are the radii of curvature of the gas and liquid streamlines, respectively, ρ_G and ρ_L are the gas and liquid densities, respectively, and $(\rho_G V_{G1}^2/R_G)$ and $(\rho_L V_{L1}^2/R_L)$ are the centrifugal forces acting on the gas and liquid, respectively, in normal directions to their streamlines. The procedure for executing the model can be divided up into three distinct parts:

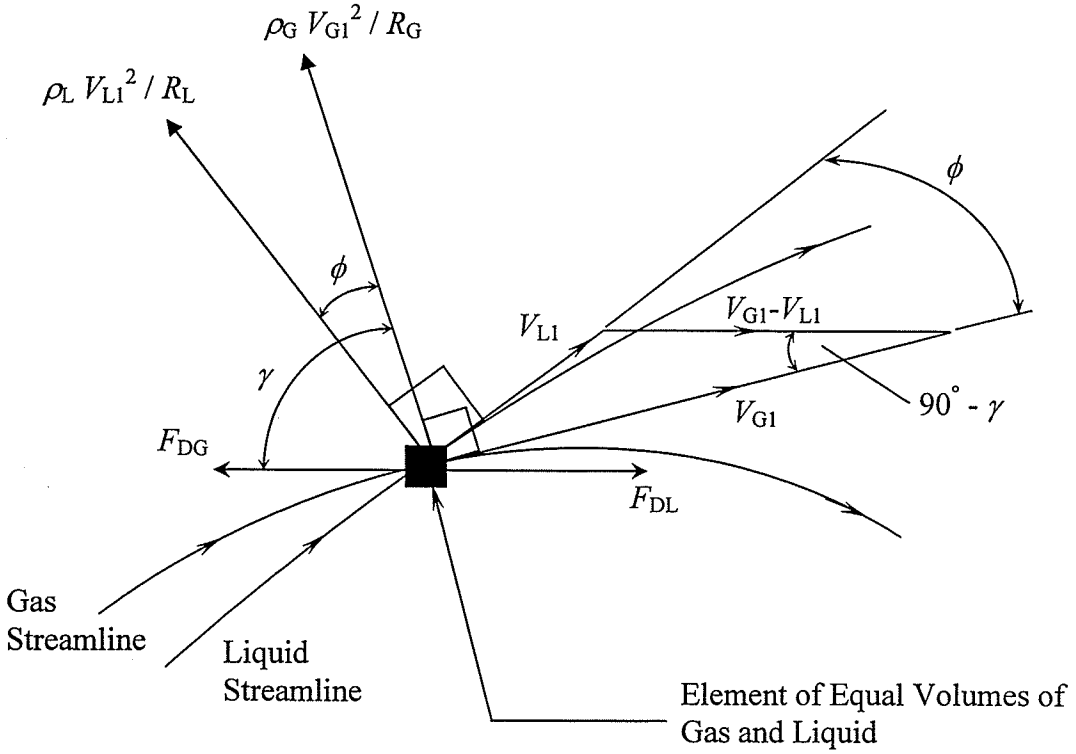

Figure 2.2 Balance of forces at a streamline crossing for the Hwang (1986) model

1- To calculate the value of the slip ratio, $S = V_{G1} / V_{L1}$.

2- To solve for δ_G and the corresponding δ_L, with reference to Figure 2.1.

3- To convert values of δ_G and δ_L to values of F_{BG} and F_{BL}.

Hwang (1986) compared the model predictions against his experimental data and the data of Azzopardi et al. (1986a). Comparisons revealed that model predictions were quite satisfactory. It should be mentioned that, the first and the third parts of the procedure are dependent on the flow regime, while the second one is common for all the flow regimes. In the present study, for stratified, wavy and annular flow regimes, the physical and geometrical models given in Shoham et al. (1987) were used for the first and third parts of the procedure. A justification for using these models is given in Section 4.2.1 and the models are described in detail in Appendix A. The inlet conditions (J_{G1} and J_{L1}), fluid properties (ρ_G, ρ_L, μ_G, and μ_L), junction geometry (D_1 and D_3), and the inlet flow regime, are required as input data for the model. The following steps demonstrate how the model was executed:

1- Using models given in Appendix A, the value of the slip ratio, S, can be determined.

2- Initiate a value for (b_G/D_1) that may be from 0 to 1; usually a value of 0.05 is recommended as a start.

3- Calculate $(R_G/D_3)_{min}$, $(R_L/D_3)_{min}$, and R_G/D_3 from

$$(R_G/D_3)_{min} = [\ 1+ (2\ D_1/D_3)^2\ ]^{3/2} / (2\ D_1/D_3)\ =\ (R_L/D_3)_{min}, \qquad (2.1)$$

$$R_G/D_3 = (R_G/D_3)_{min} / (b_G/D_1)^N, \qquad (2.2)$$

where N is an empirical coefficient and is equal to 5.

4- Solve for the value of m_G iteratively from

$$R_G/D_3 = [\ 1+ (\ m_G\ b_G\ /D_3\ )^2\ ]^{3/2} / [m_G\ (\ m_G - 1\ )\ b_G\ /\ D_3] \qquad (2.3)$$

where m_G is a coefficient that has a value between 1 and 2 and is related to the shape of the gas dividing streamline.

5- Calculate γ_{min} and γ_{max} from

$$\gamma_{min} = \cos^{-1}(1/S), \tag{2.4}$$

and

$$\gamma_{max} = \pi = 3.14159. \tag{2.5}$$

6- Assume a value for γ between γ_{min} and γ_{max}.

7- Calculate ϕ, R_L/R_G, R_L/D_3, and b_L/D_1 from

$$\phi = \gamma - \cos^{-1}(S \cos(\gamma)), \tag{2.6}$$

$$R_L/R_G = \{ [\cos(\phi) - \sin(\phi) / \tan(\gamma)] / [\rho_G \ S^2/\rho_L] \}, \tag{2.7}$$

$$R_L/D_3 = (R_L/R_G)\ (R_G/D_3), \tag{2.8}$$

and

$$b_L/D_1 = [\ (R_L/D_3)_{min} / (R_L/D_3)\ ]^{1/N}. \tag{2.9}$$

8- Solve for the value of m_L iteratively from

$$R_L/D_3 = [\ 1 + (\ m_L\ b_L/D_3\ )^2\ ]^{3/2} / [m_L\ (\ m_L - 1\ )\ b_L/D_3]. \tag{2.10}$$

where m_L is a coefficient that has a value between 1 and 2 and is related to the shape of the liquid dividing streamline.

9- Calculate b_L/D_1 from

$$b_L/D_1 = \tan [\ \tan^{-1}(\ m_G\ b_G/D_3\ ) - \phi\ ]\ ((D_3/D_1)/m_L\ )\ ]. \tag{2.11}$$

10- Compare b_L/D_1 calculated from step (9) with the one calculated from step (7). If agreement within acceptable tolerance is not achieved, the assumed value for γ in step (6) should be modified and steps (7) to (10) repeated until convergence is achieved.

11- From the converged value of b_L/D_1 and the initiated value of b_G/D_1, calculate δ_L and δ_G from

$$\delta_L = (D_1/2)\,(\,(\,b_L/D_1\,)+1\,), \tag{2.12}$$

and

$$\delta_G = [\,1+(\,b_G/D_1\,)-(\,\delta_L/D_1\,)\,]\,D_1. \tag{2.13}$$

12- Using models given in Appendix A, and with the calculated values of δ_L and δ_G, values of F_{BG} and the corresponding F_{BL} can be determined.

13- The value of b_G/D_1 initiated in step (2) was increased and the steps from (3) to (12) were repeated. The stopping criterion was that neither F_{BG} nor F_{BL} should exceed 1.0.

It should be mentioned that the Hwang (1986) model as described above generates values of F_{BG} and F_{BL} within the range from 0.5 to 1. "Symmetry of prediction" was used in order to complete the curve.

2.3.2 Ottens et al. (1995) Model

Ottens et al. (1995) developed an analytical model to predict the phase distribution at horizontal impacting tees. Their model is based on the double-stream model of Hart et al. (1991) which was developed for dividing branching junctions and for liquid hold-up less than 0.06 in the inlet. The double-stream model was derived from the steady-state macroscopic mechanical energy balance (extended Bernoulli Equation) applied to the inlet-to-run stream and the inlet-to-branch stream of both gas and liquid phases. According to the double-stream model, the value of F_{BL} is a function of the value of F_{BG}, geometry of the junction, and the ratio κ defined as the ratio of the kinetic energies of the gas and liquid per unit volume in the inlet. Ottens et al. (1995) discarded some of

the assumptions assumed earlier by Hart et al. (1991) in order to develop their own model which was called the advanced double-stream model that can work over the whole range of liquid hold-up in the inlet, from 0 to 1. Ottens et al. (1995) compared the predictions of the double-stream model and the advanced double-stream model against their experimental data. Comparison revealed that there was satisfactory agreement between the experimental data and the double-stream-model predictions. Also, the advanced double-stream model did not result in a significant improvement of the agreement between the experimental data and predictions. In the present study, we shall focus only on the double-stream model. For given inlet conditions (J_{G1} and J_{L1}), fluid properties (ρ_G, ρ_L, μ_G, and μ_L), and junction geometry (D_1), the value of F_{BL} at a certain value for F_{BG} can be determined using the following set of equations:

$$Re_{SL1} = \rho_L J_{L1} D_1 / \mu_L, \tag{2.14}$$

$$\varepsilon_{L1} = ((1 / [(J_{L1} / J_{G1})\{1+10.4 (Re_{SL1})^{-0.363} (\rho_L / \rho_G)^{0.5}\}]) + 1)^{-1}, \tag{2.15}$$

$$\alpha_1 = 1 - \varepsilon_{L1}, \tag{2.16}$$

$$V_{G1} = J_{G1} / \alpha_1, \tag{2.17}$$

$$V_{L1} = J_{L1} / \varepsilon_{L1}, \tag{2.18}$$

$$\theta_{L1} = 0.52 (\varepsilon_{L1})^{0.374} + 0.26 \{ J_{L1}^2 \rho_L / \varepsilon_{L1}^2 g D_1 (\rho_L - \rho_G) \}^{0.58}, \tag{2.19}$$

$$Re_{L1} = Re_{SL1} / \theta_{L1}, \tag{2.20}$$

$$Re_{G1} = \rho_G D_1 V_{G1} / \mu_G, \tag{2.21}$$

$$\beta_G = 1.54 \text{ if } Re_{G1} < 1500, \tag{2.22a}$$

$$\beta_L = 1.54 \text{ if } Re_{L1} < 1500, \tag{2.22b}$$

$$\beta_G = 1.54 - 0.54 [(Re_{G1} - 1500) / 500] \text{ if } 1500 < Re_{G1} < 2000, \tag{2.22c}$$

$$\beta_L = 1.54 - 0.54 [(Re_{L1} - 1500) / 500] \text{ if } 1500 < Re_{L1} < 2000, \tag{2.22d}$$

$\beta_G = 1.0$ if $Re_{G1} > 2000$, (2.22e)

$\beta_L = 1.0$ if $Re_{L1} > 2000$, (2.22f)

$\kappa = \beta_G \rho_G V_{G1}^2 / (\beta_L \rho_L V_{L1}^2)$, (2.23)

$\lambda_0 = 0.5 (1 + K_{12} - K_{13}) = 0.5$ (on average) , (2.24)

and

$F_{BL} = \lambda_0 + \kappa (F_{BG} - \lambda_0)$, (2.25)

where,

Re_{SL1} is the superficial Reynolds number of the liquid in the inlet,

ε_{L1} is the liquid hold-up in the inlet,

α_1 is the void fraction in the inlet,

V_{G1} and V_{L1} are the average inlet velocities of the gas and liquid, respectively,

θ_{L1} is the fraction of the pipe wall wetted by the liquid in the inlet,

Re_{G1} and Re_{L1} are the inlet Reynolds numbers for the gas and liquid, respectively,

β_G and β_L are constants dependent on the velocity distribution of the corresponding phase,

λ_0 is the junction energy dissipation factor, and

K_{12} and K_{13} are frictional loss coefficients between the inlet and outlets 2 and 3, respectively.

It should be noted that the Ottens et al. (1995) model is independent of the inlet flow regime. Also, with a value of 0.5 for λ_0 Equation (2.25) would be a straight-line equation.

2.3.3 Concluding Remarks

Two empirical correlations (Hong and Griston (1995) and Chien and Rubel (1992)) and two analytical models (Hwang (1986) and Ottens et al. (1995)) have been developed for predicting the phase distribution at impacting tee junctions with horizontal inlet and outlet sides. An extensive study of these models and correlations was reported in El-Shaboury (2000) and El-Shaboury et al. (2001). It was found that the Hong and Griston (1995) correlation does not satisfy mass balance and produces unreasonable values of F_{BL} at small values of F_{BG}. Also, it is not capable of good predictions for the bubbly, plug, and slug flow regimes. The Chien and Rubel (1992) correlation was found to be insensitive to x_1. The correlation is also limited to the applicable range of P_1, namely from 28.6 to 42.4 bar, given by the authors of the correlation. However, the correlation was found to give the best available predictions for high-inlet-pressure steam-water data. The Ottens et al. (1995) model is applicable to all the flow regimes and it was found to give reasonable agreement with the data of air-water; and it was recommended as the best available prediction tool for air-water data with annular, plug, and slug flow regimes. The Hwang (1986) model was not applied to the slug flow regime because of lack of accurate information on the void fraction for this flow regime. However, it was recommended as the best available prediction tool for air-water data with bubbly and wavy flow regimes. Based on the above, the Hwang (1986) model and the Ottens et al. (1995) model were described in the previous sections. These models will be compared against the data to be generated in this study in order to test their validity for the present conditions.

2.4 Pressure-Drop Models

To date, and to the best of the author's knowledge, no pressure-drop model for two-phase flow in impacting tee junctions exists. On the other hand, there are some correlations for single-phase pressure drop in impacting tee junctions. The following sections describe two of them.

2.4.1 Ito and Imai (1973) Correlation

Ito and Imai (1973) carried out an experimental study where they investigated the pressure drops caused by the combination and division of flow at smooth tees with a diameter ratio of unity. Ito and Imai (1973) also studied the effect of the radius of curvature of the tee junction on the pressure drops. One of the configurations tested was an impacting tee junction with a zero radius of curvature. The working fluid was water and the inlet Reynolds number, Re_1, was in the range of 1×10^5 to 2×10^5. In that range, it was found that Reynolds number has little influence on the loss coefficients. Ito and Imai (1973) gave empirical formulae that were in good agreement with their experimental results. The formula given for equal-sided sharp-edged impacting tee junctions (i.e., zero radius of curvature at pipe intersections) is

$$K_{13} = 0.59 + 1.18\,(W_3/W_1) - 0.68\,(W_3/W_1)^2 \qquad (2.26)$$

where W_1 and W_3 are the mass flow rates in the inlet and outlet 3, respectively, and K_{13} is the pressure loss coefficient between the inlet and outlet 3, defined as

$$K_{13} = (P_1 - P_3)_{irr} / (\rho V_1^2/2) \qquad (2.27)$$

where V_1 is the inlet velocity, and $(P_1 - P_3)_{irr}$ is given by

$$P_1 - P_3 = \rho\left(\frac{V_3^2}{2} - \frac{V_1^2}{2}\right) + (P_1 - P_3)_{irr} \qquad (2.28)$$

Here P_1 and P_3 are the junction average pressures in the inlet and outlet 3, respectively (see Figure 1.1). Equation (2.26) was recommended for the range $0.2 \leq (W_3/W_1) \leq 0.8$.

2.4.2 Hwang (1986) Correlation

Hwang (1986) carried out an experimental study where he investigated phase distribution and pressure drop in equal-sided tee junctions with a diameter ratio of unity. Hwang also conducted single-phase tests and obtained the pressure loss coefficients for different tee configurations. For the single-phase tests, the working fluid was water and the inlet Reynolds number, Re_1, was approximately in the range of 51,300 to 102,600 (assuming a temperature of 20 °C). The formula given for impacting tee junctions is

$$K_{13} = 1.755 - 1.809\,(W_3/W_1) - 0.4686\,(W_3/W_1)^2 \qquad (2.29)$$

where W_1 and W_3 are the mass flow rates in the inlet and outlet 3, respectively, and K_{13} is the pressure loss coefficient between the inlet and outlet 3, defined as

$$K_{13} = \frac{\left[(P_1 - P_3) + \frac{1}{2}\rho(V_1^2 - V_3^2)\right]}{\rho\frac{V_1^2}{2}} \qquad (2.30)$$

Here, as above, P_1 and P_3 are the junction average pressures in the inlet and outlet 3, respectively (see Figure 1.1). It can be easily verified that the pressure loss coefficient, K_{13}, defined in Equation (2.30) is the same as that defined by Equations (2.27) and (2.28). As well, Equation (2.29) does not show any dependence on the inlet Reynolds number, Re_1, similar to Equation (2.26), the correlation by Ito and Imai (1973). Figure 2.3 shows the variation of K_{13} with W_3/W_1 given by Equations (2.26) and (2.29). It can be seen that the two correlations give completely different results in terms of trend and

magnitude. These different results suggest that more work is needed even for single-phase flow in order to confirm the junction pressure drop.

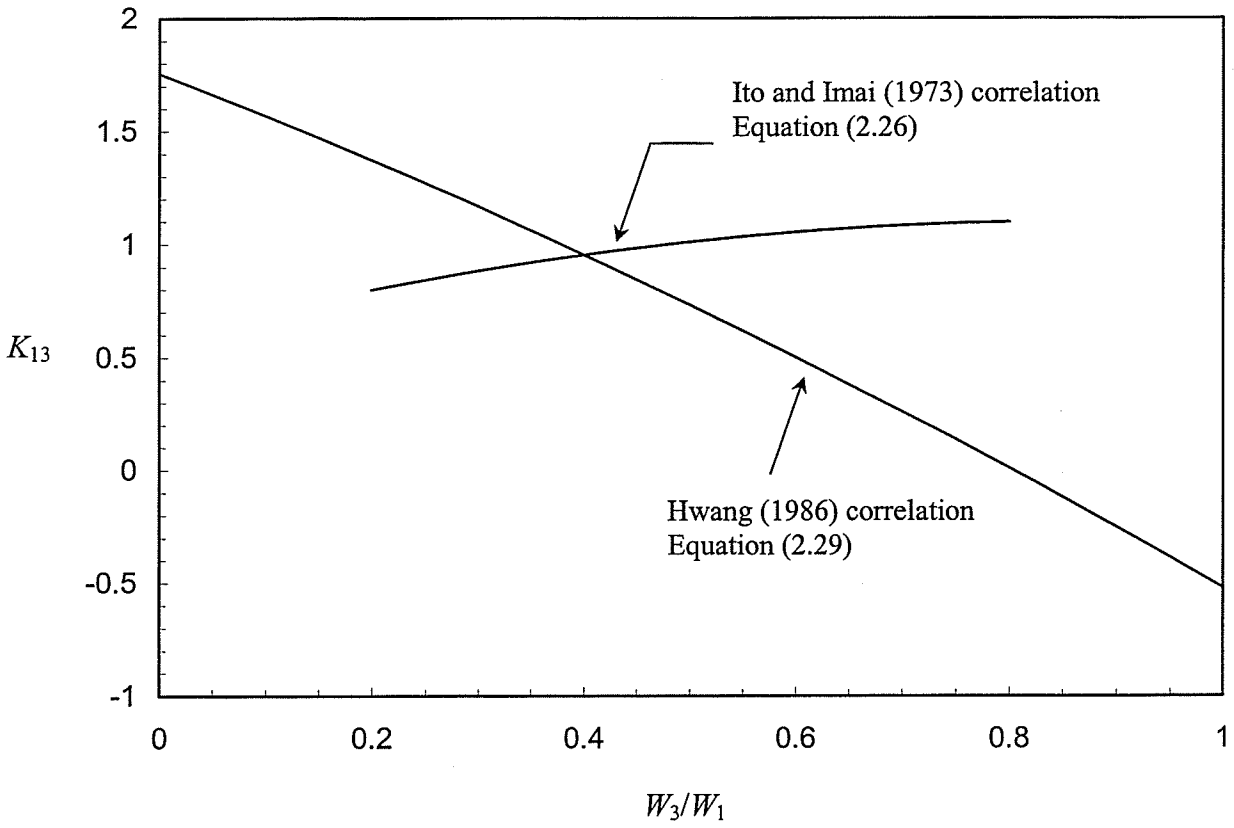

Figure 2.3 Single-phase loss coefficients K_{13}

Chapter 3

EXPERIMENTAL TEST FACILITY

3.1 Overview

One of the objectives of the present study is to generate phase-distribution and pressure-drop data for air-water two-phase flow through a horizontal impacting tee junction. The test facility constructed to achieve this objective incorporated a horizontal impacting tee junction with the three sides having equal diameters (37.85 ± 0.03 mm I.D.), and was designed for the following operating conditions: pressure (P_s) of about 150 kPa (abs) at the junction, near ambient temperature (T_1), inlet superficial gas velocities (J_{G1}) ranging between 0.5 and 40 m/sec, inlet superficial liquid velocities (J_{L1}) ranging between 0.0026 and 0.18 m/sec, and extraction ratios (W_3/W_1) between 0 and 1. These conditions were selected for the following reasons:

1- To cover ranges of J_{G1} and J_{L1} that were not covered before. Figure 3.1 shows the inlet conditions proposed in this study and the areas previously covered for the phase distribution of air-water flows plotted on the Mandhane et al. (1974) flow-regime map. Figure 3.2 shows the same map with the areas covered in previous work on pressure drop (see Section 2.2 for details on the phase-distribution and pressure-drop data obtained before). The present inlet conditions shown in Figures 3.1 and 3.2 were labelled according to the visually observed inlet flow regime. The three major flow regimes (stratified (S), wavy (W), and annular (A)) were identified using the descriptions given in Mandhane et al. (1974). The description used in identifying the transitional stratified-wavy (SW) flow regime was as follows: the

gas-liquid interface appeared smooth most of the time with intermittent small waves appearing on the surface.

2- To test relatively high-inlet-quality flows, as most of the work done earlier on phase distribution was for low-inlet-quality flows (see Table 2.1).

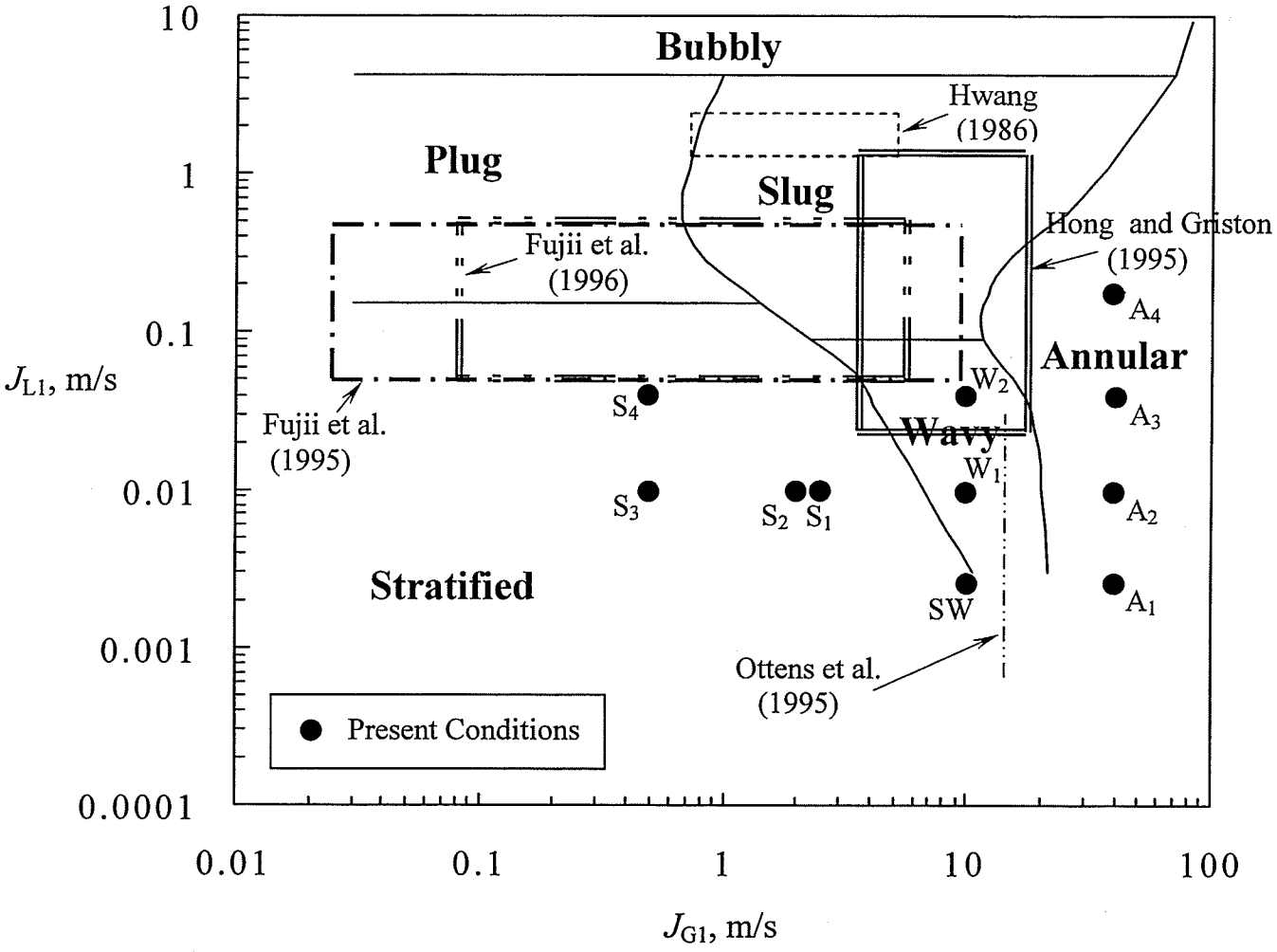

Figure 3.1 Range of inlet conditions for phase-distribution experiments (past and present) with horizontal impacting tee junctions plotted on the Mandhane et al. (1974) flow-regime map

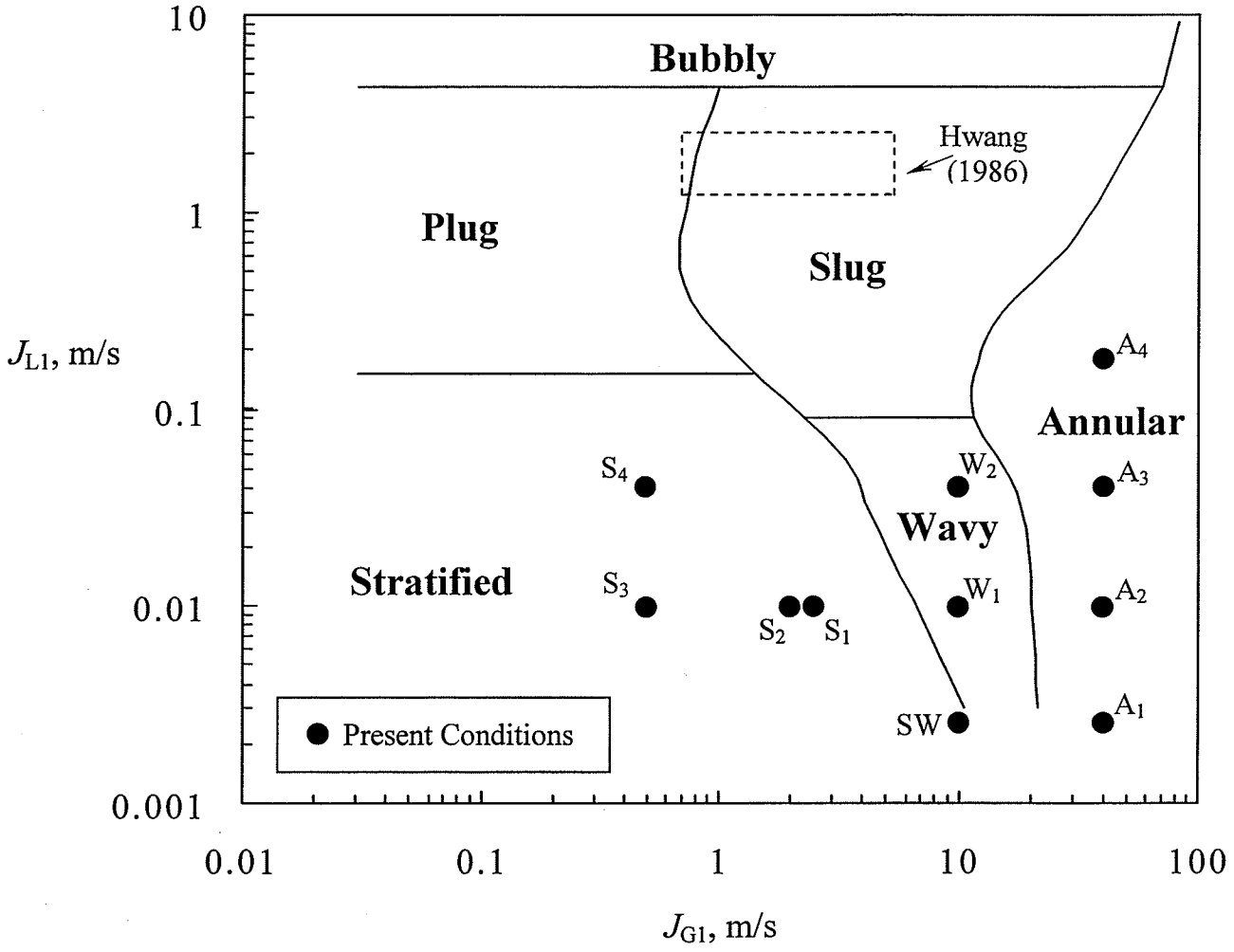

Figure 3.2 Range of inlet conditions for pressure-drop experiments (past and present) with horizontal impacting tee junctions plotted on the Mandhane et al. (1974) flow-regime map

3.2 Air-Water Loop

3.2.1 Overview

The flow loop that was designed for this study is shown in Figure 3.3. The following paragraph describes briefly the flow through the different components of the loop. A more detailed description of the design and construction of the main components of the loop is given later.

Distilled water used in the system was stored in the water reservoir. Water, fed from the reservoir by a centrifugal pump, was metered by one of two turbine meters in parallel (W_{L1}) before flowing into the two-phase mixing tee (mixer), where it was mixed with the gas phase (air). Heat absorbed by the water due to flow through the pump and from frictional losses was removed by a cooling coil installed inside the reservoir. Air flow from the building supply passed through an air filter and a pressure controller for cleaning and pressure control, respectively. The air flow was metered using one of two turbine meters in parallel (W_{G1}) before flowing into the mixer. A developing length of 67.5 tube diameters was allowed before the two-phase mixture entered a visual section, and a further 66 tube diameters was provided before entering the tee junction which was made from acrylic for visualization. Forty-one pressure taps were installed along the test-section inlet and the two outlets in order to determine the pressure distribution around the junction. Each of the two outlet two-phase mixtures was directed to its respective separation tank. The flow rate of liquid from each separation tank was metered using a combination of five rotameters, arranged in parallel, to give individual measurements of each outlet liquid flow rate, W_{L2} and W_{L3}. The two outlet liquid lines were then rejoined before returning to the water reservoir.

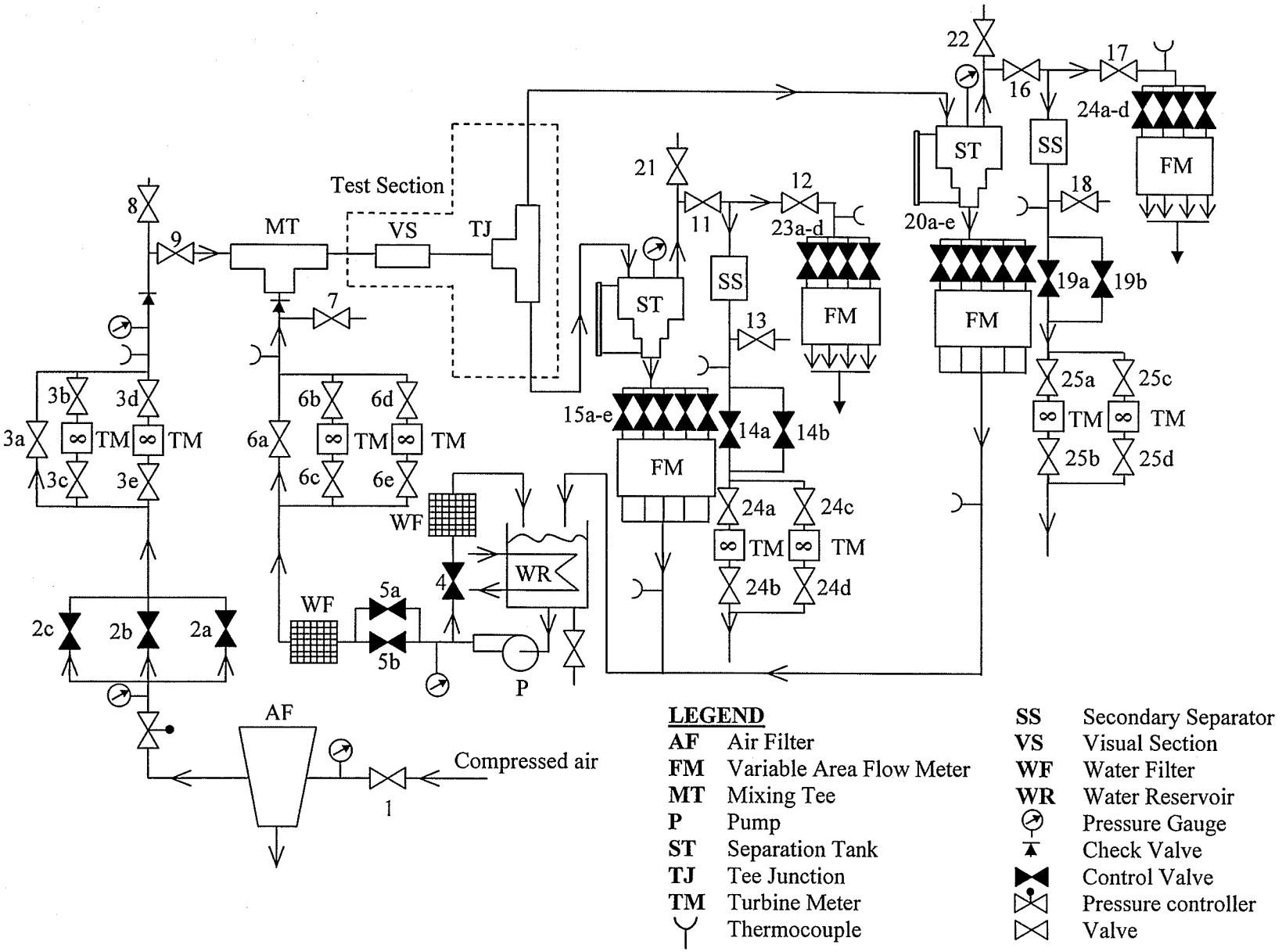

Figure 3.3 Schematic diagram of the experimental facility

The gas phase exited each of the two separation tanks through its respective throttling valve, which were used to control both the extraction ratio W_3/W_1 and the test-section pressure, before being metered by one of two turbine meters in parallel (for high flow rates), or a combination of four rotameters arranged in parallel (for low flow rates). This gave individual measurements of the two outlet air flow rates, W_{G2} and W_{G3}. Both air flows were then discharged into the atmosphere. The control valves appearing in parallel in Figure 3.3 were of different sizes, allowing, with appropriate selection, fine control of the flow.

3.2.2 Water-Flow-Rate Measurement

The inlet water flow rate, W_{L1}, was metered using one of two turbine meters arranged in parallel. Both turbine meters were manufactured by Flow Technology Inc. The model numbers and flow ranges were as follows:

Model	**Calibrated Range**
FT0-4C1YW-LHC-1	0.457 – 4.645 l/min
FT6-8C1YW-LED-1	3.065 – 16.075 l/min

Depending on the inlet flow conditions, the turbine with the appropriate range was selected. Output from each turbine meter was fed into its respective signal converter (Flow Technology Inc., RC51-1-C-0000-6) which converted the turbine meter output into a 0 to 10 volt DC signal. This DC signal was then fed to a channel in the data-acquisition system where a calibration curve was applied.

These two turbine meters were calibrated using a collection tank, scale, and timer. By collecting the water that passed through a turbine meter over a measured period of time and weighing the collected water, the mass flow rate was obtained and compared

against the meter reading. In the working ranges, the calibrations obtained were typically within ±3 % of the manufacturer's values.

The water flow rates from the two separation tanks, W_{L2} and W_{L3}, were metered using rotameters. Each flow-measurement station consisted of a bank of five rotameters arranged in parallel to give a wide measurement range, as shown below.

For the outlet-2 bank of rotameters:

Model	**Calibrated Range**
Cole-Parmer, tube number N082-03ST	3.0 - 44.3 ml/min
Cole-Parmer, tube number FM102-05ST	11.4 - 260 ml/min
Cole-Parmer, tube number N044-40C	74.2 - 1903 ml/min
Cole-Parmer, tube number N044-40C	77.8 - 1895 ml/min
Fisher Porter, 10A3555A	2661 - 12647 ml/min

Thus, this flow measurement station was capable of flow-rate measurement over the range of 3 to 12647 ml/min.

For the outlet-3 bank of rotameters:

Model	**Calibrated Range**
Cole-Parmer, tube number FM082-03ST	0.81 - 46.6 ml/min
Cole-Parmer, tube number FM102-05ST	6.2 – 209 ml/min
Cole-Parmer, tube number FM044-40C	73.1 – 1915 ml/min
Cole-Parmer, tube number FM044-40C	95.6 - 1925 ml/min
Fisher Porter, 10A3555A	2636 – 13019 ml/min

Thus, this flow measurement station was capable of flow-rate measurement over the range of 0.81 to 13019 ml/min.

Depending on the inlet water mass flow rate, W_{L1}, and the extraction ratio, W_3/W_1, the flows through the two outlets were directed to the appropriate rotameter or group of rotameters. The reading of the rotameter in use was entered manually into the data-acquisition system where a calibration curve was applied.

All rotameters were calibrated using a collection tank, scale, and timer with the same method as the inlet water turbine meters. In the working ranges, the calibrations obtained were typically within ±4 % deviation from the manufacturers' values.

3.2.3 Air-Flow-Rate Measurement

The inlet air flow rate, W_{G1}, was metered using two turbine meters manufactured by Flow Technology Inc. These turbine meters were arranged in parallel with the following standard-conditions calibrated ranges:

Model	Calibrated Range
FT-12C1YA-PEA-1	0.062 – 0.597 m^3/min
FT-24C1YA-GEA-1	0.673 – 3.413 m^3/min

Depending on the inlet flow conditions, the turbine with the appropriate range was selected. Output from each turbine meter was fed into its respective signal converter (Flow Technology Inc., RC51-1-C-0000-6) which converted the turbine meter output into a 0 to 10 volt DC signal. This DC signal was then fed to a channel in the data-acquisition system where a calibration curve was applied.

These two turbine meters were calibrated using a combination of three venturi tubes of varying sizes. The venturi tubes were manufactured by Fox Valve Development Corp. and have throat diameters of 0.375, 0.625, and 1.00 inches. In the working ranges, the calibrations obtained were typically within ±6 % deviation from the manufacturer's values.

The air flow rates through outlets 2 and 3, W_{G2} and W_{G3}, were measured by either turbine meters (for high flow rates), or rotameters (for low flow rates). For each outlet, two turbine meters were arranged in parallel, as was a bank of four rotameters. The four

air turbine meters were manufactured by Flow Technology Inc. The calibrated ranges at standard conditions are given below.

For the outlet-2 turbine meters:

Model	Calibrated Range
FT-12C1YA-PEA-1	0.062 – 0.662 m^3/min
FT-24C1YA-GEA-1	0.725 – 3.372 m^3/min

For the outlet-2 bank of rotameters:

Model	Calibrated Range
Cole-Parmer, tube number FM082-03ST	47.5 – 1474 ml/min
Cole-Parmer, tube number FM102-05ST	630 – 8209 ml/min
Cole-Parmer, tube number FM044-40C	2929 – 48290 ml/min
Cole-Parmer, tube number FM044-40C	3057 – 48941 ml/min

For the outlet-3 turbine meters:

Model	Calibrated Range
FT-12C1YA-PEA-1	0.062 – 0.646 m^3/min
FT-24C1YA-GEA-1	0.691 – 3.302 m^3/min

For the outlet-3 bank of rotameters:

Model	Calibrated Range
Cole-Parmer, tube number FM082-03ST	47.5 – 1528 ml/min
Cole-Parmer, tube number FM102-05ST	650 – 8797 ml/min
Cole-Parmer, tube number FM044-40C	3096 – 51412 ml/min
Cole-Parmer, tube number FM044-40C	2772 – 52570 ml/min

The air leaving through each of the two outlets was directed through the appropriate turbine meter, rotameter, or combination of rotameters, depending on the inlet air mass flow rate, W_{G1}, and the extraction ratio, W_3/W_1. If a turbine meter was selected, its output was fed into its signal converter (Flow Technology Inc., RC51-1-C-

0000-6), which converted the turbine meter output into a 0 to 10 volt DC signal. The DC signals were then fed into individual channels in the data-acquisition system. If a rotameter was selected instead, its reading was entered manually into the data-acquisition system.

The outlet air turbine meters were calibrated using the same method as that for the inlet air turbine meters. In the working ranges, the calibrations obtained were typically within ±6 % deviation from the manufacturer's values.

The rotameters were calibrated using a combination of large and small wet test-meters. The wet test meters were manufactured by Elster-Handel GmbH. At standard conditions, the small and large wet test meters have a maximum flow rate of 0.6 and 15 m^3/hr, respectively. In the working ranges, the calibrations obtained were typically within ±3 % deviation from the manufacturers' values.

3.2.4 Temperature Measurement

Eight thermocouples, located as indicated in Figure 3.3, were used to measure the temperature in the experimental facility. The three thermocouples used to measure the water temperature were type T, copper-constantan. The other five used to measure the air temperature were type J, iron-constantan. The readings of the thermocouples were fed into prescribed channels in the data-acquisition system.

Calibration of the thermocouples and the data-acquisition system was done using a water bath and a precision mercury thermometer. The distilled water was set to temperatures corresponding to the water triple point (≈ 0° C), boiling point (100° C), and some other intermediate points. The difference between the precision thermometer and the data-acquisition-system readings were usually in the range of ±0.5° C.

3.2.5 Mixer

A schematic diagram of the two-phase mixer is shown in Figure 3.4. The entire mixer was constructed from copper tubing and fittings, which were soldered together. Air was brought in through a 51-mm I.D. tube. Water entering the mixer through a 12.7-mm I.D. copper tube was injected into the air flow through a large number of 1.6-mm diameter holes. The resulting two-phase mixture was then discharged from the mixer and allowed to become fully developed over a length of 67.5 diameters before entering the visual section.

3.2.6 Test Section

A schematic diagram of the test section and adjoining equipment is shown in Figure 3.5. The piping used for the construction of the test section was special-order copper tubing with 37.8-mm I.D. and 41.3-mm O.D. The entire test section, including the mixer, was supported by a rigid steel frame. A differential water level (accurate to 1.5 mm) was used to ensure horizontality of the test section. The water level consisted of two connected water columns, one of them was placed on a reference point and the other was placed on the point to be levelled. The height of this point was adjusted to match the height of the reference point. Once this procedure was done and repeated for many points on the test section, the test section was assumed horizontal. Special care was taken in levelling the tee junction using more sensitive means. The following is a brief description of the major components in the test section:

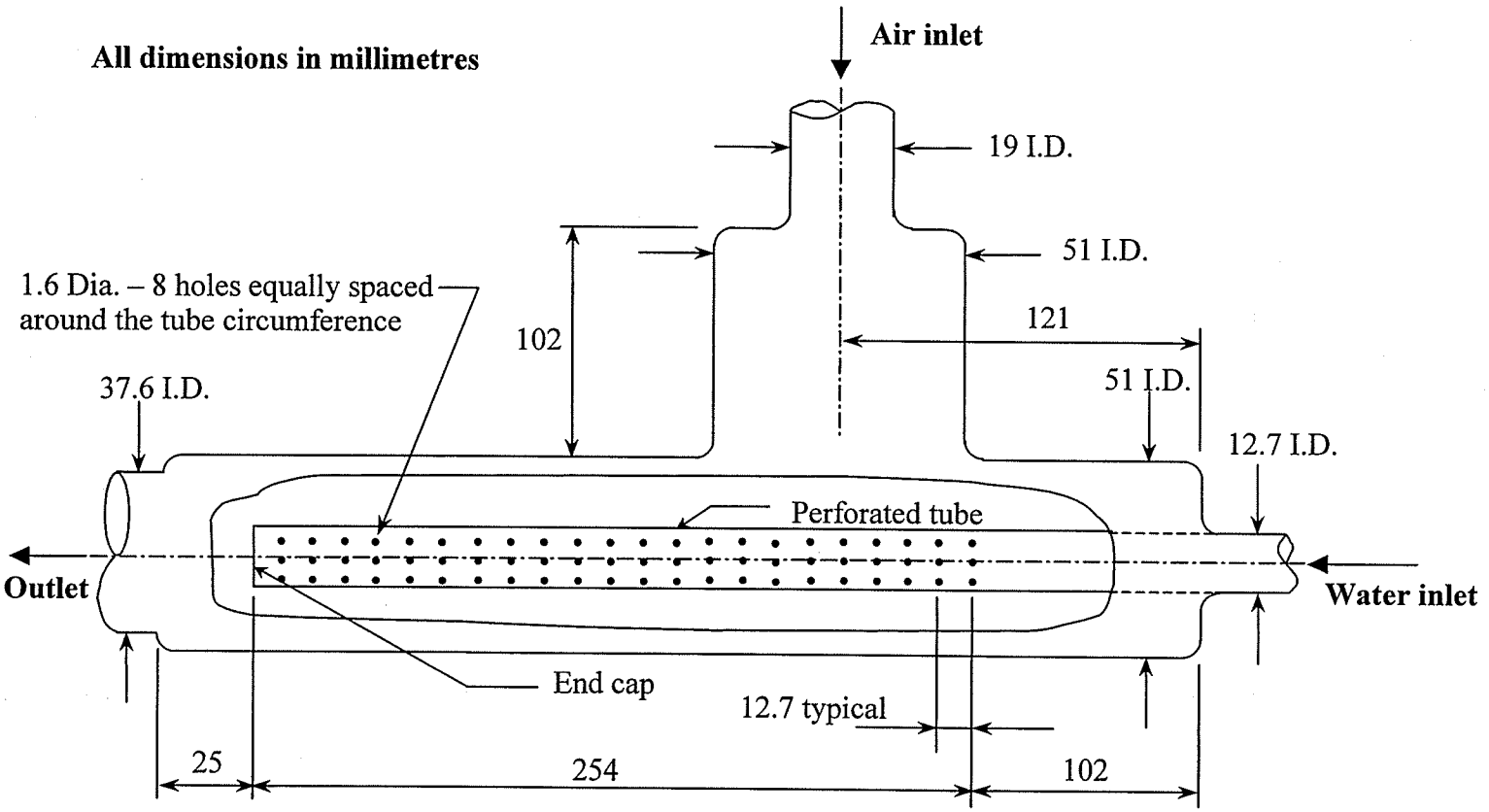

Figure 3.4 Schematic of the two-phase mixer; from Van Gorp (1998)

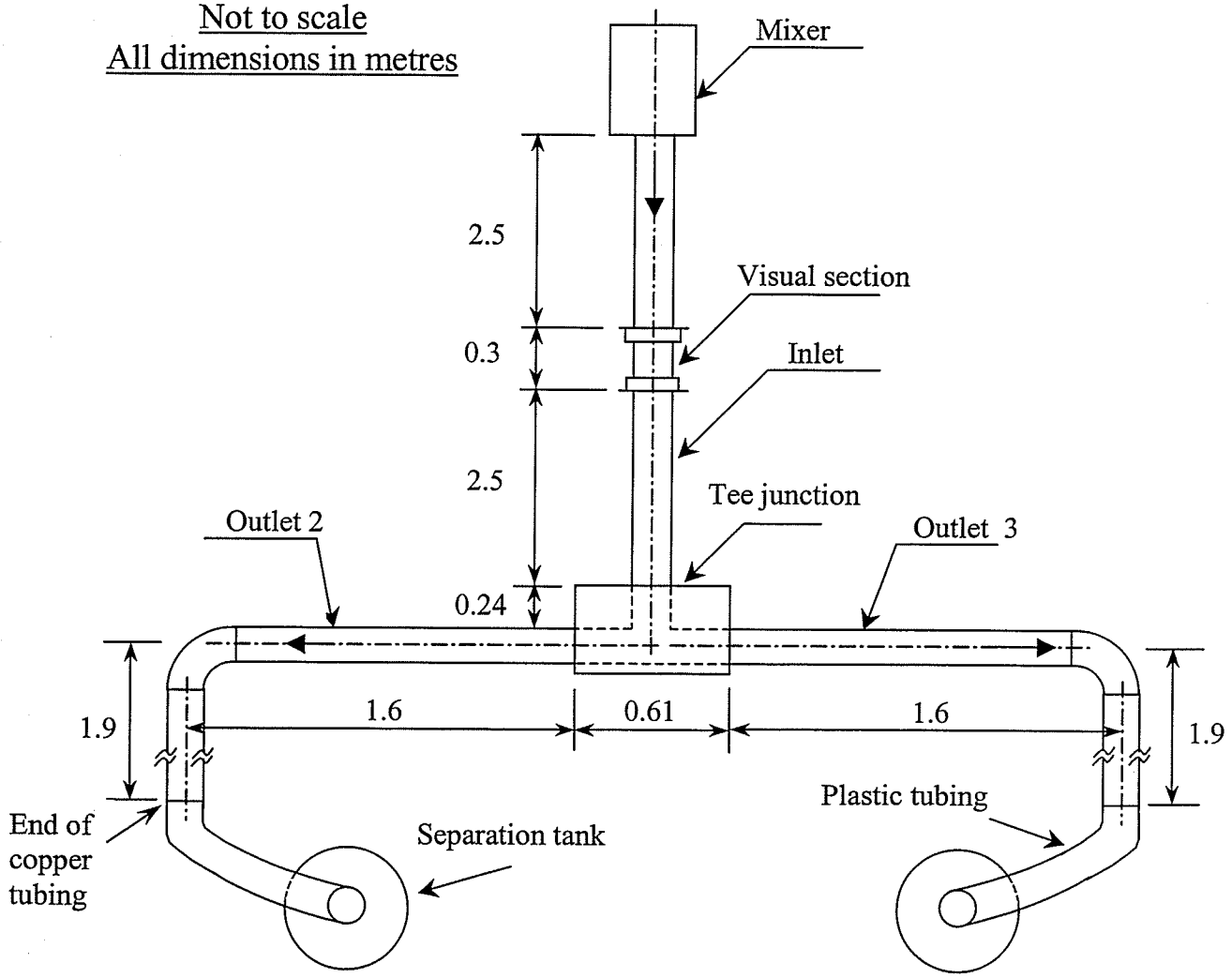

Figure 3.5 Top view of the test section (visual section, inlet, tee junction, outlet 2, and outlet 3) and adjoining equipment

Visual Section

A visual section was incorporated in the inlet pipe 67.5 diameters downstream from the mixer. This visual section was used to observe and classify the inlet flow regime. For the two outlets, the acrylic tee junction was used for visualization. The

visual section, shown in Figure 3.6, consists of a 254-mm long glass tube supported at both ends by special stuffing boxes. The design of the glass tube and stuffing boxes is such that the inside diameter of the glass tube and stuffing boxes are almost identical to the inside diameter of the copper tubing entering and exiting visual section. This eliminated any disturbance to the flow. After assembly, a clear length of about 150 mm was available for flow-regime observation. Since the inside diameter of the commercial glass tubing did not match that of the copper tubing, custom-manufactured glass was used. This also allowed for the selection of a thick-wall (3.45 mm) glass tubing. In assembling the visual section, extreme care was taken to ensure alignment and coaxiality between the copper tubing, stuffing boxes, and the glass tube. The entire assembly was enclosed by a plastic protective shield to guard against injury in case of fracture of the glass tube.

Tee Junction

In order to ensure consistency with other research laboratories, a square-edged tee is used. The tee junction was machined in a 101.6 x 304.8 x 609.6 mm acrylic block. Two perpendicular holes of 37.85±0.03 mm I.D. were drilled out to construct the junction, as shown in Figure 3.7. The three sides of the tee junction were connected to the copper tubing using three specially-machined copper flanges 101.6 x 101.6 mm (Figure 3.8). These copper flanges were soldered to the copper tubing and bolted to the acrylic block. At the acrylic-copper interfaces, O-rings were used for sealing. The inside diameters of the tee-junction holes and the copper flanges were the same as those of the copper tubing with differences within the range 0-0.05 mm. Care was taken in order to ensure that the junction, copper flanges, and the copper tubing were coaxial.

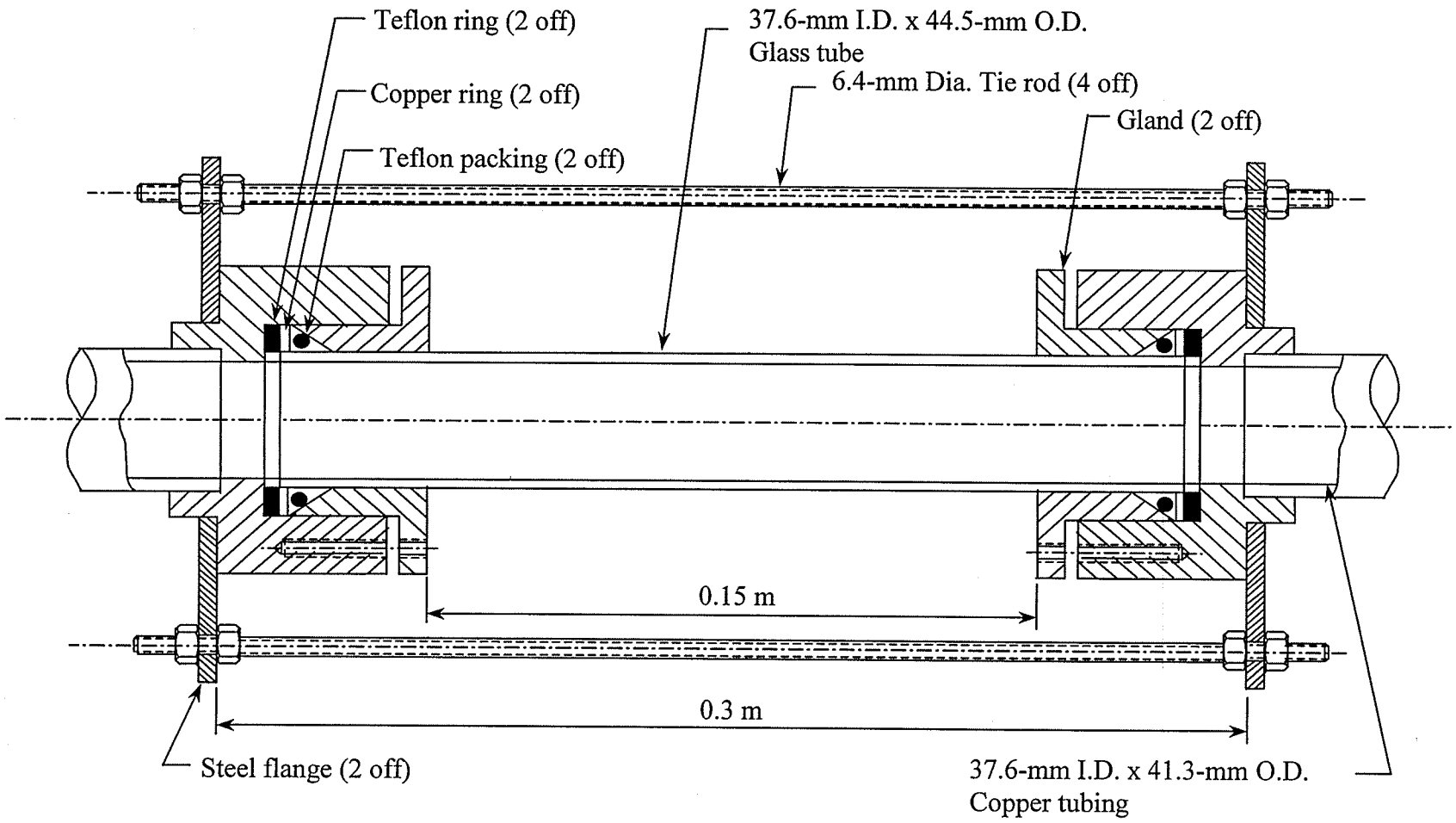

Figure 3.6 Details of the visual section; from Van Gorp (1998)

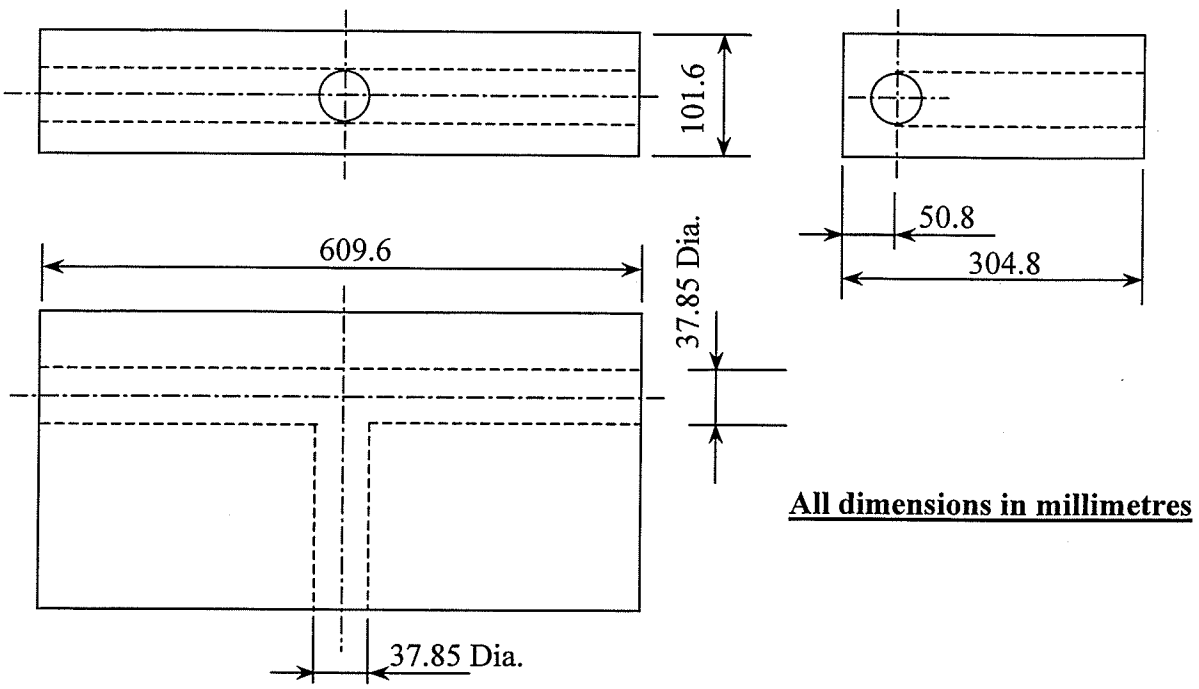

Figure 3.7 Tee junction machined in the acrylic block

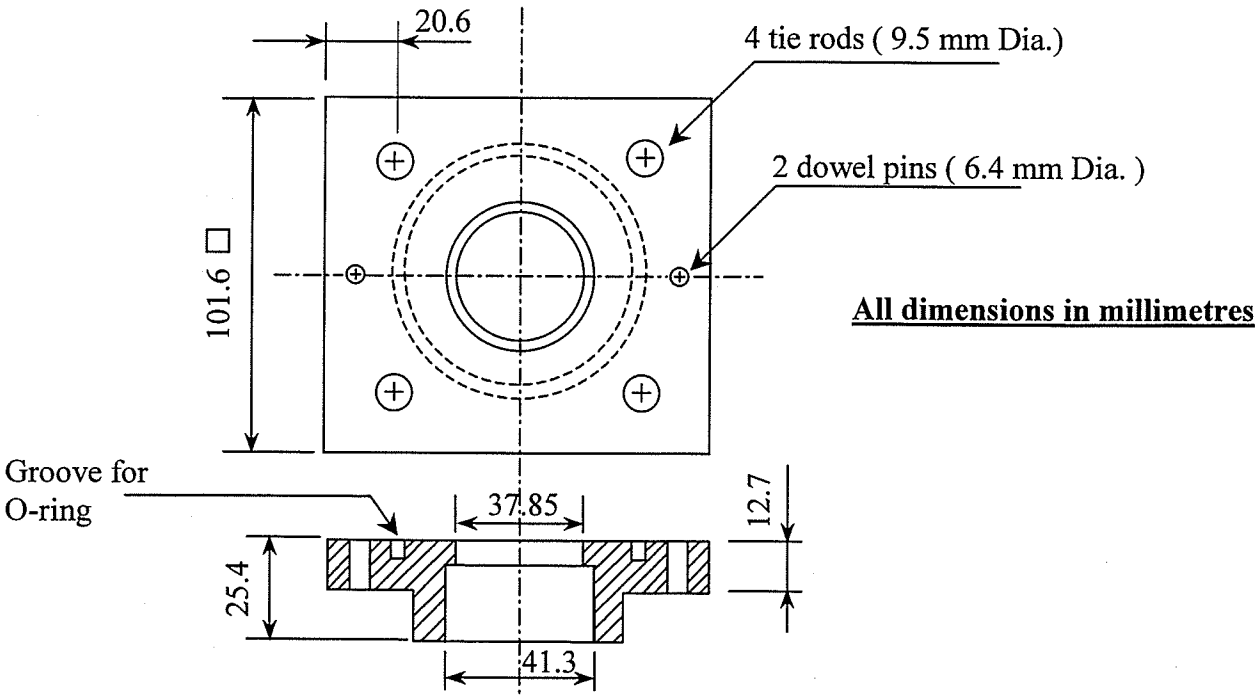

Figure 3.8 Detailed dimensions of the copper flanges

Pressure Taps

Forty-one pressure taps were installed along the whole test section, as shown in Figure 3.9. Twelve taps were drilled in the acrylic block, while the others were drilled in the copper tubing. For those drilled in copper tubing, a 1.6-mm hole was drilled through the tube wall. After drilling, any internal burrs were removed from the inside of the tube. Hose-nipple fittings were soldered onto the outside of the copper tube to facilitate connection between the tap and the differential pressure transducers used to measure the pressure distribution in the test section. Clear plastic tubing (Tygon) was used to connect the pressure taps to the pressure transducers. The pressure taps were located along the bottom side of the test section in order to avoid air entrapment in the plastic tubing pressure lines, which were filled with distilled water. For those taps drilled in the acrylic block, a special arrangement was used in order to connect the pressure tap hole to the pressure transducer. The details of this arrangement are shown in Figure 3.10.

3.2.7 Separation Tanks

The two-phase mixture discharging from both outlets goes into separation tanks located downstream of the test section. The two tanks, shown in Figure 3.11, were identical in design. They were made of type 304 stainless steel Sch. 40 pipe. All the fittings connecting the stainless steel tanks to copper tubing were dielectric unions. A 600-mm long sight glass was used to observe visually the liquid level in the tank, and it was equipped with a vertical scale. A pressure gauge and a safety valve set at 3.45 atm (50 psi) were installed on the tank top blind flange.

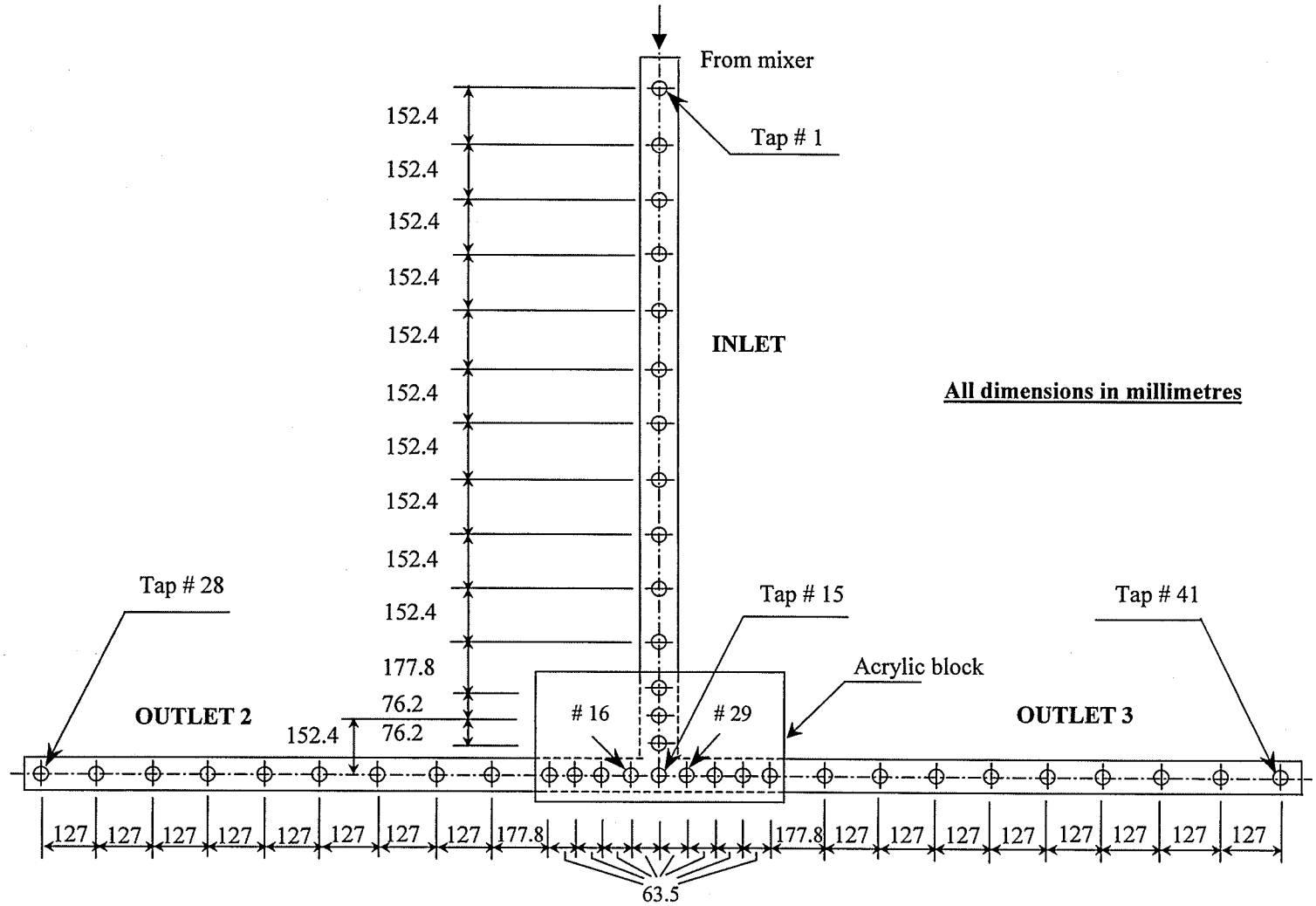

Figure 3.9 Pressure taps locations

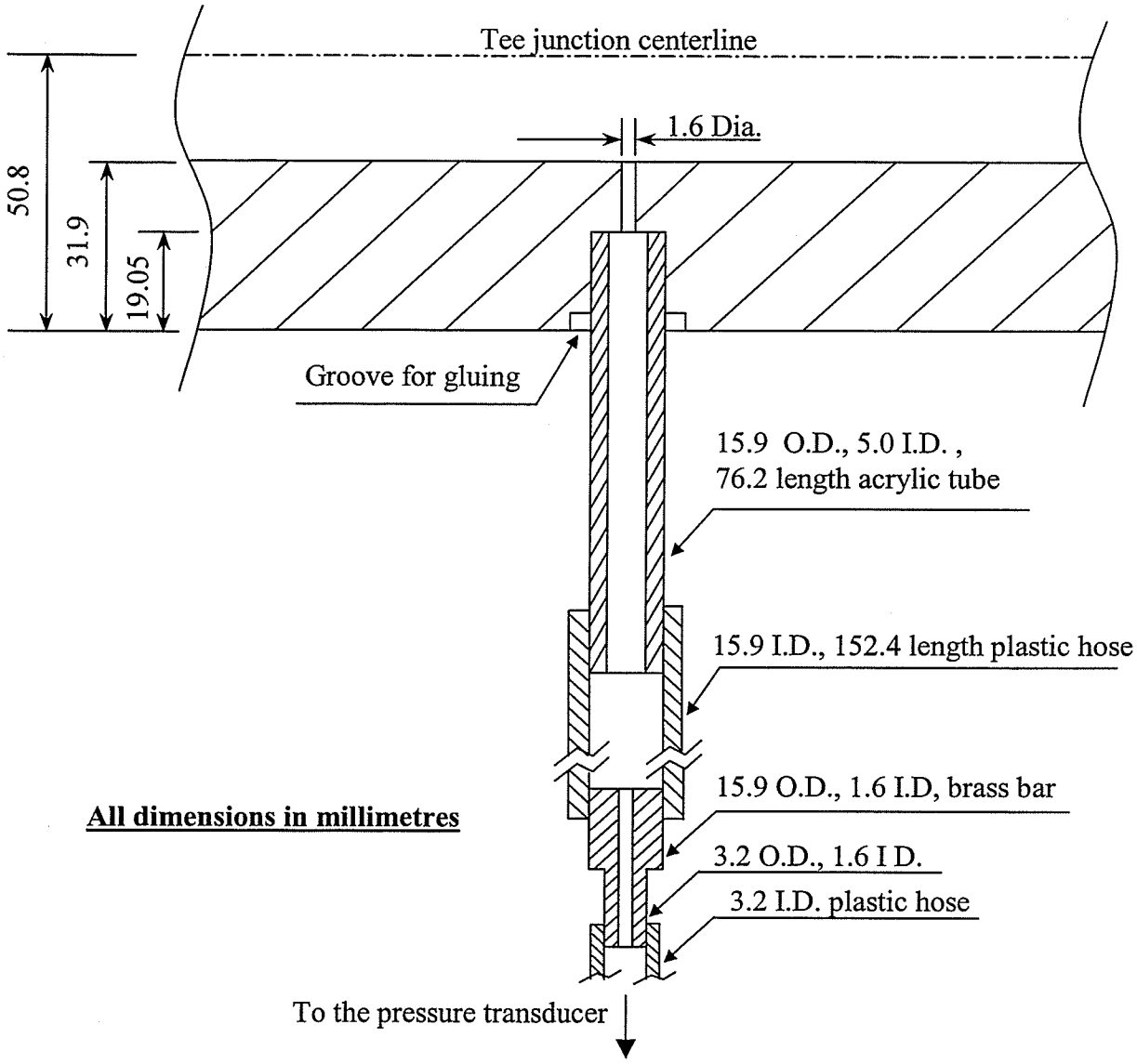

Figure 3.10 Arrangement for the tee-junction pressure taps

The two-phase mixture entering from the top of each separation tank was separated using centrifugal action. This was achieved by forcing the flow in a downward spiralling direction. Water exiting from the nozzles flows along the tank wall where it drained downward. Air exited through the top of each separation tank. Baffle 1 was

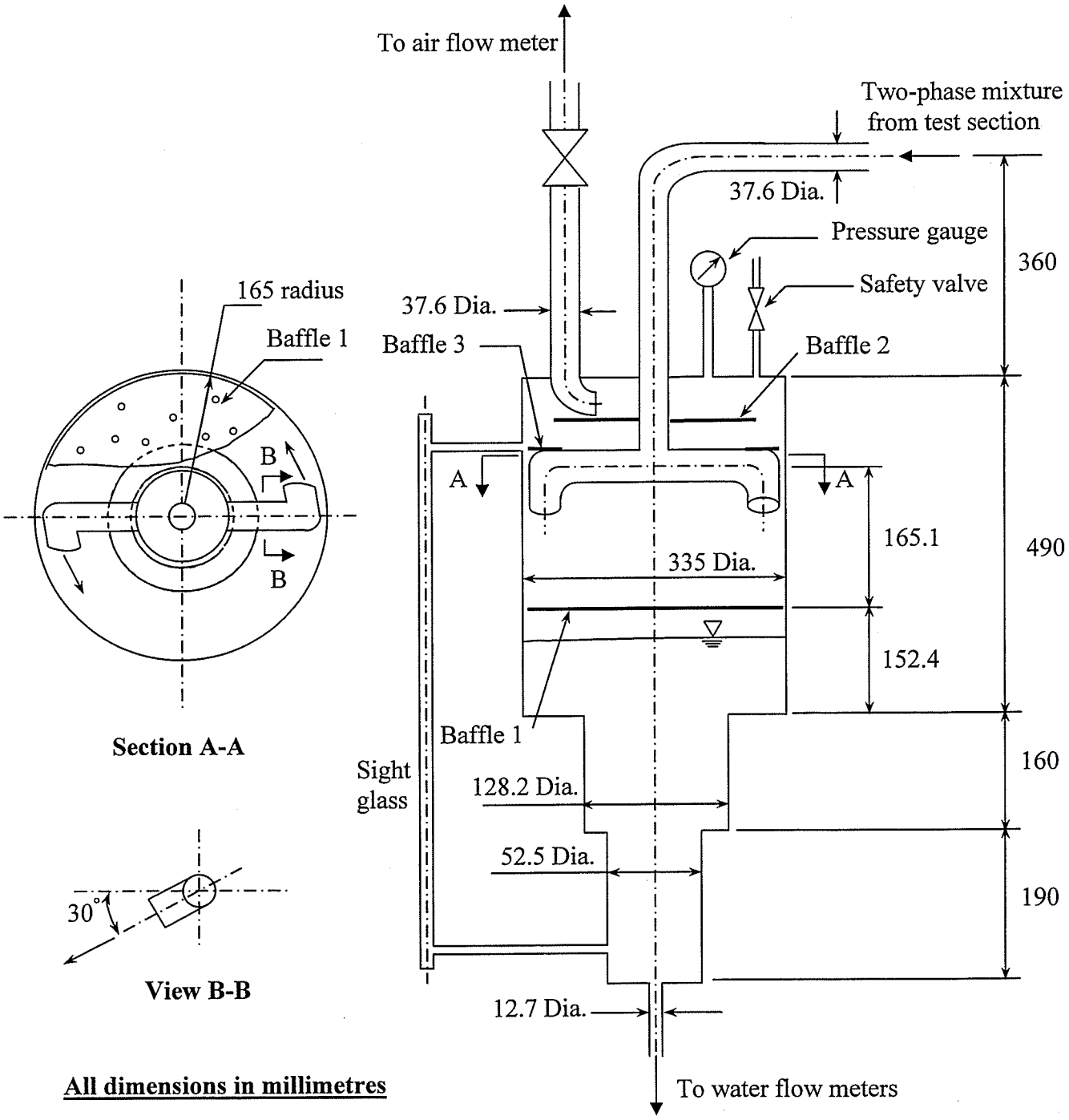

Figure 3.11 Details of a separation tank

located above the gas-liquid interface to isolate the interface from the flow above it so that the interface remained reasonably undisturbed. Baffle 1 is a circular disk made of stainless steel and perforated with many small holes (4.8-mm dia.). It has a diameter smaller than that of the inside of the separation tank; a gap of 3.2 mm was left for the water to flow downward through. Baffle 2 is a circular disk made of stainless steel and located 6.35 mm beneath the air outflow elbow to protect the air outflow from tiny water droplets expected to be formed due to the impact of the incoming two-phase flow on baffle 1. Baffle 2 has a diameter of 239 mm, which makes its area almost half of the tank cross-sectional area. Baffle 3 is an annulus made of stainless steel and located 63.5 mm beneath baffle 2. The inside diameter of baffle 3 is 213 mm and therefore, there is an overlap between baffles 2 and 3 of 13 mm on the radius. The outside diameter of baffle 3 is 305 mm, which leaves a gap of 15 mm between baffle 3 and the inside wall of the separation tank for the water to flow downward. The function of baffle 3 is the same as baffle 2, i.e., to prevent the exiting air from entraining water droplets.

The tanks incorporate two abrupt changes in the cross-sectional area. If the liquid flow rate into a particular tank was low, the gas-liquid interface in the tank was maintained in one of the smaller diameter sections. This procedure decreased the error in measuring the outlet liquid flow rate resulting from small changes in the height of the interface with time.

As a precaution, two secondary separators were installed downstream of the main separation tanks on the air pipes. The purpose of these secondary separators was to eliminate any water droplets which might have escaped from the main separators. The secondary separators were basically air filters installed without the filtration element.

The filters had built-in sight glasses to observe the water accumulation. For all the experiments done in this study, water was not accumulated in the secondary separators, i.e., complete phase separation was achieved in the main separators.

3.3 Pressure Measurement

3.3.1 System Pressure

The system (test section) pressure, P_s, is defined as the absolute pressure right at the centre of the tee junction. This location corresponds to tap number 15 in Figure 3.9. The system pressure was always set to a value of about 150 kPa (abs).

The system pressure was measured using a Rosemount 1151DP6E22B2C6 pressure transducer. The DP-Rosemount pressure transducers measure the pressure difference between two compartments separated by a diaphragm. The transducer output is a current signal varying between 4 and 20 mA. Using a 500-ohm resistor, that signal was converted to a DC-voltage signal which in turn was fed into the data-acquisition system. The Rosemount-1151DP6E22B2C6 pressure transducer can be set to measure any differential pressures in the range of 0-689.5 kPa. This transducer was calibrated and set to measure pressure differentials in the range of 0-101.6 kPa. The calibration process was done using a mercury manometer, foot pump, and multimeter. The calibration curve was found to be highly linear, as expected.

During the experiment, the low leg of the system-pressure transducer (transducer 0 in Figure 3.12) was open to the atmosphere. The high leg was connected to either tap 15 or tap 14. The reason was that it was thought in the event of large pressure fluctuations at tap 15, tap 14 might give more stable readings. However, in practice, it was never necessary to measure the system pressure from tap 14.

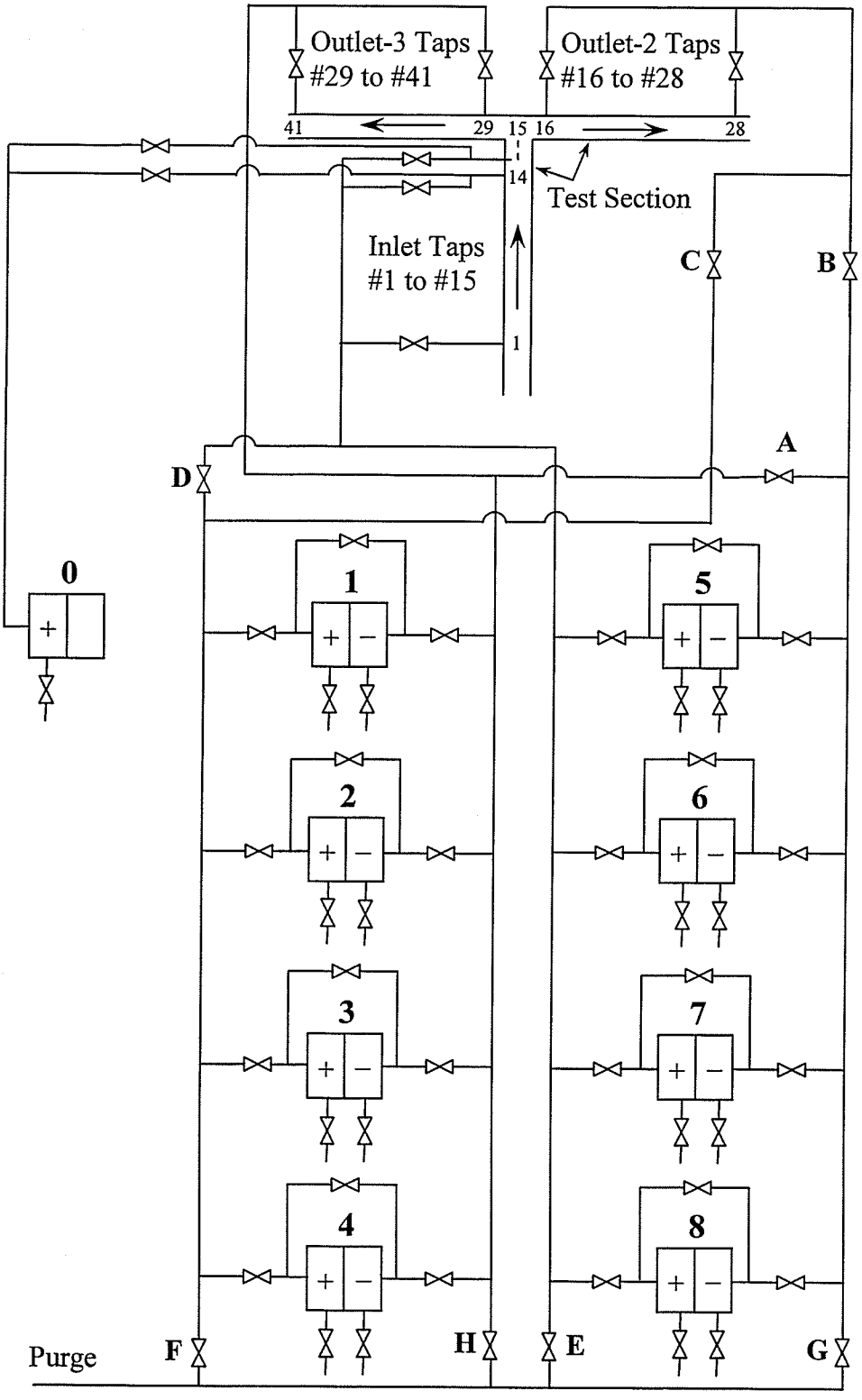

Figure 3.12 Pressure-drop measurement station

3.3.2 Pressure Distribution

The pressure measurement station is shown in Figure 3.12. The station consists of two banks with four Rosemount pressure transducers in each bank. The following are their models and ranges:

Bank 1:

Model	Calibrated Range
Transducer 1, 3051CD0A02A1AH2B1C6	± 7.62 cm water
Transducer 2, 1151DP3E22B2C6	± 76.2 cm water
Transducer 3, 1151DP4E22B2C6	± 381 cm water
Transducer 4, 1151DP5A22MB	± 1905 cm water

Bank 2:

Model	Calibrated Range
Transducer 5, 3051CD0A02A1AH2B1C6	± 7.62 cm water
Transducer 6, 1151DP3E22B2C6	± 76.2 cm water
Transducer 7, 1151DP4E22B2C6	± 381 cm water
Transducer 8, 1151DP6E22B1C6	± 1905 cm water

All the above transducers have an output-current signal varying between 4 and 20 mA. Using 500-ohm resistors, these signals were converted to DC-voltage signals which in turn were fed into the data-acquisition system.

The calibration process for the above transducers was done using a manometer, foot pump, and multimeter. Depending on the calibrated range of the transducer, one of the following manometers was used: water micromanometer, water manometer, or mercury manometer. The calibration curves were all found to be linear.

The valving system shown in Figure 3.12 allowed the pressure taps to be connected to selected transducers that have the appropriate ranges. A detailed description of the pressure measurement procedure is given in Section 3.5.1.

All pressure lines shown in Figure 3.12 were filled with distilled water. The pressure lines were clear 3.2 mm Tygon tubing that allowed for visual inspection to ensure that no air bubbles were trapped within the lines.

The purge line shown in Figure 3.12 allowed for purging the system (removing the air from the lines) using pressurized water. Purging was done, and repeated if necessary, before the start of all the experiments done in this study.

3.4 Data-Acquisition System

The data-acquisition system consists of a multifunction I/O board with its driving software, shielded connector block, shielded cable, and data-acquisition software. The system components were manufactured and developed by National Instruments Corp. The board model is PCI-6033E and it was plugged into the motherboard of a Pentium III PC computer. The board can manage up to 32 differential analog inputs and can work with a sampling rate as high as 100,000 samples/s. The driving software was NI-DAQ version 6.8.1.

The shielded block was SCB-100 with a 100 screw terminals for signal connection. A cold-junction compensation temperature sensor was included to use with thermocouples. The DC voltage signals coming from the turbine meters, thermocouples, and pressure transducers were connected to the block. The shielded cable connecting the block to the board carries those signals to the board where they were digitised.

The data-acquisition software was LabView base package version 6.0. The software receives the voltage signals from the board and the rotameters readings, which were entered manually. All the voltage signals were averaged for 120 seconds at a rate of 1000 samples per second. The calibration curves of the different devices were applied in order to convert the voltage signals and the rotameters readings into the corresponding physical quantities. The software was programmed to enable the user to monitor the independent parameters during the experiment, and do calculations of the dependent parameters.

3.5 System Operation and Data Reduction

3.5.1 Two-phase Flow

Start up and steady state

Several steps were required to start up the flow loop. The following is a list of steps, in order, which were performed each time the loop was run for a two-phase flow test (reference should be made to Figure 3.3, except where noted):

1. The turbine meter and pressure transducer power supplies were switched on.
2. The barometric pressure was noted and fed into the data-acquisition system.
3. Gas valves at the discharge of the separation tanks (valves 11 and 16) were checked to ensure that they were open. By-pass valves to inlet, outlet-2, and outlet-3 air turbine meters (3a, 13, and 18) were closed. The by-pass valve to the inlet-water turbine meters (6a) was closed. The inlet-water control valves (5a-b) were partially opened and the water by-pass control valve (4) was fully opened.

4. Control valves to the air turbine meters (2a, 14a-b, and 19a-b) were partially opened. Valves of the large air turbine meters (3c-b, 24a-b, and 25a-b) were fully open. Air calibration valve 8 was fully closed and valve 9 was fully open.
5. The valve to the air supply (valve 1) was slowly opened. The pressure controller outlet pressure was adjusted to approximately 38 kPa gauge.
6. The inlet-air control valve (2a-c) was gradually adjusted to give approximately the desired air flow rate through the loop. The proper inlet-air turbine meter was selected according to the desired flow rate (3b-d).
7. Control valves to the outlets air turbine meters (14a-b and 19a-b) were adjusted simultaneously with the inlet-air control valve (2a-b) to give the desired air flow rate at a test section pressure of 1.5 bar abs, and at the proper extraction rate. If the flow rate through either outlet-2 or outlet-3 small turbine meter was too low (output from the turbine meter below approximately 1.0 volts), then that turbine meter was shut down. The appropriate air rotameters were then activated to measure the air flow rate. This was achieved by opening either valve 12 or valve 17 and then opening the appropriate valves 23a-d or 24a-d.
8. Valves of the large inlet-water turbine meter were opened and the water pump was switched on.
9. Valves 4 and 5a-b were adjusted to give the desired water flow rate.
10. The proper inlet-water turbine meter was selected according to the desired flow rate (6b-e).

11. When the liquid levels in the separation tanks began to rise the appropriate water rotameters were activated (by opening the combination of valves 15a-e and 20a-e) to keep the liquid levels in the tanks steady.
12. The cooling water supply to the water reservoir heat exchanger was turned on, and the cooling water flow rate was set to give a test-section temperature near 21.0°C.
13. If the test-section pressure was not at the desired value, then it was restored to 1.5 bar abs by slowly adjusting the air control valves (valves 14a-b and 19a-b for turbines; valves 23a-d and 24a-d for rotameters). Since this affected the inlet air and water flow rates, the process of having the correct inlet flow rates and the correct test-section pressure was an iterative procedure. The liquid level in the separation tanks was kept steady by adjusting the water flow rates using valves 15a-e and 20a-e.
14. With the inlet flow rates and test-section pressure now set, and with the liquid level in the separation tanks steady, the extraction ratio was checked. If W_3/W_1 was different from the desired value, then it was adjusted by using the air control valves (valves 14a-b and 19a-b for turbines; valves 23a-d and 24a-d for rotameters). Adjustments were done in such a way as to maintain the correct test section pressure of 1.5 bar abs and the correct inlet flow rates. The liquid level in the separation tanks was kept steady by adjusting the outlet water flow rates using valves 15a-e and 20a-e. The extraction ratio was checked again, and if it was still incorrect, then it was re-adjusted using the above procedure.

Typically, the system required about 1½ hours of continuous adjustment to achieve the desired test conditions. After the desired test conditions were set, and before

recording any data, a steady-state condition had to be met. The following parameters had to remain the same for at least 15 minutes before taking any data:

1. The test-section pressure, P_s.

2. The extraction ratio, W_3/W_1.

3. Superficial velocities, J_{G1}, J_{L1}, J_{G2}, J_{L2}, J_{G3}, and J_{L3}.

4. The liquid level in the separation tanks.

5. The air and water temperatures throughout the system.

The above parameters were continuously monitored while data were being recorded. Two other parameters were also monitored, which are the air and water mass balances. Fine adjustments were made as needed to ensure that the above-mentioned parameters did not vary by more than approximately ±2 percent of the initial set values. If any of these parameters varied by more than this amount, the test was performed again. Usually, the system required an additional three hours of operation to record all phase-distribution and pressure-drop data.

Recording of Phase-Distribution Data

Once the system achieved steady-state condition, the phase-distribution data were recorded. Using the data-acquisition software, these data were written into a Microsoft excel worksheet (phase.xls). The data consisted of the following parameters:

1. The atmospheric pressure in Pa.
2. The absolute test-section pressure, P_s, in Pa.
3. The temperature immediately downstream of the inlet air turbine meters, T_1, in °C.
4. The inlet superficial gas velocity, J_{G1}, in m/s.
5. The inlet superficial liquid velocity, J_{L1}, in m/s.

6. The extraction ratio, W_3/W_1, and also $W_3/(W_3+W_2)$.

7. The air and water mass flow rates in the inlet and the two outlets, W_{G1}, W_{L1}, W_{G2}, W_{L2}, W_{G3}, and W_{L3} in kg/s.

8. The percentage air and water mass balances.

Reduction of Phase-Distribution Data

The above recorded phase-distribution data were used to calculate some other important parameters as follows:

1. The total inlet, outlet-2, and outlet-3 mass flow rates were calculated by

$$W_1 = W_{G1} + W_{L1}, \tag{3.1}$$

$$W_2 = W_{G2} + W_{L2}, \tag{3.2}$$

and

$$W_3 = W_{G3} + W_{L3}. \tag{3.3}$$

2. The inlet, outlet-2, and outlet-3 qualities were calculated by

$$x_1 = W_{G1} / W_1, \tag{3.4}$$

$$x_2 = W_{G2} / W_2, \tag{3.5}$$

and

$$x_3 = W_{G3} / W_3. \tag{3.6}$$

3. The fraction of total inlet gas entering outlet 3 and the fraction of total inlet liquid entering outlet 3 were calculated by

$$F_{BG} = W_{G3} / W_{G1}, \tag{3.7}$$

and

$$F_{BL} = W_{L3} / W_{L3}. \tag{3.8}$$

4. The ratio of outlet-3 to inlet quality, x_3/x_1, was calculated.

5. The density of inlet air was calculated by

$$\rho_{G1} = P_s / (287(T_1+273.15)) \tag{3.9}$$

The above calculations were done automatically in the same excel worksheet where the phase-distribution data were recorded.

It should be mentioned that among the data sets investigated in the current study, there were two data sets with relatively high J_{G1} and low J_{L1} values. For these two data sets, the inlet temperature T_1 and the mass flow rates W_{G1}, W_{L1}, W_{G2}, W_{L2}, W_{G3}, and W_{L3} were corrected for evaporation using the procedure outlined in Appendix A of Buell (1992). The procedure accounts for the evaporation of the liquid phase that occurs in the mixer, test section, and the separation tanks. At higher values of J_{L1}, the corrections were assumed to be insignificant, consistent with Buell (1992).

Recording of Pressure-Distribution Data

Once the phase-distribution data were recorded, the pressure distribution in the test section was measured. The following is a description of the procedure used to measure the pressure distribution. The layout of the pressure taps is given in Figure 3.9, while the pressure transducers and the associated valving are given in Figure 3.12. The following description assumes that all valves shown in Figure 3.12 (except those connected to transducer 0) were initially closed.

1. The voltage output from each transducer was adjusted to zero with an applied differential pressure of zero. This was accomplished by separately monitoring the instantaneous voltage output from each transducer, with the bypass valve around each transducer opened and all other valves closed. The voltage outputs from the transducers were adjusted to zero using the appropriate "zero adjustment" screw for each transducer.

The outlet-2 and outlet-3 pressure-distribution data were obtained first. The procedure is described in steps 2 through 9 below.

2. Tap 1 in the inlet was opened. The pressure at tap 1 was taken as the reference pressure.

3 Valve D was opened to connect the high sides of transducers 1-4 to the inlet pressure taps (taps 1 to 15). As the inlet pressure taps are always connected to the high sides of transducers 5-8, tap 1 is now connected to the high sides of transducers 1-8.

4. Valve B was opened to connect the low sides of transducers 5-8 to outlet-2 pressure taps (taps 16 to 28). The low sides of transducers 1-4 are always connected to outlet-3 pressure taps (taps 29 to 41).

5. Tap 16 in outlet 2, and tap 29 in outlet 3 were opened.

6. The pressure signals from tap1 in the inlet and tap 16 in outlet 2 were directed to transducers 5-8, and by monitoring the differential pressures sensed by those transducers, the transducer with the optimum range was selected.

7. The pressure signals from tap1 in the inlet and tap 29 in outlet 3 were directed to transducers 1-4. The optimum-range transducer to read the signal was obtained using a similar procedure to step 6.

8. Once the optimum-range transducers were found, the pressure value was recorded in a Microsoft excel worksheet (pressure.xls). A chart showing that value versus the tap location was also displayed on the screen using the data-acquisition software. Taps 16 and 29 were closed and the next taps in outlet 2 (tap 17) and outlet 3 (tap 30) were opened.

9. Steps 6 to 8 were repeated until all pressure taps in the two outlets were measured with respect to tap 1 in the inlet.

The inlet pressure-distribution data was obtained next. The procedure is given in steps 10 through 14 below. In the following steps, the pressures at the inlet taps were found with respect to tap 28 in outlet 2 and also with respect to tap 41 in outlet 3. Thus, for each inlet tap, two values for the pressure were measured. If the agreement between those two values was unacceptable, then all previously measured data were rejected and a new set of data was taken. Measuring the inlet-taps pressures with respect to two different taps verifies the operation of the transducers and their associated connections.

10. Tap 1 was closed and tap 2 was opened. Tap 28 in outlet 2 and tap 41 in outlet 3 were already open from step 9 above.
11. The pressure signals from tap 2 in the inlet and tap 28 in outlet 2 were directed to transducers 5-8, and by monitoring the pressure differences sensed by those transducers, the transducer with the optimum range was selected.
12. The pressure signals from tap 2 in the inlet and tap 41 in outlet 3 were directed to transducers 1-4. The optimum-range transducer to read the signal was obtained using a similar procedure to step 11.
13. Once the optimum-range transducers were found, the pressure values at tap 2 determined from steps 11 and 12 were compared and if the agreement was acceptable ($\leq$ 1.5 % for 80 % of the runs and $\leq$ 2.5 % for the rest), the value corresponding to the higher pressure differential was recorded. If not, all the previously recorded data were rejected and a new set of data was recorded starting

from step 1. The pressure value was recorded in the same excel sheet (pressure.xls). Tap 2 was closed and the next upstream tap in the inlet (tap 3) was opened.

14. Steps 11 to 13 were repeated until all pressure taps in the inlet were measured with respect to tap 28 in outlet 2 and tap 41 in outlet 3.

Reduction of Pressure-Distribution Data

The pressure-distribution data recorded in the previous section were plotted against taps locations in the same excel sheet where the data were recorded (pressure.xls). Using the data-acquisition software, this plotting process was done automatically at the same time the pressure-distribution data were recorded. Using least-squares analysis, linear equations were fit to the fully-developed data in the inlet and the two outlets. Details of this analysis are outlined in Appendix B of Buell (1992). By extrapolating the fully-developed pressure gradients in the inlet and the outlets to the centre of the tee junction, the pressure at each face of the junction (as shown in Figure 1.1) could be determined. These three junction average pressures, P_1, P_2, and P_3 were recorded in the excel sheet (phase.xls). The values of these junction pressures were also monitored on the computer screen during the experiment, and they were updated every time a new pressure-distribution data point was recorded.

The pressure drops due to the tee junction were defined as

$$\Delta P_{1i} = P_1 - P_i \qquad (3.10)$$

where i = 2 for outlet 2 and i = 3 for outlet 3.

3.5.2 Single-Phase Flow

Start-Up and Steady-State

Single-phase air and water tests were conducted in order to obtain pressure-drop data. These data were used to calculate the loss coefficients given by the pressure-drop correlations in Chapter 2. The following steps were performed each time the loop was run for single-phase air tests (refer to Figure 3.3):

1. Steps 1 through 7 of the two-phase start-up and steady-state routine were followed.
2. When the required inlet flow rate and test-section pressure were achieved, the extraction ratio was checked. If W_3/W_1 was different from the desired value, then it was adjusted using the outlets control valves (valves 14a-b and 19a-b in the case of air, and 15a-e and 20a-e in the case of water). If this adjustment resulted in a change in the test-section pressure and/or the inlet flow rate, they were adjusted back to the desired values. This procedure was repeated iteratively until the inlet flow rate, test-section pressure, and the extraction ratio were correctly set.

For single-phase water tests, steps 1 and 2 described above were performed without setting the test-section pressure. For water, the test-section pressure was left as determined by the mass flow rates in the inlet and the two outlets. Typically, the system required about 1 hour of continuous adjustment to achieve the desired inlet flow rate, test-section pressure, and the extraction ratio. Before recording any data, these parameters had to remain steady for at least 15 minutes in order to assume steady state. During data recording, the same parameters were monitored and fine adjustments were made, if needed, to ensure that the parameters did not vary by more than approximately ±2 percent of the initially set values. If any of these parameters varied by more than

this amount, the test was performed again. Usually, the system required an additional two hours of operation to record all phase-distribution and pressure-drop data.

Recording and Reduction of Data

Once the system achieved a steady-state condition, inlet-flow data were recorded. Using the data-acquisition software, these data were written into a Microsoft excel worksheet (phase1.xls). The data consisted of the following parameters:

1. The atmospheric pressure in Pa.
2. The absolute test-section pressure, P_s, in Pa.
3. The temperature immediately downstream of the inlet air turbine meters, T_1, in °C.
4. The inlet average velocity, J_{G1} or J_{L1}, in m/s.
5. The extraction ratio, W_3/W_1, and also $W_3/(W_3+W_2)$.
6. The air or water mass flow rates in the inlet and the two outlets, W_{G1}, W_{G2}, and W_{G3}, or W_{L1}, W_{L2}, and W_{L3} in kg/s.
7. The percentage air or water mass balance.

The single-phase pressure-distribution data were measured and reduced in a manner similar to that of two-phase flow, which was described earlier.

Chapter 4

EXPERIMENTAL RESULTS AND DISCUSSION

4.1 Data Range

The present experimental investigation consists of two components: single-phase pressure-drop experiments, and two-phase pressure-drop and phase-distribution experiments. For the single-phase component, a total of 18 test runs were performed. Four of these runs were performed using water and the remaining were performed using air. For the air runs, two nominal inlet-air velocity were tested; 20 and 40 m/s with the actual values within ±0.6 % of these values. The test-section pressure was kept nominally at 1.5 bar (abs) with the actual values within ±0.02 bar. The average test-section temperature was 23.5 °C with the actual values within ±3.5 °C. For each nominal inlet-air velocity, the extraction ratio was set to 0.0, 0.1, 0.3, 0.5, 0.7, 0.9, and 1.0. For the water runs, the nominal inlet-water velocity was 0.18 m/s with the actual values within ±1.1 % of this value. The test-section pressure was not set to a specific value but it was within the range 1.04 – 1.1 bar (abs) for all the runs. The average and actual values for the test-section temperature were close to those of the air runs. The extraction ratio was set to 0.0, 0.1, 0.9, and 1.0. In case of the extraction ratio of 0.5, values of ΔP_{12} and ΔP_{13} (see Equation 3.10 in Section 3.5.1) were very small which resulted in large uncertainty. As a result, it was decided not to include the extraction ratios of 0.3, 0.5, and 0.7 for the single-phase water runs. Table 4.1 shows the range of operating conditions for the single-phase air runs while Table 4.2 shows those for the single-phase water runs. Values of ΔP_{12} and ΔP_{13} for the single-phase pressure-drop

runs are tabulated in Appendix B. The mass-balance errors correspond to the percentage deviation between the inlet flow rate and the sum of the two outlet flow rates. The mass-balance error is positive when the sum of the two outlet flow rates is greater than the inlet flow rate and vice versa. The inlet Reynolds number was calculated from

$$Re_1 = \frac{4W_1}{\pi D_1 \mu} \tag{4.1}$$

where W_1 is the inlet mass flow rate, μ is the dynamic viscosity of the phase, and D_1 is the inlet diameter.

Table 4.1 Ranges of operating conditions for the single-phase air runs

Total number of runs	14
Inlet gas velocity, J_{G1}, in m/s	20 and 40
Inlet Reynolds number, Re_1	72,850 and 145,700
Test-section pressure, P_s, in bar	1.48 – 1.51
Extraction ratio W_3/W_1	0.0 – 1.0
Air mass balance errors	-4.9 to +0.5 %

Table 4.2 Ranges of operating conditions for the single-phase water runs

Total number of runs	4
Inlet liquid velocity, J_{L1}, (m/s)	0.18
Inlet Reynolds number Re_1	7170
Extraction ratio W_3/W_1	0.0, 0.1, 0.9 and 1.0
Water mass balance errors	0.0 to +0.9 %

It should be mentioned that before conducting the single-phase experiments, and in order to test the accuracy of the pressure transducers, a no-flow experiment was conducted. In this experiment a water level, with a trapped air bubble on top of it, was achieved in the test loop in all the three sides of the junction. With no flow, the water level should be horizontal and as a result the relative-pressure measurements at all the pressure taps should be equal to zero. The most sensitive transducers (numbers 1 and 5 in Figure 3.12) were used in this experiment. Figure 4.1 shows the relative pressure

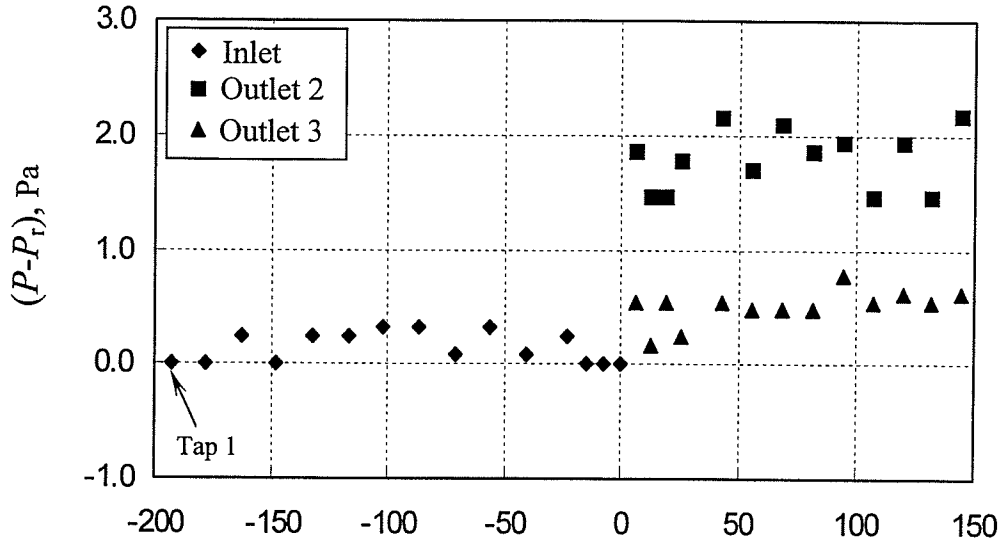

Figure 4.1 Pressure measurements for the no-flow experiment

measurements for the no-flow experiment. The pressure measurements were taken relative to the pressure at tap 1 (P_r). The figure shows that the maximum deviation from the zero value is approximately 2.2 Pa. It was thought that for pressure-drop measurements in impacting junctions, a value of 2.2 Pa (~ 0.2 mm water) is very small.

Based on that, Figure 4.1 was considered as an indicator that the pressure transducers used in this experiment were very accurate. Another no-flow experiment was conducted and results similar to the ones in Figure 4.1 were obtained.

Eleven data sets were generated in the two-phase component of the experimental investigation. Each data set corresponds to a fixed combination of J_{G1} and J_{L1}. A data set consists of data points that correspond to different extraction ratios, W_3/W_1. The number of data points varied from one data set to another. The total number of data points generated was 55 with 10 more data points generated for repeatability purposes. The nominal test-section pressure was 1.5 bar (abs) and the average test-section temperature was 24.5 °C. The actual pressure values were within ±0.2 bar of the nominal value while the actual temperature values were within ±4 °C of the average value. The nominal values of J_{G1} and J_{L1} for the 11 data sets generated are shown in Figure 4.2 on the flow-regime map of Mandhane et al. (1974). The transition boundaries shown in Figure 4.2 were plotted using the coordinates given in Mandhane et al. (1974) without any corrections for the physical properties. The boundaries shown are typical for systems with low pressures, air-water flows, and small-diameter pipes (less than 51 mm). For 87 % of the data points, the actual values of J_{G1} and J_{L1} varied within ±3 % of the nominal values. For easier future reference, data sets in Figure 4.2 are labelled according to the observed inlet flow regime. It can be seen that there is a very good agreement between the visual observations and the map predictions for the inlet flow regime. Mass-balance errors were calculated for both phases for all the two-phase tests. The air mass-balance error was within ±3.5 % for 66 % of the data and all the data were within ±5.3 %. The water mass-balance error was within ±3.5 % for

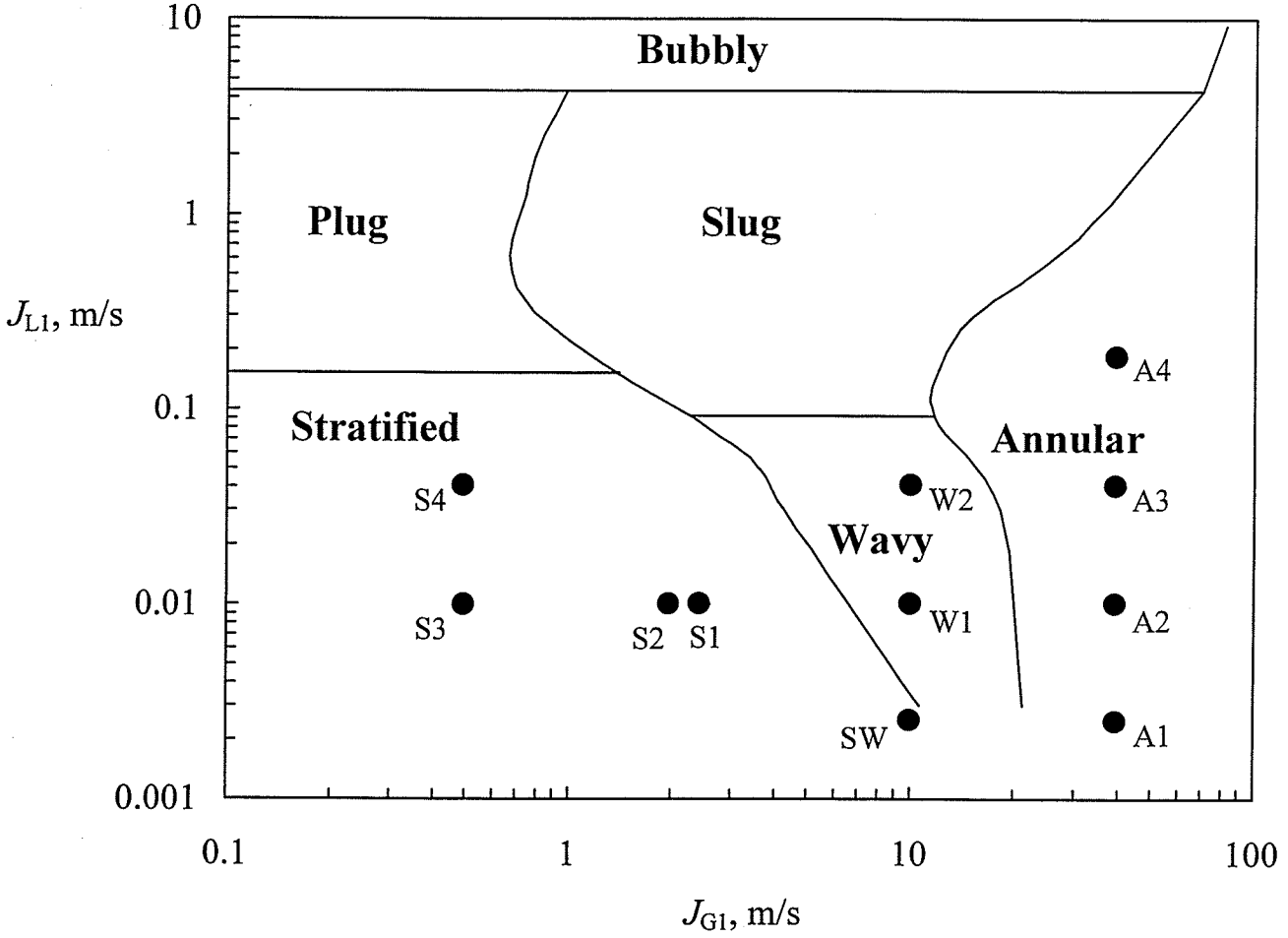

Figure 4.2 The inlet flow conditions on the Mandhane et al. (1974) flow-regime map

70 % of the data and all the data were within ±5.2 %. Table 4.3 lists the range of operating conditions for the two-phase runs while Table B.1 in Appendix B gives the complete set of phase-distribution and pressure-drop data. For data sets with J_{G1} = 0.5 m/s, the mass flow rate of the inlet air was too small to be measured as it was outside the range of the small turbine mater installed at the inlet. In these cases, the mass flow rates of the air leaving outlets 2 and 3 were measured using the appropriate rotameters and it was assumed that the sum of the two outlet flow rates was equal to the inlet flow

rate. For cases of W_3/W_1 = 1.0, 0.92, and 0.81 within data set A4, there were large pressure drops occurring at the junction and between the junction and the separation tank of outlet 3. As a result, the air leaving the separation tank of outlet 3 had to be released just downstream of the tank before being measured by the turbine meters. In order to push the air through the turbine meters, a pressure higher than 1.5 bar would have been required at the junction, which was not desirable in the experiment. In these cases, the mass flow rate of the air leaving outlet 3 was assumed to be equal to the difference between the measured mass flow rates of the inlet air and the air leaving outlet 2. For all the cases when the air mass flow rate could not be measured either at the inlet or one of the outlets, the air mass balance error in Table B.1 was not entered.

Table 4.3 Ranges of operating conditions for the two-phase runs

Total number of runs	55
Inlet flow regimes	Stratified, Stratified-Wavy, Wavy, and Annular
Inlet superficial gas velocity, J_{G1}, in m/s	0.5 – 40
Inlet superficial liquid velocity, J_{L1}, in m/s	0.0026 – 0.18
Test-section pressure, P_s, in bar	1.49 – 1.52
Inlet quality, x_1	0.02 – 0.96
Extraction ratio W_3/W_1	0.0 – 1.0
Air mass-balance errors	-5.3 to +5.3 %
Water mass-balance errors	-5.2 to +4.8 %

4.2 Phase-Distribution Data

Before starting the experimental part for the two-phase component of this study, there were two options to choose from. The first one was to cover the whole range of W_3/W_1

from 0.0 to 1.0 and the other option was to cover only half of the range from 0.0 to 0.5 and use symmetry to infer the data for the other half of the range from 0.5 to 1.0. It was decided that covering half the range only would allow for more data sets to be covered on the Mandhane et al. (1974) flow-regime map. However, the test loop had to be proved symmetric around the inlet centreline before proceeding further.

In order to test the symmetry of the test loop, two experiments were done for data set W1 with W_3/W_1 equal to 0.3 for the first experiment and 0.7 for the second one. The values of F_{BG} and F_{BL} for the first experiment were 0.311 and 0.281, respectively. For the second experiment, they were 0.690 and 0.723, respectively. The values of ΔP_{12} and ΔP_{13} for the first experiment were 22.2 Pa and -41.3 Pa, respectively. For the second experiment, they were -43.5 Pa and 21.3 Pa, respectively. The above-mentioned values of F_{BG}, F_{BL}, ΔP_{12}, and ΔP_{13} for the two experiments indicate that the test loop is symmetric around the inlet centreline.

To further examine the symmetry of the test loop, the pressure distribution in the inlet and the two outlets for the above-mentioned experiments were compared against each other. The comparison is shown in Figure 4.3. The ordinate in Figure 4.3 is P-P_r where P is the absolute pressure at a given location and P_r is the absolute pressure at tap 1 (see Figure 3.9). It can be seen that the pressure distributions in the inlet and the two outlets for the two experiments conducted obey the expected behaviour imposed by symmetry. This is further proof that the test loop is symmetric around the inlet centreline.

After the symmetry was proved as mentioned above, it was decided to cover only half the range of W_3/W_1 from 0.0 to 0.5, always including the condition $W_3/W_1 = 0.5$ in

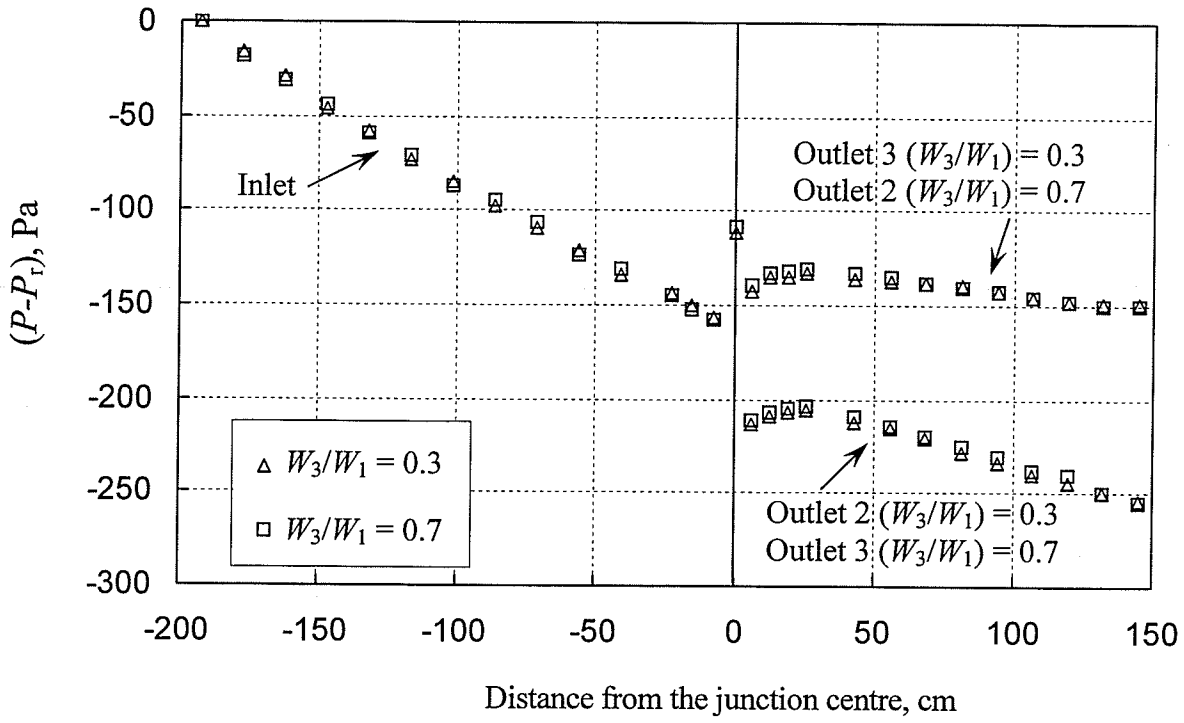

Figure 4.3 Pressure distribution for data set W1 with W_3/W_1 = 0.3 and 0.7

every data set. The experiments with W_3/W_1 = 0.5 are themselves further tests of symmetry for each combination of J_{G1} and J_{L1}. For this extraction ratio, it is expected that the pressure distribution in both outlets to be nearly identical with $\Delta P_{12} \cong \Delta P_{13}$, and $F_{BG} \cong F_{BL} \cong 0.5$.

The phase-distribution data obtained from this study are presented in this section. All the data are presented on graphs of F_{BL} ($F_{BL} = W_{L3}/(W_{L3} + W_{L2})$) versus F_{BG} ($F_{BG} = W_{G3}/(W_{G3} + W_{G2})$). The parameters W_{G1} and W_{L1} were not used in calculating F_{BG} and F_{BL} to avoid getting values of more than 1 for F_{BG} and F_{BL}. In these graphs, the data points shown for ranges of F_{BG} and F_{BL} from 0.0 to 0.5 are the actual measurements for outlet 3. The data points shown for the ranges from 0.5 to 1.0 are the actual measurements for outlet 2 but were used in the graphs for outlet 3 based on symmetry. As will be seen

later, graphs of F_{BL} versus F_{BG} show clearly the phase that preferentially exits through outlet 3 and also the relative quality (x_3/x_1) in outlet 3. The complete set of data is given in Table B.1 of Appendix B.

4.2.1 Data of the Stratified Flow Regime

Figure 4.4 shows the phase-distribution data for the stratified flow regime. It can be seen that for the four data sets there is a preference for the liquid phase to exit through outlet 3 over the range $0.0 < F_{BG} < 0.5$. This can be translated to x_3/x_1 values that are less than 1.0 over the range $0.0 < W_3/W_1 < 0.5$. In the range $0.5 < F_{BG} < 1.0$, the gas phase has a preference to go through outlet 3. This can be translated to x_3/x_1 values that are higher than 1.0 over the range $0.5 < W_3/W_1 < 1.0$. It should be noted that data sets S1, S2,

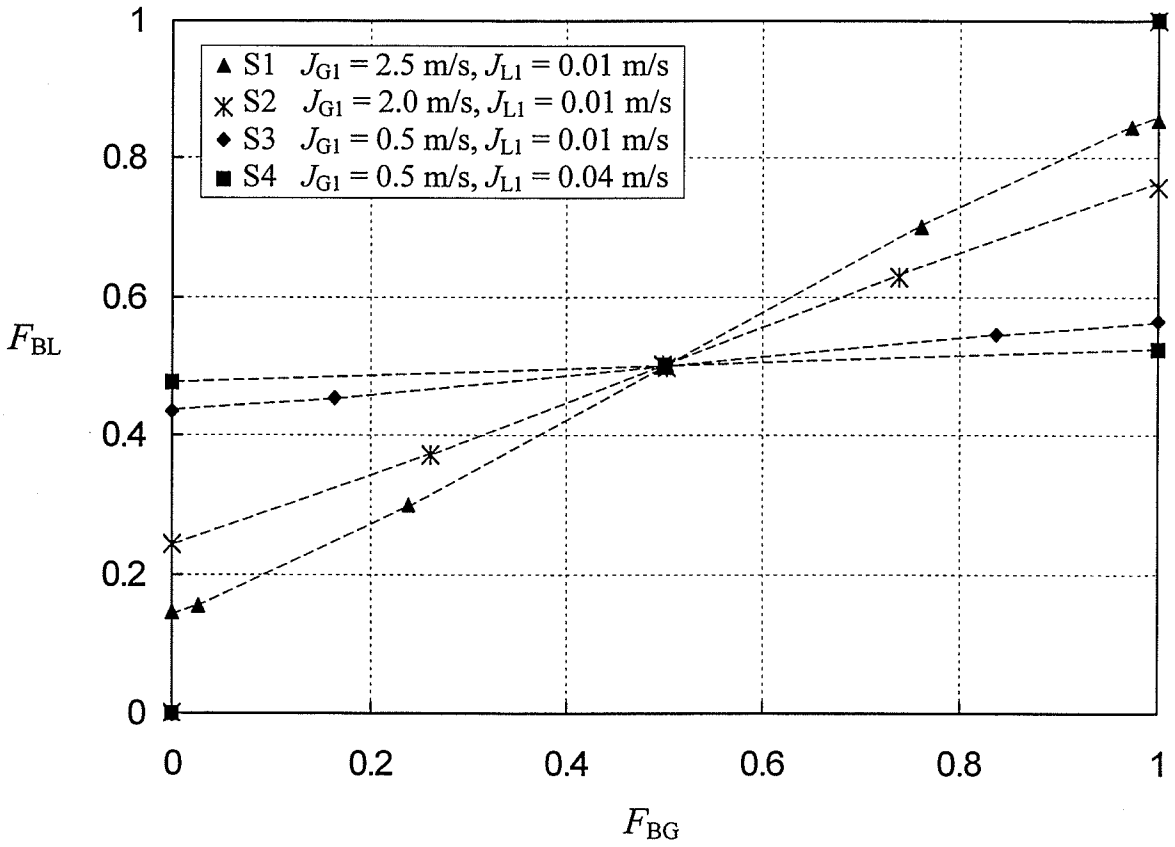

Figure 4.4 Phase-distribution data for the stratified flow regime

S3, and S4 have inlet-quality values of 0.31, 0.26, 0.08, and 0.02, respectively. Figure 4.4 shows that there is a continuous trend in the data such that as x_1 decreases, the data line (or curve) moves around the point (0.5,0.5) in a clockwise direction. We may recall from Chapter 1 that the data should approach the line $F_{BL} = 0.5$ as x_1 approaches zero and the data should approach the line $F_{BG} = 0.5$ as x_1 approaches 1.0. The trend in the data with respect to x_1 (seen in Figure 4.4) is consistent with these limits.

A parameter that was reported by different researchers (e.g., Ottens et al. (1995) and Azzopardi (1999)) to be important in determining the phase split in impacting tee junctions is the inlet-momentum-flux ratio $\dot{M}_R$, which is defined as follows:

$$\dot{M}_R = \rho_G V_{G1}^2 / \rho_L V_{L1}^2 \tag{4.2}$$

where V_{G1} and V_{L1} are the average inlet velocities of the gas and the liquid, respectively. In order to calculate these average velocities, the void fraction in the inlet, α_1, has to be calculated. The void fraction is defined as

$$\alpha_1 = A_{G1}/A_1 \tag{4.3}$$

where A_{G1} is the area occupied by the gas phase in the inlet and A_1 is the whole cross-sectional area of the inlet pipe. After calculating the void fraction, the average velocities V_{G1} and V_{L1} can be calculated as follows:

$$V_{G1} = J_{G1} / \alpha_1 \tag{4.4}$$

and

$$V_{L1} = J_{L1} / (1-\alpha_1) \tag{4.5}$$

In this study the void fraction α_1 was calculated using the equilibrium models proposed by Shoham et al. (1987); these models are described in detail in Appendix A. There is certainly a large number of theoretical models and empirical correlations

available in the literature for calculating the void fraction. One advantage of the Shoham et al. models is that they are flow-regime specific, in which case one would expect more accurate predictions relative to models and correlations that are flow-regime independent.

Using Equations (4.2) to (4.5) resulted in values of $\dot{M}_R$ of 1.15, 1.11, 0.966, and 0.394 for data sets S1, S2, S3, and S4, respectively. Figure 4.4 shows that there is a continuous trend in the data such that as $\dot{M}_R$ decreases, the data line (or curve) moves around the point (0.5,0.5) in a clockwise direction. According to the definition of $\dot{M}_R$, when x_1 approaches 0.0, $\dot{M}_R$ approaches zero and $\dot{M}_R$ approaches infinity when x_1 approaches 1.0. As mentioned earlier, when x_1 approaches zero the data approach the line of $F_{BL} = 0.5$ and when x_1 approaches 1.0, the data approaches the line of $F_{BG} = 0.5$. Based on that, the trend seen in Figure 4.4 in terms of the effect of $\dot{M}_R$ is consistent with the limiting values for $\dot{M}_R$.

It is possible to explain the importance of $\dot{M}_R$ in determining the phase split at impacting tee junctions from physical reasoning. Consider for example a situation where W_3/W_1 is less than 0.5. For this condition, the pressure on outlet 3 will always be higher than the pressure on outlet 2, i.e., there is a positive pressure gradient from outlet 3 to outlet 2. This pressure gradient causes the phase with the lower momentum to go preferentially through outlet 2 while the phase with the higher momentum will go preferentially through outlet 3. Therefore, for $W_3/W_1 < 0.5$ and $\dot{M}_R << 1.0$, such as the case for data set S4, we expect that the liquid will preferentially flow into outlet 3, as shown in Figure 4.4. Furthermore, it is expected that the liquid preference to exit through outlet 3 will decrease as $\dot{M}_R$ increases (with W_3/W_1 maintained below 0.5). This trend is

also confirmed by the four data sets in Figure 4.4. It is important to point out that $\dot{M}_R$ is not the only parameter affecting the F_{BL}- F_{BG} relation, as will be shown in the next chapter.

In Figure 4.4, the effect of varying J_{L1}, at a fixed J_{G1} on the data can be assessed by looking at data sets S3 and S4. It can be seen that as J_{L1} increases, the data line (or curve) moves around the point (0.5,0.5) in a clockwise direction. The effect of varying J_{G1}, at a fixed J_{L1}, on the data can be assessed by looking at data sets S1, S2, and S3. It can be seen that as J_{G1} increases, the data line (or curve) moves around the point (0.5,0.5) in an anti-clockwise direction. This effect is the exact opposite of the effect of increasing J_{L1}. Also, these effects are consistent with the trend seen in the data in connection with x_1. These observed effects of J_{G1} and J_{L1} are consistent with the observations made on the data of other researchers, which were reported by El-Shaboury et al. (2001).

In Figure 4.4, at the take-off points on the Y-axis, there was only liquid flowing in outlet 3 and above it there was a stagnant air layer that has the same pressure everywhere. Thus, the flow became similar to the flow in open channels and the amount of the liquid flow rate was dependent on the difference in elevation between the separation tank intake and the water surface inside the tank. As a result, no data points could be obtained on the Y-axis below the take-off points.

4.2.2 Data of the Wavy Flow Regime

Figure 4.5 shows the phase-distribution data for the wavy and stratified-wavy flow regimes. It can be seen that for data set SW with an inlet quality of 0.87, there is a preference for the gas phase to exit through outlet 3 over the range $0.0 < W_3/W_1 < 0.5$. Data set W1 with an inlet quality of 0.64 shows essentially an even phase split over the

whole range of W_3/W_1. For data set W2 with an inlet quality of 0.31, there is a preference for the liquid phase to exit through outlet 3 over the range $0.0 < W_3/W_1 < 0.5$. It can be noted that there is a continuous trend in the data such that as x_1 increases, the data line (or curve) moves around the point (0.5,0.5) in a counter-clockwise direction. The three data sets shown in Figure 4.5 have a J_{G1} of 10 m/s. Thus, the effect of J_{L1}, at a fixed J_{G1}, on the data can be assessed by examining the three data sets. It is clear that increasing J_{L1} results in turning the data line (or curve) around point (0.5,0.5) in a clockwise direction. All the observations made on Figure 4.5 are consistent with those made on Figure 4.4 for the stratified flow regime.

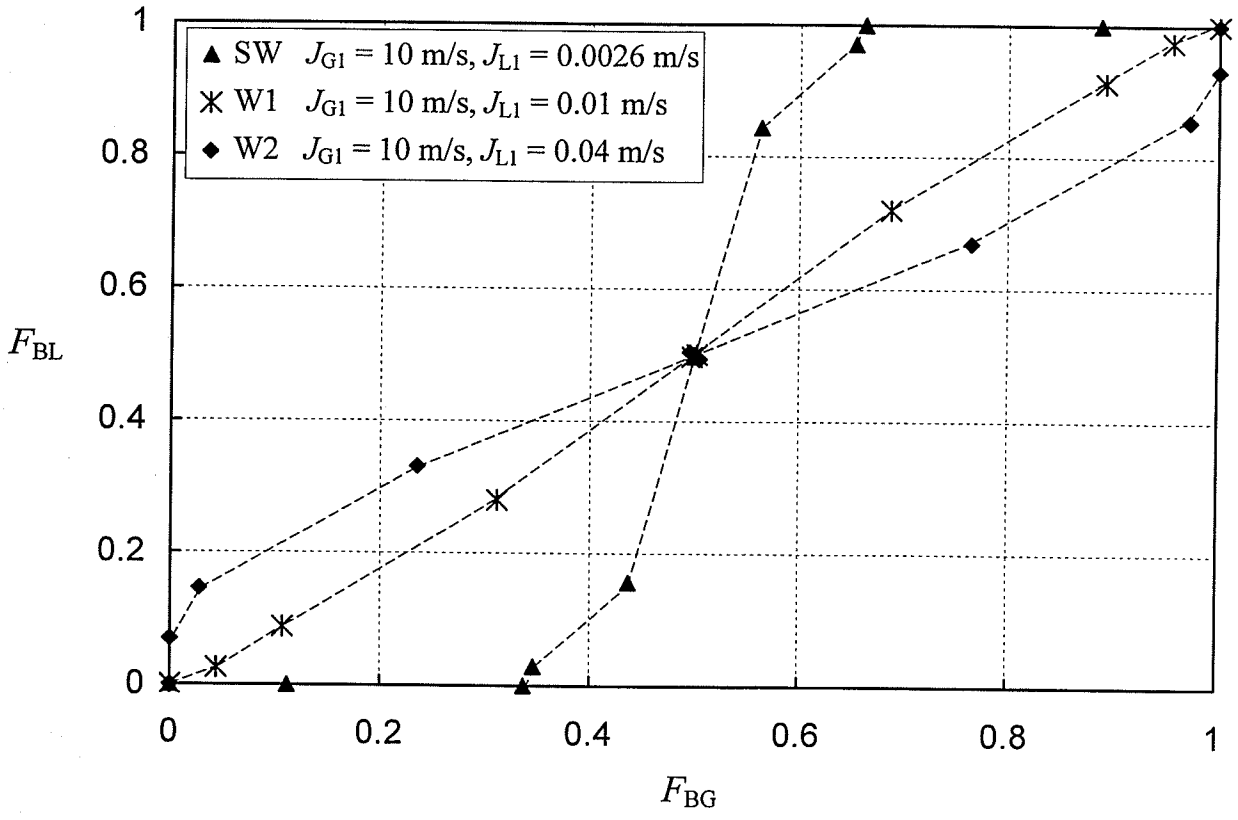

Figure 4.5 Phase-distribution data for the wavy and stratified-wavy flow regimes

In order to see the similarity or differences between the data of the stratified and wavy flow regimes, the data shown in Figures 4.4 and 4.5 were plotted on one graph, Figure 4.6. Values of x_1 and $\dot{M}_R$ are given on the figure for each data set. It can be seen that the data for data sets S1 and W2 are very close to each other and that both data sets have an inlet quality of 0.31. Keeping that in mind, it may be said that the trend related to the effect of x_1 is continuous within the stratified and wavy flow regimes. In terms of $\dot{M}_R$, there is a continuous trend within the data of each flow regime separately. However, the trend is not continuous within both flow regimes. This may be attributed

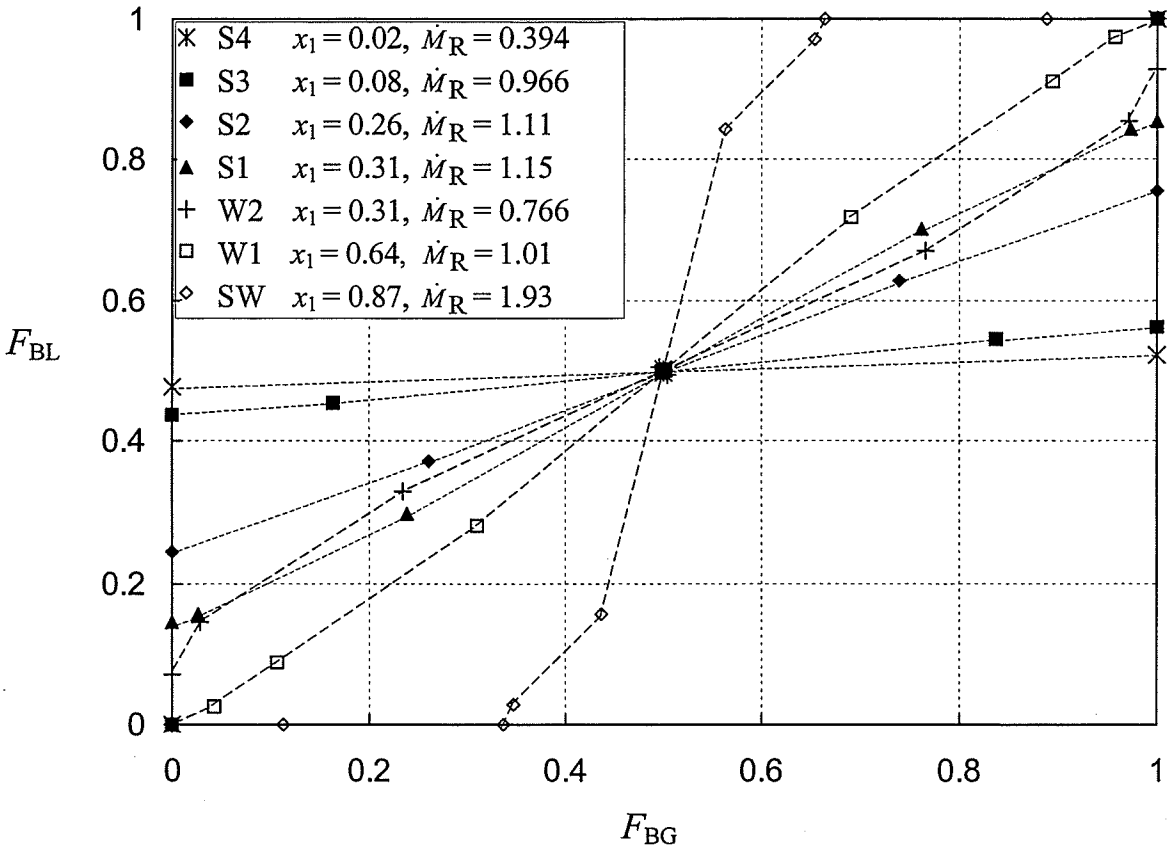

Figure 4.6 Phase-distribution data for the stratified and wavy flow regimes

to inaccuracy in the void-fraction values used in calculating $\dot{M}_R$, or the existence of other important factors influencing the phase distribution besides $\dot{M}_R$.

4.2.3 Data of the Annular Flow Regime

Figure 4.7 shows the phase-distribution data for the annular flow regime. The figure shows that for data set A1 (where $x_1 = 0.96$), there is a preference for the gas phase to exit through outlet 3 over the range $0.0 < W_3/W_1 < 0.5$. For data sets A2, A3, and A4 with inlet qualities of 0.87, 0.64, and 0.28, respectively, there is a preference for the liquid phase to go through outlet 3 over the range $0.0 < W_3/W_1 < 0.5$. Figure 4.7 also shows that there is a continuous trend in the data such that as x_1 increases, the data line (or

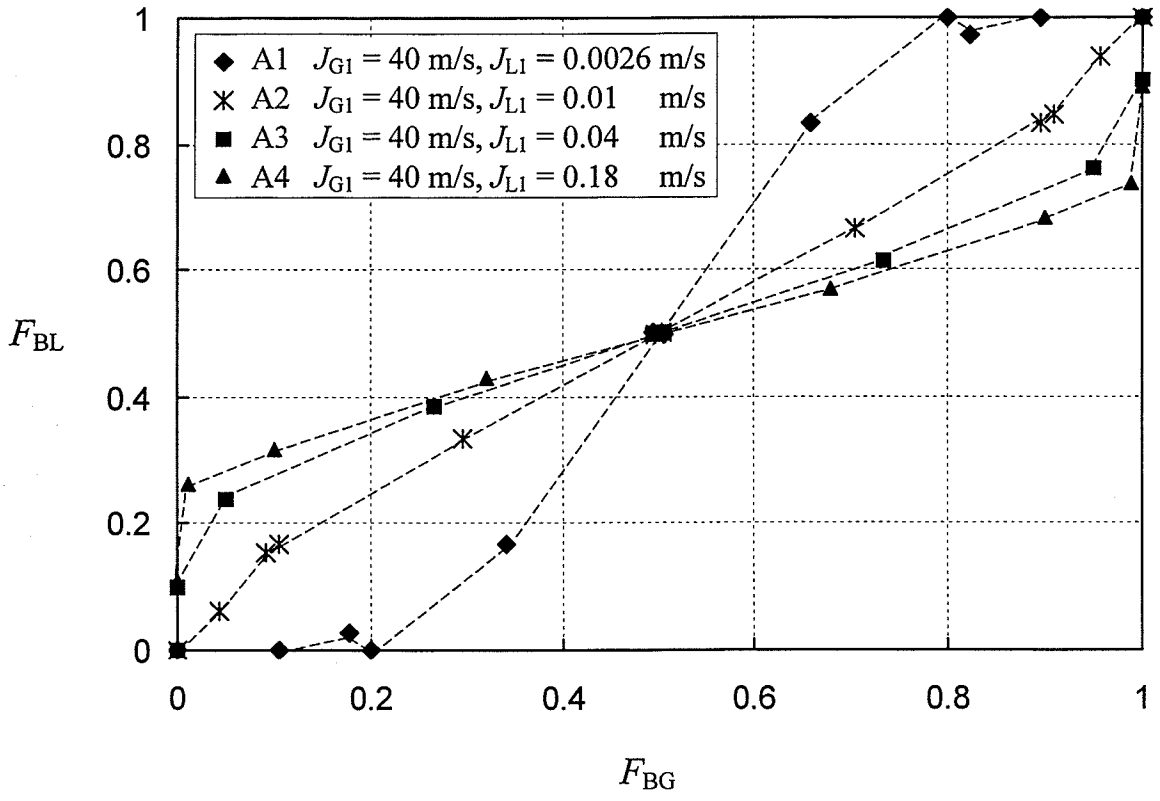

Figure 4.7 Phase-distribution data for the annular flow regime

curve) moves around the point (0.5,0.5) in a counter-clockwise direction. As the four data sets shown in Figure 4.7 have a J_{G1} of 40 m/s, the effect of varying x_1 may be viewed as the effect of varying J_{L1} at a fixed J_{G1}. In Figure 4.7, the trends seen in the data in terms of the effects of x_1 and J_{L1} are consistent with the trends found in Figures 4.4 and 4.5 for the stratified and wavy flow regimes.

4.3 Comparison Between Current Data and Other Researchers' Data

Some of the current phase-distribution data were compared against data generated by other researchers. The two data sets were selected such that they have reasonably close inlet conditions. Figure 4.8 shows data set SW compared against a data set of Ottens et al. (1995). The data of Ottens et al. were generated with atmospheric

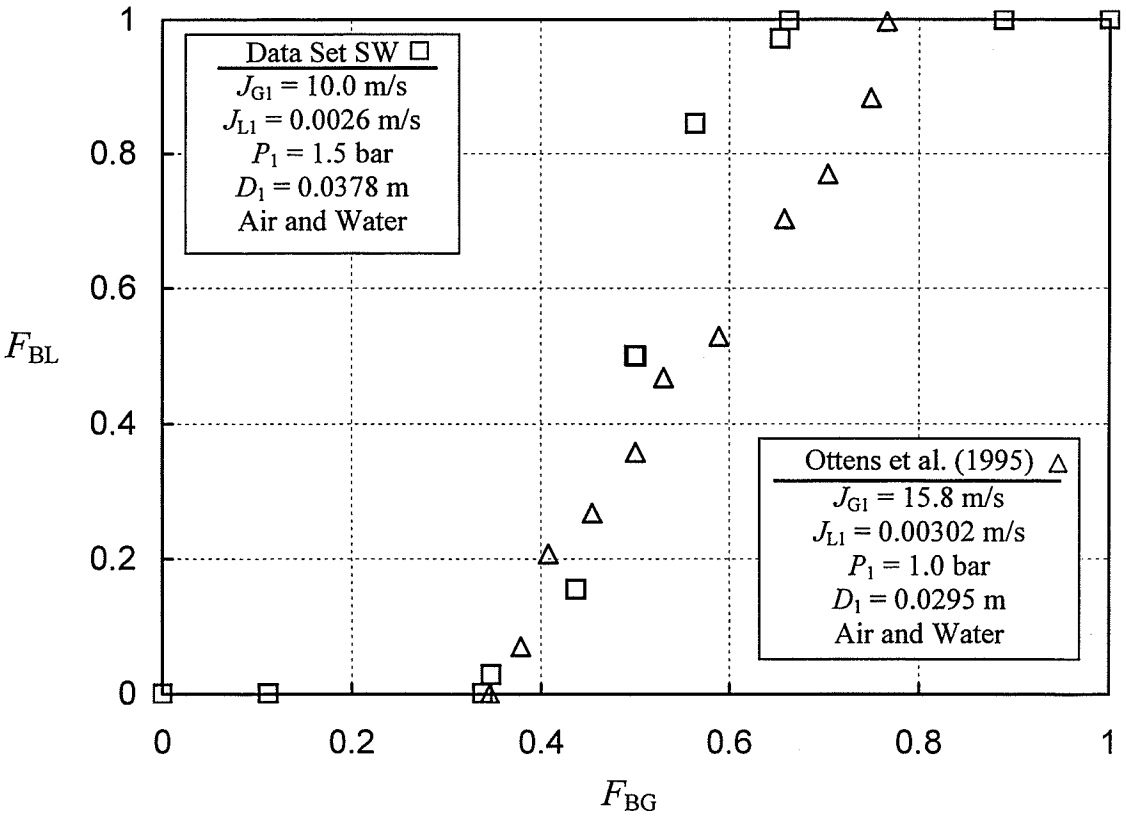

Figure 4.8 Comparison between data set SW and the data of Ottens et al. (1995)

pressures at the junction and a smaller diameter than the current study. The two values of J_{L1} are close while values of J_{G1} are somewhat different. The figure shows good agreement between the two data sets for $F_{BG} < 0.5$. For $F_{BG} > 0.5$, large deviations can be seen; however, the data of Ottens et al. do not seem to follow the symmetry conditions. Another comparison is shown in Figure 4.9, where data set W2 is compared against a data set generated by Ottens et al. The figure shows good agreement between the two data sets.

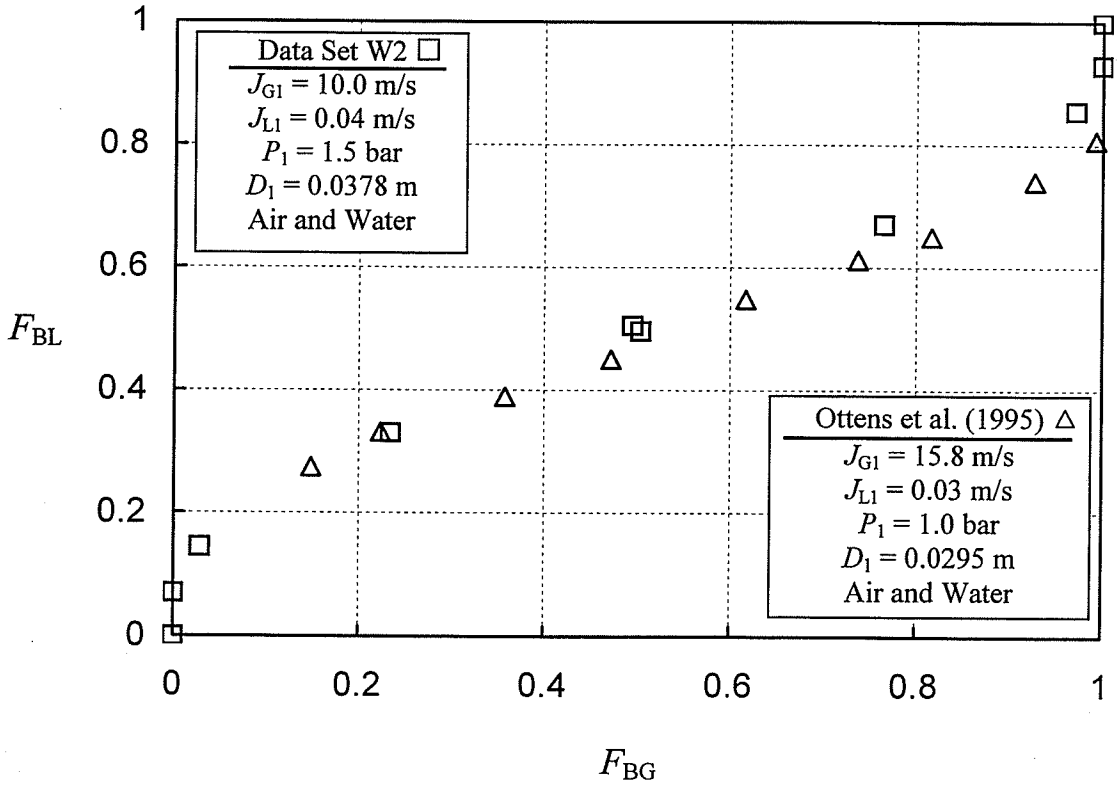

Figure 4.9 Comparison between data set W2 and the data of Ottens et al. (1995)

The current data for the annular flow regime were compared against the date of Hong and Griston (1995). Hong and Griston used a smaller diameter tee junction with atmospheric pressures at the junction. Figure 4.10 shows a comparison between data set A4 and a data set of Hong and Griston. Surprisingly, the figure shows good agreement between the two data sets even though the values of J_{G1} are considerably different. It cannot be determined whether the change in the inlet pressure and/or diameter contributed to the agreement between the two data sets. Due to a lack of data in the literature, the effects of the inlet pressure and the diameter on the phase-distribution

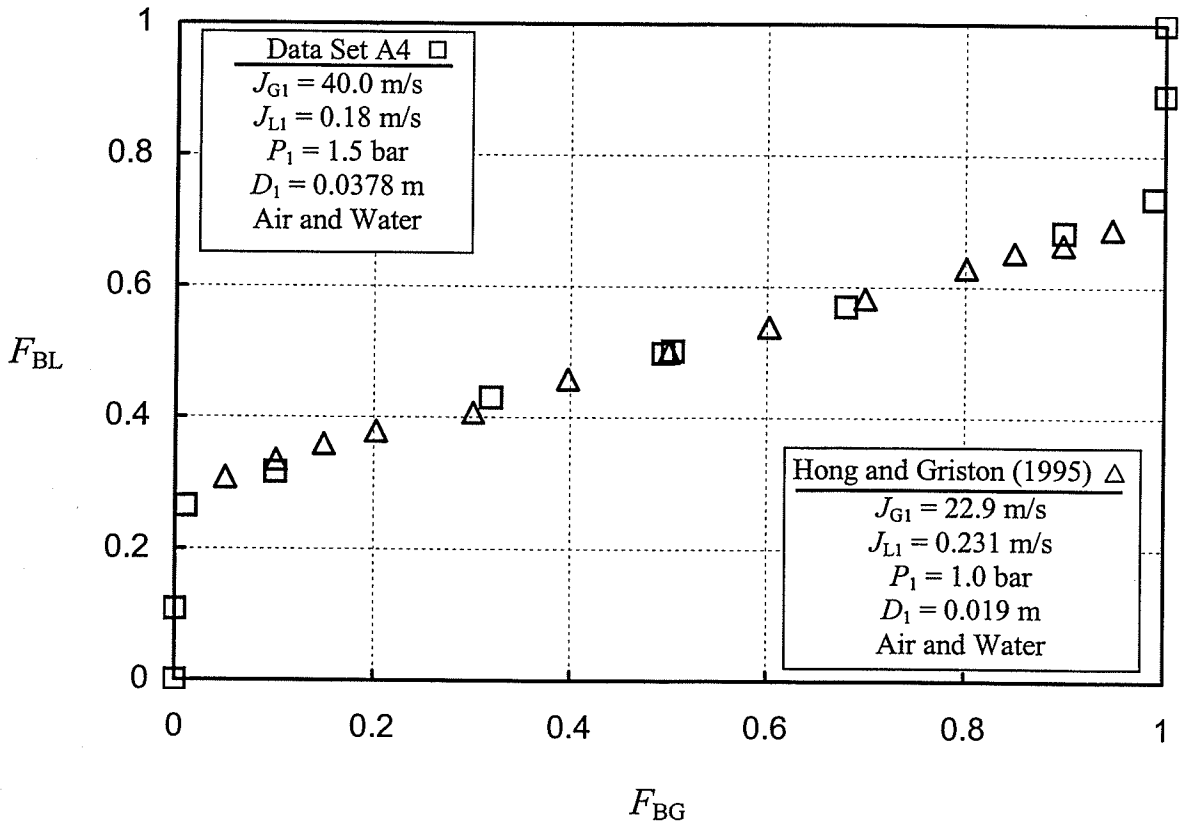

Figure 4.10 Comparison between data set A4 and the data of Hong and Griston (1995)

data are not well investigated. A comparison was also made against the data of Azzopardi et al. (1986a) for annular flow in a junction with a vertical inlet. Figure 4.11 shows a comparison between data set A3 and a data set of Azzopardi et al. (1986a). The two inlet pressures and diameters are close. The figure shows a good agreement between the two data sets even though the ratio of the J_{G1} values is almost 2:1. However, for data set A3, Both J_{G1} and J_{L1} are higher than those of Azzopardi et al. data set. Increasing J_{G1} and J_{L1} have opposite effects on the phase-distribution data and that might be the reason that the two data sets compare very well as shown.

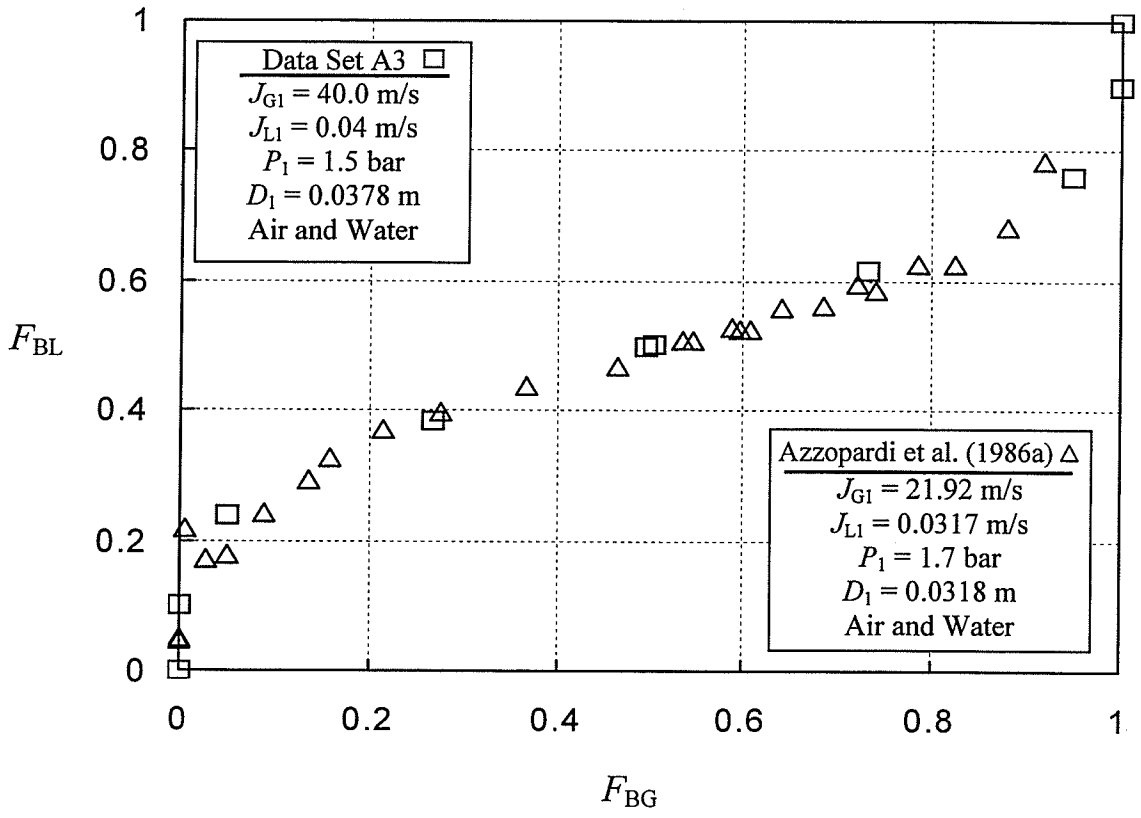

Figure 4.11 Comparison between data set A3 and the data of Azzopardi et al. (1986a)

4.4 Pressure-Drop Data

4.4.1 Single-Phase Pressure-Drop Data

Single-phase pressure-drop data were obtained under the operating conditions described in Tables 4.1 and 4.2. These data are listed in Tables B.3 and B.4.

Figures 4.12 and 4.13 show typical pressure distributions obtained during single-phase runs. Figure 4.12 shows the pressure distribution for a single-phase-air run with $W_3/W_1 = 0.1$, while the pressure distribution shown in Figure 4.13 was obtained for a single-phase-water run with $W_3/W_1 = 0.9$. The ordinate in these figures is $(P\text{-}P_r)$, where P is the absolute pressure at a given location and P_r is a reference pressure, selected in this study to be the absolute pressure at tap 1 (see Figure 3.9).

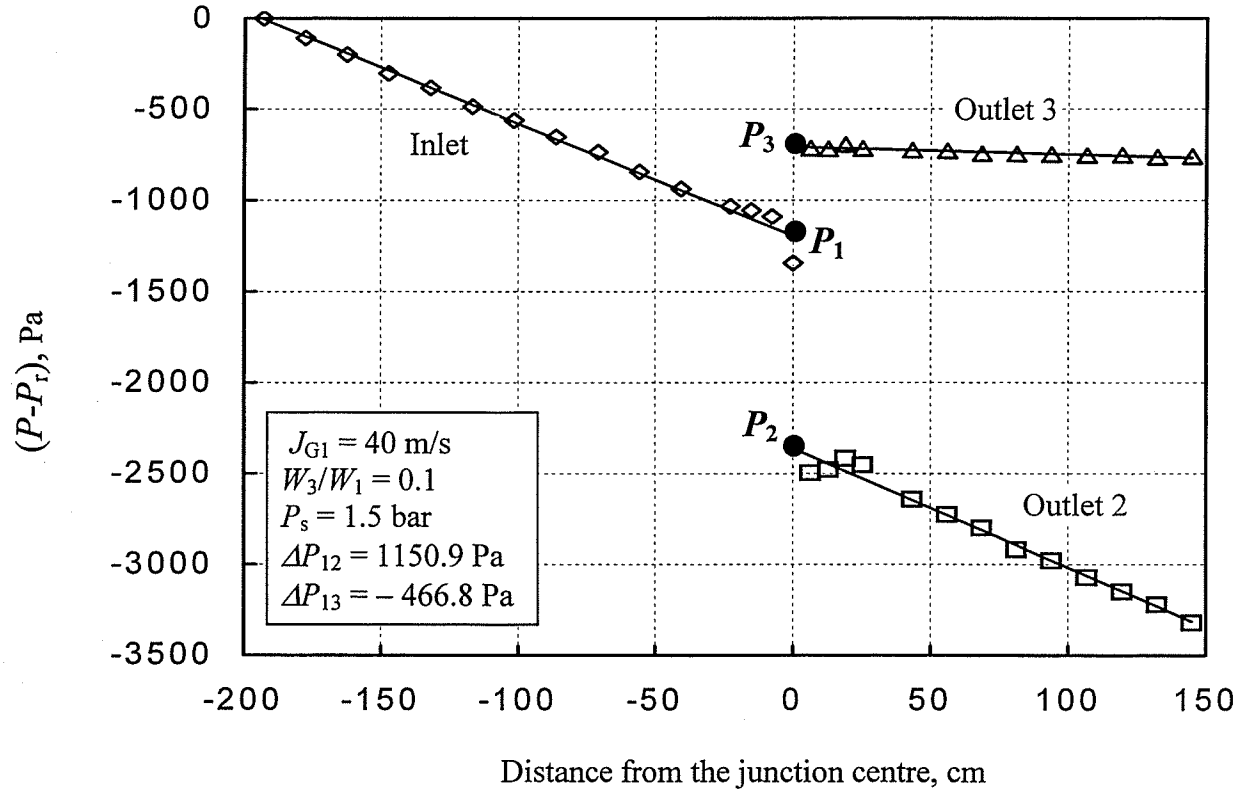

Figure 4.12 Pressure distribution for a single-phase-air run with $W_3/W_1 = 0.1$

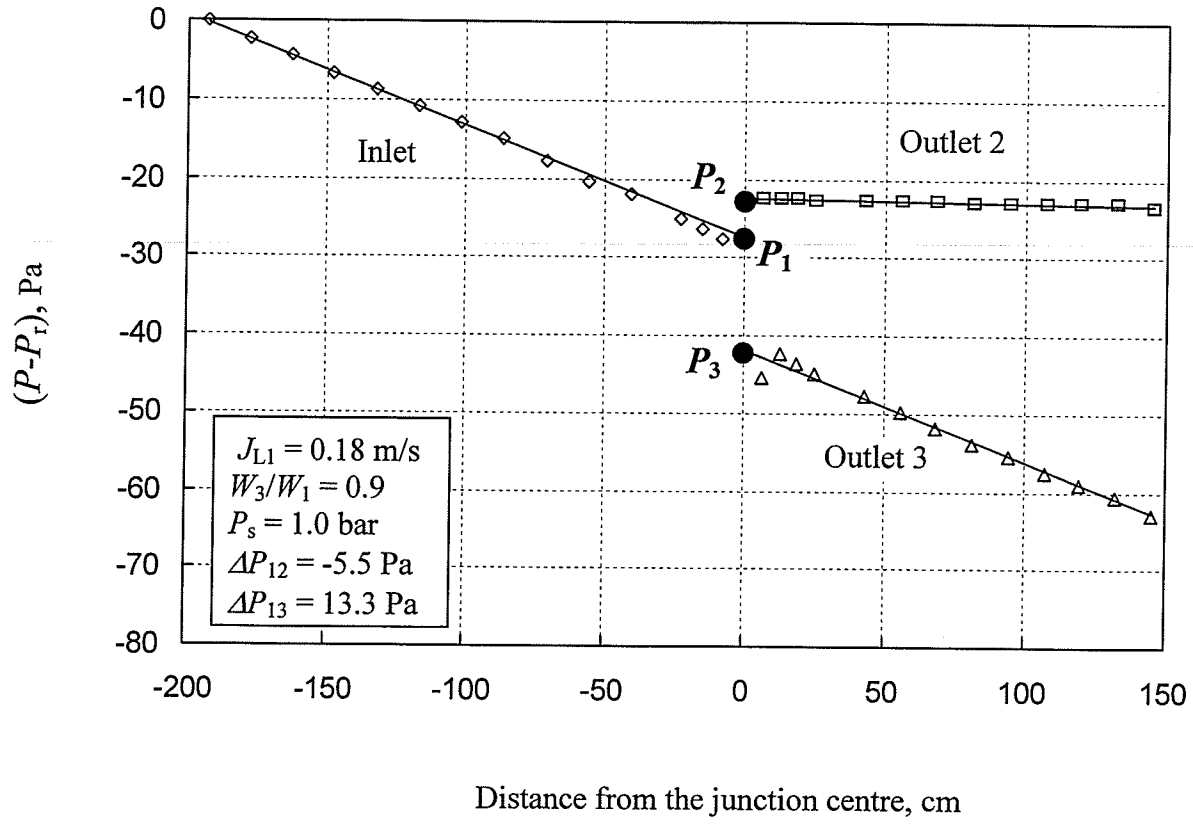

Figure 4.13 Pressure distribution for a single-phase-water run with $W_3/W_1 = 0.9$

As shown in Figures 4.12 and 4.13, values of the three junction average pressures, P_1, P_2, and P_3, were obtained by extrapolating the fully-developed pressure gradients in the inlet and the two outlets to the junction centre. The linear equations for the inlet and the two outlets were obtained using least-squares analysis as outlined in Appendix B of Buell (1992).

The measured pressure gradients in the inlet for all the single-phase experiments were compared against the predicted pressure gradients obtained from the following equation:

$$(dP/dx) = f \rho V^2 / (2D_1) \qquad (4.6)$$

where f, ρ, V, and D_1 are the friction factor, density, velocity, and inlet diameter, respectively. The friction factor was obtained from the following empirical correlations (Incropera and DeWitt, 2002):

$$f = 0.316\, Re_1^{-1/4} \qquad Re_1 \leq 2\text{x}10^4 \tag{4.7}$$

$$f = 0.184\, Re_1^{-1/5} \qquad Re_1 \geq 2\text{x}10^4 \tag{4.8}$$

where Re_1 is the inlet Reynolds number given by Equation (4.1).

Using Equations (4.6) to (4.8), the predicted pressure gradients for all the single-phase experiments were calculated. For single-phase-water runs, the average predicted pressure gradient was 14.7 Pa/m while the average measured pressure gradient was 14.6 Pa/m. For single-phase air runs with J_{G1} of 20 and 40 m/s, the average predicted pressure gradients were 182.7 and 636.7 Pa/m, respectively, while the average measured pressure gradients were 168.8 and 586.7 Pa/m, respectively. Therefore, the measured pressure gradients are in good agreement with the predicted ones with a maximum percentage deviation of 7.8 %.

Values of the three junction average pressures were used to calculate the pressure loss coefficient K_{13} and its counterpart for outlet 2, K_{12}, using Equation (2.30). Figure 4.14 shows the variation of K_{13} with the extraction ratio W_3/W_1 for the two nominal air velocities and the nominal water velocity. The empirical correlations of Ito and Imai (1973) and Hwang (1986), Equations (2.26) and (2.29), respectively, are also shown in the figure. Also in the figure, values of K_{12} evaluated at (W_2/W_1) are shown in order to confirm the symmetry of the test section. The figure shows that values of K_{13} at W_3/W_1 and those of K_{12} at (W_2/W_1) are very close to each other. As mentioned before, this confirms the symmetry of the test section. It can also be seen that, for the two different air velocities,

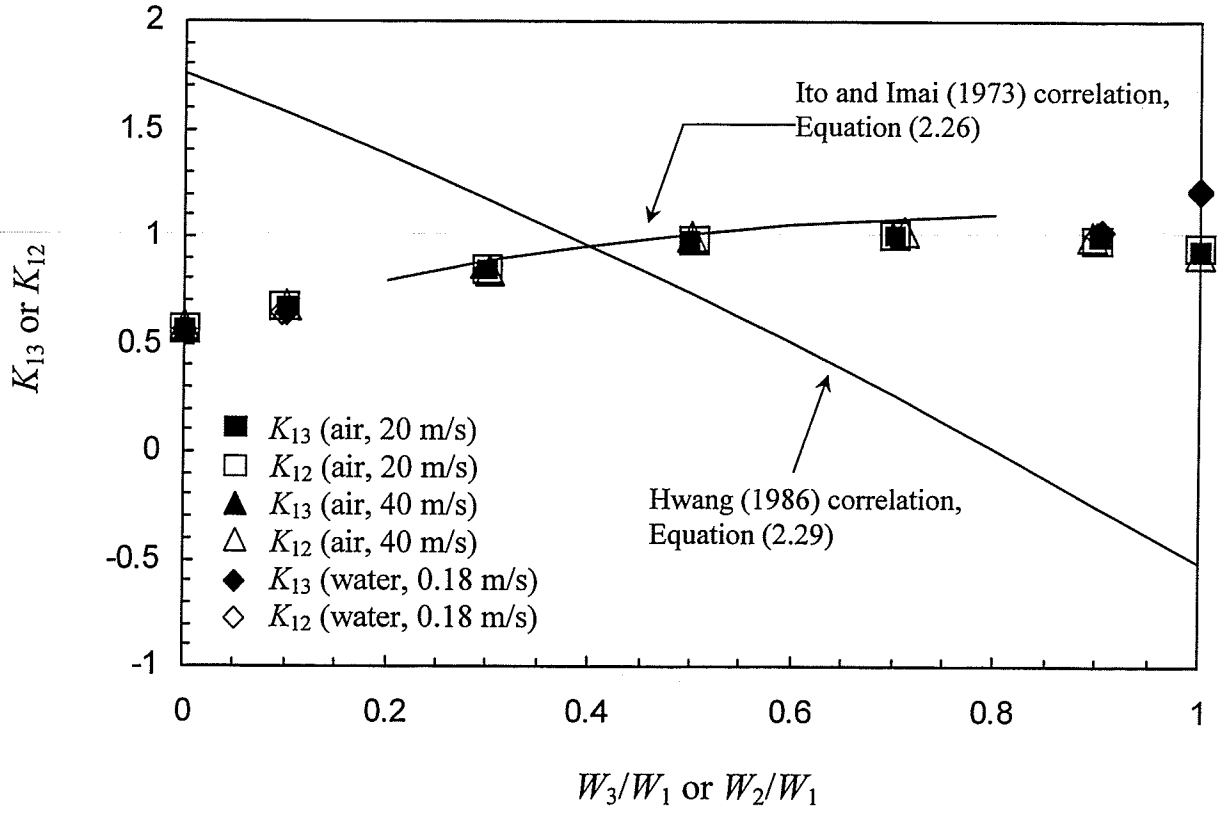

Figure 4.14 Single-phase loss coefficients, K_{13} and K_{12}

values of K_{13} and K_{12} are very close to each other. Also, values of K_{13} and K_{12} for the air flow are close to those of the water flow except at $W_3/W_1 = 1.0$. The experimental data fit the correlation of Ito and Imai (1973), Equation (2.26), very well over the whole correlation range. It should be mentioned that Equation (2.26) was based on experimental data for single-phase-water flow over the range $10^5 \leq Re_1 \leq 2(10^5)$. However, the correlation by Hwang, Equation (2.29), does not follow the experimental-data trend of Ito and Imai or the present investigation. Figure 4.14 suggests that values of the pressure loss coefficients K_{13} and K_{12} are dependent only on the extraction ratio W_3/W_1. No dependence on the fluid properties or the inlet Reynolds number is observed.

4.4.2 Two-Phase Pressure-Drop Data

Two-phase pressure-drop data were obtained under the operating conditions described in Table 4.3. These data are listed in Table B.1 of Appendix B.

In the following sections, samples of the pressure-distribution data for different inlet flow regimes are given. These data are presented on graphs of $(P\text{-}P_r)$ versus the distance from the junction centre, similar to Figures 4.12 and 4.13 for single phase.

Pressure-Distribution Data for Annular Flow

Figure 4.15 shows pressure-distribution data for data set A1 with $W_3/W_1 = 0.5$. The figure shows that the pressure distributions in the two outlets are very close to each other which is further evidence of the symmetry of the test loop around the inlet centreline. As a

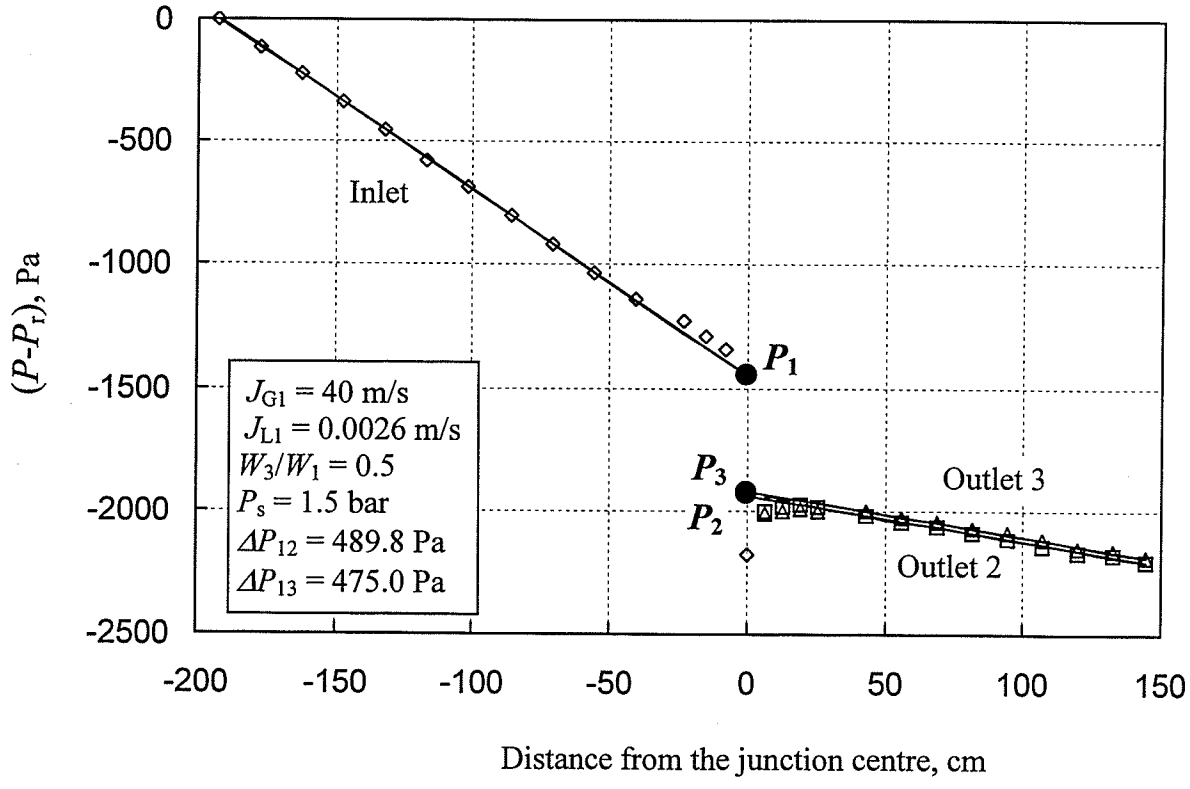

Figure 4.15 Pressure distribution for data set A1 with $W_3/W_1 = 0.5$

result, values of ΔP_{12} and ΔP_{13} are very close to each other with a percentage difference of 3 %. Also, the figure shows that the pressure gradient in the inlet is larger than those in the outlets, which is expected due to the larger mass flow rate in the inlet. In the inlet, the last three taps before the junction centre have pressures that slightly deviate from the straight line due to the slight change in diameter between the copper pipe and the acrylic piece. That difference in diameter is approximately equal to 0.05 mm or 0.13 % of the diameter. It can be seen that for both outlets, the flow becomes fully developed at approximately 50 cm away from the junction centre. The developing length in both outlets was always close to 50 cm for all the data sets except for data set A4, as will be seen later.

Figure 4.16 shows pressure-distribution data for data set A4 with $W_3/W_1 = 0.8$. The figure shows that in outlet 3 the flow becomes fully-developed at approximately 130 cm from the junction centre. As mentioned before, that developing length is larger than those found in other data sets. Data set A4 has the highest values for J_{G1} and J_{L1} in the current study. As a result, for large values of W_3/W_1, the mass flow rate in outlet 3 becomes very large and consequently requires large developing lengths.

Outlet 3 had originally 15 pressure taps (see Figure 3.9) with the last tap at a distance of 144.78 cm from the junction centre. With this configuration, there will not be enough data points for determining the slope of the straight line that represents the fully-developed pressure distribution in outlet 3. Determining the correct slope for that straight line is very important because the value of P_3 greatly depends on that slope. As a result, it was decided to drill two additional pressure taps in outlet 3. These two taps are 12.7 cm apart and the first one of them is 12.7 cm away from the last original tap (tap 41 in Figure 3.9). With the two additional taps, the straight line for outlet 3 is based on four points and as a result the

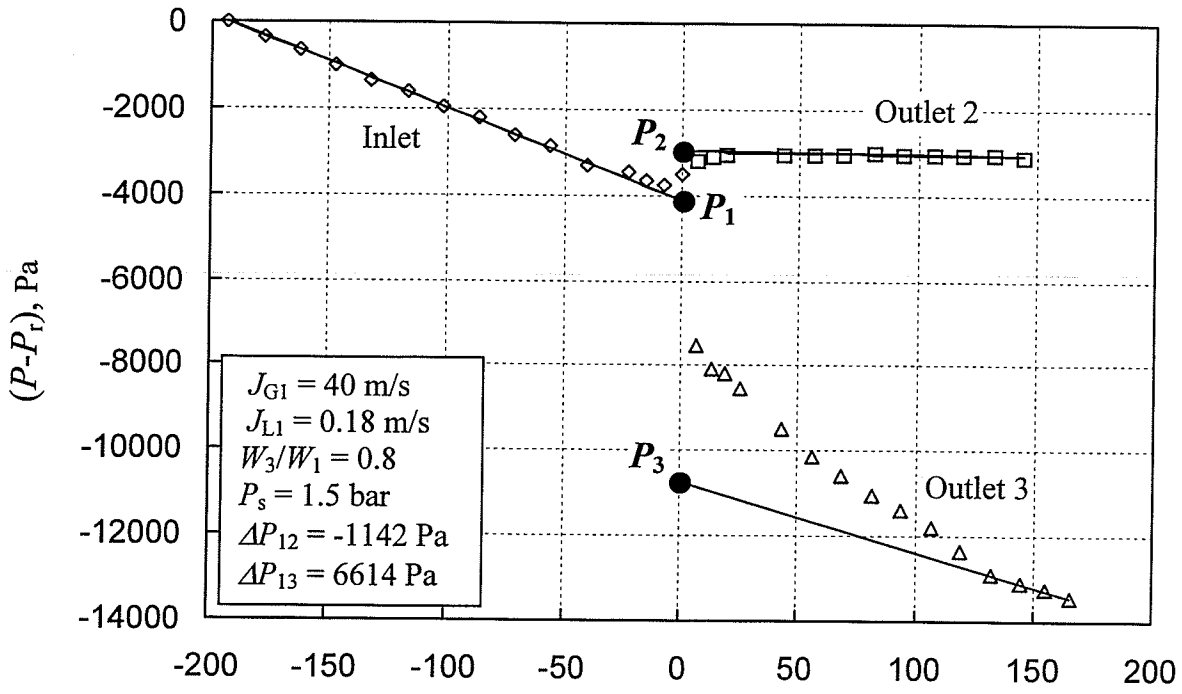

Figure 4.16 Pressure distribution for data set A4 with $W_3/W_1 = 0.8$

value of P_3 was determined with more confidence. All other data were gathered using the original configuration of taps as shown in Figure 3.9.

Pressure-Distribution Data for Wavy and Stratified-Wavy Flows

Figure 4.17 shows pressure-distribution data for data set W2 with $W_3/W_1 = 0.1$. The figure shows that when 90 % of the inlet flow goes through outlet 2, it reaches fully-developed conditions at approximately 50 cm from the junction centre. As mentioned before, this distance was consistent for all the data sets except data set A4, as seen in Figure 4.16. The figure also shows that the inlet pressure gradient for data set W2 is much lower than the values in Figures 4.15 and 4.16 for data sets A1 and A4, respectively. This is of course due to the lower mass flow rate that goes through the inlet for data set W2. In

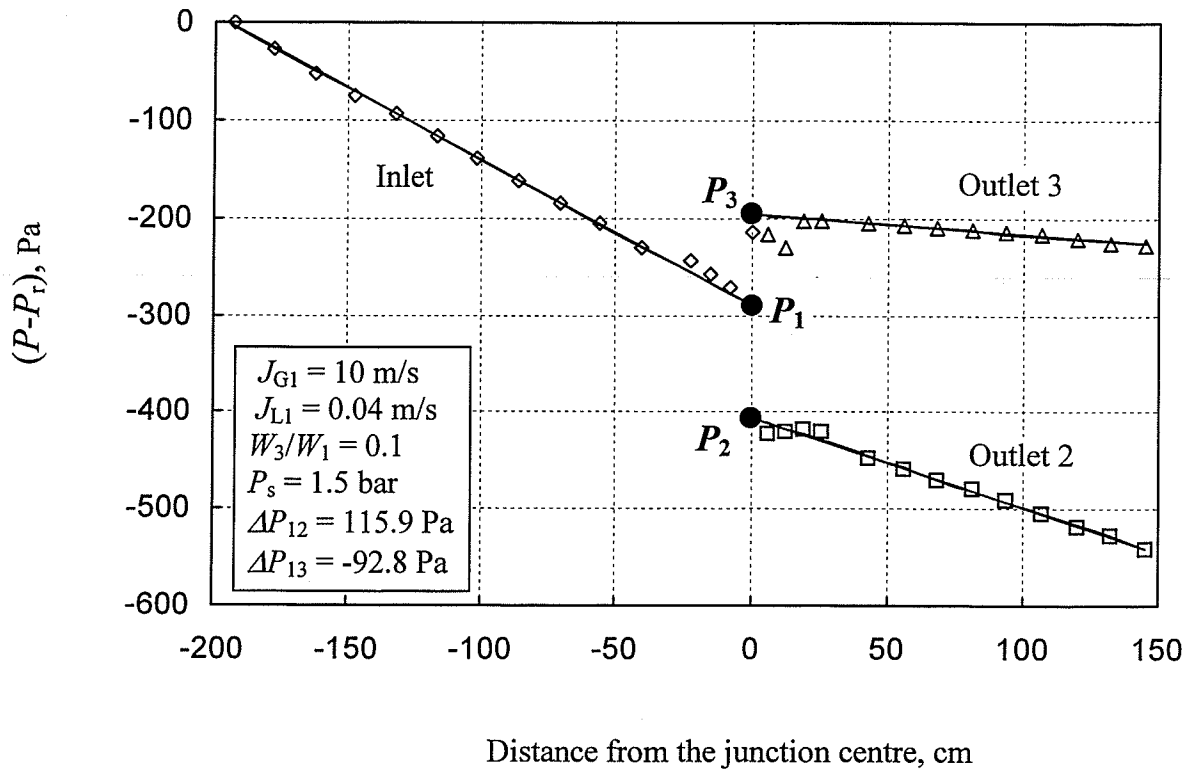

Figure 4.17 Pressure distribution for data set W2 with $W_3/W_1 = 0.1$

Figure 4.17, the inlet has the highest pressure gradient and outlet 3 has the smallest one. All these observations on Figure 4.17 are consistent with those for Figures 4.15 and 4.16.

Pressure-Distribution Data for Stratified Flow

Figure 4.18 shows the pressure-distribution data for data set S1 with $W_3/W_1 = 0.1$. The values of P_1, P_2, and P_3 are shown in the figure. These values were obtained by extrapolating the pressure data from the straight-line regions in the three sides of the junction, as was done for annular and wavy flows. The figure shows that the pressure-drop values (ΔP_{12} and ΔP_{13}) are considerably smaller than those for wavy and annular flows. In Figure 4.18, the maximum difference in pressure between any two taps is

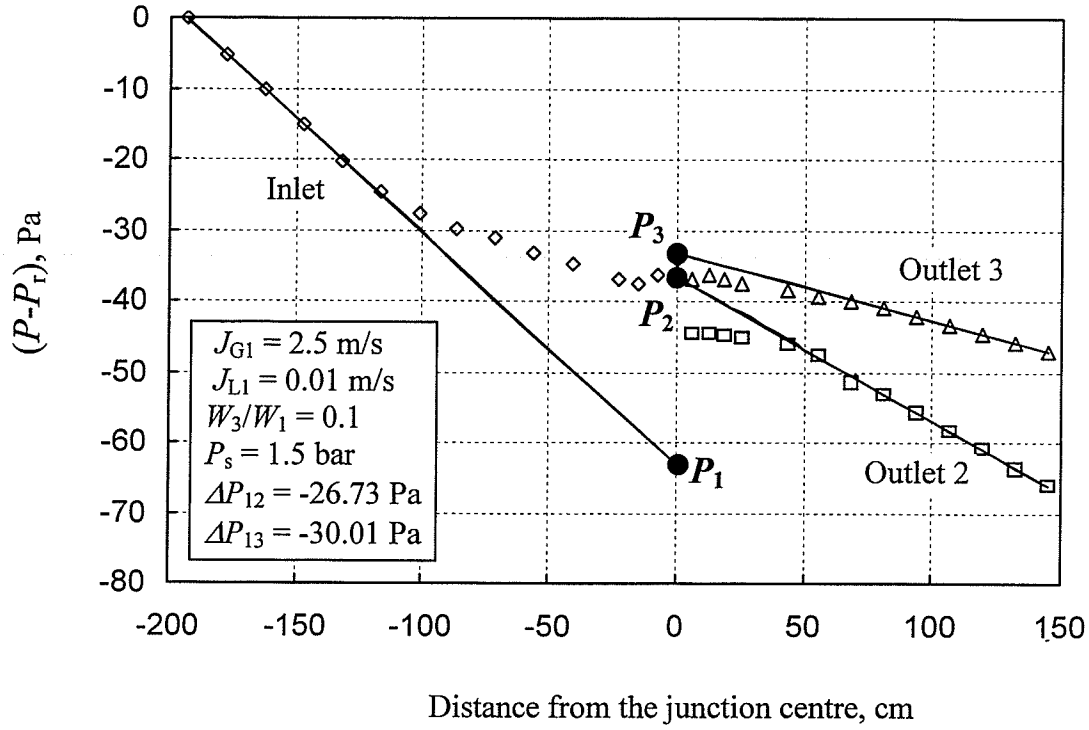

Figure 4.18 Pressure distribution for data set S1 with $W_3/W_1 = 0.1$

approximately 65 Pa, a value that is much smaller than its counterpart for wavy and annular flows. This observation was found to be consistent in all the data for stratified flow. The reason for these small values is that for stratified flows, the value of J_{G1} is relatively small leading to a small inlet mass flow rate and as a result the pressure-drop values become very small. Another observation that can be made on Figure 4.18 is that the pressure-distribution data in the inlet deviate from the linear behaviour at a large distance from the junction centre (approximately 120 cm in Figure 4.18). This observation was also found to be consistent in all the data for stratified flow. However, the location at which the data start to deviate from the linear behaviour was found to vary with the inlet conditions, as will be seen later.

The possible reasons for the deviation of the inlet pressure-drop data from the linear behaviour were investigated. Figure 4.19 shows a picture taken from the back of the junction for data set S1 with $W_3/W_1 = 0.1$. In the figure, the inlet appears as an ellipse and the interface, outlet 2, and outlet 3 are marked as shown. The figure shows that there is a swelling of the interface level at the junction. The figure also shows that the heights of the interfaces in outlets 3 and 2 are different with outlet 3 having a lower interface due to the smaller mass flow rate in it. The fact that the interface height swells at the junction may be explained by looking at the junction as an obstruction to the incoming flow. The visual observation shown in Figure 4.19 was consistent for all the data of stratified flow; however, it was found that the magnitude and shape of the interface swelling at the junction varied with the inlet conditions and the split ratio.

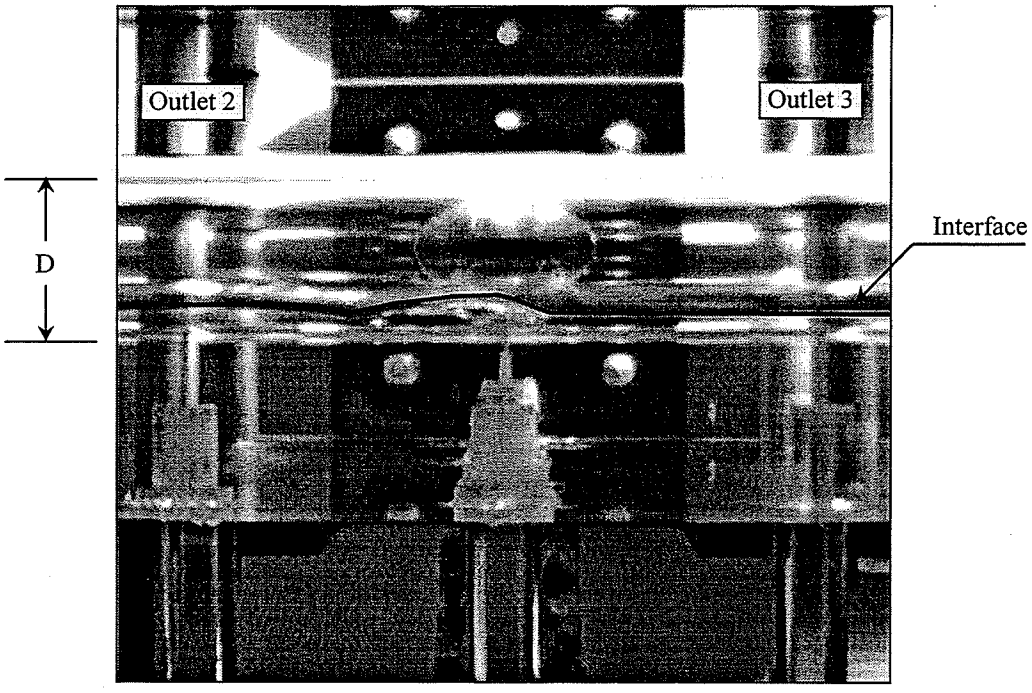

Figure 4.19 Back picture of the junction for data set S1 with $W_3/W_1 = 0.1$

The visual observation shown in Figure 4.19 together with the pressure measurements shown in Figure 4.18 gave rise to the question about the effect of the interface level in all three sides of the junction on the magnitude and form of the pressure distribution. A difference in elevation of 2 mm results in a 20 Pa pressure difference, which is significant when the difference between the highest and lowest pressures is 65 Pa. On the other hand, differences in elevation have little impact in annular and wavy flows because of the much-higher pressure differences.

It should be mentioned that in the current study, values of the pressure measurements consist of two parts; the static pressure and the hydrostatic pressure. Thus, for the current pressure-distribution data such as the ones given in Figure 4.18, the parameter P can be defined as follow:

$$P = P_{st} + \rho_L g\, h \tag{4.9}$$

where P_{st} is the static pressure of the gas phase, ρ_L is the density of water, g is the gravitational acceleration, and h is the vertical height of the interface above the pressure transducer compartment. The height h given in Equation (4.9) may be expressed as:

$$h = h_L + L \tag{4.10}$$

where h_L is the liquid height in the tube and L is the vertical height of the bottom of the tube above the pressure transducer compartment. Consequently, the parameter P can now be defined as:

$$P = P_{st} + \rho_L g\, (h_L + L) \tag{4.11a}$$

Similarly, the parameter P_r is defined as follow:

$$P_r = (P_{st})_r + \rho_L g\, [(h_L)_r + L] \tag{4.11b}$$

where $(P_{st})_r$ and $(h_L)_r$ are the static pressure and the interface height, both at tap 1, respectively. The height L is the same for all pressure taps. Thus,

$$(P-P_r) = P_{st} - (P_{st})_r + \rho_L g [h_L - (h_L)_r] \qquad (4.12)$$

Equation (4.12) emphasizes that the pressure distributions shown in Figures 4.15 to 4.18 have static and hydrostatic components.

In order to investigate the possible effect of the height change of the interface in the three sides of the junction, an experiment was conducted with the following conditions: $J_{G1} = 0.0$, $J_{L1} = 0.04$ m/s, and $W_3/W_1 = 1.0$. The value of J_{L1} was small enough so that the water did not fill the entire pipe. Instead, a stagnant air bubble existed on top of the flowing water. The pressure-distribution data obtained for this experiment are shown in Figure 4.20, while Figure 4.21 shows a back picture of the junction. Since there is no

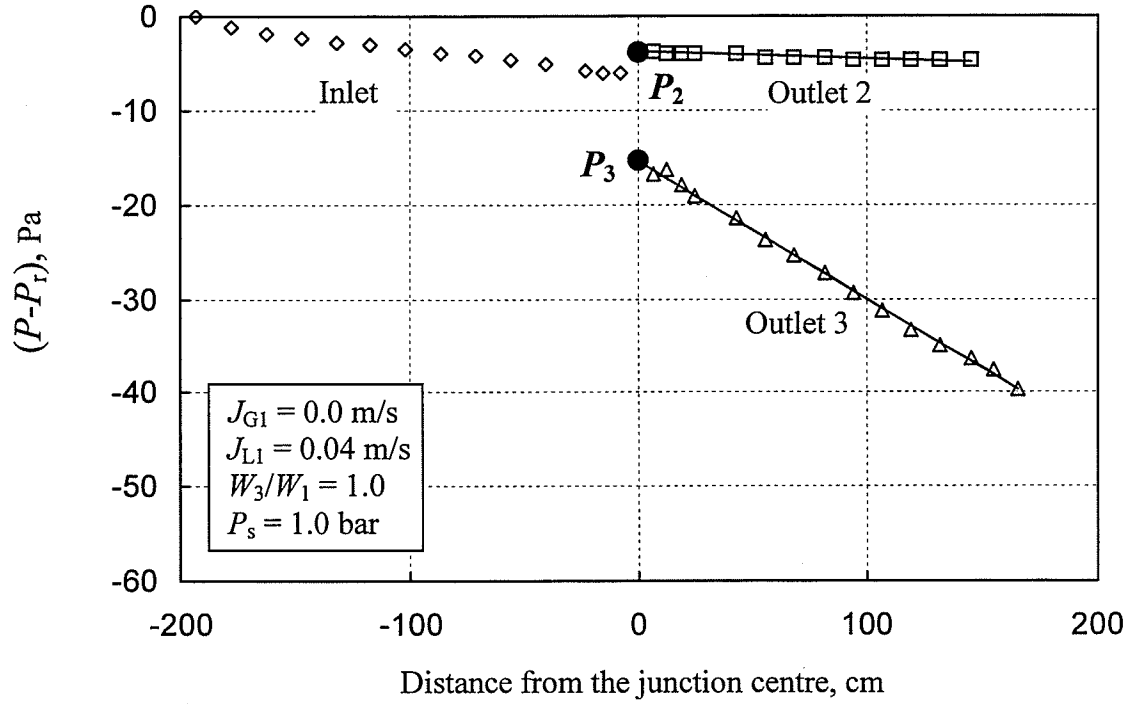

Figure 4.20 Pressure distribution for the no-gas-flow experiment

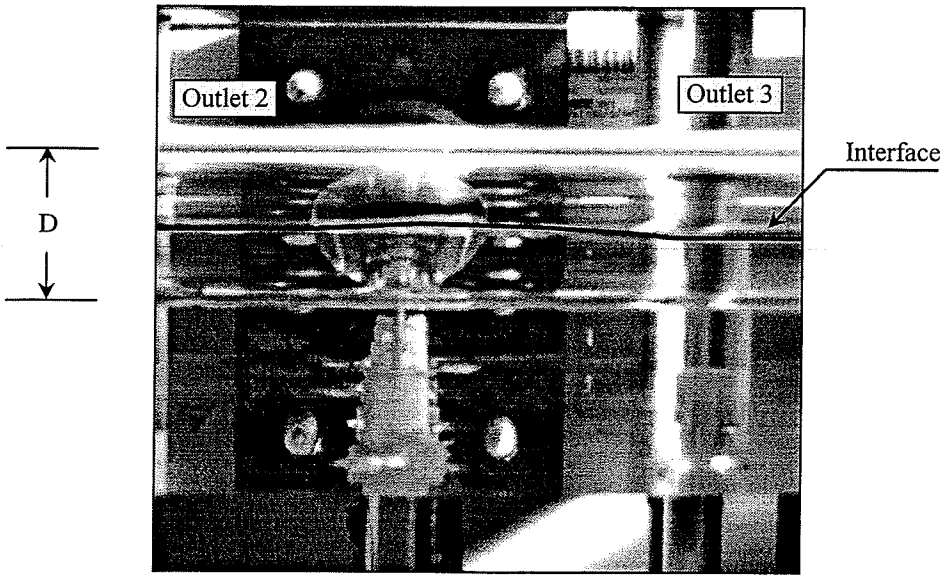

Figure 4.21 Back picture of the junction for the no-gas-flow experiment

gas flow, the static pressure above the interface is expected to be uniform throughout and according to Equation (4.12), the measured pressure distribution shown in Figure 4.20 indicates the height of the interface in the three sides of the junction. Figure 4.20 indicates that a change in the interface level occurs not only at the junction but also along the three sides of the junction. In the figure, the maximum pressure difference is 40 Pa and, when compared to its counterpart in Figure 4.18 (65 Pa), the significant effect of the interface level change on the pressure distribution for stratified flow becomes evident. As will be seen later, for the no-gas-flow experiment, the change in the interface level is the only driving force that helps the flow overcome the wall friction. Figure 4.20 shows that a horizontal interface was established in outlet 2, which is expected because there was no flow in that outlet. The figure also shows that there is approximately a 25-Pa pressure drop along outlet 3, while only a 6-Pa pressure drop

exists along the inlet. The fact that the pressure drops along the inlet and outlet 3 are different even though $W_3/W_1 = 1.0$ is discussed in Appendix C.

Figure 4.22 shows pressure-distribution data for data sets S1 to S4 with $W_3/W_1 = 0.5$. The figure shows that the location at which the data start to deviate from the linear behaviour in the inlet varies with the inlet conditions with J_{G1} being the dominant factor (compared to J_{L1}) in determining that location. The figure also shows that for all the data sets, the data in the two outlets are symmetric, which is expected with a $W_3/W_1 = 0.5$. That symmetry of the data in the two outlets was achieved even though for stratified flow, the pressure-distribution data are very sensitive to any slight variation in the interface level.

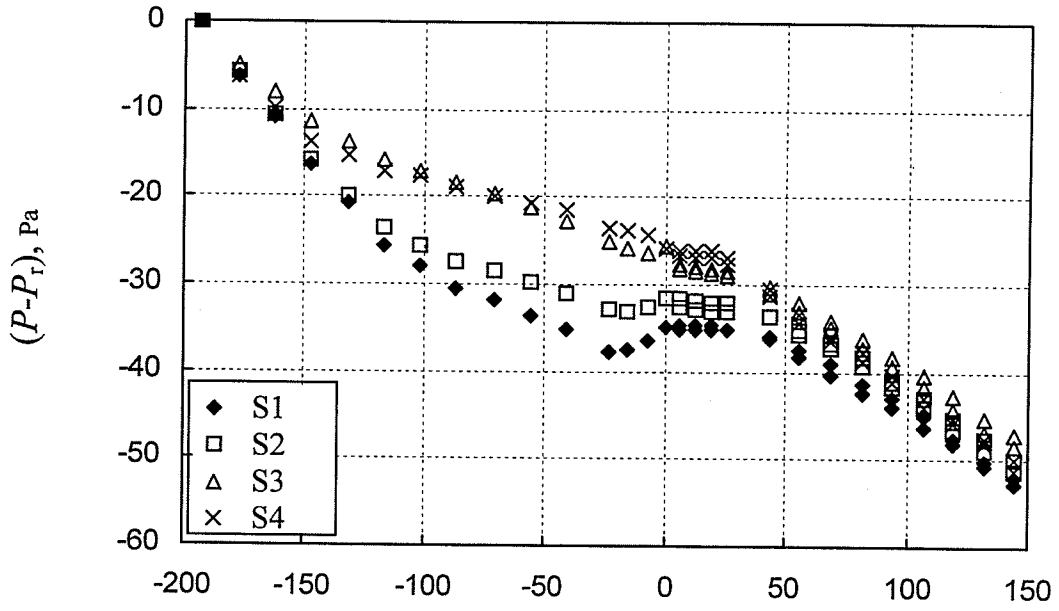

Figure 4.22 Pressure distribution for data sets S1 to S4 with $W_3/W_1 = 0.5$

Based on the discussion given above on Figures 4.18 and 4.20, it was concluded that there were changes in the interface level occurring in the three sides of the junction for stratified flow and that these changes had a significant effect on the shape and magnitude of the pressure-distribution data. As pointed out by Equation (4.12), the pressure differences measured by the transducers consist of two parts; a static component and a hydrostatic component. These two components had comparable values and it was not possible to determine the value of each component from the measured pressure distribution. As a result, it was decided not to report any pressure-drop data (ΔP_{12} and ΔP_{13}) for the stratified flow. However, all the current pressure-distribution data for stratified flow are given in Appendix C.

Assessment of the Measured Fully-Developed Pressure Gradients

The fully-developed pressure gradients measured in the inlet were compared against the predictions of the correlations proposed by Lockhart and Martinelli (1949) and Chisholm (1967). This was done for all the experiments of the wavy, stratified-wavy, and annular flow regimes. Also, the pressure gradients for the experiments of the wavy and stratified-wavy flow regimes were compared against the model of Grolman and Fortuin (1997). This model was developed to predict the pressure gradients for the following conditions $1.5 < J_{G1} < 35$ m/s and $0.0001 < J_{L1} < 0.1$ m/s. As mentioned before, for the stratified-flow experiments, it was not possible to determine the pressure gradient in the inlet and therefore these experiments are excluded from the current assessment. Dukler et al. (1964) tested five pressure-drop correlations and concluded that Lockhart and Martinelli (1949) correlation gave the best agreement. Also, Mandhane et al. (1976) assessed a total of sixteen pressure-drop correlations and they

concluded that Lockhart and Martinelli (1949) correlation is the third best for annular and wavy flow regimes. Chisholm (1967) correlation was the second best for annular flow regime. Table 4.4 shows the predicted and the average of the measured values of the pressure gradients in the inlet. The percentage differences shown in the table were calculated as follow:

$$\% \text{ difference} = ((\text{measured-predicted})/\text{measured})*100 \qquad (4.13)$$

Table 4.4 Measured and predicted values of the pressure gradients in the inlet

Data Set	Measured pressure gradient (Pa/m)	Predicted pressure gradient (Pa/m)					
		Lockhart and Martinelli (1949)	% diff.	Chisholm (1967)	% diff.	Grolman and Fortuin (1997)	% diff.
SW	77.36	73.53	4.95	68.21	11.83	54.43	29.64
W1	86.02	94.06	-9.34	98.89	-14.96	57.32	33.36
W2	149.2	192.8	-29.25	169.2	-13.41	89.57	39.97
A1	750	707.8	5.62	357.1	52.39	-	-
A2	1054	778	26.2	587.1	44.3	-	-
A3	1291	1118	13.41	1070	17.14	-	-
A4	2091	2441	-16.78	2095	-0.22	-	-

The table shows that the correlation of Lockhart and Martinelli (1949) gives the better predictions of the pressure gradients for annular flow. For wavy and stratified-wavy flows, the predictions of Lockhart and Martinelli (1949) and Chisholm (1967) are in good agreement with the measured pressure gradients.

Examination of the Two-Phase Pressure-Drop Data

Figure 4.23 shows the variation of the measured pressure drop with the split ratio W_3/W_1 for the annular-flow experiments. In the figure, the data points shown for the range of W_3/W_1 from 0.0 to 0.5 are the actual measurements for outlet 3. The data points shown for the range of W_3/W_1 from 0.5 to 1.0 are the actual measurements for outlet 2 but were used in the graphs for outlet 3 based on symmetry. The figure shows that for all the data sets, as the split ratio increases the pressure drop also increases. However, the rate of change of the pressure drop with respect to the split ratio varies from one data set to another. Data set A4 has the highest rate of change of the pressure drop with respect to the split ratio and data set A1 has the smallest one. For data sets A1 and A2, the rate of change of the pressure drop with respect to the split ratio is almost constant over the

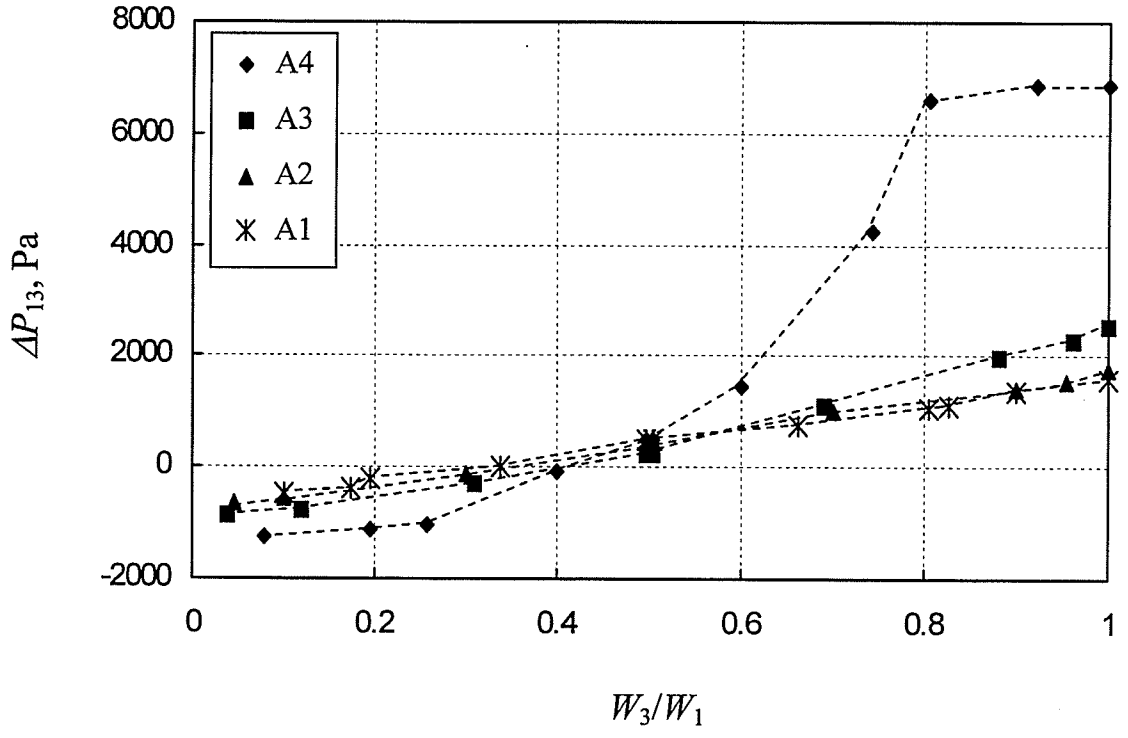

Figure 4.23 Variation of the pressure drop with the split ratio for the annular flow regime

entire range of the split ratio, i.e., the data points can be fit with a straight line. For data sets A3 and A4, the rate of change of the pressure drop with respect to the split ratio varies with the split ratio.

As the four data sets shown in Figure 4.23 have the same J_{G1} (40 m/s), the effect of varying J_{L1} (at a constant J_{G1}) on the pressure drop may be concluded. The figure shows that at a fixed split ratio, the absolute value of ΔP_{13} increases with the increase in J_{L1}.

Figure 4.24 shows the variation of the measured pressure drop with the split ratio W_3/W_1 for the wavy and wavy-stratified flow regimes. Similar to Figure 4.23, the data points shown in Figure 4.24 represent the measurements taken for outlet 3 and outlet 2. The figure shows that for data set SW, as the split ratio increases the pressure drop increases. For data sets W1 and W2, the pressure drop increases with the increase in the

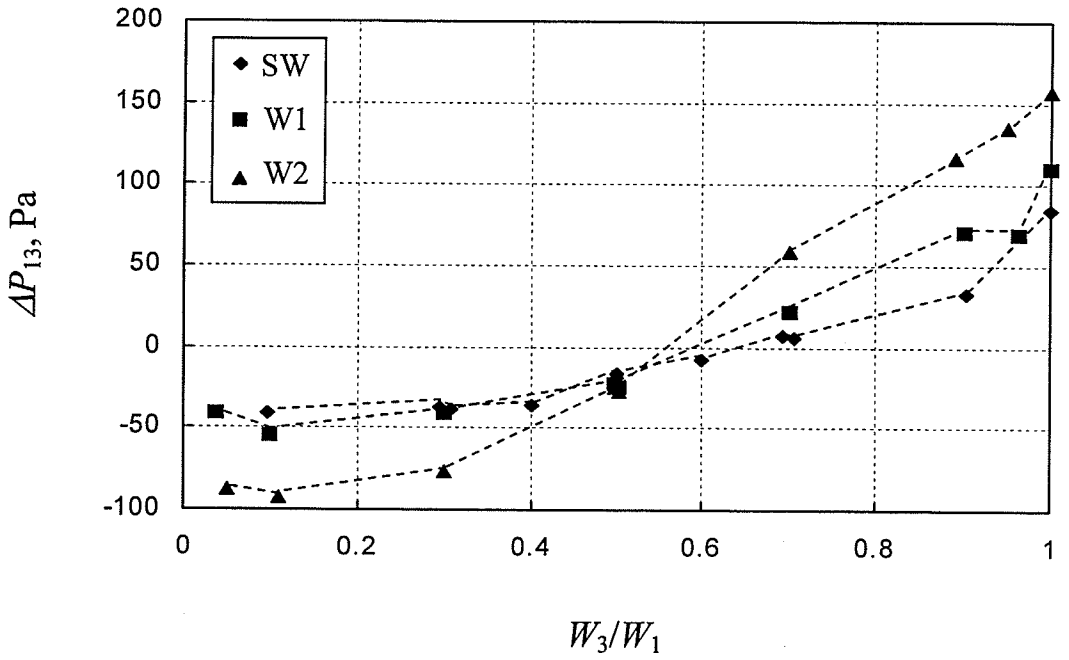

Figure 4.24 Variation of the pressure drop with the split ratio for the wavy and stratified-wavy flow regimes

split except in the range of $0 < W_3/W_1 < 0.1$. It should be mentioned that the pressure drop values at $W_3/W_1 = 0$ have no physical meaning and that is why they were not shown in Figures 4.23 and 4.24. The three data sets shown in Figure 4.24 have the same J_{G1} (10 m/s). Thus, the effect of varying J_{L1} (at a constant J_{G1}) on the pressure drop may be concluded. The figure shows that at a fixed split ratio, the absolute value of ΔP_{13} increases with the increase in J_{L1}. The observations made on Figure 4.24 are consistent with those made on Figure 4.23.

The effect of varying J_{G1} (at a constant J_{L1}) on the pressure drop may be seen in Figure 4.25. Data sets A3 and W2 have the same J_{L1} (0.04 ms) and J_{G1} values of 40 and 10 m/s, respectively. Data sets A2 and W1 have the same J_{L1} (0.01 ms) and J_{G1} values of 40 and 10 m/s, respectively. The figure shows that at a fixed split ratio, the absolute

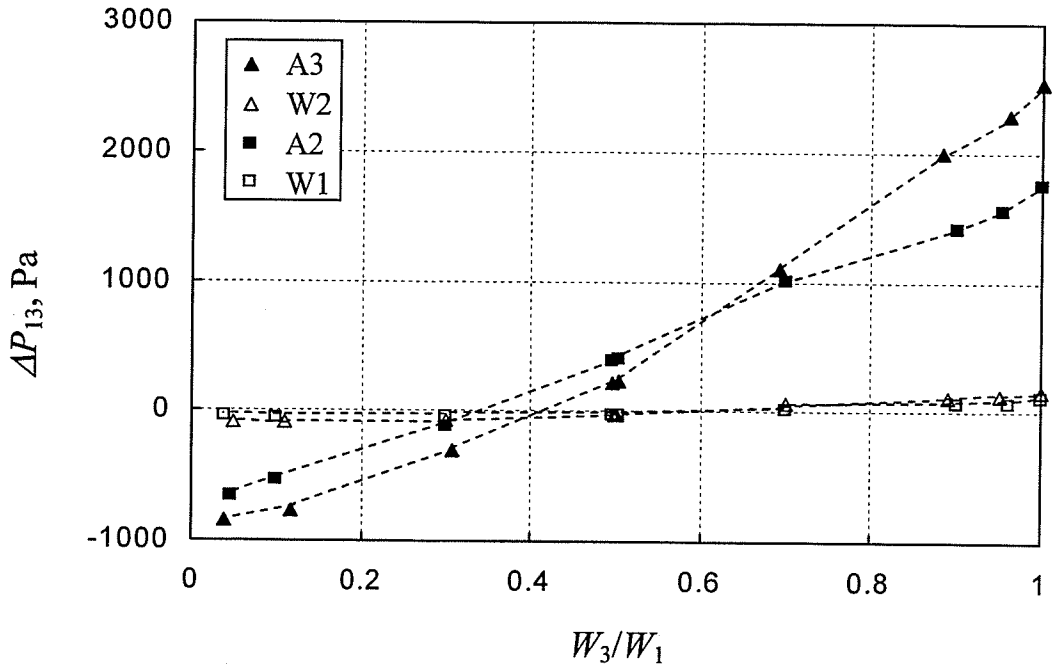

Figure 4.25 Effect of J_{G1} on the pressure drop

value of ΔP_{13} increases with the increase in the value of J_{G1}. This effect is similar to the effect of J_{L1} on the pressure drop. Therefore, it may be concluded that the absolute value of ΔP_{13} increases with the increase in J_{G1} and/or J_{L1}.

4.5 Experimental Uncertainty

An uncertainty analysis was conducted for both the phase-distribution and pressure-drop data. The analysis was done based on the methods of Kline and McClintock (1953) and Moffat (1988). These methods are explained in detail in Appendix E of Buell (1992). A summary of the analysis is given here and a complete set of the results is given in Appendix D. All uncertainties given in the current study are at "odds" (as used by the above-given authors) of 20 to 1. The uncertainties are meant to accommodate: discrimination uncertainties in the measuring instruments, the error in fitting an equation to the calibration data, and the accuracy of the calibrating devices.

The uncertainties in the values of J_{G1}, J_{L1}, and x_1 were found to be within ±4.4 %. For W_3/W_1, x_3/x_1, F_{BG}, and F_{BL}, the uncertainties were within ±11.7 % except for one measurement of F_{BL} at 14.8 %. The uncertainty in the test-section pressure was found to be within ±1 %.

For ΔP_{12} and ΔP_{13}, 82 % of the data had uncertainties less than ±30 %. The experiments A1-4 and A4-5 had very large values for the uncertainty of ΔP_{13}. For both experiments, the uncertainty values for P_1 and P_3 were very small (< 2.8 %). However, because the value of ΔP_{13} was very small relative to the values of P_1 and P_3, the uncertainty value of ΔP_{13} became very large.

Chapter 5

MODELLING OF PHASE SEPARATION AND PRESSURE DROP

5.1 Comparison Between Current Phase-Distribution Data and Models

The predictions of the models proposed by Hwang (1986) and Ottens et al. (1995) (see Section 2.3) were compared against the current phase-distribution data. As mentioned in Section 2.3.3, these models were found to be the best available tools in the literature for predicting phase distribution in horizontal impacting tee junctions.

5.1.1 Hwang (1986) Model

Figure 5.1 shows predictions of the Hwang (1986) model against the phase-distribution data for the annular flow regime. The figure shows that the predictions

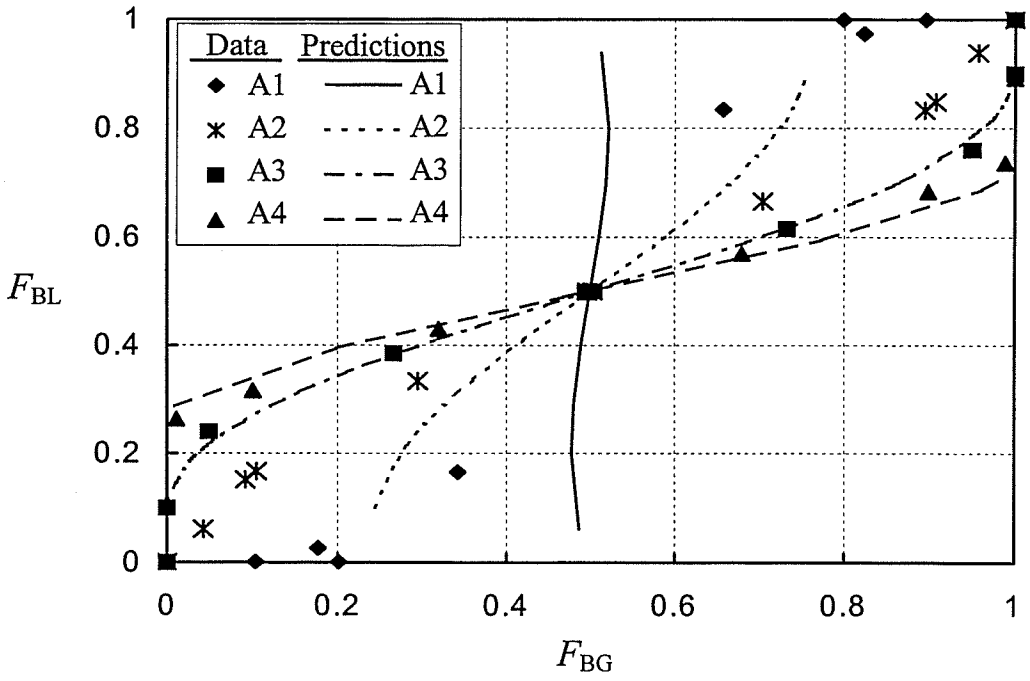

Figure 5.1 Predictions of the Hwang (1986) model against the current data for annular flow

follow the correct trend in terms of the effect of J_{L1}. The predictions rotate around the point (0.5,0.5) in a clockwise direction as J_{L1} increase from data set A1 to A4. Qualitatively, for data sets A3 and A4, the predictions are in very good agreement with the data. For data sets A1 and A2, the model underpredicts the values of F_{BL} in the range $0 \leq W_3/W_1 \leq 0.5$.

Figure 5.2 shows predictions of the Hwang (1986) model against the phase-distribution data for the stratified-wavy and wavy flow regimes. The figure shows that the predictions follow the correct trend in terms of the effect of J_{L1}. For data set SW, the predictions are in very good agreement with the data. However, for data sets W1 and W2, the data are poorly predicted as the model significantly underpredicts the

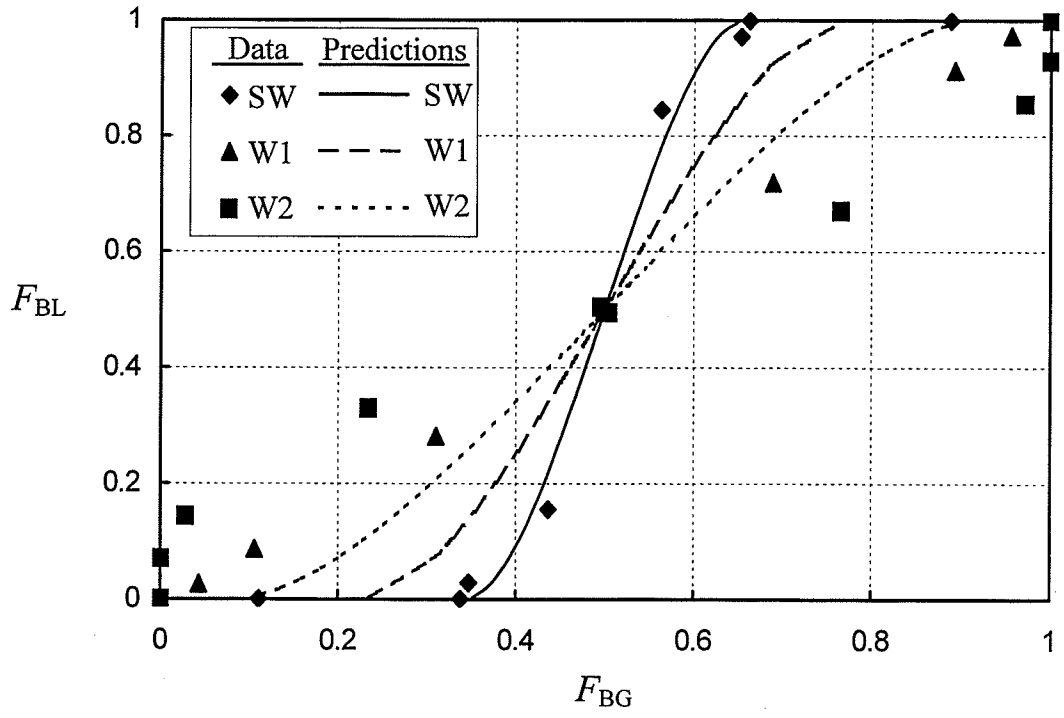

Figure 5.2 Predictions of the Hwang (1986) model against the current data for stratified-wavy and wavy flows

values of F_{BL} in the range $0 \leq W_3/W_1 \leq 0.5$.

Figure 5.3 shows predictions of the Hwang (1986) model against the phase-distribution data for the stratified flow regime. In the figure, the model predicts the correct trend in terms of the effects of varying J_{G1} and J_{L1}. However, all the data in the figure are poorly predicted as the model severly underpredicts the values of F_{BL} in the range $0 \leq W_3/W_1 \leq 0.5$.

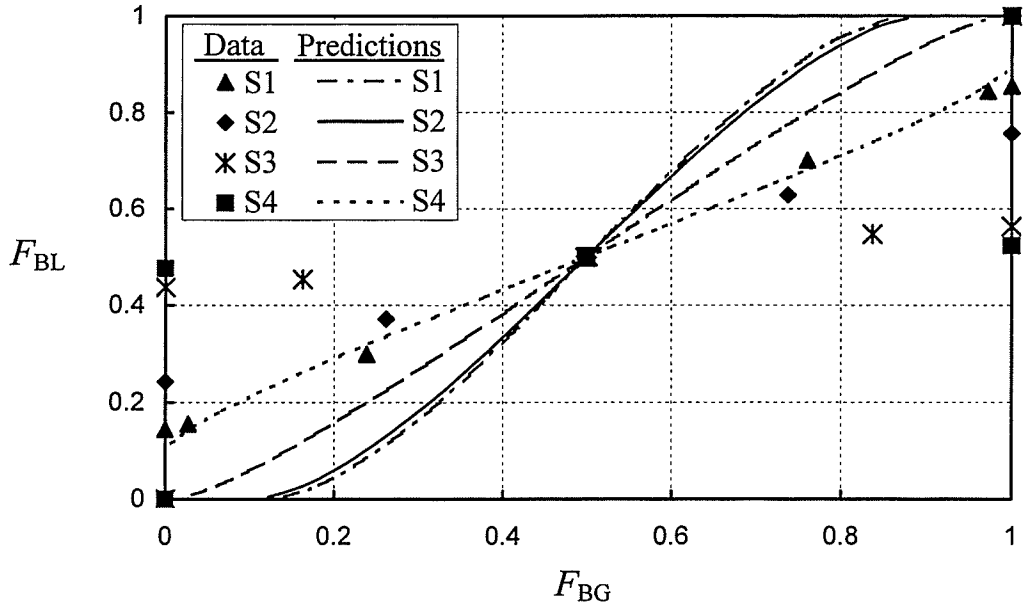

Figure 5.3 Predictions of the Hwang (1986) model against the current data for stratified flow

5.1.2 Ottens et al. (1995) Model

Figure 5.4 shows predictions of the Ottens et al. (1995) model against the phase-distribution data for the annular flow regime. The figure shows that the model predicts the correct trend in terms of varying J_{L1}. For all the data sets, the predictions are in

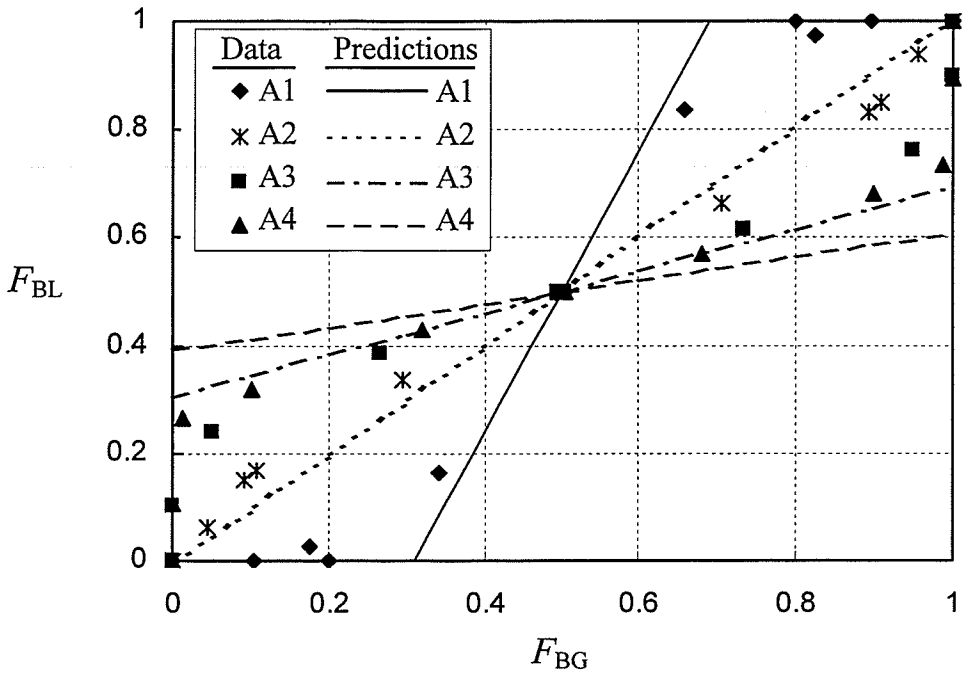

Figure 5.4 Predictions of the Ottens et al. (1995) model against the current data for annular flow

reasonable agreement with the data. For data sets A1 and A2, the model slightly underpredicts the values of F_{BL} in the range $0 \leq W_3/W_1 \leq 0.5$. For data sets A3 and A4, the model overpredicts the values of F_{BL} in the range $0 \leq W_3/W_1 \leq 0.5$.

Figure 5.5 shows predictions of the Ottens et al. (1995) model against the phase-distribution data for the stratified-wavy and wavy flow regimes. The figure shows that the predictions are in good agreement with the data in magnitude and trend with a slight overprediction of F_{BL} in the range $0 \leq W_3/W_1 \leq 0.5$ for data set SW.

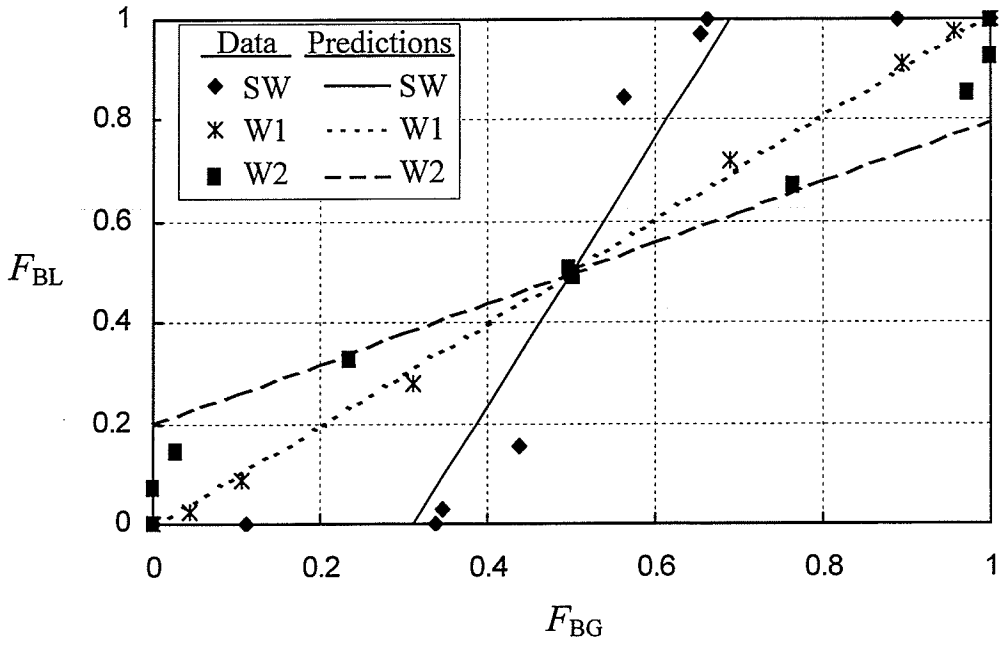

Figure 5.5 Predictions of the Ottens et al. (1995) model against the current data for stratified-wavy and wavy flows

Figure 5.6 shows predictions of the Ottens et al. (1995) model against the phase-distribution data for the stratified flow regime. In the figure, the model predicts the correct trend in terms of varying J_{L1}. However, the model does not predict the correct trend in terms of varying J_{G1}. Data sets S1, S2, and S3 have the same J_{L1} and different J_{G1}. The predictions for these three data sets lie on the same straight line. The overall poor predictions seen in Figure 5.6 may be attributed to the fact that the Ottens et al. (1995) model was developed for two-phase flows with an inlet liquid hold-up of less than 0.06. This might explain why the model works best for data set S1 which has the lowest liquid hold-up amongst the data sets in Figure 5.6.

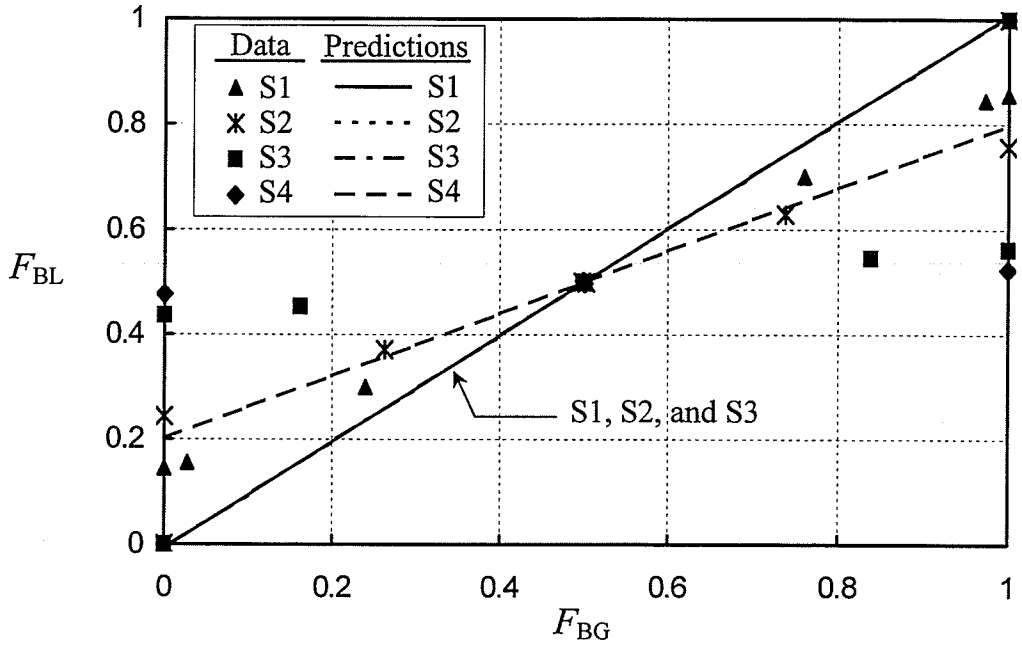

Figure 5.6 Predictions of the Ottens et al (1995) model against the current data for stratified flow

5.1.3 Concluding Remarks

From Figures 5.1 to 5.6, the following (applicable only to the current phase-distribution data) conclusions may be drawn:

- The model of Ottens et al. (1995) produces better predictions (in general) than the model of Hwang (1986), particularly in the wavy and annular regions.
- Neither model is capable of predicting the stratified-flow data.
- There are no models or correlations available yet for predicting the two-phase pressure drop in impacting tees.

In view of the above observations, the need for further modelling efforts for predicting the pressure drop and phase distribution of two-phase flow in impacting tees is clearly apparent.

5.2 Proposed Model

One of the objectives of the current study was to develop a model capable of predicting the phase distribution and pressure drop during two-phase flow in horizontal impacting tees. This model should work for all the flow regimes investigated in the current study. In the following sections, this model will be presented and tested against the current data and data of other researchers.

It should be mentioned that a numerical study of single-phase flow in two-dimensional tee junctions was done as part of the current study. The results of this numerical study are given in Appendix E. The objective of this numerical study was to gain some insight into the physics of the flow splitting in tee junctions. That in turn should help when developing a model for the case of two-phase flow. Reference will be made to this work in some of the following sections.

5.2.1 Overview

For the analysis of a steady-state flow in a horizontal impacting junction, many parameters are involved. Assuming known geometry (D_1, D_2, and D_3) and known properties (ρ_L, ρ_G, μ_L, μ_G,....), the remaining parameters may be categorized as follow: mass flow rates (W_1, W_2, and W_3), qualities (x_1, x_2, and x_3), and pressure drops (ΔP_{12} and ΔP_{13}). Typically, three independent parameters are specified (e.g., W_1, x_1, and W_3). In order to determine the remaining five unknown parameters, five equations are required. Typically two continuity equations and two energy equations are used. The two continuity equations are selected from among three possible equations, one for the mixture and one for each phase. Only two continuity equations should be used because the third equation would be redundant (if used). The two continuity equations used in

the current study were the continuity equations for the mixture and the gas phase. The two energy equations may be selected from among many possible equations. Energy balance equations can be applied to the inlet-to-outlet-3 stream, the inlet-to-outlet-2 stream, or the inlet to both outlets. Also, energy balance equations can be applied for the gas phase, liquid phase, or the mixture. Thus, there are nine energy balance equations that can be applied to the flow. Only two energy equations should be used because any other equation would be redundant (if used). The two energy equations used in the current study were the energy equations for the gas phase applied to inlet-to-outlet 3 stream and inlet-to-outlet 2 stream. The fifth equation used in the current study was a momentum balance applied on a control volume within the junction.

5.2.2 Model Equations

From an overall mass balance, we get

$$W_1 = W_2 + W_3 \tag{5.1}$$

A mass balance on the gas phase gives

$$x_1 W_1 = x_2 W_2 + x_3 W_3 \tag{5.2}$$

Assuming equilibrium conditions, the pressure drop experienced by the gas from inlet to outlet 3 of the junction is equal to the pressure drop experienced by the liquid from side 1 to side 3. From energy considerations, this pressure drop can be expressed as:

$$\Delta P_{13} = \frac{\rho_G}{2}(V_{G3}^2 - V_{G1}^2) + K_{G,13}\frac{\rho_G}{2}V_{G1}^2 \tag{5.3}$$

where the first term on the right hand side of Equation (5.3) represents the reversible component and the second term represents the irreversible component of the pressure drop. Similarly, for the pressure drop on the gas phase from inlet to outlet 2, we have

$$\Delta P_{12} = \frac{\rho_G}{2}(V_{G2}^2 - V_{G1}^2) + K_{G,12}\frac{\rho_G}{2}V_{G1}^2 \qquad (5.4)$$

where, ρ_G is the density of the gas phase, V_G is the average gas velocity, $K_{G,12}$ is the inlet-to-outlet 2 mechanical-energy loss coefficient for the gas phase, and $K_{G,13}$ is the inlet-to-outlet 3 mechanical-energy loss coefficient for the gas phase.

The average gas velocity V_G was calculated from the following equation:

$$V_{Gi} = \frac{W_{Gi}}{\rho_G \alpha_i A} \quad ,i = 1,2,3 \qquad (5.5)$$

where, W_G is the gas mass flow rate, A is the cross-sectional area of the pipe, and α is the void fraction calculated using the model of Shoham et al. (1987).

The fifth equation of the proposed model is the momentum-balance equation at the junction. Figure 5.7 shows a control volume situated at the junction with the relevant momentum rates and forces indicated at the control surfaces. In the figure, the parameter F_D is the net drag force acting on the control volume at the back wall of the

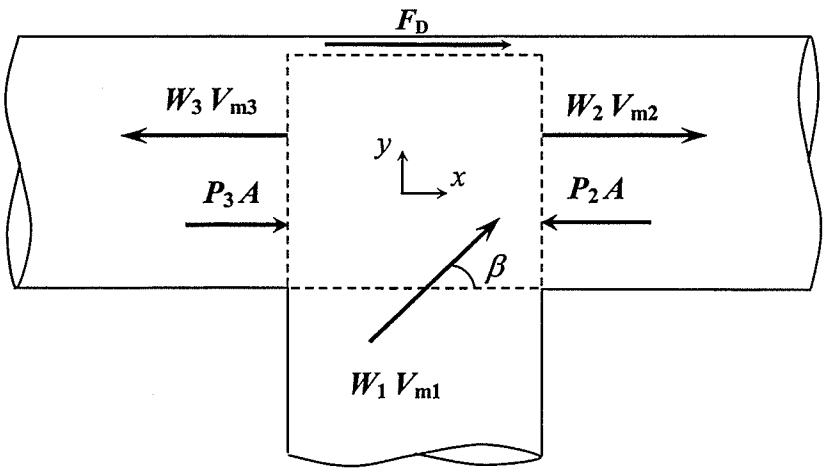

Figure 5.7 Momentum-balance parameters at the junction

junction and V_m is the momentum velocity of the mixture to be defined later. This force can be positive or negative depending on the value of W_3/W_1. Due to symmetry, when $W_3/W_1 = 0.5$, F_D must be equal to zero. The results of the numerical study given in Appendix E indicate that the back wall of the junction is a region characterized by relatively high values of the wall shear stress. These high values indicate that the control volume located at the junction experience friction forces of considerable values. Consequently, these friction forces should be taken into account when applying a momentum balance at the junction.

Plots of streamlines given in Appendix E indicate that as the inlet flow approaches the junction, the part of the inlet flow going through outlet 2 deviates towards outlet 2 outlet and similarly, the part of the inlet flow going through outlet 3 deviates towards it. Thus, close to the junction, the inlet flow deviates from the y-direction. This deviation occurs for all the split ratios except for $W_3/W_1 = 0.5$. The effect of the inlet-flow deviation from the y-direction is accounted for by using the term $W_1 V_{m1}\cos\beta$. For the flows in outlets 2 and 3, it was assumed that the momentum rates of these flows in the x-direction are $W_2\, V_{m2}$ and $W_3\, V_{m3}$, respectively. The angle β shown in Figure 5.7 is a hypothetical angle between the inlet flow and the positive x-direction. According to the definition of β, when $W_3/W_1 = 0.5$, β must be equal to 90°. Thus, when $W_3/W_1 = 0.5$, F_D and β must be equal to zero and 90°, respectively. This guarantees that the momentum equation satisfies the symmetry irrespective of the formulation of F_D and β.

From a simple momentum balance in the x-direction, we get

$$P_3 A + F_D - P_2 A = W_2\, V_{m2} - W_3\, V_{m3} - W_1\, V_{m1} \cos\beta \qquad (5.6)$$

where V_m is the momentum velocity of the mixture defined as

$$V_{mi} = \frac{W_i}{\rho_{mi} A} \quad ,i = 1,2,3 \tag{5.7}$$

where W_i is the total mass flow rate in side i, and ρ_m is the momentum-weighted density defined as

$$\rho_{mi} = \left[\frac{(1-x_i)^2}{(1-\alpha_i)\rho_L} + \frac{x_i^2}{\alpha_i \rho_G} \right]^{-1} \quad ,i = 1,2,3 \tag{5.8}$$

where ρ_L is the density of the liquid phase and x is the mixture quality.

The force F_D may be formulated as follows:

$$F_D = A_w \, C_f \, (\frac{1}{2} \rho_{ml} \, V_{ml}^2) \tag{5.9}$$

where A_w is the area of the back, top, and bottom walls of the control volume shown in Figure 5.7, and C_f is a friction coefficient. The parameter A_w can be approximated as

$$A_w = \pi D.D - A_{CO} \tag{5.10a}$$

where A_{CO} is the surface area cut out of the control volume wall by virtue of the intersection with the inlet pipe. The parameter A_{CO} can be expressed as

$$A_{CO} = a \, \frac{\pi}{4} D^2 \tag{5.10b}$$

where a is a constant. Equation (5.10a) can then be written as

$$A_w = \pi D.D - a \frac{\pi}{4} D^2 = (4-a) \frac{\pi}{4} D^2 \tag{5.10c}$$

Substituting the expression for A_w into Equation (5.9) and rearranging gives

$$F_D = \frac{\pi}{4} D^2 \, \rho_{ml} \, V_{ml} \left[\frac{(4-a)}{2} C_f \, V_{ml} \right] \tag{5.11}$$

Using Equation (5.7), Equation (5.11) can be re-written as

$$F_D = W_1 V_{m1} \left[\frac{(4-a)}{2} C_f \right] \tag{5.12}$$

Substituting in Equation (5.6) and rearranging yields

$$P_3 A - P_1 A - P_2 A + P_1 A = W_2 V_{m2} - W_3 V_{m3} - W_1 V_{m1} \cos\beta - W_1 V_{m1} \left[\frac{(4-a)}{2} C_f \right] \tag{5.13}$$

The formulations for the angle β and the friction coefficient C_f have to be determined empirically. In order to reduce the empiricism in the proposed model, it was decided to sum up the effects of the friction forces and the deviations from the main directions in one term only as follows:

$$(\Delta P_{12} - \Delta P_{13}) A = W_2 V_{m2} - W_3 V_{m3} - W_1 V_{m1} \beta' \tag{5.14}$$

where β' $\left(= \cos\beta + \frac{(4-a)}{2} C_f \right)$ is a parameter that will be determined empirically as will be seen later.

It should be mentioned that for the symmetry of an equal-sided horizontal impacting junction to be satisfied, the following equation applies:

$$\Delta P_{12} \Big|_{W_3/W_1 = \delta} = \Delta P_{13} \Big|_{W_3/W_1 = 1-\delta} \tag{5.15}$$

Equation (5.15) implies that ΔP_{12} can be obtained from Equation (5.3) by replacing the outlet-3 parameters with outlet-2 parameters. Consequently, the second energy equation, (Equation (5.4)), may be eliminated and the model reduces to four equations only. These equations are the two continuity equations (Equations (5.1) and 5.2)), the energy equation (Equation (5.3)), and the momentum equation (Equation (5.14)). These equations and the symmetry condition (Equation (5.15)) will hereafter be referred to as the model main equations.

5.2.3 Evaluation of Model Coefficients ($K_{G,13}$ and β')

The coefficient $K_{G,13}$ appears in terms that represent the irreversible component of the pressure drop. This coefficient can be determined from an application of the full Navier-Stokes equations (as was done in the numerical study in Appendix E). Another way of determining this coefficient is empirically via the correlation of the two-phase pressure-drop data. For the current modelling approach, the latter method is the only available option. It should be mentioned that in some previous studies dealing with branching junctions, the single-phase energy loss coefficient (K_{13}) with various correction factors was used to replace the coefficient $K_{G,13}$.

The current data, together with Equation (5.3), were used to determine values of the gas- phase mechanical-energy loss coefficient, $K_{G,13}$. These results are shown in Figures 5.8 and 5.9 for wavy and annular flows, respectively. Figures 5.8 and 5.9 show that $K_{G,13}$ versus W_3/W_1 follows approximately a parabolic curve for each inlet condition. The curves seen in Figures 5.8 and 5.9 passing through the experimental data are parabolas that were obtained by least-square fitting of the experimental data. Figure 5.10 shows a comparison between values of $K_{G,13}$ obtained in the current study for data sets SW and A1 against the correlation for K_{13} developed by Ito and Imai (1973) for single-phase flow. Data sets SW and A1 were selected as they represent two different flow regimes and they have the highest values for the inlet quality x_1 (compared to other data sets in the current study). Figure 5.10 shows that the correlation for K_{13} is in very good agreement with values of $K_{G,13}$ for data set A1, which is expected since A1 has an inlet quality of 0.96. The figure also shows that there is no agreement between the correlation for K_{13} and values of $K_{G,13}$ for data set SW. A possible reason for this

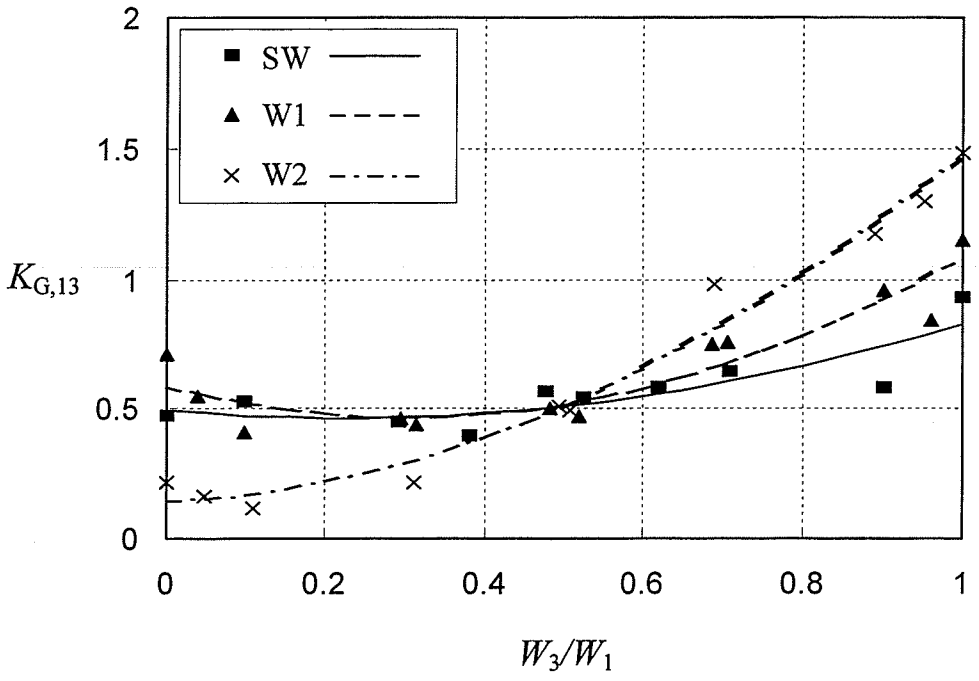

Figure 5.8 $K_{G,13}$ values for wavy and stratified-wavy flows

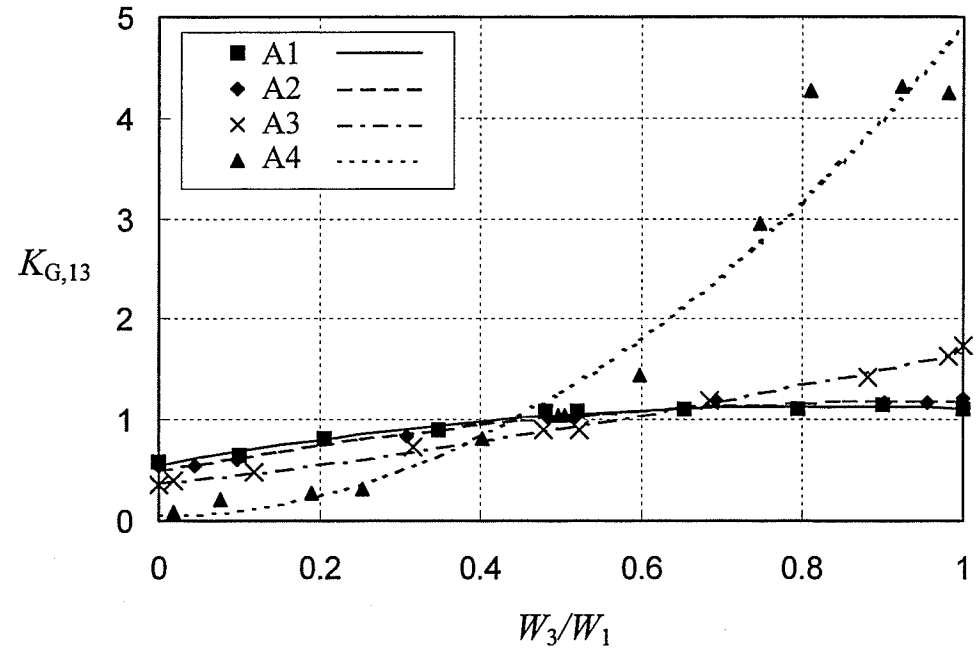

Figure 5.9 $K_{G,13}$ values for annular flow

disagreement is that data set SW has an inlet quality of 0.87. However, Figure 5.9 indicates that values of $K_{G,13}$ for data set A2 (with $x_1 = 0.87$) are very close to those of data set A1. Consequently, values of $K_{G,13}$ for data set A2 are expected to be in good agreement with the single-phase correlation for K_{13}. This indicates that the disagreement seen in Figure 5.10 between values of $K_{G,13}$ for data set SW and the single-phase correlation for K_{13} is not due to the inlet quality value. Instead, this disagreement is probably due to the type of the flow regime.

Based on the results shown in Figures 5.8 and 5.9, we can write

$$K_{G,13} = C_1 + C_2 (W_3/W_1) + C_3 (W_3/W_1)^2 \qquad (5.16)$$

For single-phase flow, the coefficients in Equation (5.16) are independent of fluid properties and flow rate, as confirmed by our results and other data in the literature.

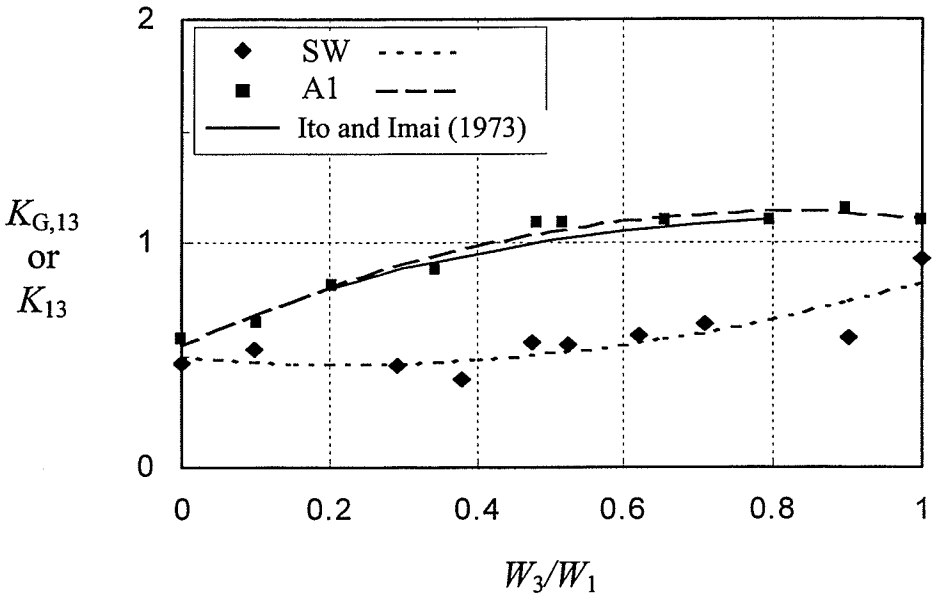

Figure 5.10 Mechanical-energy loss coefficients

However, for two-phase flow, these coefficients appear to depend on the flow regime and the flow rate within the flow regime. For both flow regimes, C_1, C_2, and C_3 are assumed to be functions of the inlet Reynolds number, Re_1, defined as follows:

$$Re_1 = \frac{4W_1}{\pi D_1 \mu_G} \tag{5.17}$$

The data of stratified-wavy and wavy flows were found to correlate well with the following equations:

$$C_1 = -4.5688 [\log (Re_1)]^2 + 43.569 [\log (Re_1)] - 103.28 \tag{5.18}$$

$$C_2 = 14.469 [\log (Re_1)]^2 - 139.51 [\log (Re_1)] + 335.44 \tag{5.19}$$

$$C_3 = -11.424 [\log (Re_1)]^2 + 112.14 [\log (Re_1)] - 273.69 \tag{5.20}$$

For annular flow, the following equations were found to give good correlations for the coefficients C_1, C_2, and C_3:

$$C_1 = 0.1908 [\log (Re_1)]^2 - 2.9917 [\log (Re_1)] + 10.924 \tag{5.21}$$

$$C_2 = 1.6012 [\log (Re_1)]^2 - 20.249 [\log (Re_1)] + 63.446 \tag{5.22}$$

$$C_3 = 9.1961 [\log (Re_1)]^2 - 89.465 [\log (Re_1)] + 215.72 \tag{5.23}$$

Correlations for the parameter β' in Equation (5.14) were obtained for stratified, stratified-wavy, and wavy flow regimes using the following steps. In the following steps, the current phase-distribution data were used whenever necessary.

1- Equations (5.18) to (5.20) were substituted into Equation (5.16) to get the correlated values for $K_{G,13}$. It should be mentioned that Equations (5.18) to (5.20) were developed for stratified-wavy and wavy flows only. For reasons mentioned in Section 4.4.2, it was not possible to determine ΔP_{12} and ΔP_{13} from the current pressure-distribution data for stratified flow. As a result, values of $K_{G,13}$ for

stratified flow were not available. It was decided then to use Equations (5.18) to (5.20) for the stratified flow regime as well.

2- With the calculated values of $K_{G,13}$ and the current phase-distribution data, Equation (5.3) was used to determine the values of ΔP_{13}.

3- Values of ΔP_{12} were determined from Equation (5.3) with outlet-3 parameters replaced by outlet-2 parameters.

4- The values of ΔP_{12} and ΔP_{13} were used in Equation (5.14) to determine values of the parameter β'.

For the annular flow regime, Equations (5.21) to (5.23) were used instead of Equations (5.18) to (5.20) in step 1 above. Steps 2 to 4 remained unchanged.

Values of β' obtained in step 4 are shown in Figures 5.11, 5.12, and 5.13 for the stratified, wavy, and annular flows, respectively. In these figures, the data points that corresponded to values of F_{BG} or F_{BL} less than 0.05 or higher than 0.95 were not included. Excluding these results enabled the model predictions to be in better agreement with the current phase-distribution data. In the figures, straight lines were fitted through the data using least-square analysis. These figures show that β' versus W_3/W_1 follows a nearly linear relation for each inlet condition. The figures also show that for all the inlet conditions, β' is approximately zero at $W_3/W_1 = 0.5$. This is expected according to the definition of β'. In Figures 5.11 to 5.13, there are two opposite trends in the data with the increase in W_3/W_1: a decrease and an increase in the value of β'. Recalling that β is measured with the outlet-2 direction (see Figure 5.7), it is expected that the value of β increases with the increase in W_3/W_1. As a result, $\cos\beta$

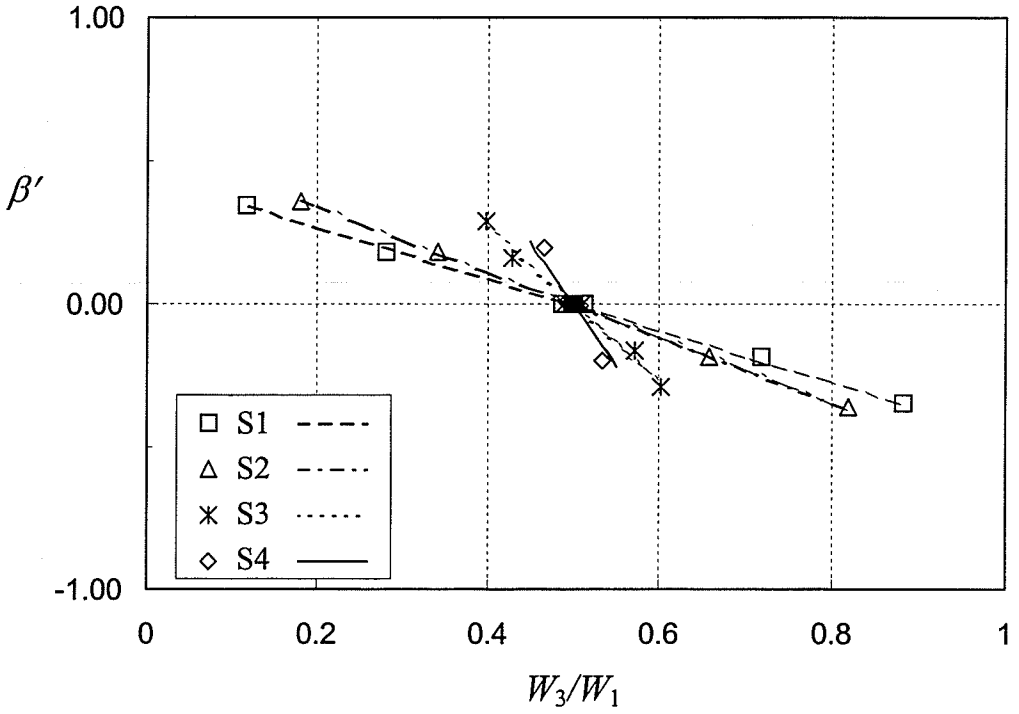

Figure 5.11 β' values for stratified flow

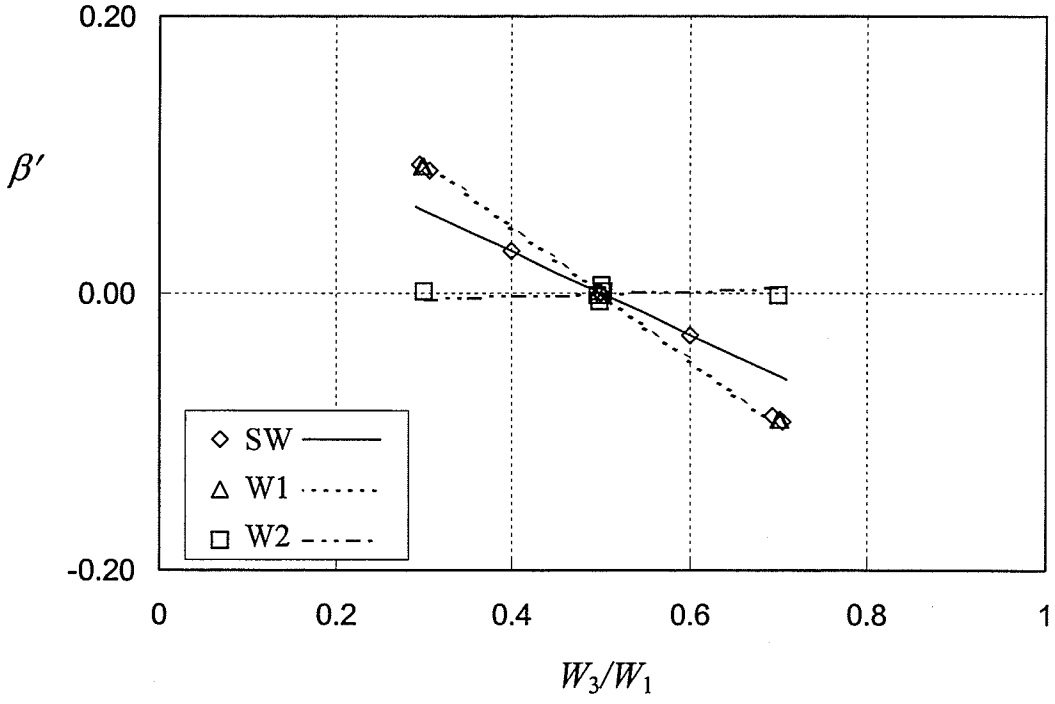

Figure 5.12 β' values for stratified-wavy and wavy flows

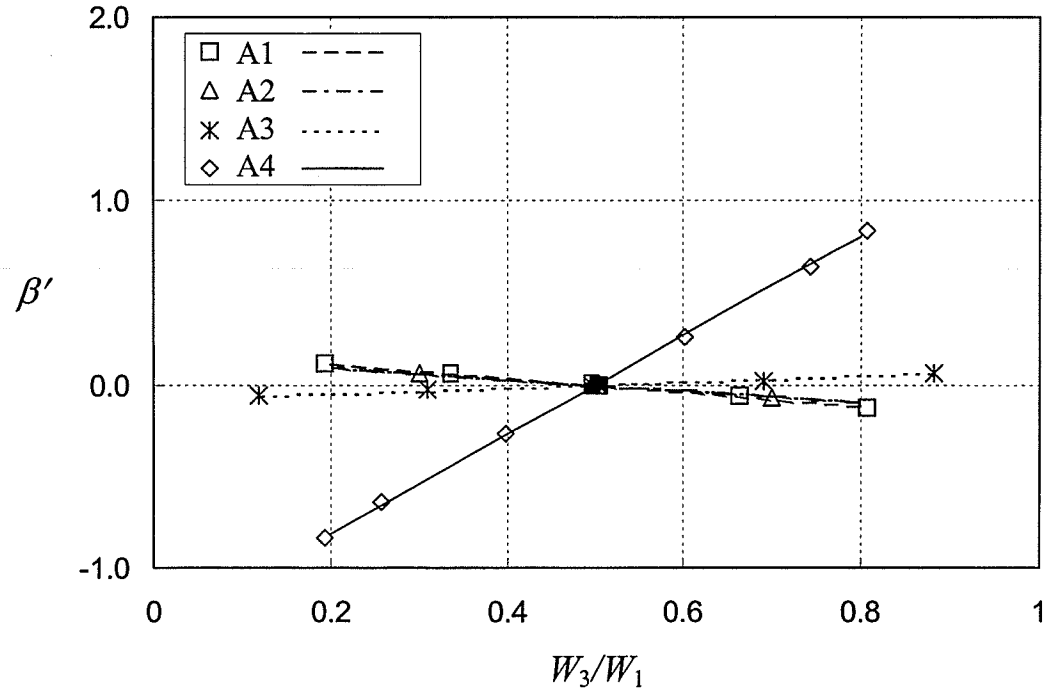

Figure 5.13 β' values for annular flow

decreases with increasing W_3/W_1. Recalling that F_D is the net drag force at the junction in the direction of outlet 2 (see Figure 5.7), it is expected that F_D increases with the increase in W_3/W_1. Thus, increasing W_3/W_1 has opposite effects on the two terms that β' is composed of.

As mentioned before, straight lines were fitted through the data in Figures 5.11 to 5.13. These lines were given the following form:

$$\beta' = Y\,(W_3/W_1 - 0.5) \qquad (5.24)$$

where Y is the slope of the straight line.

Equation (5.24) ensures that β' is zero when $W_3/W_1 = 0.5$. The following set of correlations were obtained for the slope Y:

For the stratified flow regime:

$$Y = -1.3137(\log(\dot{M}_R Re_l x_l))^2 + 11.94(\log(\dot{M}_R Re_l x_l)) - 27.696 \quad (5.25)$$

For the stratified-wavy and wavy flow regimes:

$$Y = -0.5347(\log(\dot{M}_R Re_l))^2 + 6.5693(\log(\dot{M}_R Re_l)) - 19.63 \quad (5.26)$$

and for the annular flow regime:

$$Y = 11.735(\log({Re_l}^{1.5} {x_l}^{0.8}))^3 - 263.44(\log({Re_l}^{1.5} {x_l}^{0.8}))^2 + 1971.4(\log({Re_l}^{1.5} {x_l}^{0.8})) - 4918.38 \quad (5.27)$$

where Re_l and $\dot{M}_R$ are defined by Equations (5.17) and (3.2), respectively.

5.3 Calculation Procedure

As mentioned before, for the proposed model, three inputs; W_1, x_1, and W_3 have to be specified and then the model main equations can be solved to obtain the following parameters: W_2, x_2, x_3, ΔP_{12}, and ΔP_{13}. When solving the model main equations, values of $K_{G,13}$, and β' were obtained from the appropriate correlations. It was found that the model could not obtain a solution when solving for phase-distribution data with a zero value for F_{BG} or F_{BL}. This might be attributed to the reason that for such data, the term $W_3.V_{m3}$ in Equation (5.14) was very small in magnitude. As a result, the percentage balance in Equation (5.14) was not small enough to meet the convergence criterion even though the difference between the right and left hand sides of the equation was small in magnitude. As a result, it was decided to specify the value of F_{BG} (or F_{BL}) as an input instead of W_3. This ensures that F_{BG} and F_{BL} will always have finite values, i.e., nonzero values. The following steps demonstrate how the model was executed:

1- Values for the three parameters W_1, x_1, and F_{BG} along with values of D_1, ρ_L, ρ_G, μ_L, and μ_G were specified.

2- For values of F_{BG} that are less than 0.5, a solution can only exist within the range $0.0 < F_{BL} < 0.5$. For values of F_{BG} that are greater than 0.5, a solution can only exist within the range $0.5 < F_{BL} < 1.0$ (see Figure 1.2(a)). Therefore, according to the specified value of F_{BG} in step 1, values of $F_{BL,min}$ and $F_{BL,max}$ can be determined as follows:

$$F_{BL,min} = 0.0 \text{ and } F_{BL,max} = 0.5 \qquad 0.0 > F_{BG} > 0.5 \qquad (5.28a)$$

$$F_{BL,min} = 0.5 \text{ and } F_{BL,max} = 1.0 \qquad 0.5 > F_{BG} > 1.0 \qquad (5.28b)$$

3- Select a value of F_{BL} within the range where a solution can exist.

4- Calculate x_3 from

$$x_3 = \frac{F_{BG}}{F_{BG} + F_{BL}\left[\frac{1-x_1}{x_1}\right]} \qquad (5.29)$$

5- Calculate W_3 from

$$W_3 = W_1 x_1 F_{BG} + W_1(1 - x_1) F_{BL} \qquad (5.30)$$

6- Calculate W_2 from Equation (5.1).

7- Calculate x_2 from Equation (5.2).

8- Determine J_{G1} and J_{L1} using values of W_1, x_1, D_1, ρ_L, and ρ_G. Determine the inlet flow regime using Mandhane et al. (1974) map.

9- Repeat step 8 for outlet 2 and outlet 3.

10- With the flow regimes known in the three sides of the junction, calculate α_1, α_2, and α_3 using the model of Shoham et al. (1987) given in Appendix A.

11- Calculate V_{G1}, V_{G2}, and V_{G3} from Equation (5.5).

12- Calculate ρ_{m1}, ρ_{m2}, and ρ_{m3} from Equation (5.8). Calculate V_{m1}, V_{m2}, and V_{m3} from Equation (5.7).

13- Calculate Re_1 from Equation (5.17).

14- For stratified, stratified-wavy, and wavy inlet flow regimes, calculate C_1, C_2, and C_3 from Equations (5.18) to (5.20). For annular inlet flow regime, calculate C_1, C_2, and C_3 from Equations (5.21) to (5.23).

15- Calculate $K_{G,13}$ from Equation (5.16).

16- Calculate ΔP_{13} from Equation (5.3) and ΔP_{12} from the same equation with outlet-3 parameters replaced by outlet-2 parameters.

17- For stratified inlet flow regime, calculate Y from Equation (5.25). For stratified-wavy and wavy inlet flow regimes, calculate Y from Equation (5.26). For annular inlet flow regime, calculate Y from Equation (5.27).

18- Calculate β' from Equation (5.24).

19- Substitute the values obtained above into Equation (5.14). Convergence was assumed if the two sides of Equation (5.14) were within 0.01 % of each other. In that case, the value of F_{BL} was assumed to be the correct value. If the deviation between the two sides of Equation (5.14) was higher than 0.01 %, a new value of F_{BL} was chosen and steps 4 to 19 were repeated till convergence.

Figure 5.14 shows the three possible types of F_{BL}-F_{BG} relations that could be obtained depending on the inlet conditions, geometry, and fluid properties. The above calculations procedure was found to work for curve types (a) and (b) in Figure 5.14. For curve type (c), the above procedure was found to produce solutions only within the range $CL < F_{BG} < CH$.

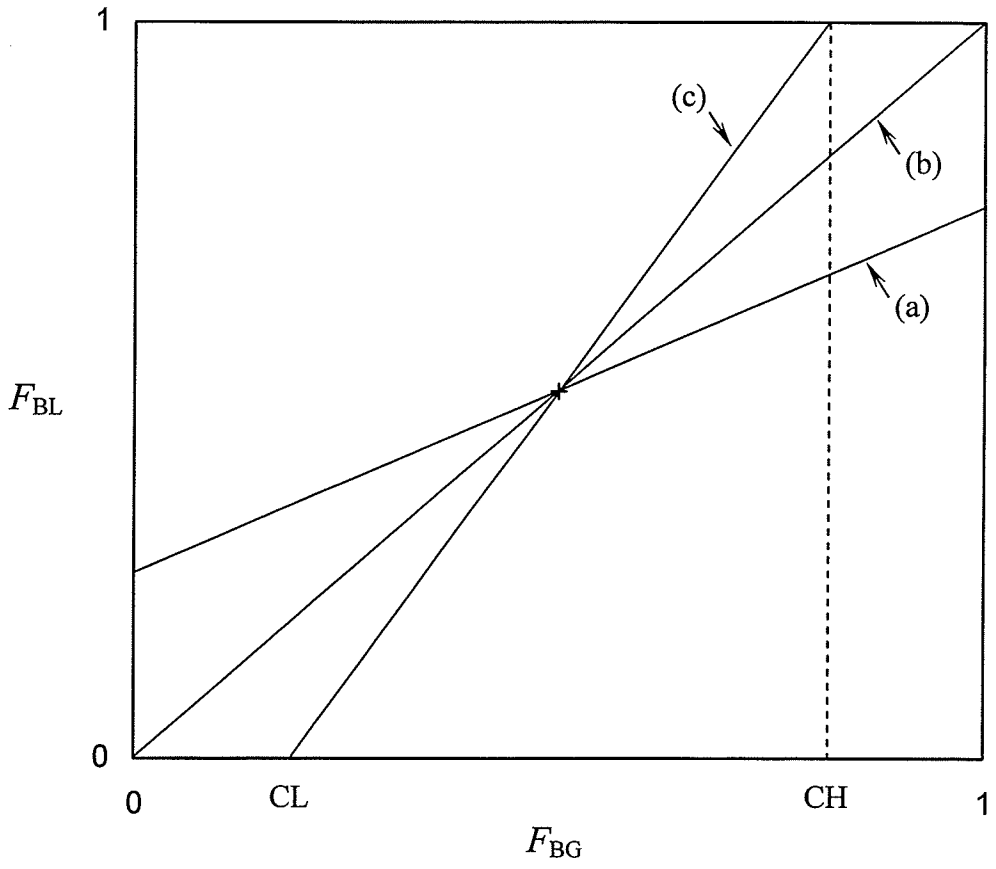

Figure 5.14 Possible types of F_{BL}-F_{BG} relations

5.4 Results and Discussion

5.4.1 Pressure-Drop Predictions

The calculated values of ΔP_{13} and ΔP_{12} obtained from steps 2 and 3 in Section 5.2.3, respectively, were compared against the current experimental values. These calculated values of ΔP_{13} and ΔP_{12} were obtained using the measured phase-distribution data. The comparisons are shown in Figures 5.15 and 5.16 for wavy and annular flows,

respectively. The figures show that most of the predicted values of ΔP are within ±20 % of the corresponding measured values.

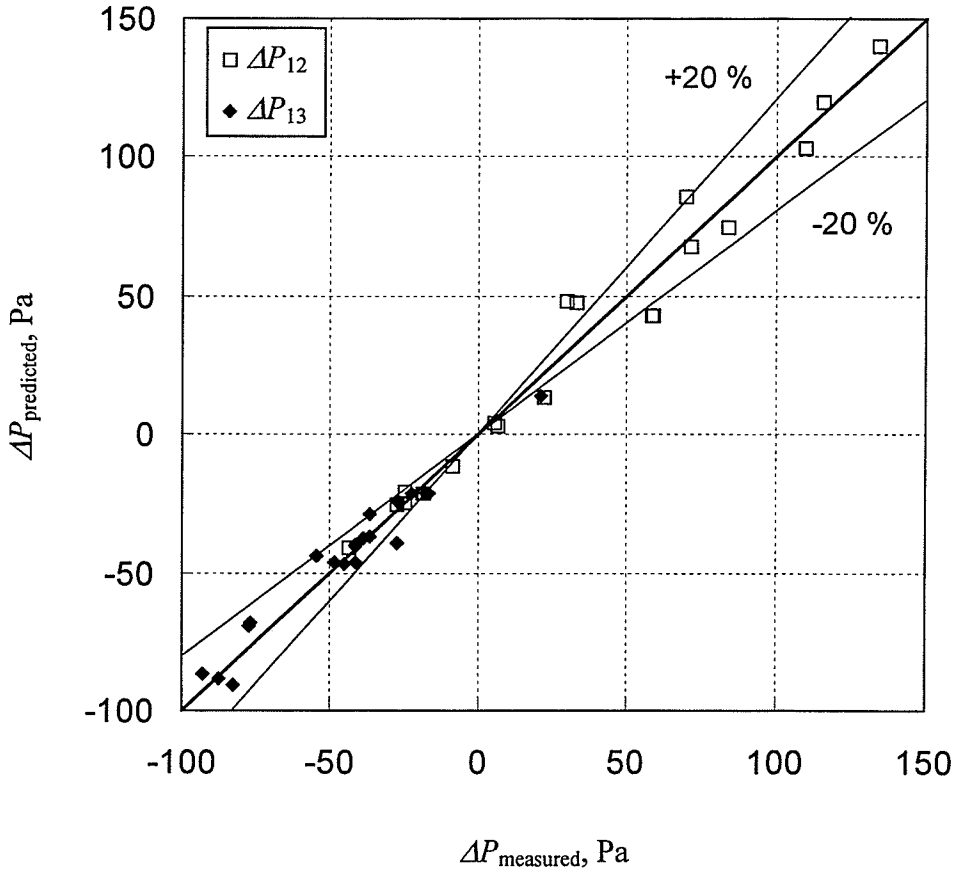

Figure 5.15 Comparison of measured and predicted values of ΔP for stratified-wavy and wavy flows

5.4.2 Phase-Distribution and Pressure-Drop Predictions

Stratified Flow

Figure 5.17 shows the current phase-distribution predictions against the current measured phase-distribution data for stratified flow. The figure shows that there is good

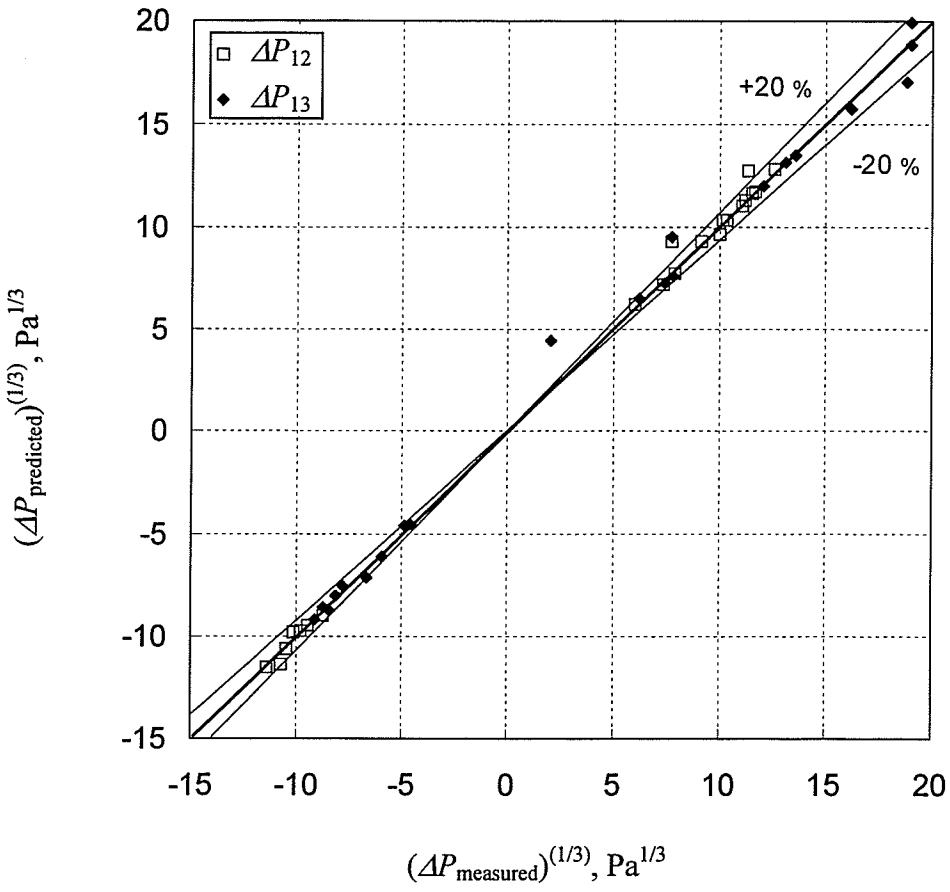

Figure 5.16 Comparison of measured and predicted values of ΔP for annular flow

agreement between the predictions and the data in terms of magnitude and trend. The trend in the data is such that as J_{G1} decreases and/or J_{L1} increases, the data line (or curve) moves around the point (0.5,0.5) in a clockwise direction. Figure 5.18 shows the current pressure-drop predictions for stratified flow. These pressure-drop predictions were obtained using the phase-distribution predictions and not the measured phase-distribution data. In the figure, the predictions are plotted against F_{BG}. The pressure-drop predictions can be obtained in terms of W_3/W_1 using Figure 5.17 and Equation (5.30). In the current study, the pressure-drop data (values of ΔP_{12} and ΔP_{13}) were not

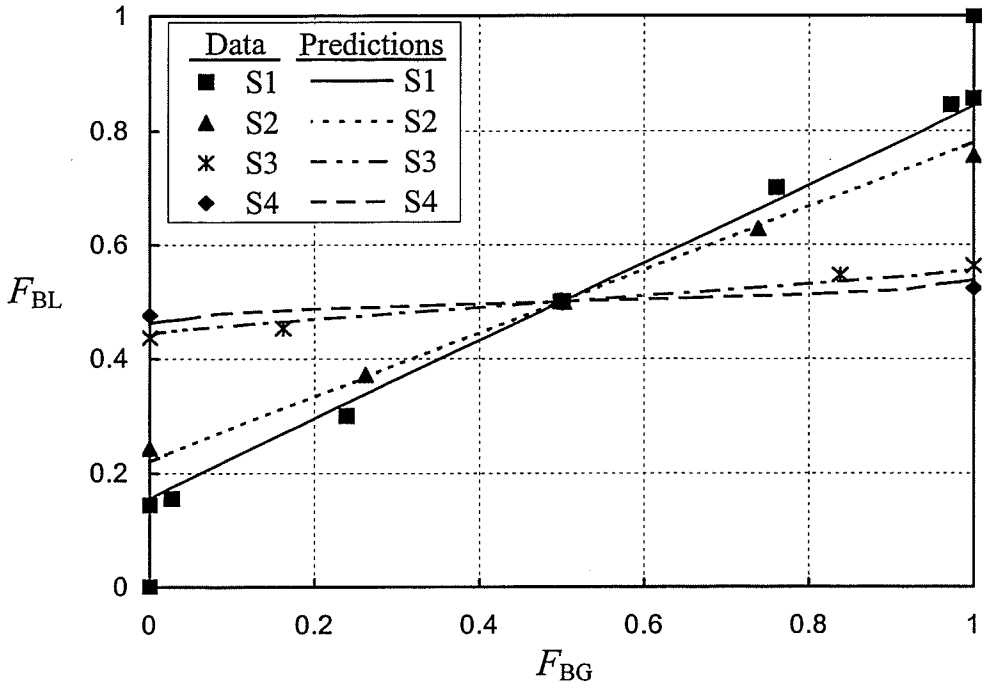

Figure 5.17 Phase-distribution predictions of the current model against the current data for stratified flow

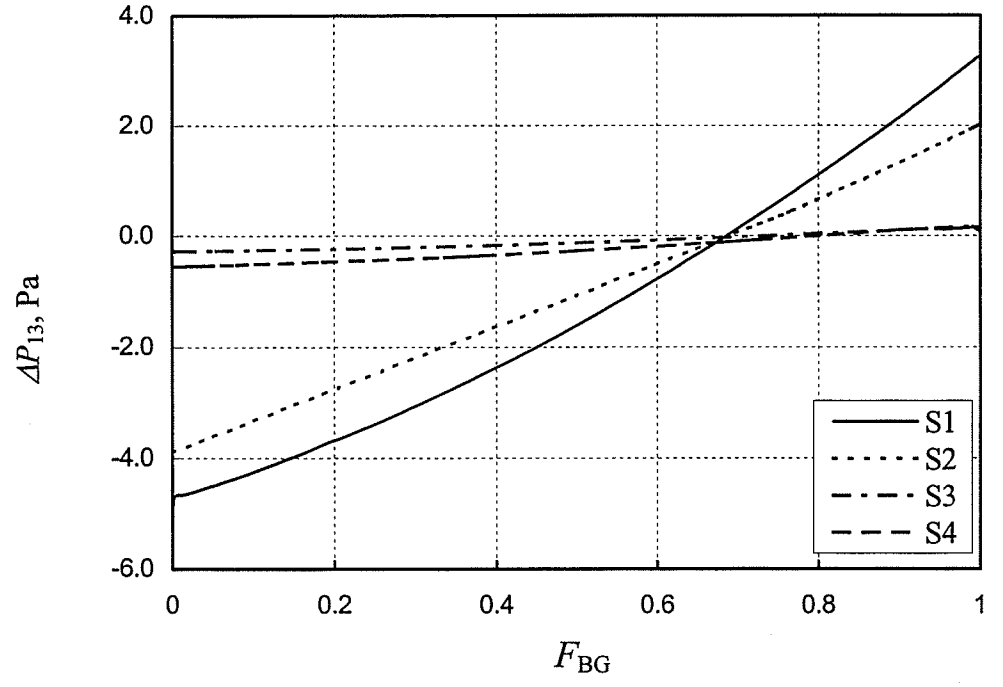

Figure 5.18 Pressure-drop predictions of the current model for stratified flow

obtained for stratified flow for reasons mentioned in Section 4.4.2. Figure 5.18 shows that for each data set, values of ΔP_{13} increase with increasing F_{BG}. Also, at a fixed F_{BG}, the magnitude of ΔP_{13} increases with the increase in the inlet quality x_1. The figure also shows that the magnitudes of the pressure-drop predictions are very small, which is expected for stratified flow.

Stratified-Wavy and Wavy Flows

Figure 5.19 shows the current phase-distribution predictions against the current measured phase-distribution data for stratified-wavy and wavy flows. The figure shows that in terms of magnitude, there is a good agreement between the predictions and the data for data sets SW and W1 over the whole range of W_3/W_1. For data set W2, there is a reasonable agreement between the data and the predictions in the range $0.2 < W_3/W_1 <$

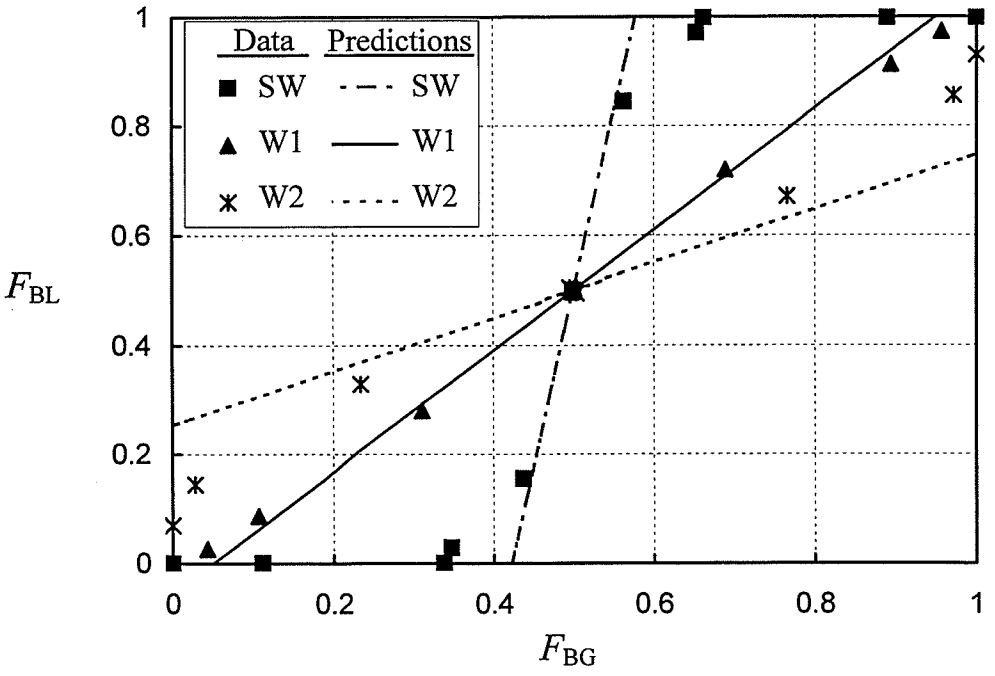

Figure 5.19 Phase-distribution predictions of the current model against the current data for stratified-wavy and wavy flows

0.8. Figure 5.19 also shows that the predictions follow the same trend as the data.

Figure 5.20 shows the current pressure-drop predictions against the current measured pressure-drop data for stratified-wavy and wavy flows. Again, the pressure-drop predictions shown in Figure 5.20 were obtained using the phase-distribution predictions. Also, Figure 5.20 was obtained such that the predicted pressure-drop values (ΔP_{12} and ΔP_{13}) and their measured counterparts have the same F_{BG}, but not necessarily the same F_{BL} due to the deviation between the measured and predicted phase-distribution. The figure shows good agreement between the predictions and the data

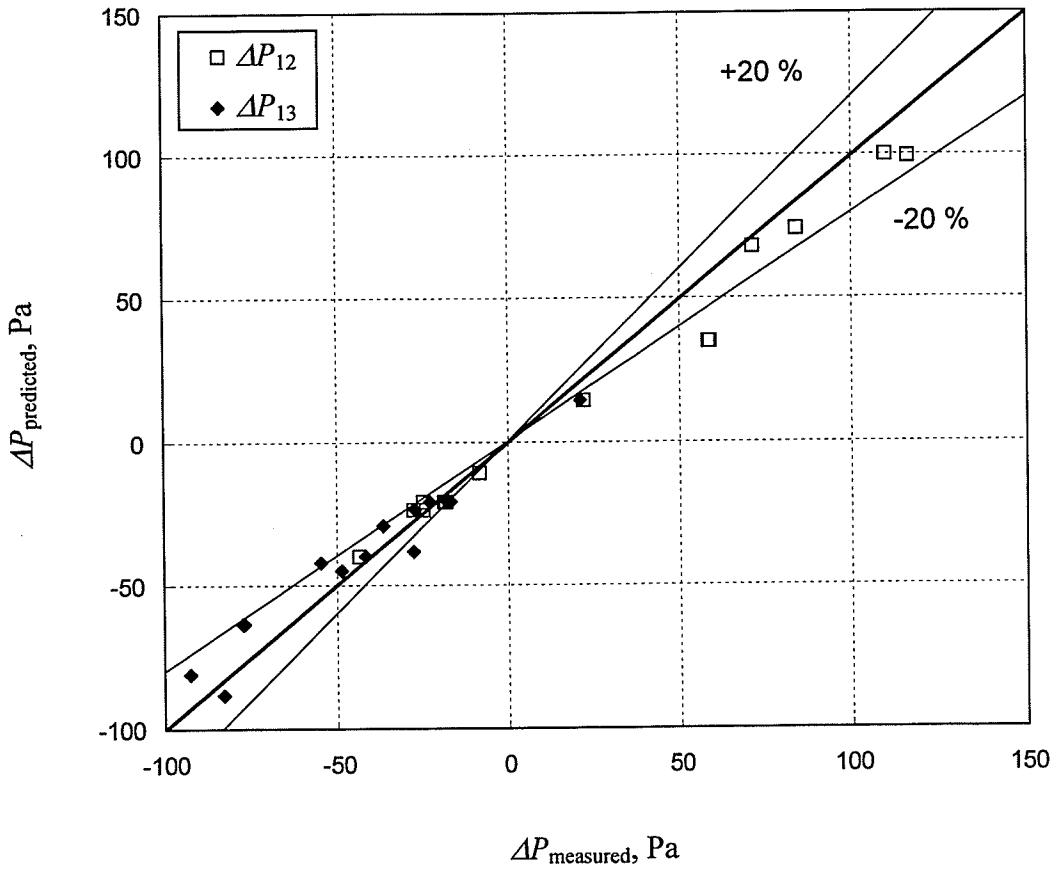

Figure 5.20 Pressure-drop predictions of the current model against the current data for stratified-wavy and wavy flows

with 73 % of the data predicted within ±20 % while 83 % of the data were predicted within ±30 %.

The predictions of the current model were compared against the data of other researchers for wavy flow. Figure 5.21 shows the current phase-distribution predictions against the phase-distribution data of Hong and Griston (1995) for wavy flow. Values of J_{G1} and J_{L1} for the wavy-flow data sets of Hong and Griston (1995) are: (4.57, 0.046), (9.14, 0.092), and (4.57, 0.093) m/s. For easier future reference, the three data sets of Hong and Griston will be referred to as HG1, HG2, and HG6, respectively. The numbering of the data sets is such that it is consistent with the numbering in El-Shaboury (2000). It should be mentioned that, while all three data sets fall in the wavy

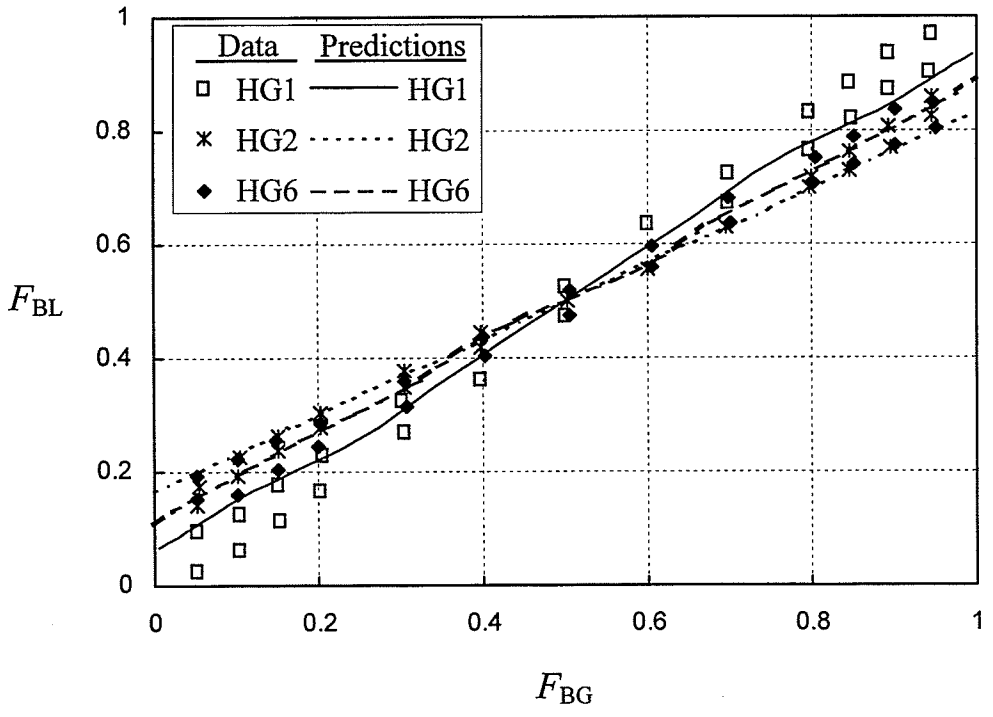

Figure 5.21 Phase-distribution predictions of the current model against the data of Hong and Griston (1995) for wavy flow

region of the flow-regime map of Mandhane et al. (1974), data sets HG2 and HG6 are very close to the wavy-slug boundary. Figure 5.21 shows that in terms of magnitude, there is a good agreement between the predictions and the data for all the data sets. In Figure 5.21, there is a change in the slopes of the prediction lines, which can be seen clearly for data set HG1. This might be attributed to the reason that the flow regime in one (or both) of the outlets was near a transition line. Treating the transition lines on the flow regime map as sharp lines, the regimes in both outlets changed abruptly rather than gradually as physically happens. These abrupt flow-regime changes caused the changes in slope in the prediction lines in Figure 5.21.

Figures 5.22 and 5.23 show the current phase-distribution predictions against the phase-distribution data of Ottens et al. (1995). The data of Ottens et al. (1995) have a fixed value of J_{G1} = 15.8 m/s, while values of J_{L1} were 0.00063, 0.00302, 0.012, and 0.03 m/s. For easier future reference, the four data sets of Ottens et al. will be referred to as O1, O2, O3, and O4, respectively. Figure 5.22 shows the current predictions against data sets O1 and O3 while Figure 5.23 shows the current predictions against data sets O2 and O4. It should be mentioned that Ottens et al. reported a stratified-wavy flow regime based on visual observation. In terms of magnitude, Figures 5.22 and 5.23 show reasonable agreement between the predictions and the data for all the data sets. The trends seen in the predictions are consistent with the expected effect of varying J_{L1}.

Annular Flow

Figure 5.24 shows the current phase-distribution predictions against the current measured phase-distribution data for annular flow. The figure shows that there is good agreement between the predictions and the data in terms of magnitude and trend. In

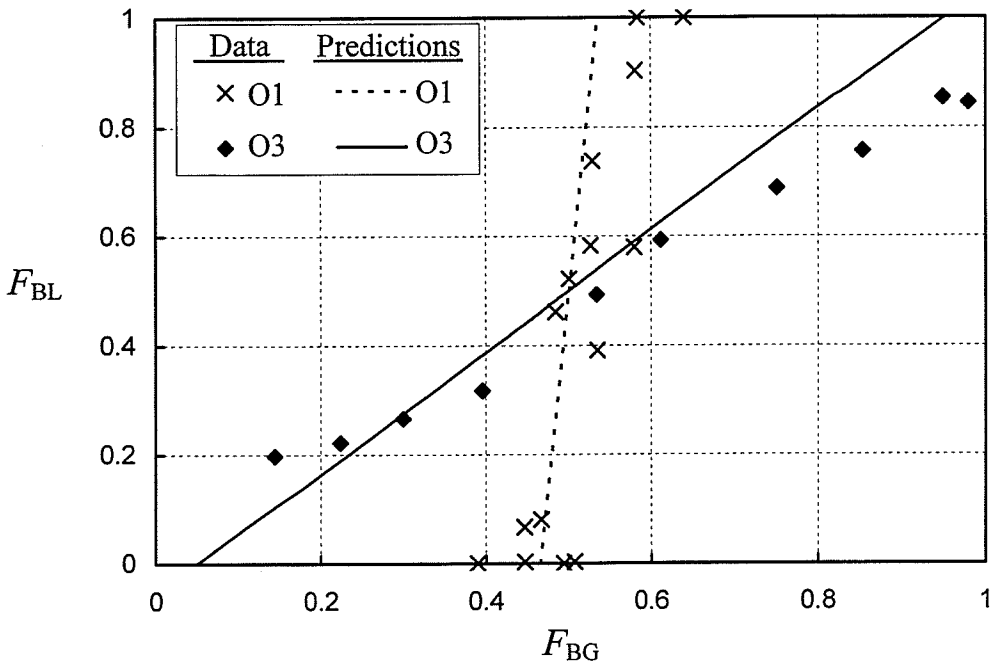

Figure 5.22 Phase-distribution predictions of the current model against data sets O1 and O3 of Ottens et al. (1995)

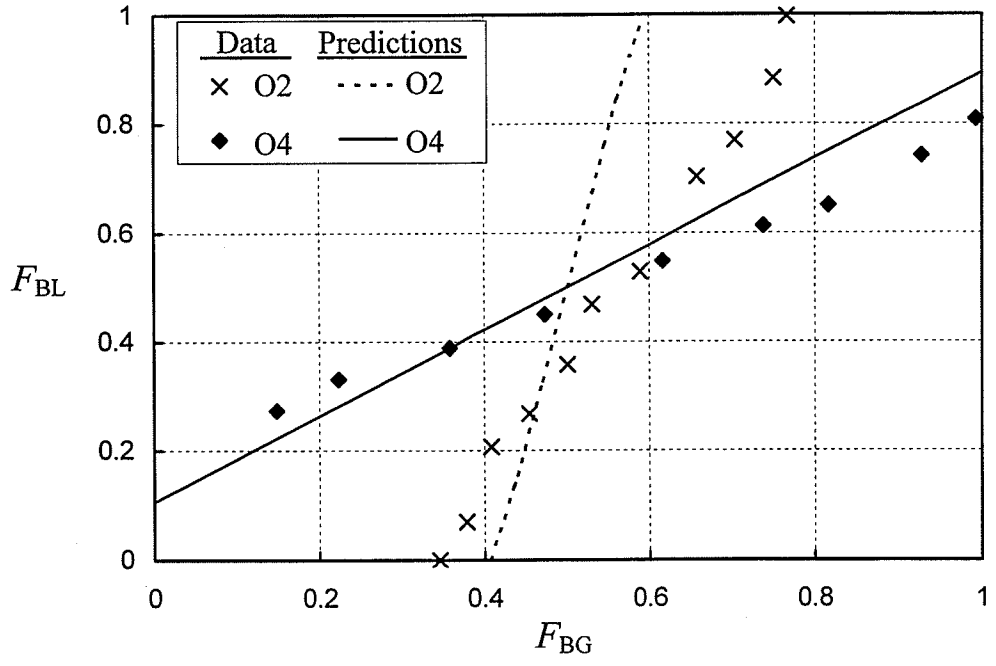

Figure 5.23 Phase-distribution predictions of the current model against data sets O2 and O4 of Ottens et al. (1995)

Figure 5.24, the predictions for data set A1 experience a slight change in the slope at approximately F_{BG} = 0.4 and 0.6. This is attributed to the reason that the flow regime in one (or both) of the outlets experienced a sharp change, as mentioned in the discussion on Figure 5.21. Figure 5.25 shows the current pressure-drop predictions against the current measured pressure-drop data for annular flow using the phase distribution predicted by the model. Also, Figure 5.25 was obtained such that the predicted pressure-drop values (ΔP_{12} and ΔP_{13}) and their measured counterparts have the same F_{BG}, but not necessarily the same F_{BL} due to the deviation between the measured and predicted phase-distribution. The figure shows good agreement between the predictions and the data with 79 % of the data predicted within ±20 % while 85 % of the data were predicted within ±30 %.

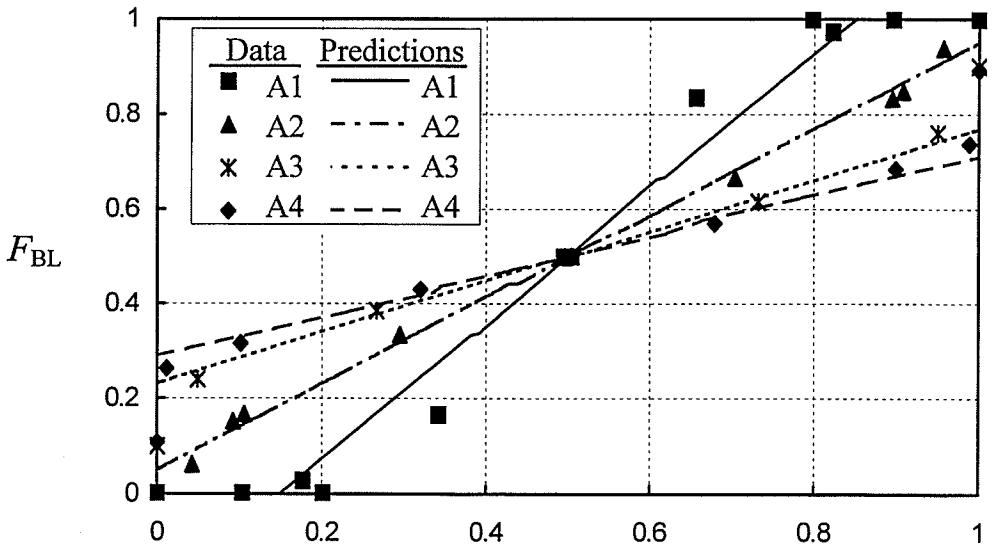

Figure 5.24 Phase-distribution predictions of the current model against the current data for annular flow

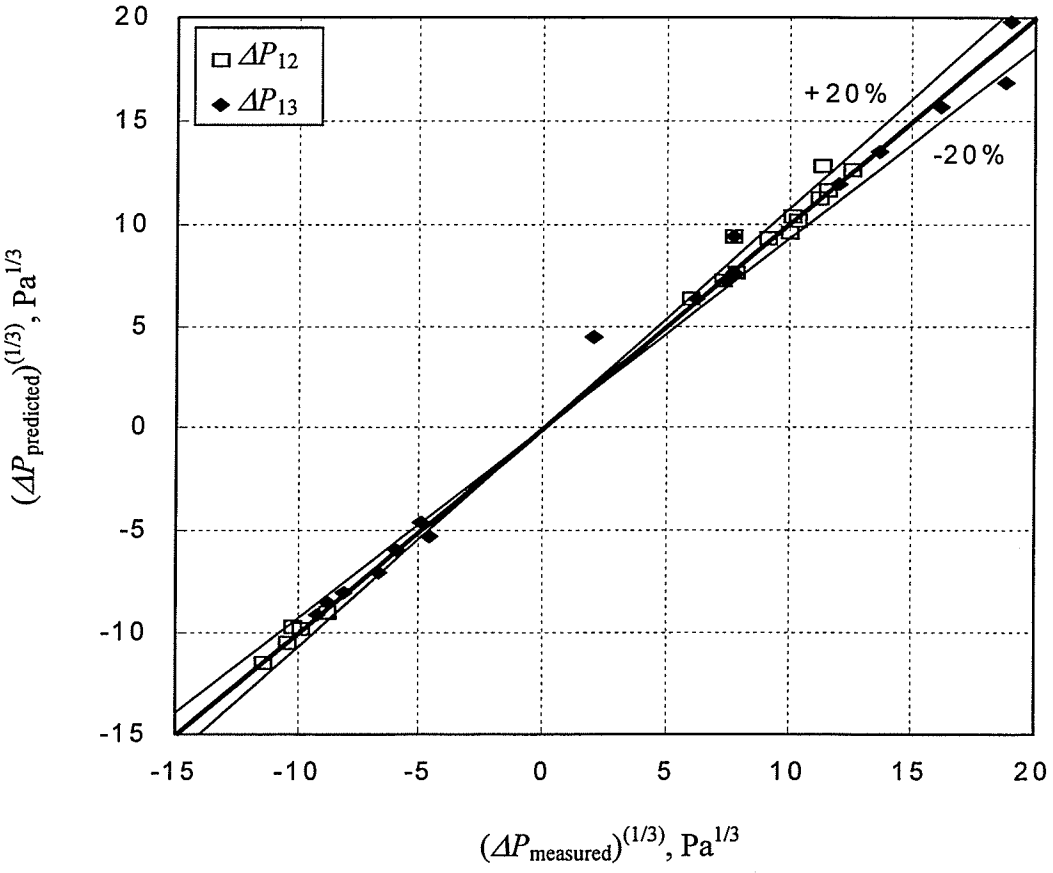

Figure 5.25 Pressure-drop predictions of the current model against the current data for annular flow

The predictions of the current model were compared against the data of other researchers for annular flow. Figures 5.26 and 5.27 show the current phase-distribution predictions against the phase-distribution data of Hong and Griston (1995) for annular flow. Values of J_{G1} and J_{L1} for the annular-flow data sets of Hong and Griston (1995) are: (13.7, 0.139), (18.3, 0.185), (22.9, 0.231), (18.3, 0.373), and (22.9, 0.467) m/s. For easier future reference, the five data sets of Hong and Griston will be referred to as HG3, HG4, HG5, HG9, and HG10, respectively. The numbering of the data sets is such that it is consistent with the numbering in El-Shaboury (2000). While all data sets fall in

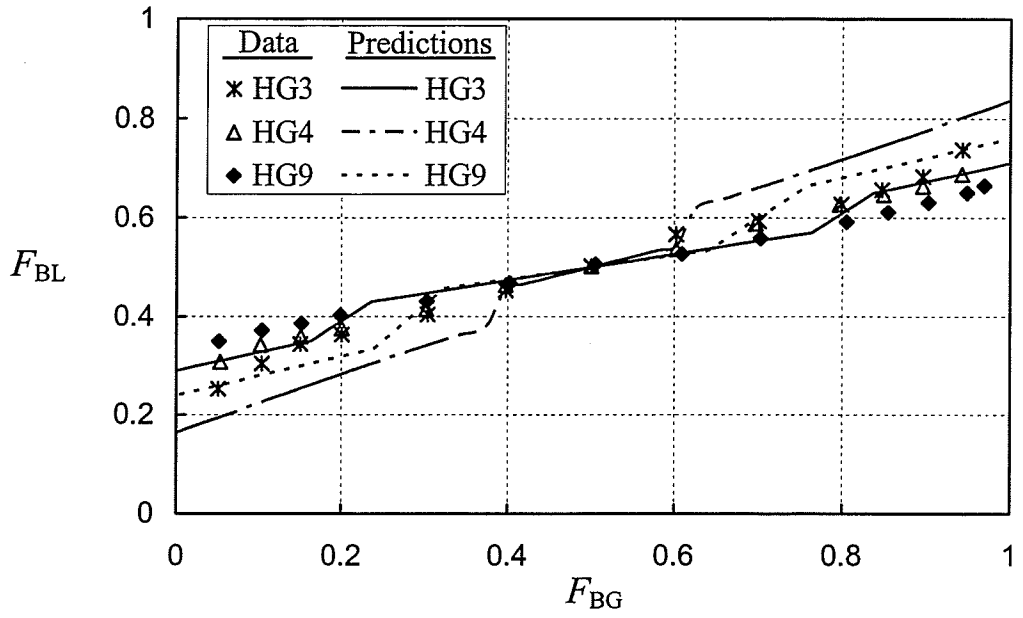

Figure 5.26 Phase-distribution predictions of the current model against data sets HG3, HG4, and HG9 of Hong and Griston (1995)

the annular region of the flow-regime map of Mandhane et al. (1974), data sets HG9 and HG10 are very close to the annular-slug boundary. Figure 5.26 shows the current predictions against data sets HG3, HG4, and HG9 while Figure 5.27 shows the current predictions against data sets HG5 and HG10. In the figures, reasonable agreement exists between the data and the predictions for all the data sets. The changes in the slopes of the prediction lines shown in Figures 5.26 and 5.27 are attributed to two reasons. First, the flow regime in one (or both) of the outlets was predicted to change abruptly, as mentioned in the discussion on Figure 5.21. The other reason is that, for some cases the flow regime in one (or both) of the outlets was predicted as slug or plug. In the current model, for void fraction calculations, slug and plug flow regimes were assumed to be wavy and stratified flow regimes, respectively. These assumptions might have affected the accuracy of the void-fraction values and consequently caused the sudden changes in

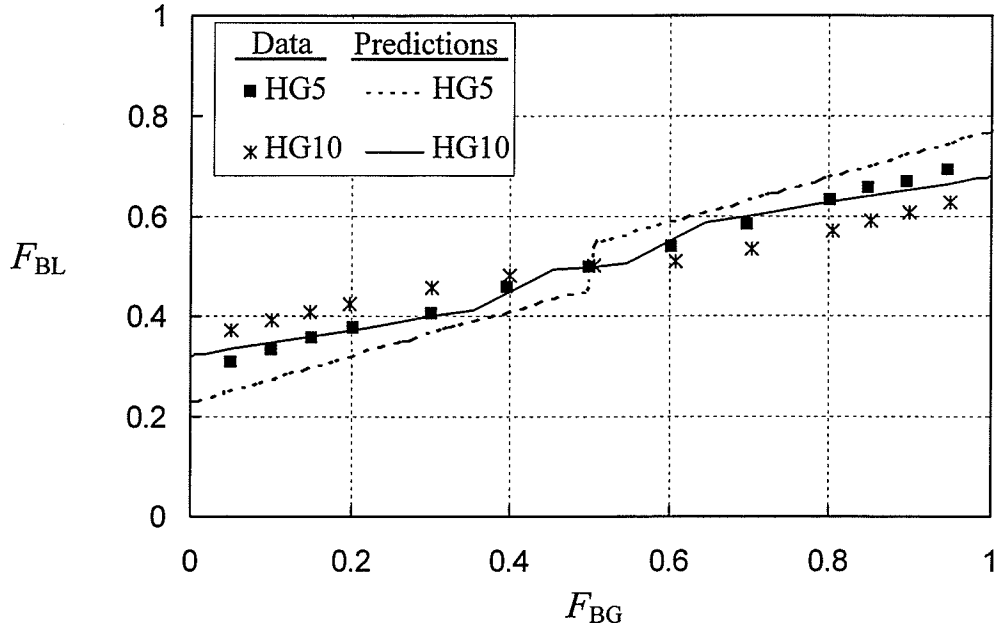

Figure 5.27 Phase-distribution predictions of the current model against data sets HG5 and HG10 of Hong and Griston (1995)

the slopes seen in Figures 5.26 and 5.27. In Figures 5.26 and 5.27, the trends in the predictions are consistent with the expected effects of varying J_{G1} and J_{L1}.

Figures 5.28, 5.29, and 5.30 show the current phase-distribution predictions against phase-distribution data from Azzopardi et al. (1986a) for annular flow in an impacting tee with a vertical inlet. The data sets of Azzopardi et al. (1986a) have two values for J_{L1}: 0.0317 and 0.079 m/s. For the first value of J_{L1}, values of J_{G1} were 10.39, 17.55, and 21.92. The corresponding data sets will be referred to as AZ1, AZ2, and AZ3, respectively. For the second value of J_{L1}, values of J_{G1} were 9.94, 13.18, 15.96, and 21.92. The corresponding data sets will be referred to as AZ4, AZ5, AZ6, and AZ7, respectively. Figures 5.28, 5.29, and 5.30 show that, in general, there is reasonable agreement between the predictions and the data in terms of magnitude for all the data sets shown, excepting data set AZ1 where the predictions deviate considerably from the

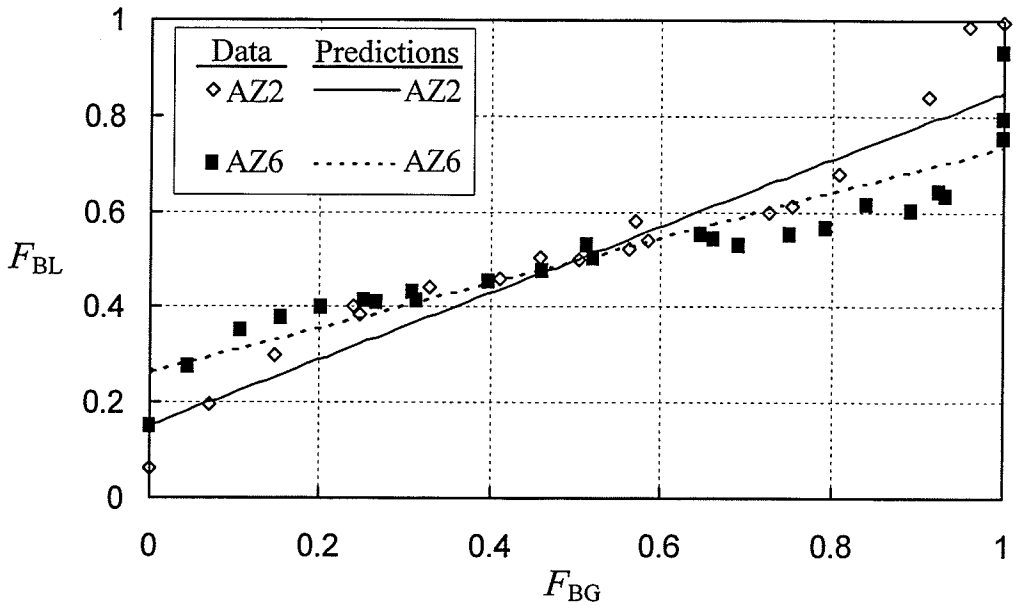

Figure 5.28 Phase-distribution predictions of the current model against data sets AZ2 and AZ6 of Azzopardi et al. (1986a)

data. The predictions for data set AZ5 (not shown because of overlap with other data) were also found to be in reasonable agreement with the data. In Figure 5.28, data sets AZ2 and AZ6 have different values of J_{L1}; while they have very close values of J_{G1}. The figure shows that the data, as well as the predictions, follow the expected trend for varying J_{L1}. The same observation can be made on Figure 5.29 where data sets AZ3 and AZ7 have the same J_{G1} but different values of J_{L1} and both the data and predictions follow the expected trend. In Figure 5.30, data sets AZ1 and AZ4 have very close values of J_{G1} but different values of J_{L1}. The figure shows that the data follow the expected trend for varying J_{L1}, while the model does not. As well, data sets AZ4 and AZ7 have the same J_{L1} but different values of J_{G1}. Neither the model, nor the data appear to follow the expected trend for J_{G1}-variation. It must be commented though that the magnitudes of the shift due to variation in J_{G1} and J_{L1} in both data and predictions are small. Based on the results in Figures 5.28 to 5.30, it is fair to conclude that the

present model succeeded in producing satisfactory predictions of the data of Azzopardi et al. (1986a).

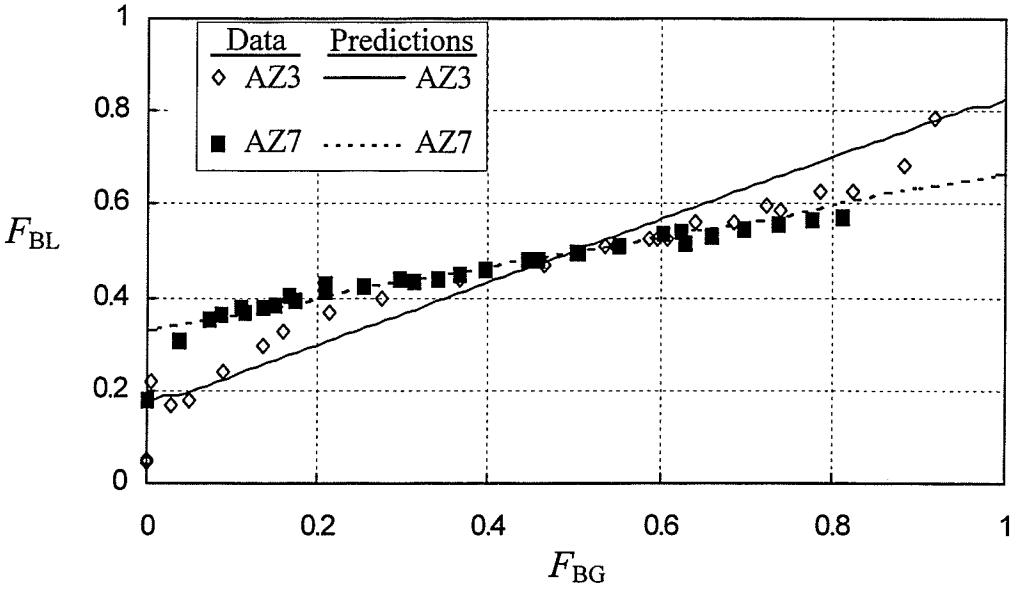

Figure 5.29 Phase-distribution predictions of the current model against data sets AZ3 and AZ7 of Azzopardi et al. (1986a)

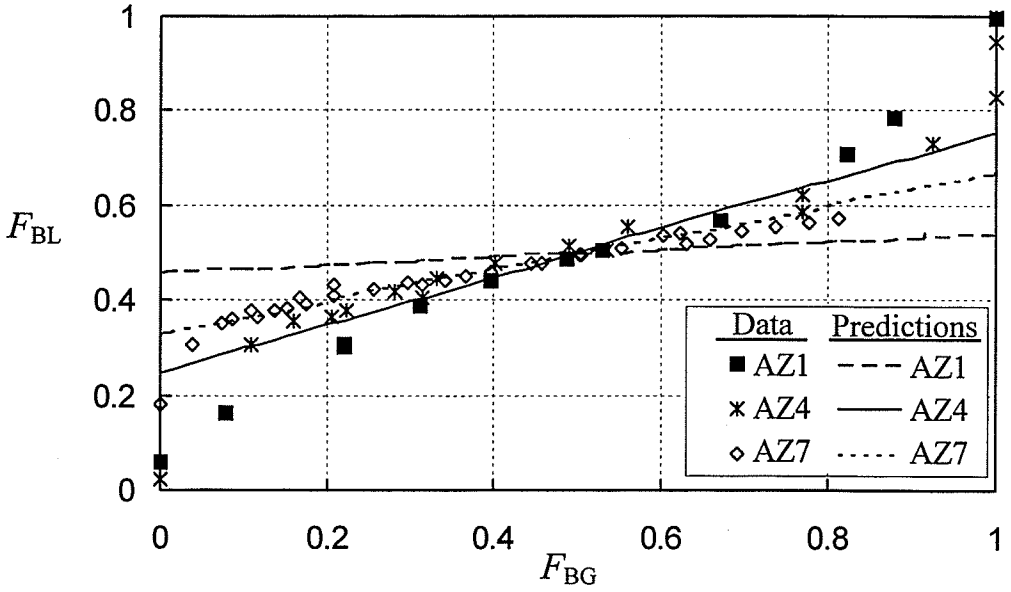

Figure 5.30 Phase-distribution predictions of the current model against data sets AZ1, AZ4, and AZ7 of Azzopardi et al. (1986a)

Chapter 6

CONCLUSIONS AND RECOMMMENDATIONS

6.1 Conclusions

In the current study, phase-distribution and pressure-drop data were obtained for air-water flows in a horizontal impacting tee junction with equal-diameter sides and a system pressure of 1.5 bar. The inlet and operating conditions for the current study are given in Figure 4.2 and Table 4.3, respectively. The current phase-distribution data were compared against data of other researchers and also against the models of Hwang (1986) and Ottens et al. (1995). Based on the current results and the aforementioned comparisons, the following conclusions can be drawn:

1- Even phase split is obtained only at the point (0.5,0.5) on an F_{BL} - F_{BG} graph.

2- At a fixed J_{L1}, and within the same flow regime, as J_{G1} increases, the data line (or curve) moves around the point (0.5,0.5) on an F_{BL} - F_{BG} graph in an anti-clockwise direction. This effect is the exact opposite of the effect of increasing J_{L1} at a fixed J_{G1}. These effects of varying J_{G1} and J_{L1} were found to be consistent in the current data and the data of other researchers for horizontal impacting junctions. Also, these effects of J_{L1} and J_{G1} on the phase distribution were found to be valid within each inlet flow regime. The effect of varying the inlet quality x_1 on the phase-distribution data can be easily deduced using the aforementioned effects of varying J_{G1} and J_{L1}.

3- Based on observations on the current phase-distribution data, the effects of varying J_{G1}, J_{L1}, and x_1 mentioned above were found to be continuous within the stratified and wavy flow regimes. However, these effects were found to be not continuous at the boundary between wavy and annular flow regimes.

4- In general, the absolute value of ΔP_{13} increases with the increase in the split ratio W_3/W_1 and also with the increase in the inlet mass flow rate W_1.

5- For annular flows, the absolute values of ΔP_{13} are much greater than those for wavy and stratified flows (Even though for stratified flow, values of ΔP_{13} were not reported in the current study, it is thought that the part of the aforementioned conclusion regarding stratified flows, is true). For data set A4, the highest inlet mass flow rate in the current study, for high values of W_3/W_1, the flow in outlet 3 needs a considerable amount of length before it becomes fully developed.

6- For stratified flow, a change in the level of the gas-liquid interface occurs in the inlet pipe. This change in the level of the interface might also occur in the outlets of the junction. Those changes in the levels of the interfaces have significant effects on the magnitude and trend of the pressure-distribution data for stratified flow. These changes in the interface levels are found to be insignificant for wavy and annular flows.

7- In general, the phase-distribution model developed by Ottens et al. (1995) produces better predictions than the model of Hwang (1986), particularly in the wavy and annular regions. Neither model was found to be capable of predicting the stratified-flow data. To the best of the author's knowledge,

there are no models or correlations available yet for predicting the two-phase pressure drop in impacting tees.

8- The proposed model in the current study is capable of predicting phase-distribution and pressure-drop for two-phase flows in horizontal equal-diameter impacting tee junctions. The model has been tested for air-water systems at pressures ranging from 1.0 to 1.7 bar, with junction diameters ranging from 19 to 37.8 mm, and for the three inlet flow regimes of stratified, wavy, and annular. In general, comparisons between the model predictions and the current phase-distribution data as well as the data of other researchers showed good agreements in terms of magnitude and trend.

9- Using the predicted phase-distribution data, the proposed model predicted pressure-drop values (ΔP_{13} and ΔP_{12}) for 79 % of the data of annular flow within ±20 %. Also, 73 % of the data of stratified-wavy and wavy flows were predicted within ±20 %.

6.2 Recommendations For Future Work

The current study generated phase-distribution and pressure-drop data for air-water flow in an equal-diameter horizontal impacting tee junction. The operating conditions were near atmospheric temperature and pressure and the inlet conditions were such that stratified, wavy, and annular flow regimes were observed in the inlet. More experimental investigations are required at untested operating and inlet conditions. Future investigations should generate both phase-distribution and pressure-drop data as there is a severe lack of pressure-drop data in the literature. Also, other junction geometries (e.g., vertical inlet and/or

unequal-diameter junctions) should be tested with other fluids. The following recommendations for future work can be made:

1- More phase-distribution and in particular pressure-drop data should be generated under wide ranges of inlet and operating conditions. This should aid in the development of more accurate empirical correlations to model the mechanical-energy loss coefficient $K_{G,13}$ and the parameter β'.

2- The effect of the inlet orientation, the outlets/inlet diameter ratio, and the orientation of the outlets should be investigated. Studying the effect of the orientation of the outlets on the phase-distribution data would be helpful in determining the possibility of using the junction as a phase separator.

3- The effect of the system pressure on phase-distribution and pressure-drop data should be investigated.

4- More data should be generated for different types of fluids (e.g., steam and water).

5- More void-faction measurements should be taken particularly in the flow regimes transitional regions. This should help in developing models to calculate void-fraction values at these transitional regions.

6- The pressure-drop data for stratified flow should be taken with the pressure taps located at the top of the pipes. This would eliminate the effect of the interface level change on the data. If additional pressure-drop data can be taken with the taps located at the bottom of the pipes, then the effect of the interface level change can be isolated and identified.

7- Accurate methods for measuring the gas-liquid interface height would be a great help in understanding the mechanism of the interface level change in the inlet for stratified flow.

8- Detailed measurement of the velocity of the phases would be a great help in analyzing the experimental results and determining the size and location of the re-circulation zones that occur in the vicinity of the junction.

9- Different types of geometries should be tested (e.g., impacting wyes with different angles). The effect of the junction geometry on the size and location of the re-circulation zones should be investigated. This would be of great interest in some biomedical applications.

10- Data should be generated for industrial- and biomedical-size junctions to determine if any scale effects exist.

11- Data should be generated for a series of junctions set up in series to see whether a required even-phase split and/or separation of phases may be obtained.

REFERENCES

Asano, H., Fujii, T., Takenaka, N., Sakoda, K. and Arakawa, T., "Phase Separation Characteristics of Gas-Liquid Two-Phase Flow in a T-Junction (Experiments for a One-Component Two-Phase Flow)", Proceeding of the 16th Multiphase Flow Symposium, Lake Toya, Japan, pp. 103-104, 1997.

Azzopardi, B.J., Purvis, A. and Govan, A.H., "Two-Phase Flow Split at an Impacting T", UKAEA Report, AERE-R-12179, 1986a.

Azzopardi, B.J., Purvis, A. and Govan, A.H., "Flow Split of Churn Flow at a Vertical Impacting T", UKAEA Report, AERE-R-12440, 1986b.

Azzopardi, B.J. and Hervieu, E., "Phase Separation at Junctions", Multiphase Science and Technology, Vol. 8, pp. 645-714, 1994.

Azzopardi, B.J., "Phase Separation at T Junctions", Multiphase Science and Technology, Vol. 11, pp. 223-329, 1999.

Barnea, D., Luninski, Y. and Taitel, Y., "Flow Pattern in Horizontal and Vertical Two-Phase Flow in Small Diameter Pipes", Canadian Journal of Chemical Engineering, Vol. 61, pp. 617-620, 1983.

Buell, J.R., "Two-Phase Pressure Drop and Phase Distribution In a Horizontal Tee Junction", M.Sc. Thesis, University of Manitoba, 1992.

Chien, S.-F. and Rubel, M.T., "Phase Splitting of Wet Steam in Annular Flow Through a Horizontal Impacting Tee", SPE Production Engineering, Vol. 7, pp. 368-374, 1992.

Chisholm, D., "A Theoretical Basis for the Lockhart-Martinelli Correlation for Two-Phase Flow", International Journal of Heat and Mass Transfer, Vol. 10, pp. 1767-1778, 1967.

Dukler, A.E., Wicks, M. and Cleveland, R.G., "Frictional Pressure Drop in Two-Phase Flow: A. A Comparison of Existing Correlations for Pressure Loss and Holdup", AIChE Journal, Vol. 10, pp. 38-43, 1964.

El-Shaboury, A.M.F., "Two Phase Flow in Horizontal Impacting Tee Junctions: Current State of the Art", M.Sc. Thesis, University of Manitoba, 2000.

El-Shaboury, A.M.F., Soliman, H.M. and Sims, G.E., "Current State of Knowledge on Two-Phase Flow in Horizontal Impacting Tee Junctions", Multiphase Science and Technology, Vol. 13, pp. 139-178, 2001.

El-Shaboury, A.M.F., Soliman, H.M. and Ormiston, S.J., "Laminar Forced Convection in Two-Dimensional Equal-Sided and Reduced Branching Ducts", Numerical Heat Transfer, Part A, Vol. 42, pp. 487-512, 2002.

El-Shaboury, A.M.F., Soliman, H.M. and Ormiston, S.J., "Laminar Forced Convection in Two-Dimensional Impacting Tee Junctions", Heat and Mass Transfer, Vol. 39, pp. 815-824, 2003.

Fujii, T., Asano, H., Takenaka, N. and Sakoda, K., "Phase Separation Characteristics of Gas-Liquid Two-Phase Flow in T-Junction (Effects of the Geometry of Junctions)", Proceeding of the 15th Multiphase Flow Symposium, Fukui, Japan, pp. 61-64, 1996.

Fujii, T., Takenaka, N., Nakazawa, T. and Asano, H., "The Phase Separation Characteristics of a Gas-Liquid Two-Phase Flow in the Impacting T-Junction",

Proceeding of the 2nd International Conference on Multiphase Flow, Kyoto, Japan, pp. 6.27-6.32, 1995.

Grolman, E. and Fortuin, J.M.H., "Liquid Hold-up, Pressure Gradient, and Flow Patterns in Inclined Gas-Liquid Pipe Flow", Experimental Thermal and Fluid Science, Vol. 15, pp. 174-182, 1997.

Hart, J., Hamersma, P.J. and Fortuin, J. M. H., "A Model For Predicting Liquid Route Preference During Gas-Liquid Flow Through Horizontal Branched Pipelines", Chemical Engineering Science, Vol. 46, pp. 1609-1622, 1991.

Hatziavramidis, D., Sun, B. and Gidaspow, D., "Gas-Liquid Flow through Horizontal Tees of Branching and Impacting Type", AIChE Journal, Vol. 43, pp. 1675-1683, 1997.

Hong, K.C., "Two-Phase Flow Splitting at a Pipe Tee", Journal of Petroleum Technology, Vol. 2, pp. 290-296, 1978.

Hong, K.C. and Griston, S., "Two-Phase Flow Splitting at an Impacting Tee", SPE Production and Facilities, Vol. 10, pp. 184-190, 1995.

Hwang, S.T., "A Study on Phase Separation Phenomena in Branching Conduits", Ph.D. Thesis, Rensselaer Polytechnic Institute, 1986.

Hwang, S.T., Soliman, H.M. and Lahey, R.T., "Phase Separation in Impacting Wyes and Tees", International Journal of Multiphase Flow, Vol. 15, pp. 965-975, 1989.

Incropera, F.P. and DeWitt, D.P., "Fundamentals of Heat and Mass Transfer", 5th edition, John Wiley & Sons, New York, page 470, 2002.

Ito, H. and Imai, K., "Energy Losses at 90° Pipe Junctions", Journal of the Hydraulics Division, ASCE, Vol. 99, Paper No. HY9, pp. 1353-1368, 1973.

Kline, S.J. and McClintock, F.A., "Describing the Uncertainties in Single-Sample Experiments", Mechanical Engineering, Vol. 75, pp. 3-8, 1953.

Kreid, D.K., Chung, C.-J. and Crowe, C.T., "Measurement of the Flow of Water in a T Junction by the LDV Technique", Journal of Applied Mechanics, Vol. 42, pp. 498-499, 1975.

Lahey, R.T., "Current Understanding of Phase Separation Mechanisms in Branching Conduits", Nuclear Engineering and Design, Vol. 55, pp. 145-161, 1986.

Liepsch, D., Moravec, S., Rastogi, A.K. and Vlachos, N.S., "Measurements and Calculation of Laminar Flow in a Ninety Degree Bifurcation", Journal of Biomechanics, Vol. 15, pp. 473-485, 1982.

Lightstone, L., Osamusali, S.I. and Chang J.-S., "Gas-Liquid Two-Phase Flow in Symmetrically Dividing Horizontal Tubes", AIChE Journal, Vol. 37, pp. 111-121, 1991.

Lockhart, R.W. and Martinelli, R.C., "Proposed Correlation of Data for Isothermal Two-Phase, Two-Component Flow in Pipes", Chemical Engineering Progress, Vol. 45, pp. 39-48, 1949.

Mandhane, J.M., Gregory, G.A. and Aziz, K., "A Flow Pattern Map For Gas-Liquid Flow in Horizontal Pipes", International Journal of Multiphase Flow, Vol. 1, pp. 537-553, 1974.

Mandhane, J.M., Gregory, G.A. and Aziz, K., "Critical Evaluation of Friction Pressure Drop Prediction Methods for Gas-Liquid Flow in Horizontal Pipes", Journal of Petroleum Technology, Vol. 29, pp. 1348-1358, 1977.

Moffat, R.J., "Describing the Uncertainties in Experimental Results", Experimental Thermal and Fluid Science, Vol. 1, pp. 3-17, 1988.

Ottens, M., De Swart, A., Hoefsloot, H.C.J. and Hamersma, P.J., "Gas-Liquid Flow Splitting in Regular, Reduced and Impacting Tee Junctions", Impiantistica Italiana, Vol. 8, pp. 23-33, 1995.

Patankar, S.V., "Numerical Heat Transfer and Fluid Flow", Hemisphere, New York, 1980.

Rouhani, S.Z., "Modified Correlations for Void and Two-Phase Pressure Drop", Zentralstelle für Atomkernenergie, AE-RTV-841, 1974.

Shoham, O., Brill, J.P. and Taitel, Y., "Two-Phase Flow Splitting in a Tee Junction-Experiment and Modeling", Chemical Engineering Science, Vol. 42, pp. 2667-2676, 1987.

Van Gorp, C.A., "Two-Phase Pressure Drop and Phase Distribution at a Reduced Horizontal Tee Junction: The Effect of System Pressure", M.Sc. Thesis, University of Manitoba, 1998.

Wang, S. and Shoji, M., "Fluctuations Characteristics of Two-Phase Flow Splitting at a Vertical Impacting T-Junctions", International Journal of Multiphase Flow, Vol. 28, pp. 2007-2016, 2002.

Wang, S.F., Mosdorf, R. and Shoji, M., "Nonlinear Analysis on Fluctuation Feature of Two-Phase Flow through a T-Junction", International Journal of Heat and Mass Transfer, Vol. 46, pp. 1519-1528, 2003.

Appendix A

GEOMETRICAL AND PHYSICAL MODELS FOR DIFFERENT FLOW REGIMES (SHOHAM et al., 1987)

The geometrical and physical models proposed by Shoham et al. (1987) are given in this appendix. These models were used in association with the Hwang (1986) model to calculate the slip ratio (S), F_{BG}, and F_{BL} (See Section 2.3.1). They were also used to calculate the void fraction in Section 5.2.2.

Stratified, Wavy, and Annular Flow Regimes

In order to calculate the void fraction in case of the annular flow regime, the liquid-film thickness (δ) must be known. Also, for the stratified and wavy flow regimes, the liquid level (h) must be known. The following is a physical model, given in Shoham et al. (1987), that applies a momentum balance on the two phases in order to get the previously mentioned values. The model uses the geometrical models, given also in Shoham et al. (1987) and shown in Figures A.1 and A.2 for stratified and annular flow regimes, respectively.

A momentum balance on the liquid and gas phases yields

$$-A_L\,(dp/dx) - \tau_L\,S_L + \tau_i\,S_i = 0 \qquad \text{(A.1)}$$

and

$$-A_G\,(dp/dx) - \tau_G\,S_G + \tau_i\,S_i = 0 \qquad \text{(A.2)}$$

where, A_L and A_G are the cross-sectional areas occupied by the liquid and gas, respectively, τ_L, τ_G, and τ_i are the liquid, gas, and interfacial shear stresses acting on

the perimeters S_L, S_G, and S_i, respectively. Equating the pressure drop (dp/dx) in Equations (A.1) and (A.2) yields the following:

$$\tau_G (S_G / A_G) - \tau_L (S_L / A_L) + \tau_i S_i [(1/A_L) + (1/A_G)] = 0. \quad \text{(A.3)}$$

The shear stresses are evaluated as follows:

$$\tau_L = f_L (\rho_L V_{L1}^2 / 2), \quad \text{(A.4)}$$

$$\tau_G = f_G (\rho_G V_{G1}^2 / 2), \quad \text{(A.5)}$$

and

$$\tau_i = f_i (\rho_G V_{G1}^2 / 2). \quad \text{(A.6)}$$

where,

f_L, f_G, and f_i are the friction factors of the liquid, gas, and interface, respectively, while V_{L1} and V_{G1} are the average velocities of the liquid and gas, respectively.

The friction factors f_L and f_G are given by:

$$f_L = c_L (D_L V_{L1} / \nu_L)^{-n} \quad \text{(A.7)}$$

and

$$f_G = c_G (D_G V_{G1} / \nu_G)^{-m} \quad \text{(A.8)}$$

where,

D_L and D_G are the hydraulic diameters of the liquid and gas, respectively, ν_L and ν_G are the kinematic viscosities of the liquid and gas, respectively, and c_L, c_G, m, and n are empirical coefficients given as follows:

for turbulent flow : $c_L = c_G = 0.046$, $m = n = 0.2$

and

for laminar flow : $c_L = c_G = 16$, $m = n = 1.0$. (A.9)

The hydraulic diameters D_L and D_G are given by:

$$D_L = 4 A_L / S_L \tag{A.10}$$

and

$$D_G = 4 A_G / (S_G + S_i). \tag{A.11}$$

The friction factor, f_i, is given by:

for annular flow: $f_i = f_G (1.0+300\delta/D_1)$,

for stratified flow: $f_i = f_G$,

and

for wavy flow: $f_i = 0.009$. (A.12)

It should be mentioned that Equations (A.1) to (A.12) are valid for annular, stratified, and wavy flow regimes with the only difference that $S_G = 0$ in case of the annular flow regime.

For given inlet conditions (J_{G1} and J_{L1}), fluid properties (ρ_G and ρ_L), and tube diameter (D_1), the inlet gas and liquid mass flow rates may be calculated by the following equations:

$$W_{G1} = (\pi/4) D_1^2 J_{G1} \rho_G \tag{A.13}$$

and

$$W_{L1} = (\pi/4) D_1^2 J_{L1} \rho_L \tag{A.14}$$

Then the void fraction in the inlet α_1 for stratified and wavy flow regimes may be calculated by executing the following steps:

(1) Assume a value for the liquid height (h), see Figure A.1.

(2) Calculate A_L using Equation (A.25).

(3) Calculate A_G from:

$$A_G = (\pi/4)\, D_1^2 - A_L \tag{A.15}$$

(4) Calculate V_{G1} and V_{L1} from:

$$V_{G1} = W_{G1} / (A_G \rho_G) \tag{A.16}$$

and

$$V_{L1} = W_{L1} / (A_L \rho_L) \tag{A.17}$$

(5) Calculate f_L, f_G, and f_i using Equations (A.7) to (A.12).

(6) Calculate τ_L, τ_G, and τ_i using Equations (A.4), (A.5), and (A.6), respectively.

(7) Calculate S_G from:

$$S_G = D_1 \cos^{-1}(2h - 1.0), \tag{A.18}$$

S_L from:

$$S_L = \pi D_1 - S_G, \tag{A.19}$$

and

S_i from Equation (A.27).

(8) Check that Equation (A.3) is satisfied. If Equation (A.3) is not satisfied, change the value of h and repeat steps 2 to 8.

(9) When Equation (A.3) is satisfied, the void fraction in the inlet α_1 is calculated from:

$$\alpha_1 = A_G / ((\pi/4)\, D_1^2) \tag{A.20}$$

(10) For Hwang (1986) model, the slip ratio in the inlet (S) may be calculated from:

$$S = V_{G1} / V_{L1}. \tag{A.21}$$

After calculating the slip ratio (S), the second part of the Hwang (1986) model may be executed to solve for δ_G and the corresponding δ_L, see Section 2.3.1 for more details

on the Hwang (1986) model. The value of δ_G is converted to a value of F_{BG} using Equations (A.25) to (A.33) with parameter a, in the equations, replaced by δ_G. Similarly, the value of δ_L is converted to a value of F_{BL} using Equations (A.25) to (A.34), excluding Equation (A.33), with parameter a, in the equations, replaced by δ_L.

For the annular flow regime, W_{G1} and W_{L1} may be calculated using Equations (A.13) and (A.14), respectively. Then void fraction in the inlet α_1 may be calculated by executing the following steps:

(1) Assume a value for the film thickness (δ), see Figure A.2.

(2) Calculate A_L using Equations (A.36) and (A.38).

(3) Calculate A_G using Equation (A.15).

(4) Calculate V_{G1} and V_{L1} from Equations (A.16) and (A.17), respectively.

(5) Calculate f_L, f_G, and f_i using Equations (A.7) to (A.12).

(6) Calculate τ_L, τ_G, and τ_i using Equations (A.4), (A.5), and (A.6), respectively.

(7) Calculate S_G from:

$S_G = 0.0,$ (A.22)

S_L from:

$S_L = \pi D_1,$ (A.23)

and

S_i from:

$S_i = \pi D_G.$ (A.24)

(8) Check that Equation (A.3) is satisfied. If Equation (A.3) is not satisfied, change the value of δ and repeat steps 2 to 8.

(9) When Equation (A.3) is satisfied, the void fraction in the inlet α_1 is calculated from Equation (A.20).

(10) For Hwang (1986) model, the slip ratio (S) may be calculated from Equation (A.21).

After calculating the slip ratio (S), the second part of the Hwang (1986) model may be executed to solve for δ_G and the corresponding δ_L, see Section 2.3.1 for more details on the Hwang (1986) model. The value of δ_G is converted to a value of F_{BG} using Equations (A.35) to (A.42) with parameter a, in the equations, replaced by δ_G. Similarly, the value of δ_L is converted to a value of F_{BL} using Equations (A.35) to (A.43), excluding Equation (A.42), with parameter a, in the equations, replaced by δ_L.

It should be mentioned that Equations (A.1) to (A.20) can also be used for outlet 2 and outlet 3 in order to calculate the void fractions α_2 and α_3, respectively.

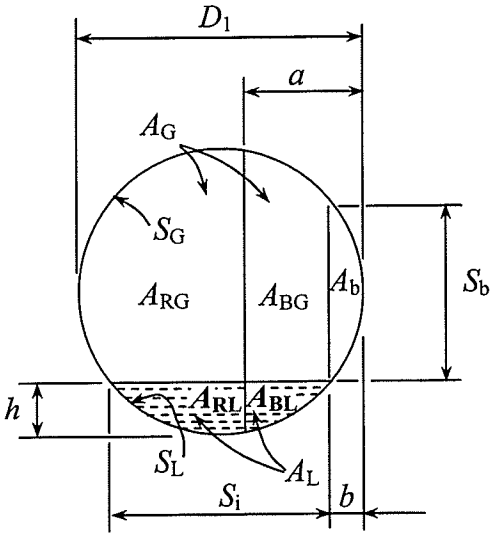

$$A_L = A_{RL}+A_{BL} = 0.25\, D_1^2\, [\pi - \cos^{-1}((2h/D_1)-1)+((2h/D_1)-1)\ \text{sqrt}\{1-((2h/D_1)-1)^2\}] \quad \text{(A.25)}$$

$$A_B = A_{BG}+A_{BL} = 0.25\, D_1^2\, [\pi - \cos^{-1}((2a/D_1)-1)+((2a/D_1)-1)\ \text{sqrt}\{1-((2a/D_1)-1)^2\}] \quad \text{(A.26)}$$

$$S_i = D_1\ \text{sqrt}\ \{1-((2h/D_1)-1)^2\} \quad \text{(A.27)}$$

$$b = 0.5(D_1 - S_i) \quad \text{(A.28)}$$

$$A_b = 0.25\, D_1^2\, [\pi - \cos^{-1}((2b/D_1)-1)+((2b/D_1)-1)\ \text{sqrt}\ \{1-((2b/D_1)-1)^2\}] \quad \text{(A.29)}$$

$$S_b = D_1\ \text{sqrt}\ \{1-((2b/D_1)-1)^2\} \quad \text{(A.30)}$$

$$A_{BL} = 0.5(A_B - (a-b)S_b - A_b) \quad \text{(A.31)}$$

$$A_{BG} = A_B - A_{BL} \quad \text{(A.32)}$$

$$F_{BG} = A_{BG}/A_G \quad \text{(A.33)}$$

$$F_{BL} = A_{BL}/A_L \quad \text{(A.34)}$$

Figure A.1 Geometrical model for the stratified and wavy flow regimes

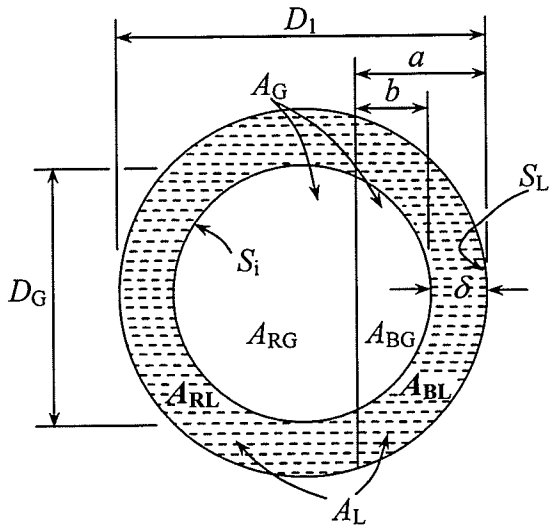

$$A_B = A_{BG}+A_{BL}= 0.25\ D_1^2\ [\pi - \cos^{-1}((2a/D_1)-1)+((2a/D_1)-1)\ \mathrm{sqrt}\{1-((2a/D_1)-1)^2\}] \quad \text{(A.35)}$$

$$D_G = D_1 - 2\delta \quad \text{(A.36)}$$

$$A_G = A_{RG} + A_{BG} = (\pi/4)\ D_G^2 \quad \text{(A.37)}$$

$$A_L = A_{BL} + A_{RL} = (\pi/4)\ (D_1^2 - D_G^2) \quad \text{(A.38)}$$

$$b = a - \delta \quad \text{(A.39)}$$

$$A_{BG} = 0.25\ D_G^2\ [\pi - \cos^{-1}((2b/D_G)-1)+((2b/D_G)-1)\mathrm{sqrt}\{1-((2b/D_G)-1)^2\}] \quad \text{(A.40)}$$

$$A_{BL} = A_B - A_{BG} \quad \text{(A.41)}$$

$$F_{BG} = A_{BG}/A_G \quad \text{(A.42)}$$

$$F_{BL} = A_{BL}/A_L \quad \text{(A.43)}$$

Figure A.2 Geometrical model for the annular flow regime

Nomenclature for Appendix A

Symbol	Description	Units
a	Parameter in the geometrical models given in Figures A.1 and A.2 that is equivalent to δ_L and/or δ_G	m
A_G	Area occupied by the gas at the inlet	m^2
A_L	Area occupied by the liquid at the inlet	m^2
b	Parameter in the geometrical models given in Figures A.1 and A.2	m
c_G	Empirical coefficient; see Equation (A.13)	-
c_L	Empirical coefficient; see Equation (A.13)	-
C_o	Empirical coefficient in the drift flux model; see Equation (A.1)	-
D_1	Diameter of the inlet	m
D_G	Hydraulic diameter of the gas at the inlet	m
D_L	Hydraulic diameter of the liquid at the inlet	m
f_G	Friction factor of the gas at the inlet	-
f_i	Friction factor at the gas-liquid interface at the inlet	-
f_L	Friction factor of the liquid at the inlet	-
F_{BG}	Fraction of inlet gas exiting through outlet 3	-
F_{BL}	Fraction of inlet liquid exiting through outlet 3	-
h	Liquid level at the inlet in case of stratified and wavy flow regimes	m
J_{G1}	Superficial inlet-gas velocity	m/s
J_{L1}	Superficial inlet-liquid velocity	m/s
m	Empirical coefficient; see Equation (A.13)	-
n	Empirical coefficient; see Equation (A.13)	-

S	Slip ratio = V_{G1} / V_{L1}	-
S_G	The part of the circumference of the inlet pipe that is adjacent to gas	m
S_i	Length of the gas-liquid interface at the inlet	m
S_L	The part of the circumference of the inlet pipe that is adjacent to liquid	m
V_{G1}	Average inlet gas velocity	m/s
V_{L1}	Average inlet liquid velocity	m/s
W_{G1}	Inlet-gas mass flow rate	kg/s
W_{L1}	Inlet-liquid mass flow rate	kg/s
x_1	Inlet quality = W_{G1} / W_1	-

Greek Symbols

δ	Liquid-film thickness in the inlet pipe in the case of annular flow	m
δ_G	Parameter defining the location of the gas dividing streamline in the inlet pipe, as in Figure 2.1	m
δ_L	Parameter defining the location of the liquid dividing streamline in the inlet pipe, as in Figure 2.1	m
ρ_G	Gas density	kg/m^3
ρ_L	Liquid density	kg/m^3
τ_G	Shear stress acting on S_G	Pa
τ_i	Shear stress acting on S_i	Pa
τ_L	Shear stress acting on S_L	Pa
ν_G	Kinematic viscosity of the gas	m^2/s
ν_L	Kinematic viscosity of the liquid	m^2/s

Appendix B

PHASE-DISTRIBUTION AND PRESSURE-DROP DATA

Table B.1 provides a listing of the operating conditions and the corresponding phase-distribution and pressure-drop data for all the two-phase experiments conducted in the current study. For some experiments in Table B.1, values of the mass balance errors for air were not entered. For these experiments, the air mass flow rate was not measured either at the inlet or one of the outlets (See Section 4.1). Also, the pressure-drop data for the stratified data sets were not reported for reasons mentioned in Section 4.4.2. Table B.2 provides a listing of the mass flow rates of air and water in the three sides of the junction. As mentioned in Section 3.5.1, the mass flow rates for data sets SW and A1 were corrected for evaporation. Tables B.3 and B.4 provide a listing of the operating conditions and corresponding pressure-drop data for the single-phase-air and water runs, respectively.

Legend

Test	Test number
F_{BG}	Fraction of inlet gas entering outlet 3
F_{BL}	Fraction of inlet liquid entering outlet 3
G_1	Inlet mass flux, kg/m^2s
J_{G1}	Inlet superficial gas velocity, m/s
J_{L1}	Inlet superficial liquid velocity, m/s
P_s	Test-section pressure, bar
Re_1	Inlet Reynolds number for single-phase flow using Equation (4.1)
T_1	Temperature at the tee junction inlet, °C
W_3/W_1	Extraction ratio
x_1	Inlet quality, percentage
ΔP_{12}	Pressure drop from inlet to outlet 2, Pa
ΔP_{13}	Pressure drop from inlet to outlet 3, Pa
Error %:	
Air	Mass balance error for air, percentage
Water	Mass balance error for water, percentage

Table B.1 Two-phase phase-distribution and pressure-drop data

Test	J_{G1} (m/s)	J_{L1} (m/s)	P_s (bar)	T_1 (°C)	x_1 (%)	W_3/W_1	F_{BG}	F_{BL}	ΔP_{12} (Pa)	ΔP_{13} (Pa)	Error (%) Air	Error (%) Water
S1-1	2.50	0.0100	1.50	21.6	30.8	0.000	0.000	0.000	-	-	1.6	-0.9
S1-2	2.49	0.0105	1.50	21.4	29.5	0.000	0.000	0.000	-	-	0.3	4.4
S1-3	2.50	0.0100	1.52	23.8	30.9	0.100	0.000	0.144	-	-	2.4	0.4
S1-4	2.50	0.0100	1.50	21.5	30.8	0.115	0.027	0.156	-	-	0.8	3.4
S1-5	2.50	0.0101	1.49	22.4	30.5	0.281	0.239	0.299	-	-	0.8	3.1
S1-6	2.48	0.0097	1.50	21.6	31.2	0.487	0.499	0.482	-	-	-0.9	0.8
S1-7	2.50	0.0100	1.50	21.6	30.8	0.499	0.499	0.499	-	-	-0.2	0.2
S2-1	2.00	0.0101	1.50	21.7	26.1	0.000	0.000	0.000	-	-	2.7	-1.4
S2-2	1.96	0.0100	1.50	21.6	25.9	0.180	0.000	0.243	-	-	2.3	2.2
S2-3	2.04	0.0097	1.51	21.6	27.5	0.342	0.262	0.371	-	-	2.6	1.5
S2-4	2.00	0.0099	1.51	21.4	26.5	0.500	0.502	0.499	-	-	0.2	3.1
S3-1	0.50	0.0101	1.52	21.7	8.19	0.000	0.000	0.000	-	-	-	-4.0
S3-2	0.49	0.0098	1.52	21.4	8.27	0.429	0.163	0.454	-	-	-	0.0
S3-3	0.51	0.0097	1.51	21.5	8.63	0.398	0.000	0.437	-	-	-	3.7
S3-4	0.48	0.0100	1.51	21.4	7.93	0.488	0.506	0.487	-	-	-	0.5
S3-5	0.50	0.0100	1.51	21.4	8.23	0.499	0.499	0.499	-	-	-	-0.1
S4-1	0.50	0.0403	1.51	21.8	2.16	0.000	0.000	0.000	-	-	-	-0.4
S4-2	0.50	0.0404	1.51	21.5	2.16	0.466	0.000	0.477	-	-	-	-0.7
S4-3	0.49	0.0395	1.50	21.6	2.15	0.491	0.500	0.491	-	-	-	-0.9
S4-4	0.50	0.0400	1.50	21.5	2.17	0.498	0.501	0.497	-	-	-	-0.2

Table B.1 (continued)

Test	J_{G1} (m/s)	J_{L1} (m/s)	P_s (bar)	T_1 (°C)	x_1 (%)	W_3/W_1	F_{BG}	F_{BL}	ΔP_{12} (Pa)	ΔP_{13} (Pa)	Error (%) Air	Error (%) Water
SW-1	10.01	0.0026	1.50	22.0	87.1	0.000	0.000	0.000	84.2	-48.4	4.0	4.4
SW-2	10.00	0.0026	1.51	24.9	87.0	0.097	0.111	0.001	33.1	-41.4	0.1	4.6
SW-3	10.03	0.0027	1.51	24.0	87.0	0.097	0.111	0.001	29.8	-45.4	-0.3	3.8
SW-4	10.00	0.0026	1.50	22.5	87.2	0.307	0.347	0.029	6.6	-39.0	-5.2	-3.9
SW-5	10.00	0.0026	1.49	25.3	87.0	0.294	0.338	0.001	5.7	-36.9	-4.4	-0.6
SW-6	10.00	0.0026	1.50	25.3	87.0	0.401	0.437	0.155	-8.3	-36.5	-5.1	-4.2
SW-7	10.00	0.0026	1.50	23.6	87.1	0.501	0.501	0.499	-18.4	-16.7	-5.2	-2.1
SW-8	10.02	0.0026	1.50	24.0	87.0	0.500	0.500	0.499	-18.7	-17.9	-5.3	-2.9
W1-1	10.03	0.0101	1.51	21.4	63.9	0.000	0.000	0.000	109.7	-27.6	-1.4	0.4
W1-2	10.01	0.0104	1.50	24.9	62.8	0.037	0.043	0.026	69.8	-41.5	-4.3	-5.0
W1-3	10.03	0.0102	1.50	21.5	63.5	0.099	0.107	0.087	71.5	-54.5	1.9	0.2
W1-4	10.02	0.0103	1.50	21.3	63.4	0.299	0.311	0.281	22.2	-41.3	4.9	-3.3
W1-5	9.97	0.0102	1.50	21.6	63.4	0.497	0.496	0.497	-24.8	-22.7	4.5	0.8
W1-6	10.02	0.0104	1.51	21.6	63.3	0.703	0.690	0.723	-43.5	21.3	4.8	-2.2
W2-1	10.04	0.0406	1.50	21.0	30.6	0.000	0.000	0.000	157.2	-82.9	-5.0	3.8
W2-2	10.00	0.0403	1.50	23.1	30.6	0.049	0.000	0.070	134.6	-87.6	0.7	0.0
W2-3	10.00	0.0406	1.50	21.2	30.5	0.109	0.028	0.144	115.9	-92.8	-1.0	-0.9
W2-4	10.03	0.0403	1.50	21.2	30.7	0.300	0.234	0.329	58.9	-76.7	-4.5	-3.6
W2-5	10.04	0.0404	1.50	20.5	30.8	0.300	0.234	0.330	58.5	-77.2	-3.9	-3.4
W2-6	9.99	0.0402	1.50	21.5	30.7	0.502	0.496	0.505	-24.9	-27.2	3.9	-2.8
W2-7	10.04	0.0403	1.51	23.5	30.6	0.503	0.503	0.503	-27.7	-27.1	2.7	-2.9

Table B.1 (continued)

Test	J_{G1} (m/s)	J_{L1} (m/s)	P_s (bar)	T_1 (°C)	x_1 (%)	W_3/W_1	F_{BG}	F_{BL}	ΔP_{12} (Pa)	ΔP_{13} (Pa)	Error (%) Air	Error (%) Water
A1-1	40.01	0.0027	1.51	25.3	96.4	0.000	0.000	0.000	1583.4	-604.2	-4.8	4.4
A1-2	39.99	0.0026	1.50	25.5	96.4	0.101	0.104	0.001	1358.0	-473.9	0.5	-1.0
A1-3	40.01	0.0026	1.51	28.5	96.4	0.196	0.201	0.001	1044.4	-209.4	5.3	-3.2
A1-4	40.01	0.0026	1.50	26.4	96.4	0.338	0.343	0.166	766.4	8.3	2.6	-5.2
A1-5	40.03	0.0026	1.51	25.2	96.4	0.495	0.495	0.500	489.8	475.0	5.1	-3.4
A2-1	39.99	0.0104	1.51	26.5	87.1	1.00	1.00	1.00	-663.0	1742	-1.3	4.8
A2-2	39.93	0.0104	1.50	23.3	87.2	1.00	1.00	1.00	-665.2	1752	-0.5	3.6
A2-3	40.00	0.0099	1.51	26.2	87.6	0.045	0.043	0.062	1548.4	-662.3	-0.1	4.6
A2-4	40.00	0.0100	1.50	26.5	87.5	0.099	0.092	0.152	1409.4	-539.1	2.7	2.9
A2-5	40.00	0.0102	1.51	24.9	87.4	0.300	0.295	0.334	1012.7	-118.9	-3.5	3.5
A2-6	39.98	0.0101	1.50	24.0	87.5	0.503	0.503	0.501	395.1	408.2	-3.2	0.6
A3-1	39.94	0.0406	1.51	27.0	63.3	1.00	1.00	1.00	-949.4	2538	-1.0	-1.6
A3-2	39.91	0.0404	1.52	24.3	63.7	1.00	1.00	1.00	-988.3	2625	0.2	-1.5
A3-3	39.89	0.0409	1.49	28.3	62.8	0.962	1.00	0.900	-851.4	2283	-0.8	-3.9
A3-4	40.00	0.0399	1.51	22.6	64.1	0.118	0.049	0.241	1995.1	-768.2	1.1	1.0
A3-5	40.01	0.0399	1.51	22.7	64.1	0.309	0.267	0.385	1106.0	-302.9	-2.5	-0.1
A3-6	40.04	0.0399	1.51	24.7	63.9	0.503	0.505	0.500	217.6	238.6	-3.7	-4.0
A4-1	39.45	0.1795	1.52	20.7	28.4	1.00	1.00	1.00	-1482.0	6881	-	2.5
A4-2	39.52	0.1795	1.51	22.2	28.3	0.923	1.00	0.892	-1245.2	6872	-	-0.1
A4-3	39.71	0.1800	1.50	24.6	28.0	0.806	0.989	0.735	-1142.3	6614	-	-1.1
A4-4	39.55	0.1798	1.51	27.3	27.9	0.744	0.899	0.683	-1048.1	4236	-1.4	-0.2
A4-5	40.07	0.1808	1.50	21.6	28.3	0.399	0.320	0.430	1450.9	-100.1	-1.7	-0.7
A4-6	40.00	0.1807	1.51	22.8	28.2	0.503	0.505	0.502	469.2	468.8	-2.1	0.4
A4-7	40.09	0.1809	1.51	24.8	28.2	0.498	0.498	0.499	471.4	449.8	-1.7	-0.1

Table B.2 Two-phase mass flow rates

Test	W_{L1} (kg/h)	W_{G1} (kg/h)	W_{L2} (kg/h)	W_{G2} (kg/h)	W_{L3} (kg/h)	W_{G3} (kg/h)
S1-1	40.39	17.95	40.75	17.66	0.0000	0.0000
S1-2	42.62	17.83	40.75	17.77	0.0000	0.0000
S1-3	40.25	17.99	34.30	17.55	5.786	0.0000
S1-4	40.39	17.97	32.96	17.34	6.073	0.4875
S1-5	40.59	17.80	27.56	13.43	11.78	4.227
S1-6	39.21	17.81	20.16	9.006	18.75	8.957
S1-7	40.30	17.93	20.15	9.006	20.08	8.960
S2-1	40.61	14.37	41.17	13.99	0.0000	0.0000
S2-2	40.43	14.12	29.93	13.80	9.605	0.0000
S2-3	38.99	14.78	24.13	10.63	14.26	3.771
S2-4	40.07	14.46	19.45	7.176	19.38	7.246
S3-1	40.77	-	42.39	3.636	0.00	0.0000
S3-2	39.71	-	21.70	2.998	18.01	0.5818
S3-3	39.30	-	21.31	3.712	16.53	0.0000
S3-4	40.24	-	20.54	1.712	19.49	1.752
S3-5	40.24	-	20.17	1.811	20.11	1.800
S4-1	162.7	-	163.4	3.599	0.0000	0.0000
S4-2	163.0	-	85.88	3.599	78.20	0.0000
S4-3	159.4	-	81.82	1.751	79.01	1.752
S4-4	161.4	-	81.27	1.786	80.45	1.791
SW-1	10.31	72.16	10.77	75.04	0.0000	0.0000
SW-2	10.32	71.68	10.81	63.76	0.0000	7.998
SW-3	10.41	72.10	10.81	63.88	0.0000	8.004
SW-4	10.21	71.89	9.526	44.51	0.2821	23.63
SW-5	10.19	70.84	10.15	44.87	0.0000	22.88
SW-6	10.22	71.15	8.272	38.04	1.519	29.49
SW-7	10.23	71.74	5.021	33.94	5.005	34.04
SW-8	10.33	71.84	5.023	34.00	5.013	34.05
W1-1	40.92	72.43	40.75	73.46	0.0000	0.0000
W1-2	42.12	70.97	43.04	70.81	1.166	3.214
W1-3	41.31	72.01	37.63	63.11	3.588	7.524
W1-4	41.66	72.07	30.96	47.27	12.08	21.29
W1-5	41.20	71.52	20.57	34.39	20.31	33.89
W1-6	41.85	72.15	11.83	21.29	30.96	47.43

Table B.2 (continued)

Test	W_{L1} (kg/h)	W_{G1} (kg/h)	W_{L2} (kg/h)	W_{G2} (kg/h)	W_{L3} (kg/h)	W_{G3} (kg/h)
W2-1	164.0	72.22	157.7	75.82	0.0000	0.0000
W2-2	162.7	71.59	151.2	71.08	11.41	0.0000
W2-3	163.9	71.80	141.5	70.43	23.87	2.052
W2-4	162.8	72.10	113.1	57.68	55.52	17.64
W2-5	163.2	72.50	113.1	57.69	55.66	17.64
W2-6	162.4	71.81	82.65	34.79	84.27	34.23
W2-7	162.8	71.86	83.31	34.77	84.22	35.15
A1-1	9.471	286.3	10.08	272.7	0.0000	0.0000
A1-2	9.264	284.7	9.135	256.4	0.0000	29.66
A1-3	9.145	283.0	8.654	237.9	0.0000	60.00
A1-4	9.205	284.7	7.140	192.1	1.420	100.1
A1-5	9.241	286.0	4.376	151.6	4.376	148.9
A2-1	42.01	283.3	0.0000	0.0000	40.02	287.0
A2-2	41.96	285.5	0.0000	0.0000	40.47	286.9
A2-3	40.14	283.6	35.92	271.6	2.362	12.07
A2-4	40.22	282.8	33.11	249.9	5.933	25.32
A2-5	41.06	285.8	26.38	208.4	13.23	87.33
A2-6	40.64	284.2	20.16	145.8	20.21	147.6
A3-1	163.9	283.0	0.0000	0.0000	166.5	285.8
A3-2	163.1	286.7	0.0000	0.0000	165.6	286.1
A3-3	165.0	278.0	17.10	0.0000	154.3	280.3
A3-4	161.2	287.6	121.2	270.5	38.40	14.08
A3-5	161.1	287.6	99.21	216.3	62.12	78.68
A3-6	161.1	285.7	83.71	146.6	83.88	149.6
A4-1	724.6	287.5	0.0000	0.0000	706.2	-
A4-2	724.6	285.5	78.12	0.0000	646.9	-
A4-3	726.6	282.6	194.4	3.164	539.9	-
A4-4	725.8	280.3	230.4	28.73	496.8	255.6
A4-5	729.9	288.1	419.1	199.1	316.0	93.76
A4-6	729.5	286.8	362.2	145.0	364.5	147.8
A4-7	730.0	286.3	366.2	146.2	364.5	144.8

Table B.3 Single-phase-air pressure-drop data

Test	J_{G1} (m/s)	G_1 (kg/m^{2}s)	Re_1	T_1 (°C)	W_3/W_1	ΔP_{12} (Pa)	ΔP_{13} (Pa)	Error %
A-1	20	35.6	72,850	21.3	0.000	337.8	-155.8	-0.4
A-2	20	35.6	72,850	20.0	0.102	276.1	-115.9	-2.5
A-3	20	35.6	72,850	20.0	0.299	190.4	-27.3	0.1
A-4	20	35.6	72,850	20.0	0.498	83.1	78.2	-4.9
A-5	20	35.6	72,850	20.8	0.702	-32.6	198.8	-3.2
A-6	20	35.6	72,850	20.0	0.903	-116.6	13.3	-0.2
A-7	20	35.6	72,850	20.0	1.00	-153.4	337.3	-0.9
A-8	40	71.2	145,700	21.8	0.000	1311	-588.0	0.4
A-9	40	71.2	145,700	22.1	0.106	1151	-466.8	0.5
A-10	40	71.2	145,700	20.3	0.291	752.6	-107.4	-2.7
A-11	40	71.2	145,700	20.0	0.500	356.1	355.1	-3.0
A-12	40	71.2	145,700	20.5	0.699	-107.9	751.4	-0.4
A-13	40	71.2	145,700	20.0	0.898	-466.6	1164	0.4
A-14	40	71.2	145,700	20.8	1.00	-590.7	1319	0.3

Table B.4 Single-phase-water pressure-drop data

Test	J_{L1} (m/s)	G_1 (kg/m^{2}s)	Re_1	T_1 (°C)	W_3/W_1	ΔP_{12} (Pa)	ΔP_{13} (Pa)	Error %
W-1	0.18	179.5	7170	22.3	0.000	19.36	-7.04	0.9
W-2	0.18	179.5	7170	22.3	0.100	13.33	-5.53	0.9
W-3	0.18	179.5	7170	20.0	0.904	-5.51	13.30	0.2
W-4	0.18	179.5	7170	20.0	1.00	-6.89	19.35	0.0

Appendix C

PRESSURE-DISTRIBUTION FOR STRATIFIED FLOW

This appendix gives a possible explanation to the trends seen in Figures 4.18 and 4.20 in Section 4.4.2. Also, this appendix provides all the pressure-distribution data for stratified flow obtained in the current study. The pressure-drop data (values of ΔP_{12} and ΔP_{13}) for stratified flows could not be obtained for reasons mentioned in Section 4.4.2.

Consider the momentum balance on a small element containing gas and liquid in stratified flow with changing interface level (see Figure C.1)

$$M_{\text{in,x}} + \frac{\partial M_{\text{in,x}}}{\partial x} dx - M_{\text{in,x}} = P_{\text{st}} A + \rho_{\text{L}}\, g\, h_{\text{L}}\, \tilde{A}_{\text{L}} - (P_{\text{st}} + \frac{\partial P_{\text{st}}}{\partial x} dx)\, A$$
$$- \rho_{\text{L}}\, g\, (h_{\text{L}}\, \tilde{A}_{\text{L}} + \frac{\partial}{\partial x}(h_{\text{L}}\, \tilde{A}_{\text{L}})\, dx) - (\tau_{\text{w,L}} S_{\text{L}} + \tau_{\text{w,G}} S_{\text{G}})\, dx \qquad \text{(C.1)}$$

where $M_{\text{in,x}}$ is the inlet momentum in the x-direction, P_{st} is the gas static pressure, h_{L} is the height of the interface, $\tau_{\text{w,L}}$ is the liquid wall shear stress, $\tau_{\text{w,G}}$ is the gas wall shear stress, S_{L} is the liquid perimeter, S_{G} is the gas perimeter, A is the total cross-sectional area of the pipe, and $\tilde{A}_{\text{L}}$ is an area multiplier for the hydrostatic pressure. Equation (C.1) may be rearranged to the following form:

$$A \frac{\partial P_{\text{st}}}{\partial x} + \rho_{\text{L}}\, g \frac{\partial}{\partial x} (h_{\text{L}}\, \tilde{A}_{\text{L}}) + \tau_{\text{w,L}} S_{\text{L}} + \tau_{\text{w,G}} S_{\text{G}} + \frac{\partial M_{\text{in,x}}}{\partial x} = 0 \qquad \text{(C.2)}$$

All the figures of pressure-distribution data given in the current study have the ordinate of (P-P_{r}) which, according to Equation (4.12), can be differentiated with respect to x as follows:

$$\frac{\partial (P - P_{\text{r}})}{\partial x} = \frac{\partial P_{\text{st}}}{\partial x} + \rho_{\text{L}}\, g \frac{\partial h_{\text{L}}}{\partial x} \qquad \text{(C.3)}$$

The second term of the right hand side of Equation (C.3) is different from the second term in Equation (C.2). However, it is expected that if the interface level decreases with x, both terms become negative and vice a versa. For easier future reference, the five terms of Equation (C.2) will referred to as T1, T2, T3, T4, and T5, respectively. Also, the first and second terms of the right hand side of Equation (C.3) will be referred to as T6 and T7, respectively.

Figure 4.20 shows that there is an approximately 2.5-mm decrease in the interface level along outlet 3. When applying Equation (C.2) in outlet 3 for the case of no-gas flow, T1 and T4 representing the static pressure gradient and the gas wall shear stress, respectively, have values of zero. T3 has a positive value while T5 has a zero value. Substituting in Equation (C.2) yields the following:

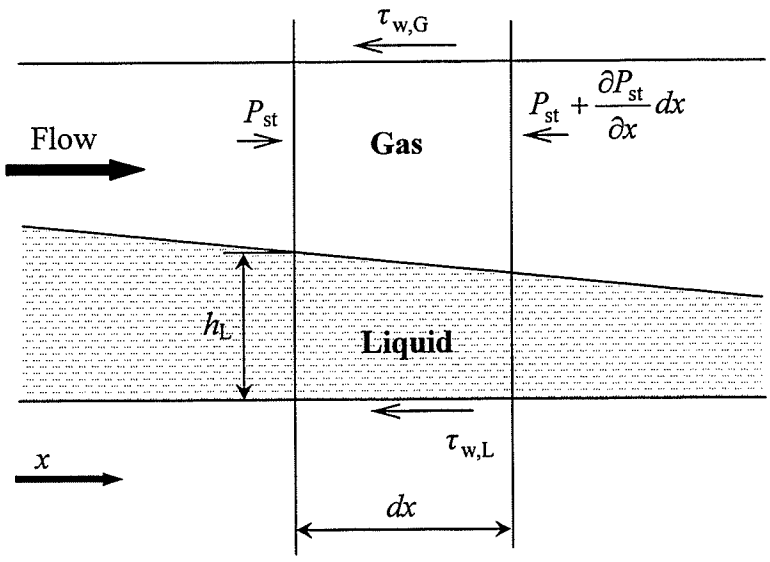

Figure C.1 Stratified flow with a changing interface height

$$\frac{\partial}{\partial x}(h_L \tilde{A}_L) = -\frac{\tau_{w,L} S_L}{\rho_L g} \qquad \text{(C.4)}$$

Equation (C.4) indicates that the interface level decreases with increasing x. As a result, T7 becomes negative. With T6 being zero, Equation (C.3) indicates that values of $(P\text{-}P_r)$ decrease with increasing x, which is consistent with the data in Figure 4.20.

When applying Equation (C.2) in the inlet for the case of no-gas flow, T1 and T4 have zero values while T3 has a positive value. Substituting in Equation (C.2) yields the following:

$$\frac{\partial}{\partial x}(h_L \tilde{A}_L) = \frac{-[(\partial M_{in,x}/\partial x) + \tau_{w,L} S_L]}{\rho_L g} \qquad \text{(C.5)}$$

In the inlet, and contrary to the case of outlet 3, T5 might have a negative value. This is due to the existence of the junction, which forces the incoming flow to deviate from the x-direction in order to get diverted into the outlets. It is thought that far enough from the junction, T5 is close to zero and that the absolute value of this term increases as we approach the junction. In Equation (C.5), if the magnitude of T5 is less than that of T3, then the left hand side of Equation (C.5) will be negative and according to Equation (C.3), values of $(P\text{-}P_r)$ will decrease with increasing x and vice a versa. Figure 4.20 shows that in the inlet, values of $(P\text{-}P_r)$ decrease up to tap 13 and increase slightly between taps 13 and 15. This suggests that, up to tap 13, the magnitude of T5 is less than that of T3 while the opposite occurs between taps 13 and 15. Figure 4.20 also shows that in the inlet, the rate of decrease of $(P\text{-}P_r)$ with respect to x is less than that in outlet 3. This might be attributed to the reason that T5 may have a negative value in the inlet while it has a zero value in outlet 3.

Figure 4.18 shows that in the inlet, values of $(P\text{-}P_r)$ first decrease linearly with increasing x (section 1), then decrease non-linearly at a lower rate (section 2), and finally increase till the junction centre (section 3). When applying Equation (C.2) in the inlet for the case of a stratified flow with nonzero values of J_{G1} and J_{L1}, T3 and T4 have positive values while T1 has a negative value. It is not known for sure what values T2 and T5 would have in the inlet. However, a possible explanation to the trends seen in the inlet in Figure 4.18 is given hereafter. In section 1, T2 is negative while T5 is zero. As T1 and T2 are both negative, T6 and T7 in Equation (C.3) become also negative. In Figure 4.18, the linear decrease in $(P\text{-}P_r)$ in section 1 suggests that T6 and T7 add up to a constant negative value. In section 2, T5 becomes negative and as a result, T2 remains negative but its magnitude decreases (assuming that T1, T3, and T4 are constants). Consequently, in Equation (C.3), T6 remains unchanged and T7 remains negative but with a smaller magnitude. As a result, values of $(P\text{-}P_r)$ decrease non-linearly (at a lower rate) with increasing x. In section 3, the magnitude of T5 increases to the extent that T2 becomes positive (assuming that T1, T3, and T4 are constants). The positive value of T2 in section 3 is consistent with the interface swelling at the junction seen in Figure 4.19. Consequently, in Equation (C.3), T6 remains unchanged (negative) while T7 becomes positive. The net result on the left hand side of Equation (C.3) is that it becomes positive and as a result, values of $(P\text{-}P_r)$ increase with increasing x.

For the case of a stratified flow with nonzero values of J_{G1} and J_{L1}, the discussion given above for section 1 of the inlet is thought to be valid also for outlet 2 and 3. In Figure 4.18, the deviation from the linear behaviour at the first four taps in each outlet is due to the re-circulation zones that are formed in the outlets in the vicinity of the junction.

The pressure-distribution data for stratified flow obtained in the current study are given in the following figures. The purpose of Figures C.2 to C.17 is to document the pressure-distribution data for data sets S1 to S4 at various split ratios. It can be seen that in all the figures that correspond to a split ratio of 0.5, the data in outlet 2 and outlet 3 are symmetric.

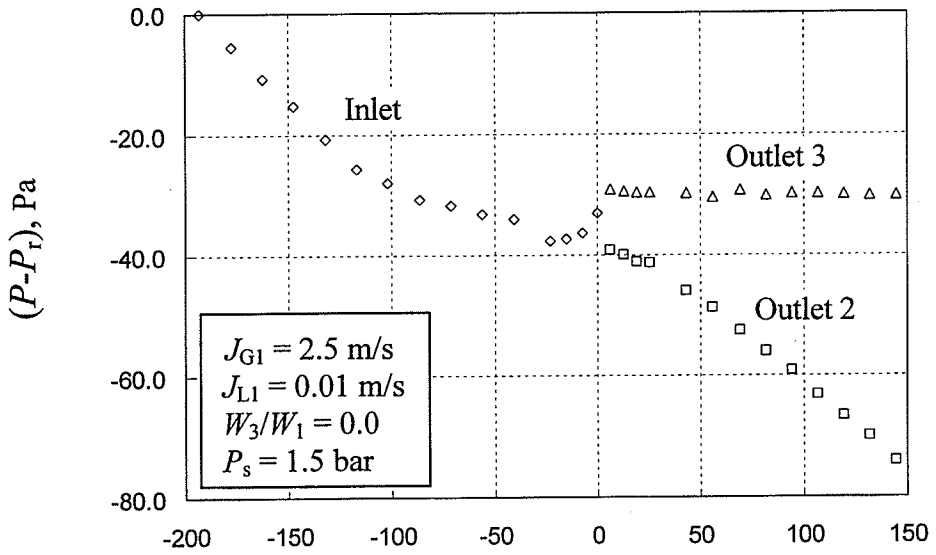

Figure C.2 Pressure distribution for data set S1 with $W_3/W_1 = 0.0$

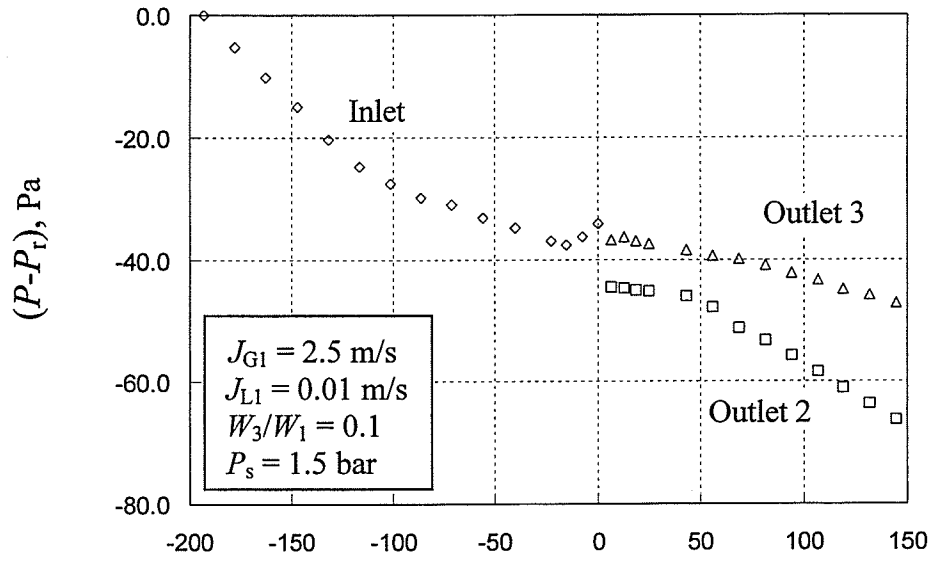

Figure C.3 Pressure distribution for data set S1 with $W_3/W_1 = 0.1$

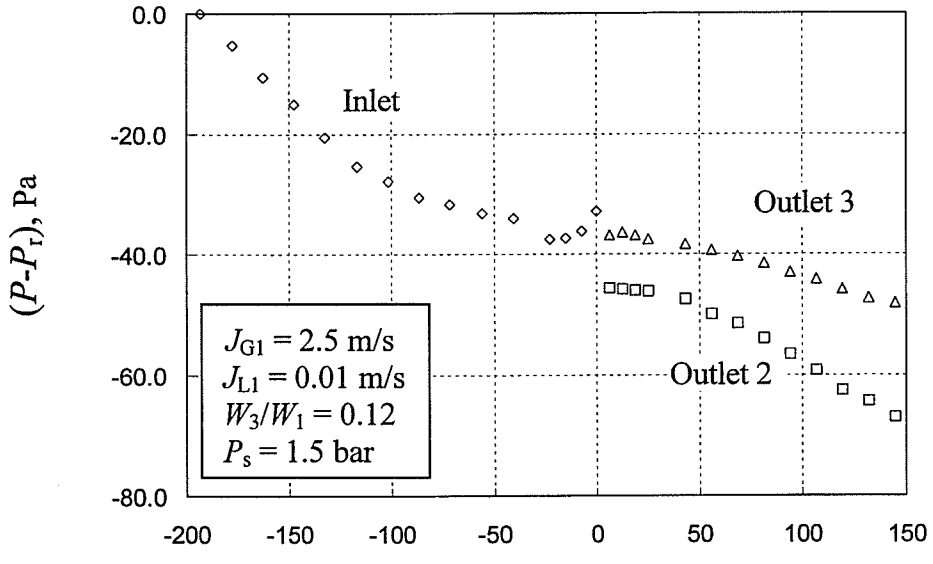

Figure C.4 Pressure distribution for data set S1 with $W_3/W_1 = 0.12$

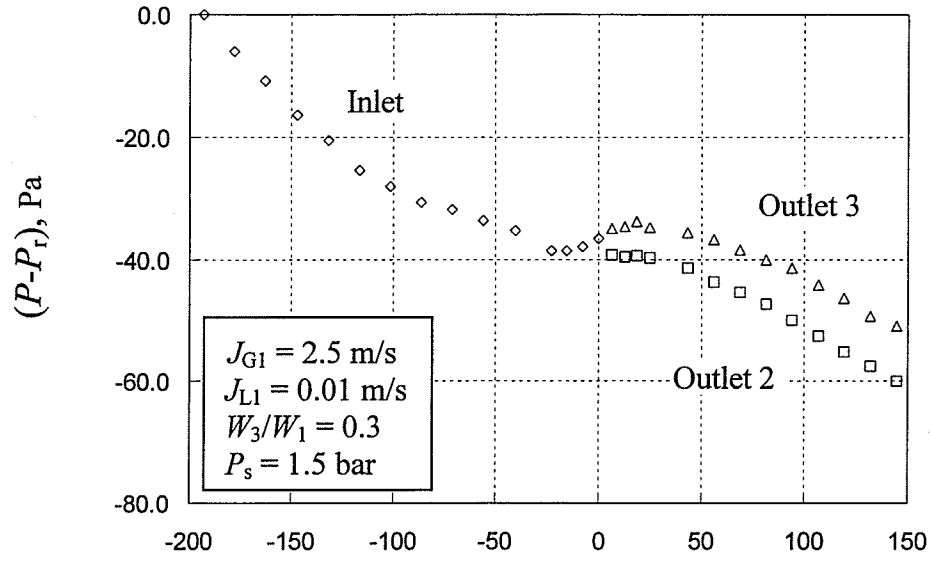

Figure C.5 Pressure distribution for data set S1 with $W_3/W_1 = 0.3$

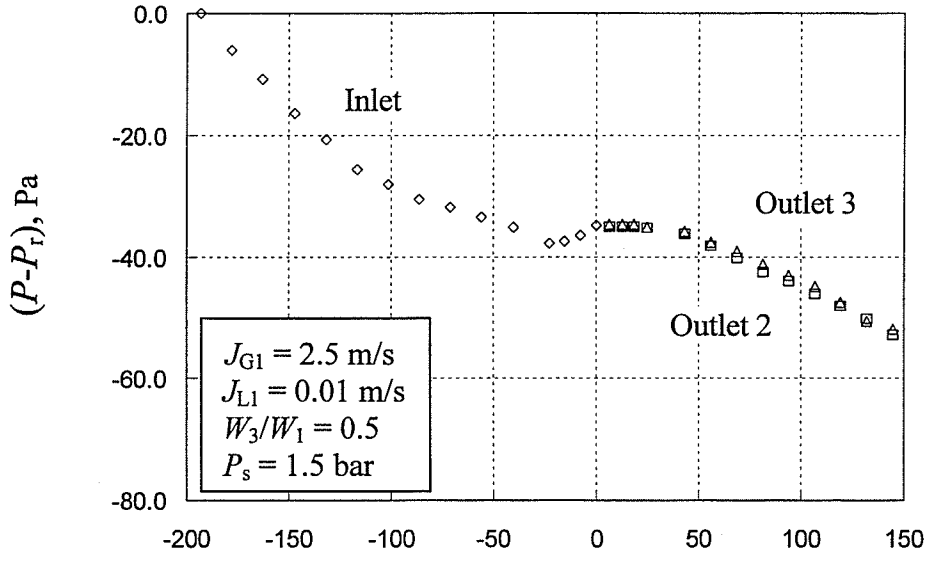

Figure C.6 Pressure distribution for data set S1 with $W_3/W_1 = 0.5$

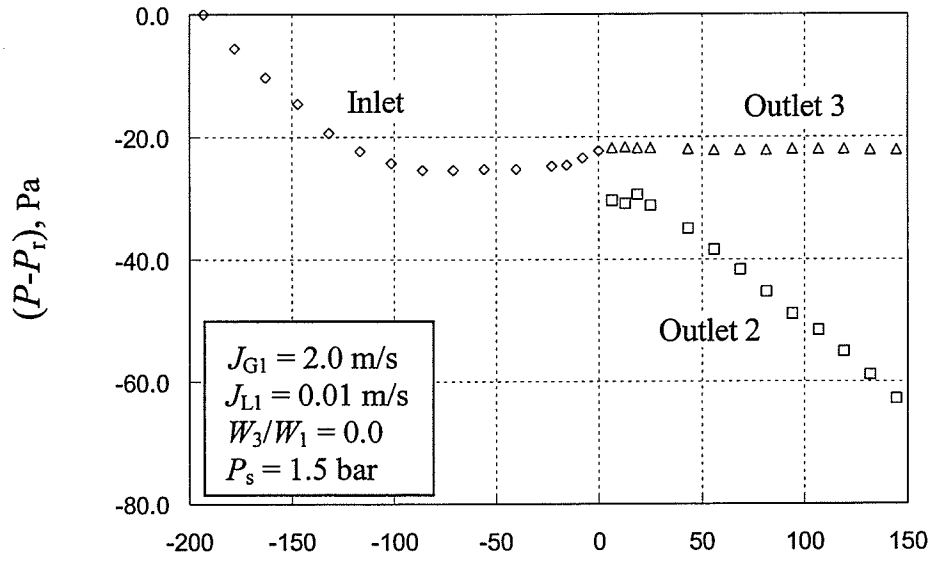

Figure C.7 Pressure distribution for data set S2 with $W_3/W_1 = 0.0$

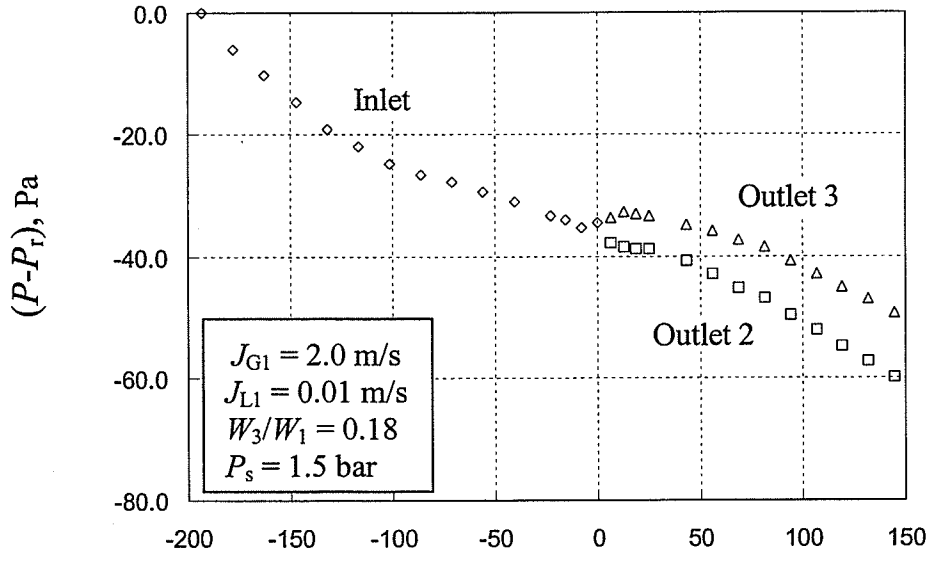

Figure C.8 Pressure distribution for data set S2 with $W_3/W_1 = 0.18$

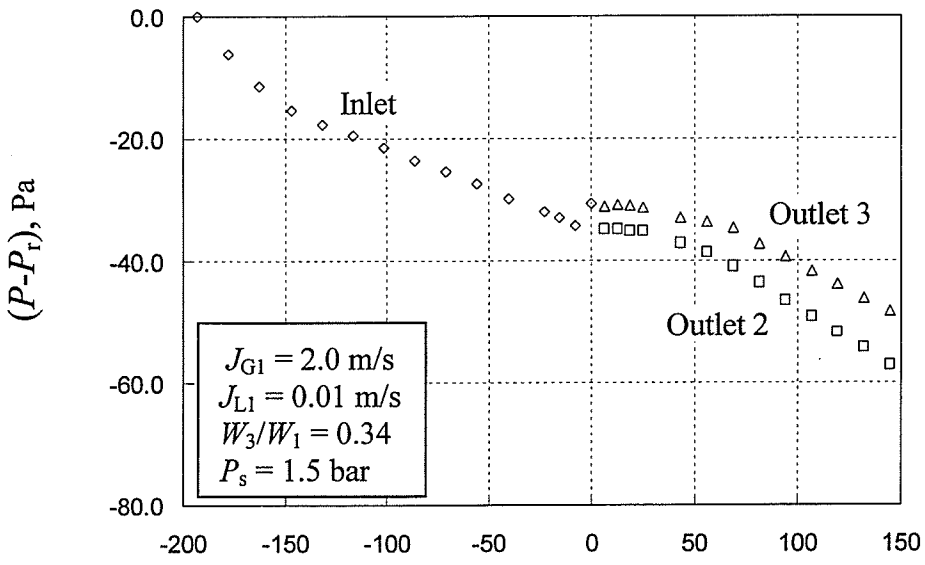

Figure C.9 Pressure distribution for data set S2 with $W_3/W_1 = 0.34$

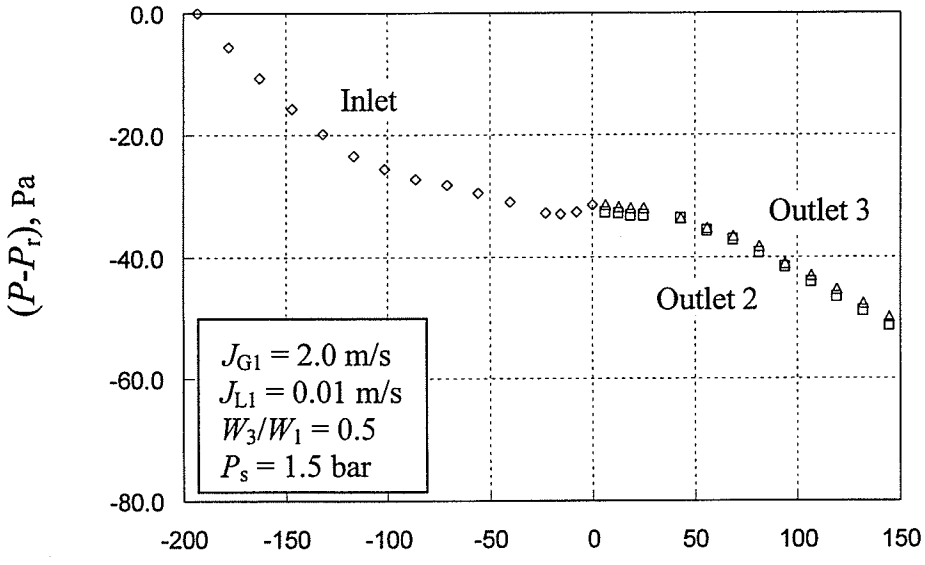

Figure C.10 Pressure distribution for data set S2 with $W_3/W_1 = 0.5$

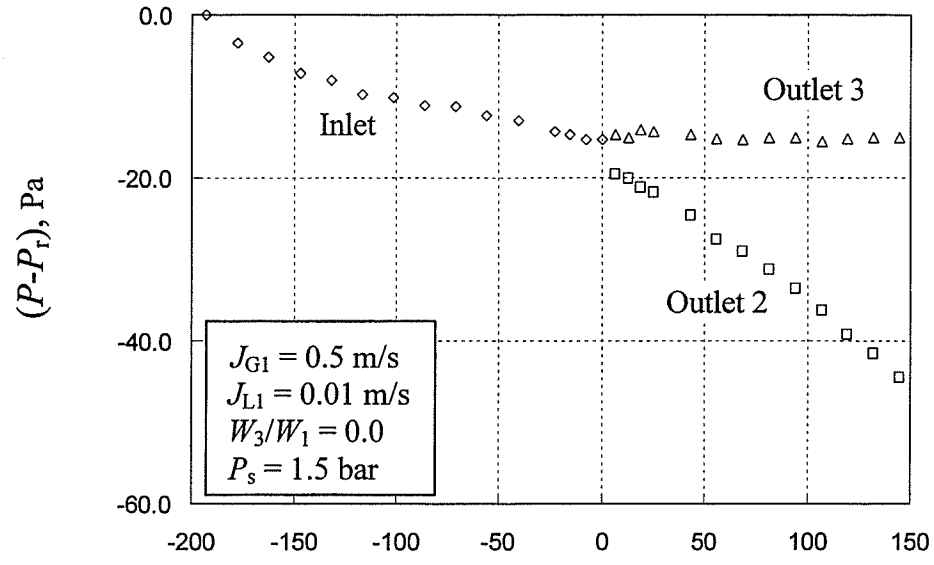

Figure C.11 Pressure distribution for data set S3 with $W_3/W_1 = 0.0$

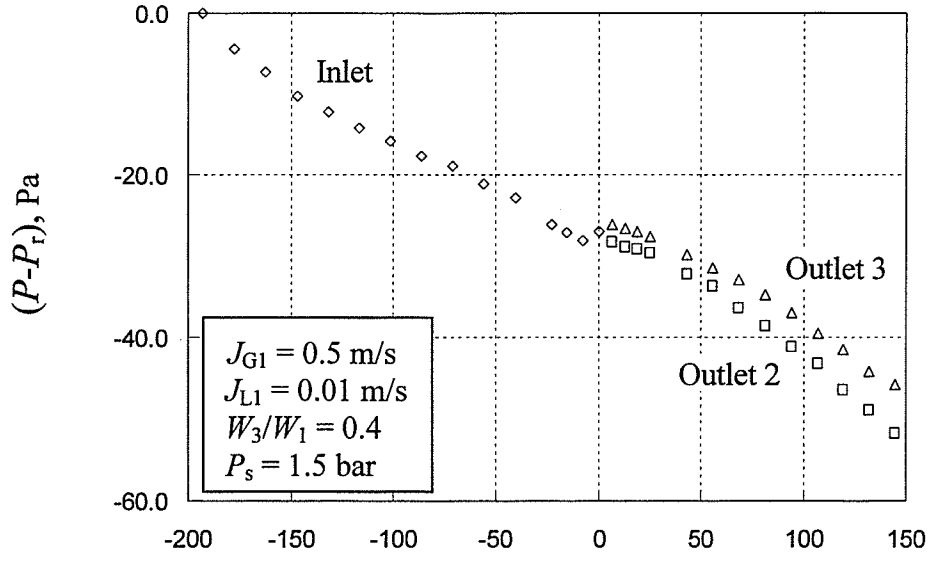

Figure C.12 Pressure distribution for data set S3 with $W_3/W_1 = 0.4$

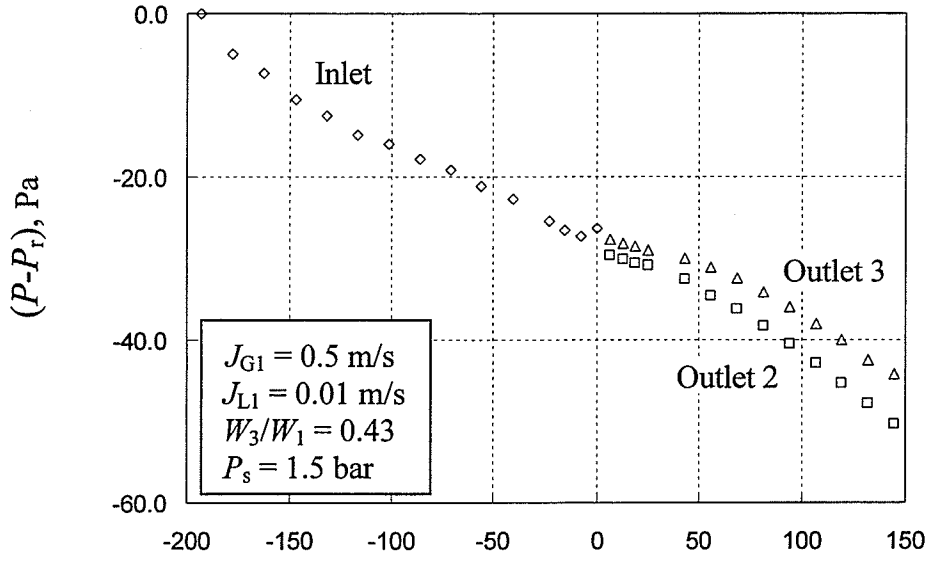

Figure C.13 Pressure distribution for data set S3 with $W_3/W_1 = 0.43$

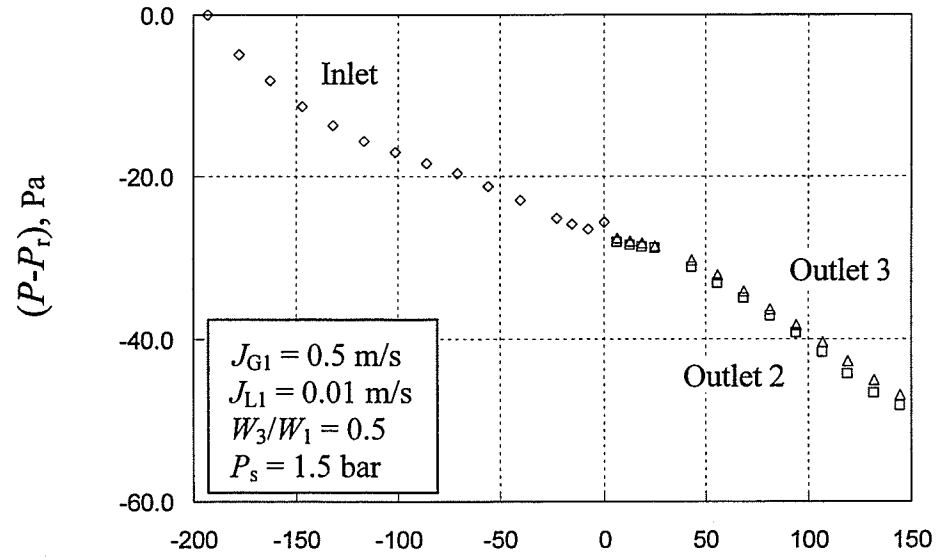

Figure C.14 Pressure distribution for data set S3 with $W_3/W_1 = 0.5$

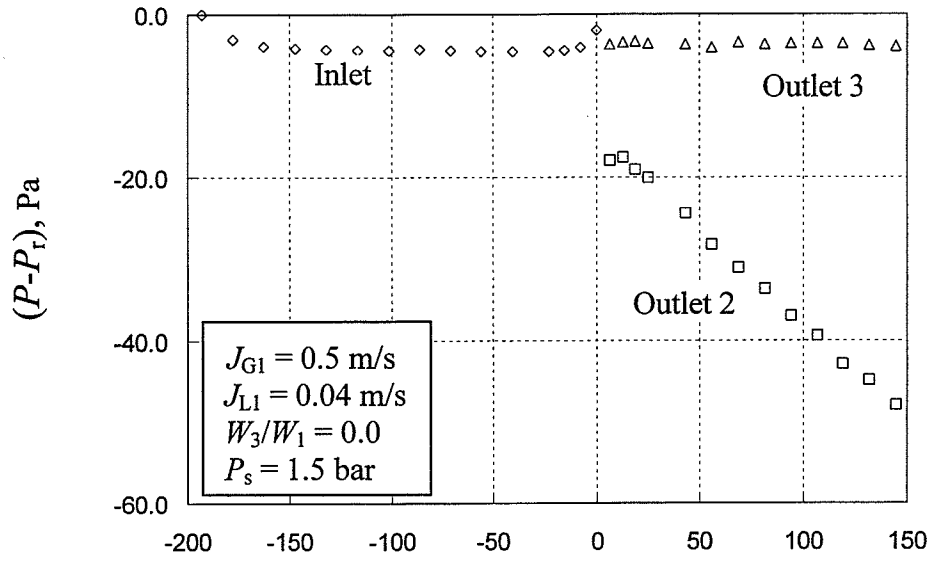

Figure C.15 Pressure distribution for data set S4 with $W_3/W_1 = 0.0$

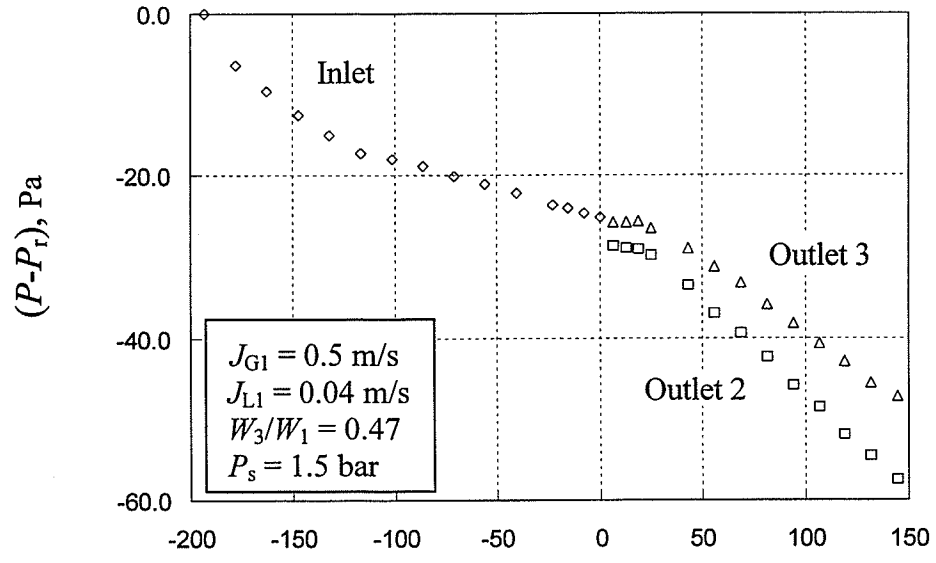

Figure C.16 Pressure distribution for data set S4 with $W_3/W_1 = 0.47$

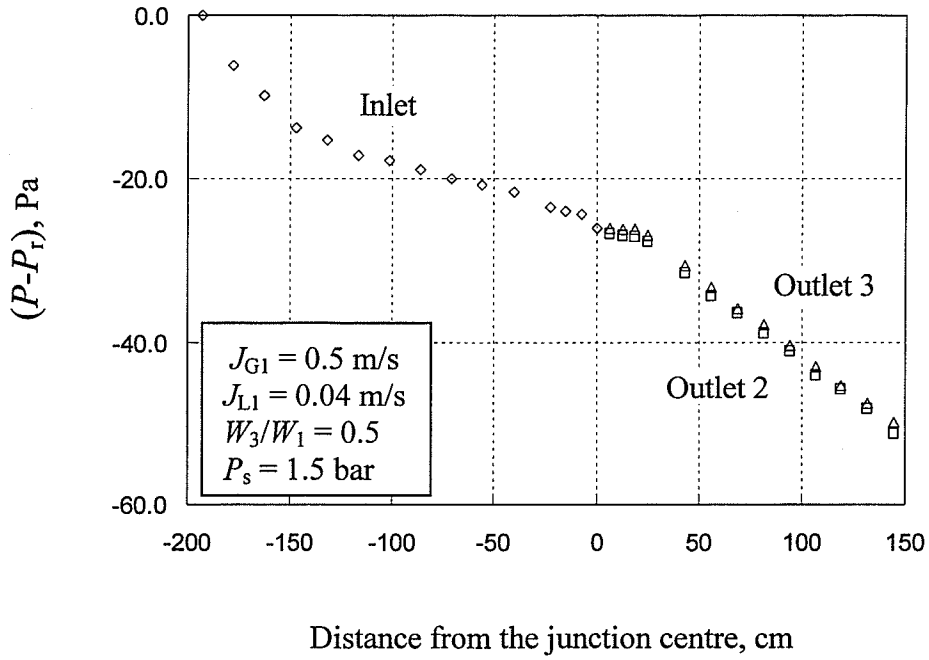

Figure C.17 Pressure distribution for data set S4 with $W_3/W_1 = 0.5$

Appendix D
UNCERTAINTY ANAYLYSIS

This appendix provides results of the uncertainty analysis for both the measured and calculated quantities. The term "uncertainty" is defined as a possible value for the error, where the error is the difference between the correct value and the reported (either measured or calculated) one. The uncertainties are meant to accommodate: discrimination uncertainties in the measuring instruments, the error in fitting an equation to the calibration data, and the accuracy of the calibrating devices. The uncertainty analysis was done based on the methods of Kline and McClintock (1953) and Moffat (1988). These methods are explained in detail in Appendix E of Buell (1992). All uncertainties given in the current study are at "odds" (as used by the above-given authors) of 20 to 1.

Table D.1 shows the results of the uncertainty analysis for the two-phase flow experiments. For the stratified data sets, values of ΔP_{12} and ΔP_{13} were not reported. As a result, for these data sets, uncertainty intervals for ΔP_{12} and ΔP_{13} were not given.

Table D.1 Uncertainty intervals for reduced data

Test	J_{GI} (%)	J_{LI} (%)	P_s (%)	x_1 (%)	W_3/W_1 (%)	x_3/x_1 (%)	F_{BG} (%)	F_{BL} (%)	ΔP_{12} (%)	ΔP_{13} (%)
S1-1	3.1	4.4	1.0	3.1	*	*	*	*	-	-
S1-2	3.1	4.4	1.0	3.1	*	*	*	*	-	-
S1-3	3.1	4.4	1.0	3.1	5.0	***	***	5.6	-	-
S1-4	3.1	4.4	1.0	3.1	4.6	3.5	4.3	5.6	-	-
S1-5	3.1	4.4	1.0	3.1	3.4	3.3	3.4	4.7	-	-
S1-6	3.1	4.4	1.0	3.1	4.2	3.6	2.6	6.1	-	-
S1-7	3.1	4.4	1.0	3.1	4.0	3.6	2.6	5.7	-	-
S2-1	3.1	4.4	1.0	3.3	*	*	*	*	-	-
S2-2	3.1	4.4	1.0	3.3	4.2	***	***	4.9	-	-
S2-3	3.1	4.4	1.0	3.2	6.7	3.5	3.4	8.3	-	-
S2-4	3.1	4.4	1.0	3.3	4.4	3.8	2.5	5.9	-	-

Table D.1 (continued)

Test	J_{G1} (%)	J_{L1} (%)	P_s (%)	x_1 (%)	W_3/W_1 (%)	x_3/x_1 (%)	F_{BG} (%)	F_{BL} (%)	ΔP_{12} (%)	ΔP_{13} (%)
S3-1	3.1	4.4	1.0	4.1	*	*	*	*	-	-
S3-2	3.1	4.4	1.0	4.1	6.3	4.2	3.3	6.4	-	-
S3-3	3.1	4.4	1.0	4.1	7.1	***	***	7.0	-	-
S3-4	3.1	4.4	1.0	4.1	5.4	5.1	2.8	5.9	-	-
S3-5	3.1	4.4	1.0	4.1	5.3	5.0	2.7	5.7	-	-
S4-1	3.1	4.4	1.0	4.4	*	*	*	*	-	-
S4-2	3.1	4.4	1.0	4.4	2.1	***	***	2.1	-	-
S4-3	3.1	4.4	1.0	4.4	2.0	5.4	2.8	2.0	-	-
S4-4	3.1	4.4	1.0	4.4	1.9	5.4	2.7	2.0	-	-
SW-1	2.9	3.9	1.0	0.5	*	*	*	*	7.1	8.7
SW-2	2.9	3.9	1.0	0.5	4.1	0.4	4.3	****	15.2	9.9
SW-3	2.9	3.9	1.0	0.5	4.1	0.4	4.3	****	17.7	9.4
SW-4	2.9	3.9	1.0	0.5	3.1	0.4	3.2	11.7	69.2	10.2
SW-5	2.9	3.9	1.0	0.5	3.2	0.4	3.2	-	81.7	11.0
SW-6	2.9	3.9	1.0	0.5	2.7	0.4	2.8	8.3	52.1	10.8
SW-7	2.9	3.9	1.0	0.5	2.1	0.6	2.4	3.4	28.0	26.7
SW-8	2.9	3.9	1.0	0.5	2.1	0.6	2.4	3.4	27.6	28.5
W1-1	3.1	3.9	1.0	1.4	*	*	*	*	6.6	19.9
W1-2	3.1	3.9	1.0	1.5	3.8	1.4	4.2	8.9	8.9	10.9
W1-3	3.1	3.9	1.0	1.4	3.7	1.6	4.3	7.0	9.9	9.4
W1-4	3.1	3.9	1.0	1.4	2.7	1.7	3.4	4.4	28.6	13.4
W1-5	3.1	3.9	1.0	1.4	2.6	1.7	2.4	5.7	22.2	23.4
W1-6	3.1	3.9	1.0	1.4	1.1	1.7	1.5	1.7	13.5	32.2
W2-1	3.1	3.9	1.0	2.7	*	*	*	*	7.1	9.2
W2-2	3.1	3.9	1.0	2.7	7.6	***	***	10.5	7.9	8.6
W2-3	3.1	3.9	1.0	2.7	9.0	4.0	4.7	11.6	9.4	8.5
W2-4	3.1	3.9	1.0	2.7	2.4	3.5	3.9	2.8	16.6	10.3
W2-5	3.1	3.9	1.0	2.7	2.4	3.5	3.9	2.8	17.0	10.4
W2-6	3.1	3.9	1.0	2.7	1.5	3.2	2.4	1.9	35.5	30.2
W2-7	3.1	3.9	1.0	2.7	1.5	3.2	2.4	1.9	29.4	33.3
A1-1	2.6	4.4	1.0	0.1	*	*	*	*	4.6	6.1
A1-2	2.6	4.4	1.0	0.1	4.3	0.1	4.4	****	5.2	8.9
A1-3	2.6	4.4	1.0	0.1	3.7	0.1	3.8	****	5.8	19.3
A1-4	2.6	4.4	1.0	0.1	3.2	0.1	3.3	8.0	7.3	525.7
A1-5	2.6	4.4	1.0	0.1	2.4	0.2	2.5	3.8	10.1	10.5

Table D.1 (continued)

Test	J_{G1} (%)	J_{L1} (%)	P_s (%)	x_1 (%)	W_3/W_1 (%)	x_3/x_1 (%)	F_{BG} (%)	F_{BL} (%)	ΔP_{12} (%)	ΔP_{13} (%)
A2-1	3.1	4.4	1.0	0.6	**	0.6	**	**	41.1	5.3
A2-2	3.1	4.4	1.0	0.6	**	0.6	**	**	41.0	5.2
A2-3	3.1	4.4	1.0	0.5	4.7	0.7	4.7	14.8	5.7	7.9
A2-4	3.1	4.4	1.0	0.5	3.9	0.8	4.5	5.6	5.9	9.7
A2-5	3.1	4.4	1.0	0.6	3.1	0.6	3.3	9.2	7.6	47.6
A2-6	3.1	4.4	1.0	0.6	2.3	0.6	2.5	5.7	17.4	16.6
A3-1	3.3	4.4	1.0	1.7	**	1.9	**	**	8.1	5.1
A3-2	3.1	4.4	1.0	1.6	**	1.9	**	**	8.5	5.6
A3-3	3.3	4.4	1.0	1.7	0.4	1.9	*****	1.4	9.5	6.0
A3-4	3.1	4.4	1.0	1.6	5.2	2.9	4.7	10.9	6.0	10.0
A3-5	3.1	4.4	1.0	1.6	2.3	1.9	3.4	2.5	9.5	27.9
A3-6	3.1	4.4	1.0	1.6	1.7	1.9	2.5	1.9	43.7	39.9
A4-1	3.3	4.4	1.0	1.9	**	3.3	**	**	7.7	5.5
A4-2	3.4	4.4	1.0	1.9	0.3	3.3	*****	0.5	9.2	7.7
A4-3	3.4	4.4	1.0	1.9	1.7	3.3	0.1	2.5	10.2	3.8
A4-4	3.4	4.4	1.0	2.0	1.8	3.3	0.5	2.6	11.3	4.7
A4-5	3.4	4.4	1.0	1.9	3.2	3.3	3.1	4.0	12.4	137.3
A4-6	3.4	4.4	1.0	1.9	2.5	3.3	2.5	3.4	29.8	29.7
A4-7	3.4	4.4	1.0	1.9	2.5	3.3	2.5	3.4	30.0	31.4

* $W_3 = 0$
** $W_2 = 0$
*** $W_{G3} = 0$
**** $W_{L3} = 0$
***** $W_{G2} = 0$

Appendix E

NUMERICAL STUDY OF SINGLE-PHASE FLOW AND HEAT TRANSFER IN TWO-DIMENSIONAL TEE JUNCTIONS

E.1 Overview

The hydrodynamics and heat transfer of a single-phase flow in two-dimensional branching and impacting junctions were studied numerically. The flow was laminar and forced convective. It is well understood that these conditions do not apply to the experimental part of the current study. However, it was thought that the numerical study would give a helpful insight into the physics of the current problem. Even though the main focus of the current study is the impacting junctions, the branching junctions were also included in the numerical study in order to see if there are any similarities between the two types of the junctions. Later, it will be very interesting to see if these similarities, if exist, can be seen in the two-phase, three-dimensional, turbulent and isothermal flow.

E.2 Mathematical Formulation

E.2.1 Geometry and Flow Conditions

The geometry of the two tee junctions considered in this investigation is shown in Figure E.1. Fully developed flow (hydrodynamically and thermally) enters the duct through the inlet region with a mass flow rate $\dot{m}'_{in}$ (per unit depth) and a bulk temperature T_{in}. At the junction region, the flow splits such that the ratio of outlet 3 mass flow rate to the inlet mass flow rate is β. The inlet, outlet 2, and outlet 3 have lengths L_1, L_2, and L_3, respectively, and the channel height in all three sides of the junction is H. The inlet length L_1 was set to a value of 20 H in order to ensure that the

(a) Branching

(b) Impacting

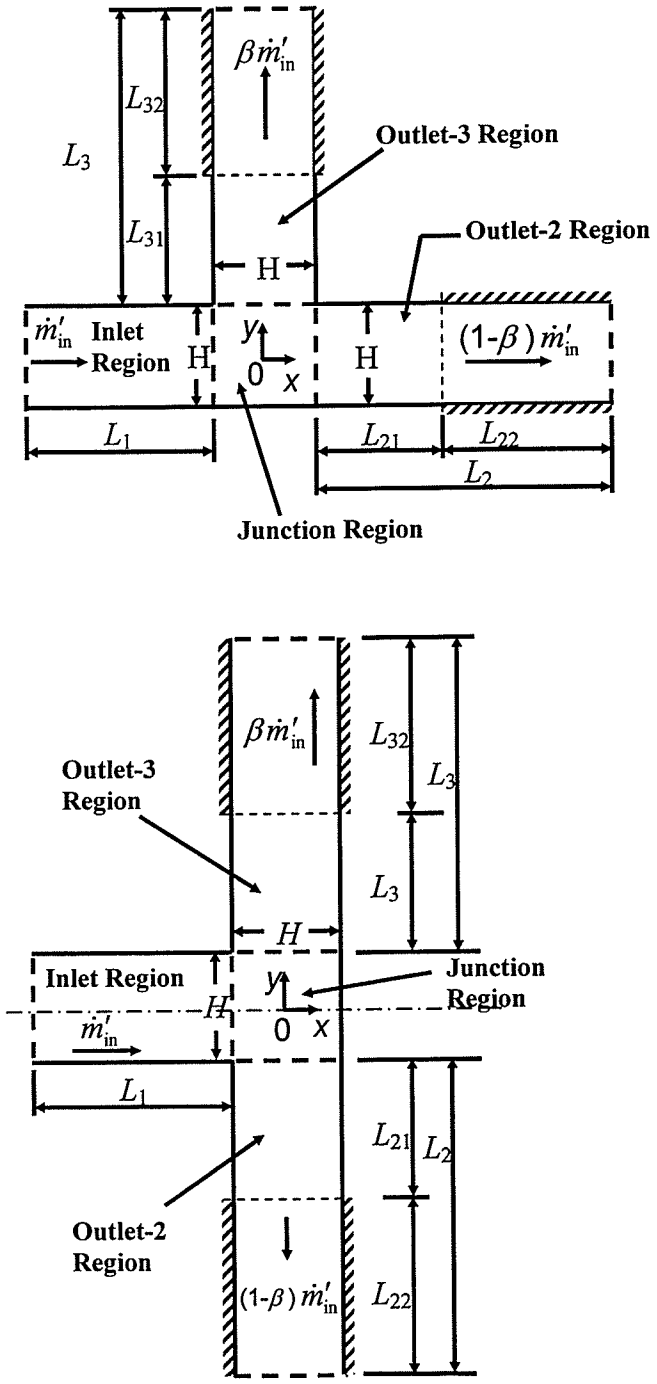

Figure E.1 Geometry and co-ordinate system

inlet flow remains fully developed over a significant length before the junction effects begin. Also, L_2 and L_3 were set to a value of 100 H in order to ensure that the flows in

outlet 2 and outlet 3 achieve fully developed conditions over a considerable length before leaving the duct.

Heat transfer takes place between the walls and the fluid throughout the inlet region, a portion of outlet 2 with length L_{21}, and a portion of outlet 3 with length L_{31}. The remaining portions of the walls in outlet 2 and outlet 3 are adiabatic. All walls in the heat-transfer section of the junction are kept at a uniform temperature T_w. The heated sections of outlet 2 and outlet 3 were selected as $L_{21}/H = L_{31}/H = 30$. These lengths were found to be sufficient (under all flow conditions considered) to achieve (or approach) thermally-fully-developed flow at the end of the heat-transfer sections in outlet 2 and outlet 3.

E.2.2 Governing Equations

The flow is considered to be two-dimensional, steady, and laminar. The fluid is incompressible and Newtonian, and the properties are assumed to be constant. Body forces and viscous dissipation are assumed to be negligible. Under these conditions, the governing continuity, momentum, and energy equations can be expressed in the following non-dimensional form:

$$\frac{\partial u^*}{\partial x^*} + \frac{\partial v^*}{\partial y^*} = 0 \tag{E.1}$$

$$u^* \frac{\partial u^*}{\partial x^*} + v^* \frac{\partial u^*}{\partial y^*} = -\frac{1}{2}\frac{\partial p^*}{\partial x^*} + \left(\frac{2}{\mathrm{Re}_1}\right)\left(\frac{\partial^2 u^*}{\partial x^{*2}} + \frac{\partial^2 u^*}{\partial y^{*2}}\right) \tag{E.2}$$

$$u^* \frac{\partial v^*}{\partial x^*} + v^* \frac{\partial v^*}{\partial y^*} = -\frac{1}{2}\frac{\partial p^*}{\partial y^*} + \left(\frac{2}{\mathrm{Re}_1}\right)\left(\frac{\partial^2 v^*}{\partial x^{*2}} + \frac{\partial^2 v^*}{\partial y^{*2}}\right) \tag{E.3}$$

$$u^* \frac{\partial T^*}{\partial x^*} + v^* \frac{\partial T^*}{\partial y^*} = \left(\frac{2}{\mathrm{Re_1 Pr}}\right)\left(\frac{\partial^2 T^*}{\partial x^{*2}} + \frac{\partial^2 T^*}{\partial y^{*2}}\right) \tag{E.4}$$

where the non-dimensional parameters are defined by

$$x^* = \frac{x}{H},\ y^* = \frac{y}{H},\ L^* = \frac{L}{H}, \tag{E.5a}$$

$$u^* = \frac{u}{V_1},\ v^* = \frac{v}{V_1},\ p^* = \frac{p}{(\rho V_1^2)/2},\ T^* = \frac{T - T_{\mathrm{in}}}{T_{\mathrm{w}} - T_{\mathrm{in}}}, \tag{E.5b}$$

$$\mathrm{Re_1} = \frac{2HV_1}{\nu} \text{ and } \mathrm{Pr} = \frac{\rho \nu c_p}{k} \tag{E.5c}$$

where V_1 is the mean inlet velocity given by

$$V_1 = \frac{\dot{m}'_{\mathrm{in}}}{\rho H} \tag{E.5d}$$

E.2.3 Boundary Conditions

The applicable boundary conditions are as follows:

1- Inlet Face: At $x^* = -(L_1^* + 0.5)$ and $-0.5 \le y^* \le 0.5$, $u^* = 1.5(1 - 4y^{*2})$, $v^* = 0$, and a fully developed temperature profile corresponding to a dimensionless bulk temperature $T_{\mathrm{in}}^* = 0$ were imposed.

2- Walls: $u^* = v^* = 0$ on all walls, $T^* = 1$ on the heated walls, and $\partial T^*/\partial n^* = 0$ on the adiabatic walls, where n is the direction normal to the walls.

3- Outlet 2 Face: A reference pressure, $p = 0$ (or $p^* = 0$), was specified at a single node on the outlet face, and $\partial T^*/\partial n^* = 0$, where n is the direction normal to the face.

4- Outlet 3 Face: At $-0.5 \le x^* \le 0.5$ and $y^* = (L_3^* + 0.5)$, a total mass flow rate of β $\dot{m}'_{\mathrm{in}}$ was specified, and $\partial T^*/\partial y^* = 0$.

The mathematical formulation of the problem consisting of the governing equations and boundary conditions suggests that the velocity, pressure, and temperature fields (u^*, v^*, p^*, and T^*) at any point (x^*, y^*) within the flow domain are functions of the following set of independent parameters:

- The geometry parameters $L_1^*, L_2^*, L_3^*, L_{21}^*$, and L_{31}^*.
- The flow parameters Re_1 and β.
- The property parameter Pr.

All the present results correspond to $L_1^* = 20$, $L_2^* = L_3^* = 100$, $L_{21}^* = L_{31}^* = 30$, and Pr = 0.7. Therefore, the only remaining independent parameters are Re_1 and β.

The velocity and temperature fields were used in calculating some parameters of engineering importance. These are the local (dimensionless) wall shear stress τ_w^*, the local (dimensionless) wall heat flux q_w^*, and the total (dimensionless) heat transfer rate Q^*. The parameter τ_w^* is defined as

$$\tau_w^* = \frac{\tau_w}{(\rho\, u_{m1}^2)/2}, \tag{E.6}$$

where τ_w is the local wall shear stress. In dimensionless form,

$$\tau_w^* = \left(\frac{4}{\mathrm{Re}_1}\right)\left.\frac{\partial u^*}{\partial n^*}\right|_{\text{wall}}, \tag{E.7}$$

where n^* is the dimensionless coordinate normal to the wall. The local wall heat flux is given by

$$q_w^* = \frac{q_w}{k(T_w - T_{in})/(2H)}, \tag{E.8}$$

where q_w is the local wall heat flux, $q_w = -k\,(\partial T / \partial n)_w$. The parameter Q^* is defined by

$$Q^* = \frac{Q}{A_w\, k (T_w - T_{in})/2H} = \left(\frac{1}{A_w}\right) \int_0^{A_w} q_w^*\, dA \qquad \text{(E.9)}$$

where Q is the overall rate of heat transfer from the junction and A_w is the total surface area of the heated sections in the whole domain.

E.3 Numerical Solution

The numerical solution of the governing equations was obtained using CFX-TASCflow, version 2.10. This code uses a finite volume method (Patankar, 1980) but is based on a finite element approach of representing the geometry. Mass conservation discretization was applied on a non-staggered grid. The discretized mass, momentum, and energy equations were solved iteratively using multi-grid additive correction to accelerate convergence. The solution was considered converged when the sum of residuals was less than 1×10^{-5}. More details can be found in (El-Shaboury et al., 2002 and 2003).

E.3.1 Computational Mesh

Four different grid blocks were created for the inlet, junction, outlet 2, and outlet 3 regions of each tee junction. The grid blocks in the outlet 2 and outlet 3 regions were each divided into two sub-blocks; the first one was for the heated section and the second was for the adiabatic section. Each sub-block had uniform grid spacing in itself; however, the two sub-blocks had different grid spacing when compared to each other. The computational grid for the whole flow domain was then formed by attaching the four grid blocks together. It was decided to use the finest possible grid spacing in the

junction region to account for the steep gradients in the solution field expected in this area. Mesh-independence tests were carried out for both types of junction by varying the number of nodes in the inlet, junction, outlet 2, and outlet 3 regions, separately. Table E.1 provides a detailed description of the grids used in the mesh independence tests for the impacting junction (similar grids were used for the branching junction). The tests were carried out for two conditions: $\beta = 0.1$ and 0.9; both with $Re_1 = 2000$ and $Pr = 0.7$.

Table E.1 Details of grids used in mesh-independence tests

	Inlet Region		Junction Region		Outlet 2 Region				Outlet 3 Region			
					Heated Section		Adiabatic Section		Heated Section		Adiabatic Section	
	nx	*ny*	*nx*	*ny*	*nx*	*ny*	*nx*	*ny*	*nx*	*ny*	*nx*	*ny*
Grid 1	40	30	30	30	30	200	30	85	30	200	30	85
Grid 2	70	60	60	60	60	400	30	170	60	400	30	170
Grid 3	100	91	91	91	91	600	31	250	91	600	31	250
Grid 4	200	121	121	121	121	800	41	350	121	800	41	350

A representative sample of the grid-independence tests is shown in Figure E.2 corresponding to $\beta = 0.1$ in an impacting junction. The results in Figure E.2 are in terms of τ_w^* and q_w^* along $x^* = 0.5$. Figure E.2(a) shows that the values of τ_w^* from grids 3 and 4 are nearly identical. On the other hand, Figure E.2(b) shows that there is a noticeable (percentage) difference in the values of q_w^* from grids 3 and 4, mainly in the region $2 \leq y^* \leq 8$. However, it can be argued that the deviation between grids 3 and 4 is small in absolute terms. Similar results were obtained for $\beta = 0.9$.

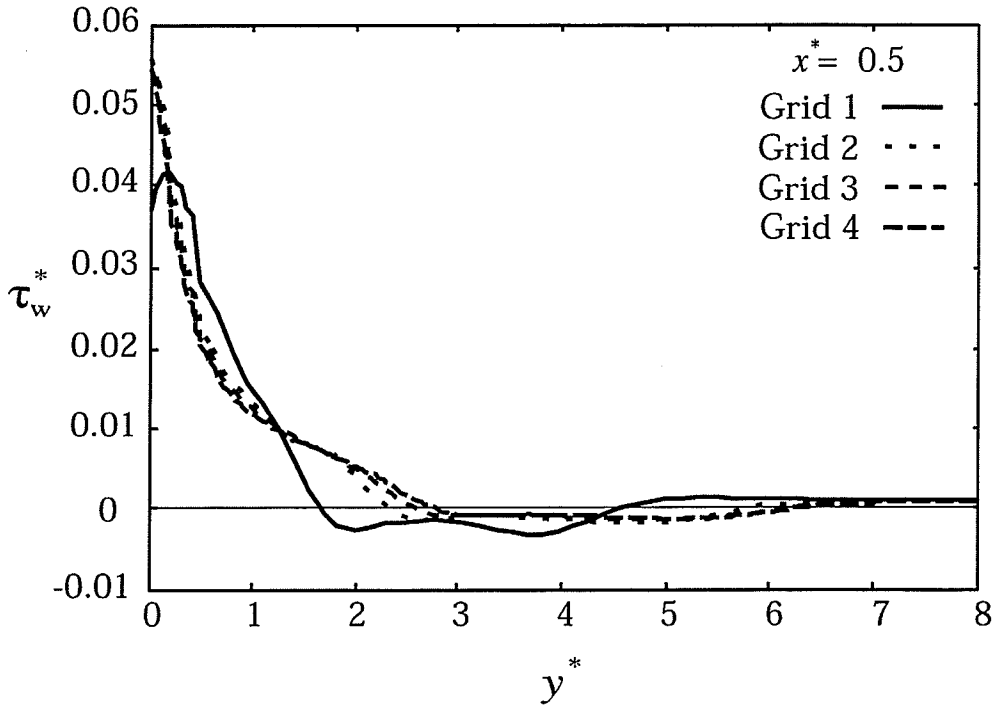

(a) Wall Shear Stress

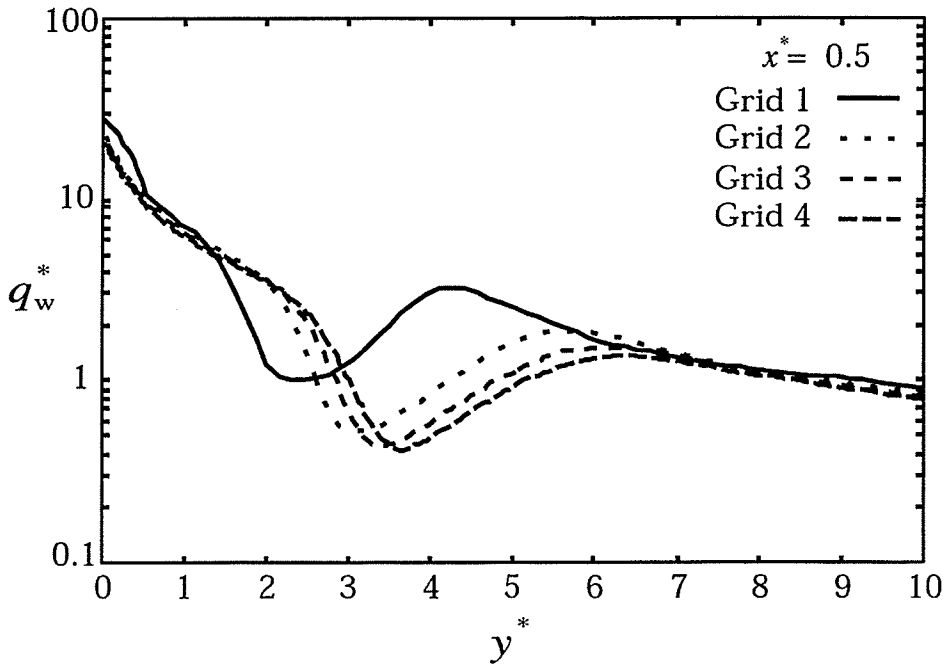

(b) Wall Heat Flux

Figure E.2 Sample of grid independence tests
(impacting junction with $\beta = 0.1$, Pr = 0.7 and $Re_1 = 2000$)

Based on the above results and other grid-independence tests (not shown), the final mesh for the present investigation was selected to be grid 3. A typical execution time using the final mesh was about 110 CPU hours on a DEC/Compaq Alphastation 500 au.

E.3.2 Comparison With Earlier Work

Several comparisons were made with earlier work in order to validate the numerical method used in the present investigation. Two comparisons are shown here as a sample; one for the branching and the other for the impacting junction. Figure E.3 shows a comparison between the computed velocity profiles and the experimental velocity profiles reported by Liepsch et al. (1982) for a branching junction at $Re_1 = 558$ and $\beta = 0.44$. These results correspond to water flow in a junction with the following geometry: $L_1^* = 109.5$, $L_2^* = 94.5$, and $L_3^* = 81$. The agreement between the numerical and experimental results is good at the various locations shown. Direct validation for the impacting junction was not possible due to lack of similar results. The closest match to the present conditions is the experimental measurements of the laminar velocity profiles in outlet 3 of an impacting junction constructed from tubes with circular cross-sections, reported by Kreid et al. (1975). The results of Kreid et al. correspond to water flow, an inside diameter of 9.5 mm on all sides of the junction, $V_1 = 0.0387$ m·s^{-1}, and $\beta = 0.0614$. Results were generated for the present (two-dimensional) geometry using water properties, $H = 9.5$ mm, and the same values of V_1 and β used in Kreid et al. It is recognized that quantitative agreement between the two sets of results is not expected due to the difference in geometry. Figure E.4 shows a comparison between the present profiles of $u/u_{cl,fd}$ and the measured profiles reported in Kreid et al. along outlet 3, where $u_{cl,fd}$ is the fully developed value of the centreline velocity in outlet 3. There is a

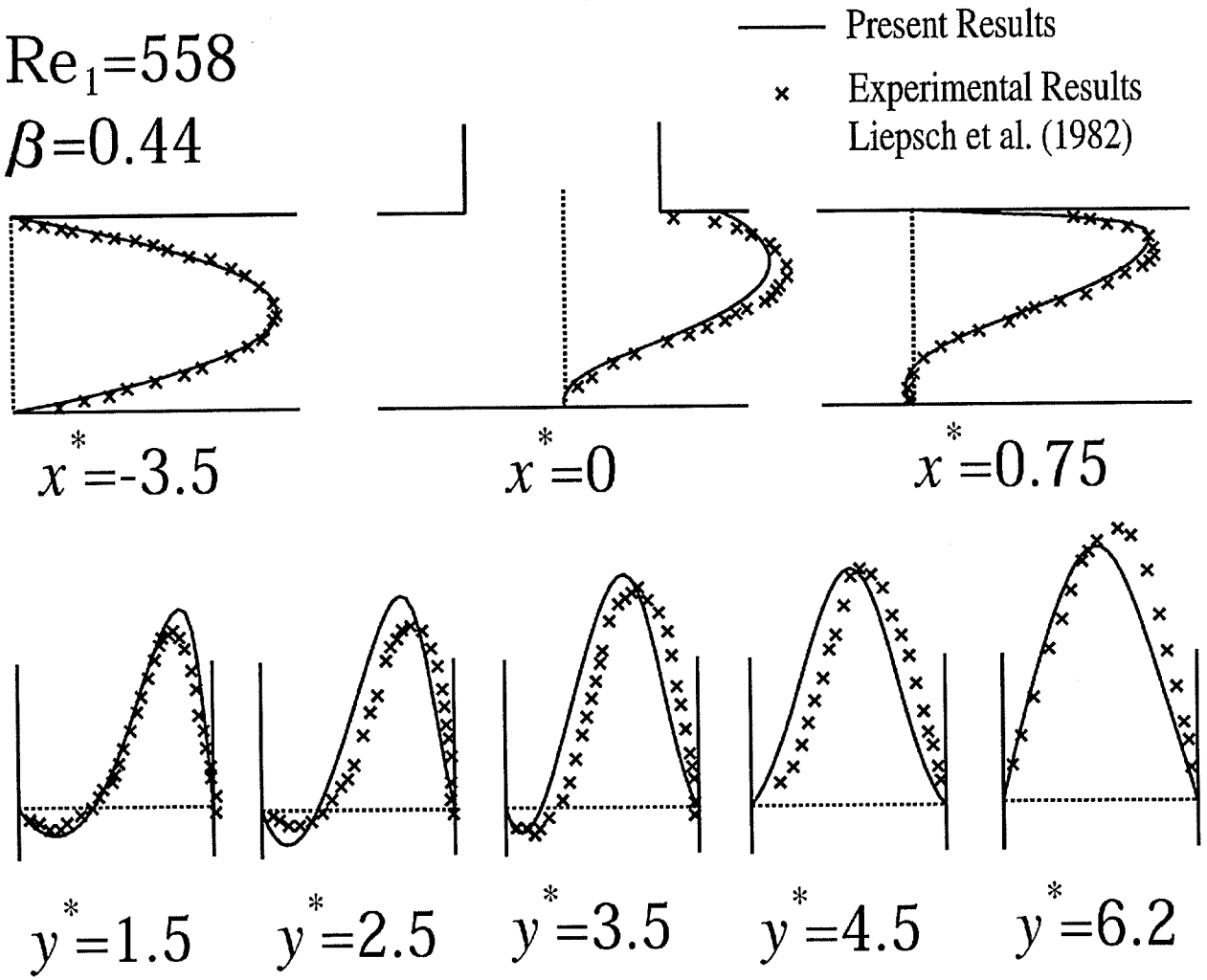

Figure E.3 Comparison with the experimental results of Liepsch et al. (1982)

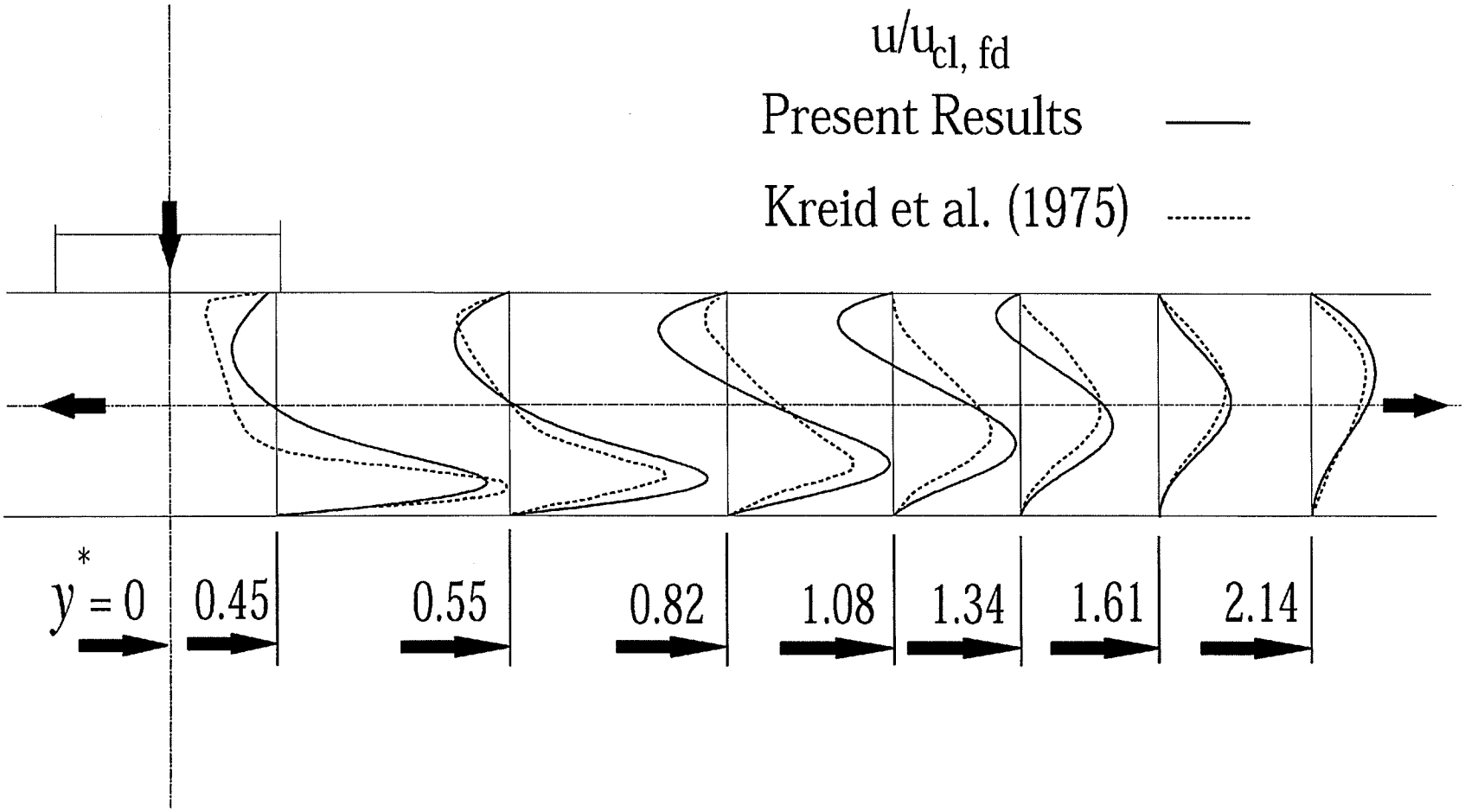

Figure E.4 Comparison with the experimental results of Kreid et al. (1975)

definite similarity in trend between the two sets of profiles. A re-circulation zone can be seen in the top part of outlet 3 in both cases. The extent of this zone in the y direction is longer for the planar junction. As well, a jetting zone exists underneath the re-circulation zone in both cases.

E.4 Results And Discussion

Results were obtained for both flow configurations corresponding to $0.1 \leq \beta \leq 0.9$, and $Re_1 = 1000$ and 2000. This allowed us to investigate the effects of Re_1 and β on the hydrodynamic and thermal characteristics. The focus here will be on the impacting tee junctions. Representative samples of the branching junction results will be also shown. These samples were chosen to show the similarity (or lack of it) between both flow configurations.

E.4.1 Wall Shear Stress

Figure E.5(a) shows the variation of τ_w^* along the wall $y^* = 0.5$ for $Re_1 = 2000$ and $0.1 \leq \beta \leq 0.9$. Fully developed flow enters the duct and the value of τ_w^* remains unchanged over a considerable portion of the inlet region. For $\beta = 0.1$ and 0.3, as the junction region is approached, the value of τ_w^* decreases until it becomes negative, indicating that a re-circulation zone is formed. As will be seen later, this re-circulation zone formed on the wall at $y^* = 0.5$ is actually a tiny part of a bigger re-circulation zone formed in outlet 3 on the wall $x^* = -0.5$. For $\beta = 0.5$, the value of τ_w^* remains almost unchanged in the inlet region. However, for $\beta \geq 0.7$, the value of τ_w^* increases rapidly upstream of the junction region indicating flow acceleration near the wall $y^* = 0.5$ for these values of β.

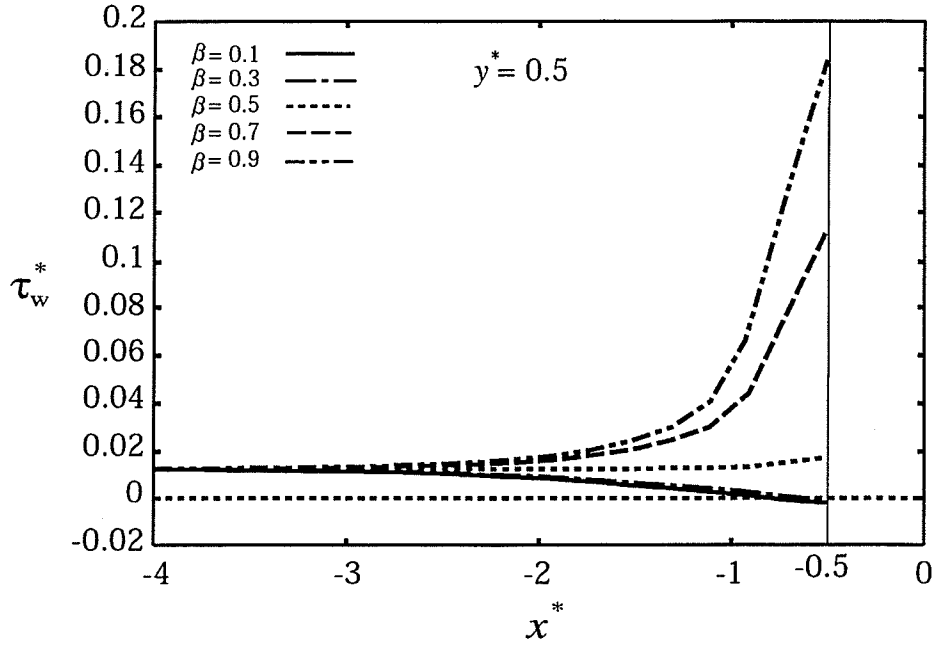

(a) Effect of β at Re_1 = 2000

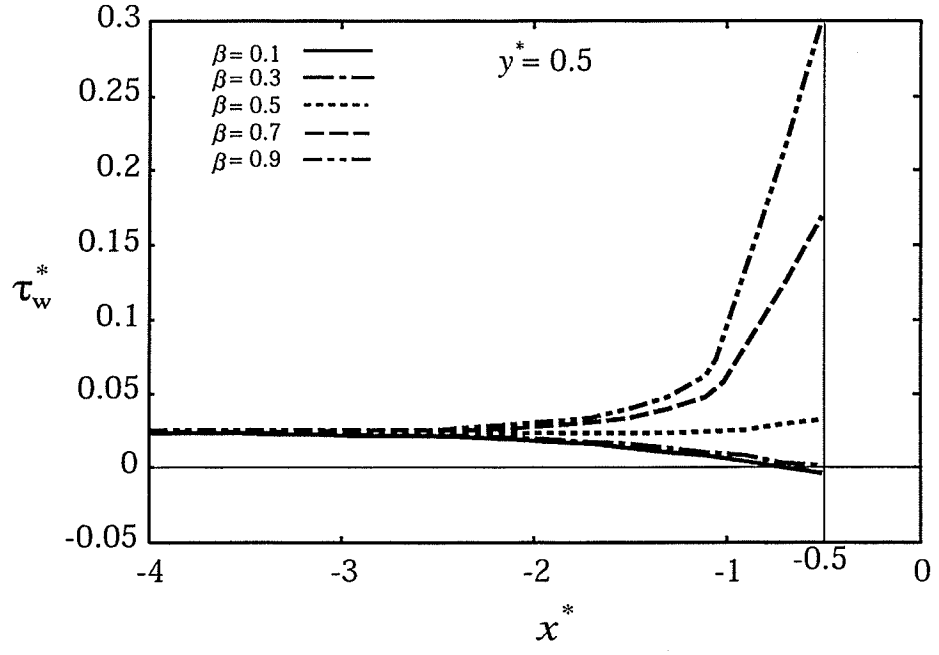

(b) Effect of β at Re_1 = 1000

Figure E.5 Distribution of τ_w^* along $y^* = 0.5$

The distribution of τ_w^* along $y^* = 0.5$ at $Re_1 = 1000$, shown in Figure E.5(b), is similar in trend to that shown in Figure E.5(a) for $Re_1 = 2000$. For all values of β, τ_w^* increases at all locations as Re_1 decreases. It should be pointed out that τ_w actually decreases with decreasing Re_1 and the increase in τ_w^* is only due to its definition. Also, the probability of re-circulation decreases as Re_1 decreases. For example, the small re-circulation zone that appeared at $\beta = 0.3$ for $Re_1 = 2000$, disappeared at $Re_1 = 1000$. Figure E.5(b) shows that re-circulation exists only at $\beta = 0.1$.

Figure E.6(a) shows the variation of τ_w^* along the wall $x^* = 0.5$ for $Re_1 = 2000$ and $0.1 \leq \beta \leq 0.9$. A re-circulation zone forms on this wall for $\beta = 0.1$, 0.3, and 0.9. This re-circulation zone will be referred to as re-circulation zone A. The size and location of re-circulation zone A depend on β with the maximum size occurring at $\beta = 0.9$, while the closest location to the junction region occurring at $\beta = 0.1$. For $\beta = 0.5$, the value of τ_w^* starts from zero at $y^* = 0$, increases to a maximum near $y^* = 0.5$, and drops gradually towards the fully developed value. Re-circulation zone A does not form at this value of β corresponding to even mass split; it is more likely to occur when the mass split is uneven. The negative values of τ_w^* close to the junction centreline for $\beta = 0.7$ and 0.9 are not due to the presence of a re-circulation zone. These negative values occur because the flow near the wall $x^* = 0.5$ is in the negative y^* direction, as will be seen later from plots of the streamlines.

In terms of trend, the variation of τ_w^* with β at $Re_1 = 1000$ was found to be similar to that shown in Figure E.6(a) for $Re_1 = 2000$. However, for $Re_1 = 1000$, re-circulation zone A was found to decrease in size for all β, and in some cases, disappear all together

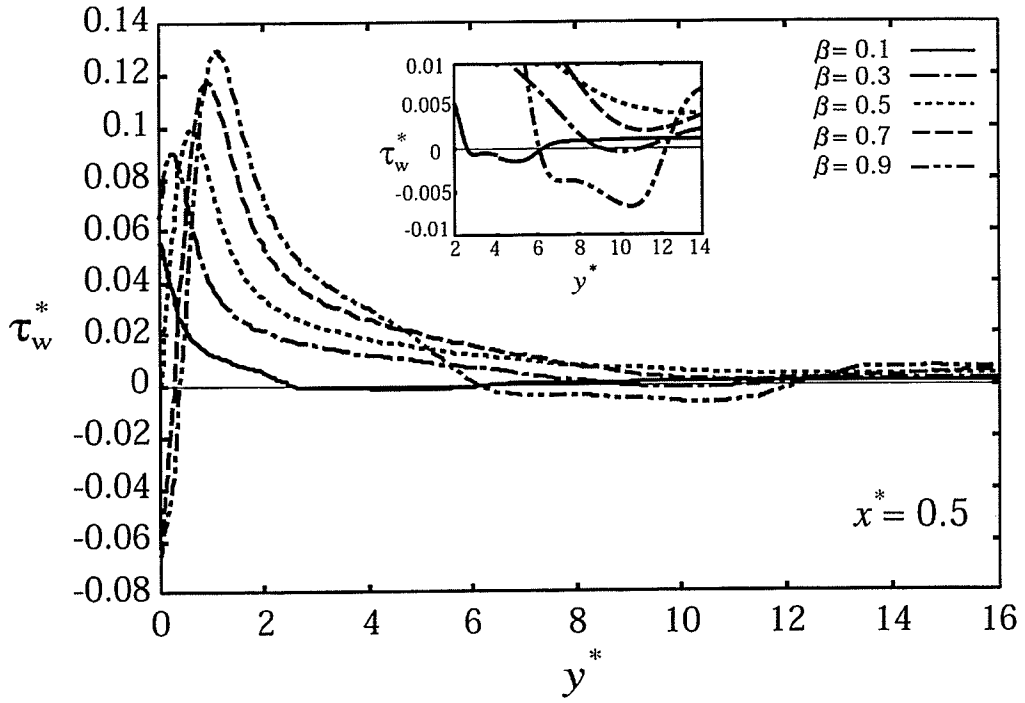

(a) Effect of β at $Re_1 = 2000$

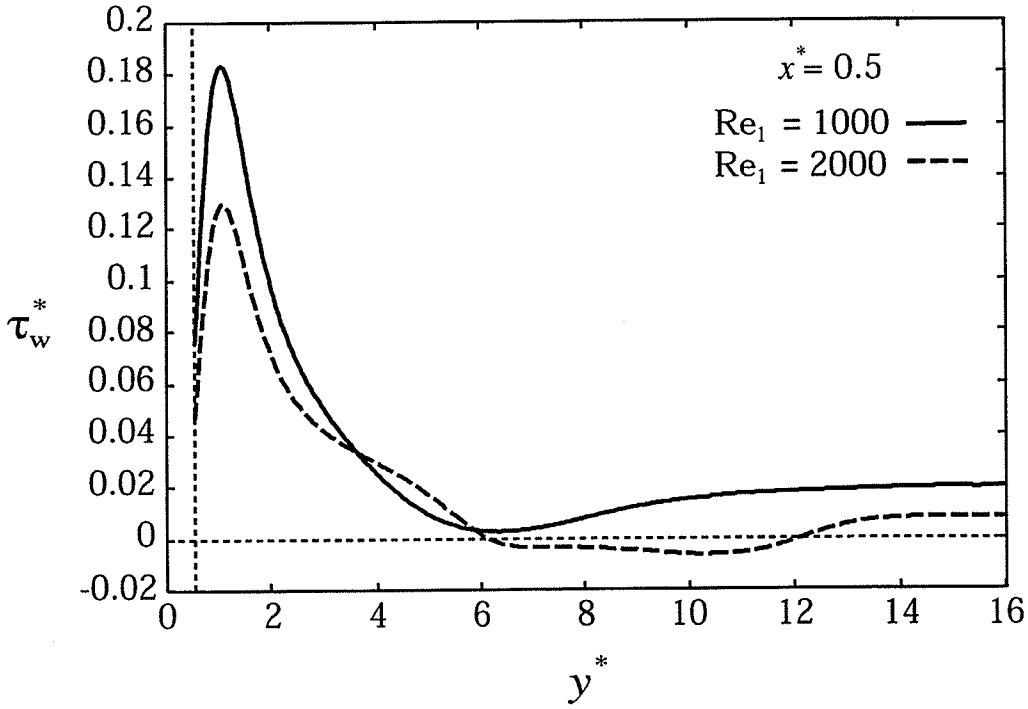

(b) Effect of Re_1 at $\beta = 0.9$

Figure E.6 Distribution of τ_w^* along $x^* = 0.5$

For example, Figure E.6(b) shows that this re-circulation zone does not form at $\beta = 0.9$. At $Re_1 = 1000$, re-circulation zone A was found to exist only at $\beta = 0.1$ and 0.2.

Figure E.7(a) shows the variation of τ_w^* along the wall $x^* = -0.5$ in outlet region-3 for $Re_1 = 2000$ and $0.1 \leq \beta \leq 0.9$. These results show that a re-circulation zone forms on this wall for all values of β. This re-circulation zone will be referred to as re-circulation zone B. For all value of β, the separation point of re-circulation zone B occurs at approximately $y^* = 0.5$. The minimum size of re-circulation zone B occurs at $\beta = 0.1$, while the maximum size occurs at $\beta = 0.5$. Downstream of re-circulation zone B for $\beta =$ 0.1 and 0.9, Figure E.7(a) shows that τ_w^* increases sharply to a peak and then decreases to a small positive value. The decrease in τ_w^* suggests that the flow has a tendency to separate from the wall; however, separation does not occur. This behaviour is attributed to the formation of re-circulation zone A for $\beta = 0.1$ and 0.9. The location of the positive peak in τ_w^* nearly coincides with the location of the maximum width of re-circulation zone A, and the location at which the flow tends to separate nearly coincides with the location of the reattachment point of re-circulation zone A.

Decreasing Re_1 had the effect of decreasing the size of re-circulation zone B, as illustrated in Figure E.7(b) for $\beta = 0.9$. As well, for the case of $Re_1 = 1000$, the maximum size of re-circulation zone B occurred at $\beta = 0.7$. Figure E.7(b) also shows that the tendency of the flow to separate again from the wall $x^* = -0.5$ downstream of re-circulation zone B was eliminated at $Re_1 = 1000$. This is attributed to the disappearance of re-circulation zone A at these conditions.

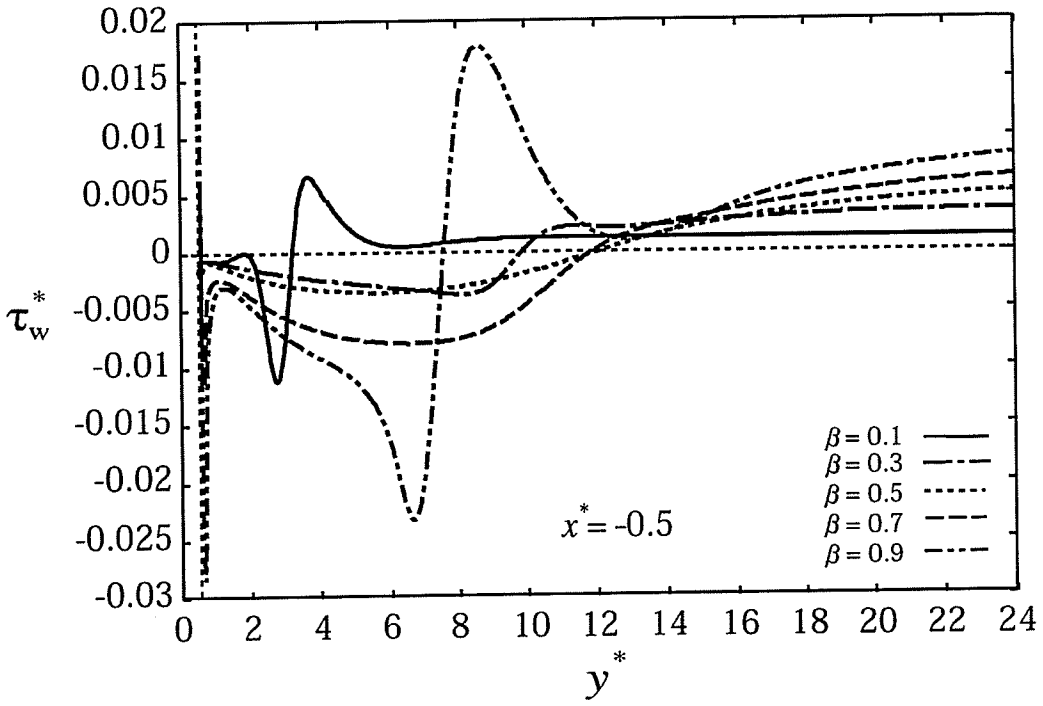

(a) Effect of β at $Re_1 = 2000$

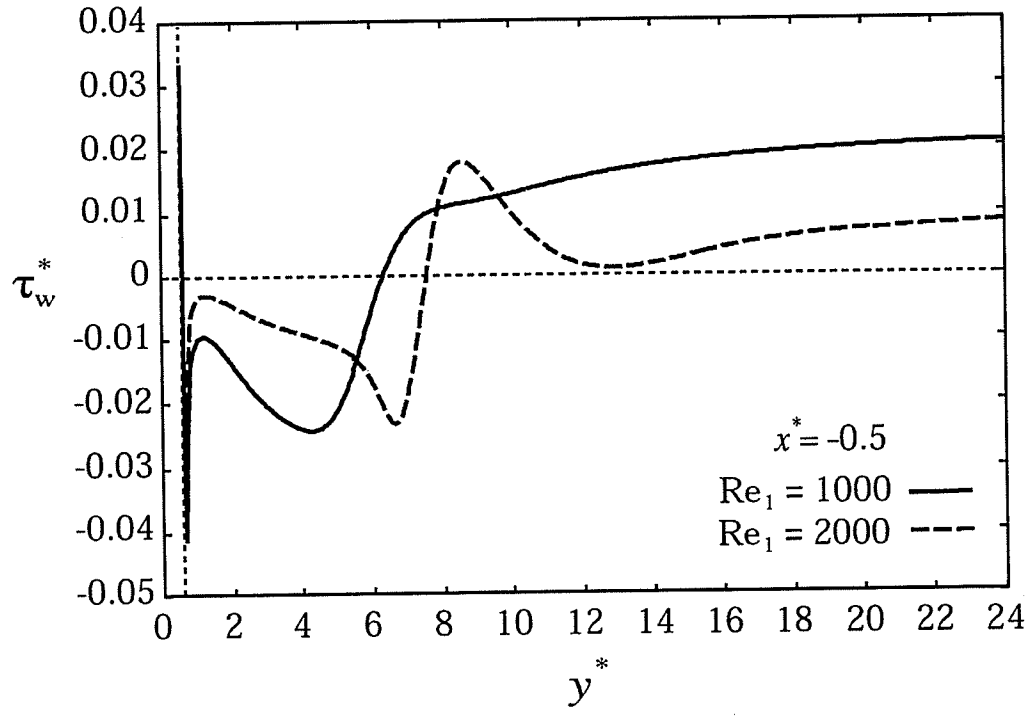

(b) Effect of Re_1 at $\beta = 0.9$

Figure E.7 Distribution of τ_w^* along $x^* = -0.5$

Figure E.8 shows the variation of τ_w^* in outlet 3 of both configurations along $x^* = 0.5$ for $Re_1 = 2000$, and $\beta = 0.1$ and 0.9. It can be seen that for $\beta = 0.9$, the distribution of τ_w^* is almost identical for the two types of junctions. For $\beta = 0.1$, there is a small difference in the results in the range of $0 \le y^* \le 3$. Also, the size and the location of the re-circulation zones (where τ_w^* becomes negative) are almost identical for both junctions. Figure E.9 shows the variation of τ_w^* on the other wall of outlet 3 ($x^* = -0.5$) with similar trends to those seen in Figure E.8. These same trends were also found to be valid at both walls of outlet 3 for $Re_1 = 1000$. This similarity in τ_w^*-distribution is very interesting in view of the significantly different flow configuration between the two junctions.

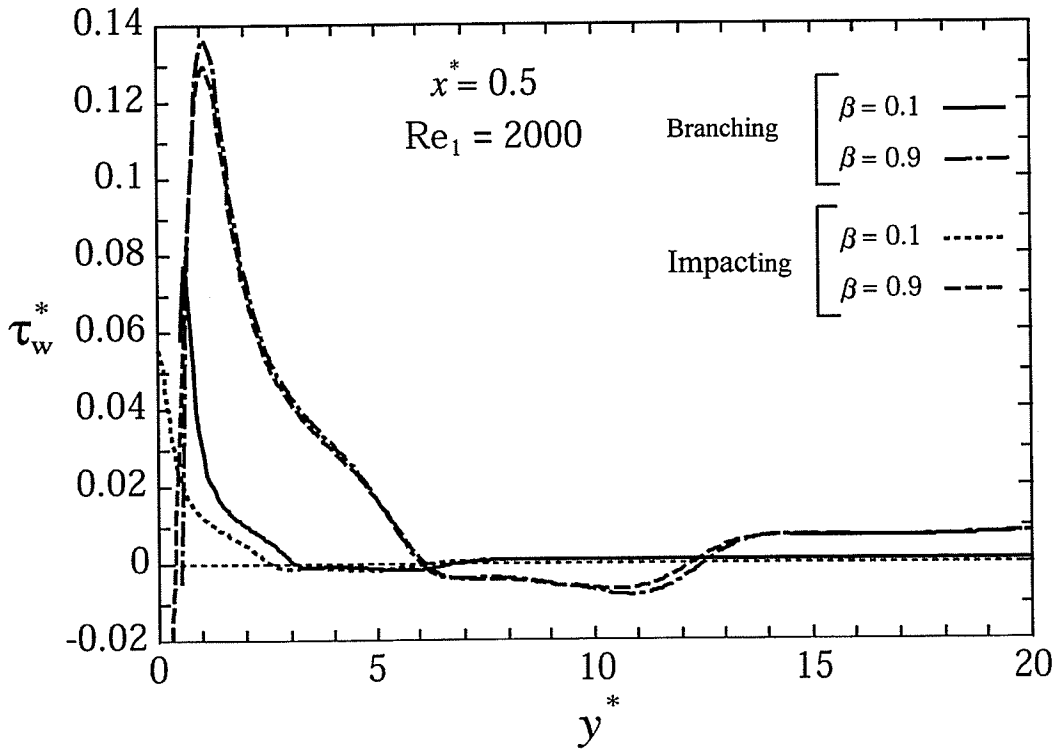

Figure E.8 Wall shear stress in outlet 3, $x^* = 0.5$

For mass splits between $\beta = 0.1$ and $\beta = 0.9$, the similarity in wall shear stress illustrated in Figures E.8 and E.9 disappeared and significant differences in magnitude and trend were found in τ_w^* between the two junctions.

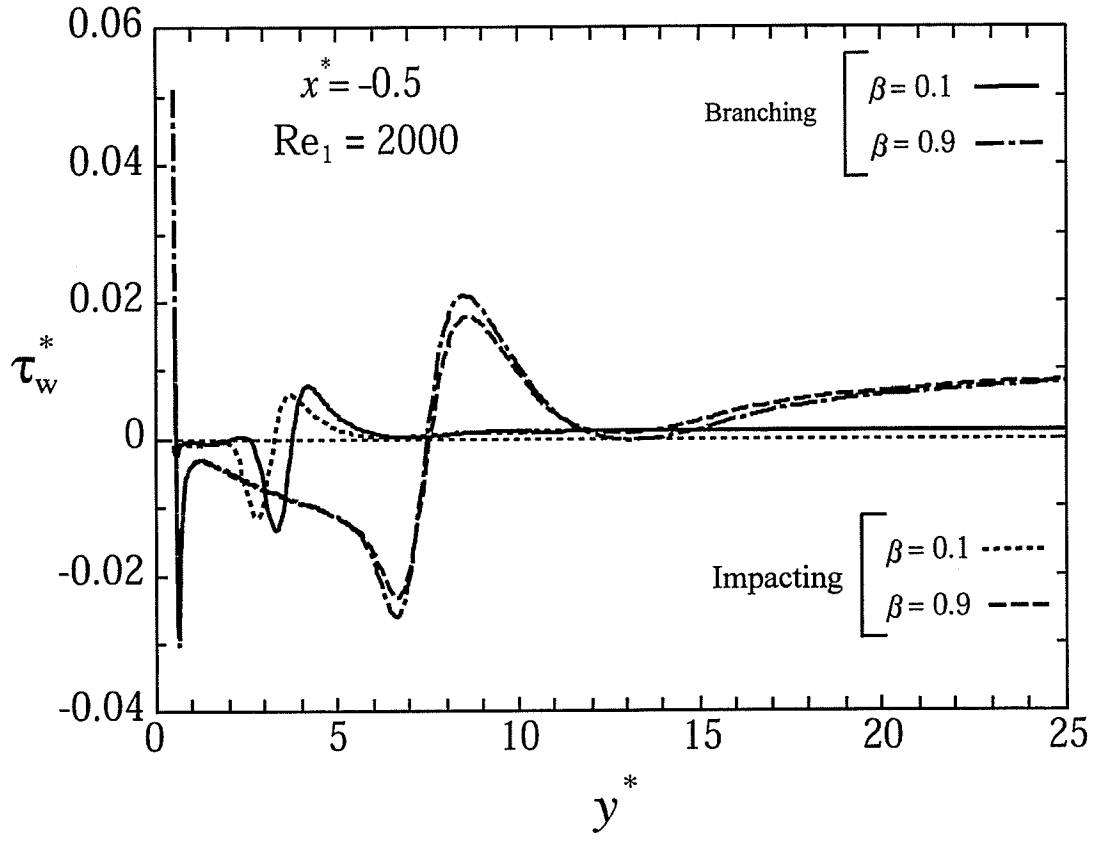

Figure E.9 Wall shear stress in outlet 3, $x^* = -0.5$

Figure E.10 shows the variation of τ_w^* along one of the walls of outlet 2 for $Re_1 = 2000$, and $\beta = 0.7$ and 0.9. It can be seen that there is similarity in trend between the two junctions. In terms of magnitudes, there are small deviations only in the range $0 \leq y^* \leq 3$. These exact trends were also found to be valid along the other wall of outlet 2 at the same values of β.

All the above observations (regarding the similarity -or lack of it- between the two types of junctions) made for $Re_1 = 2000$ were also found to be valid for $Re_1 = 1000$.

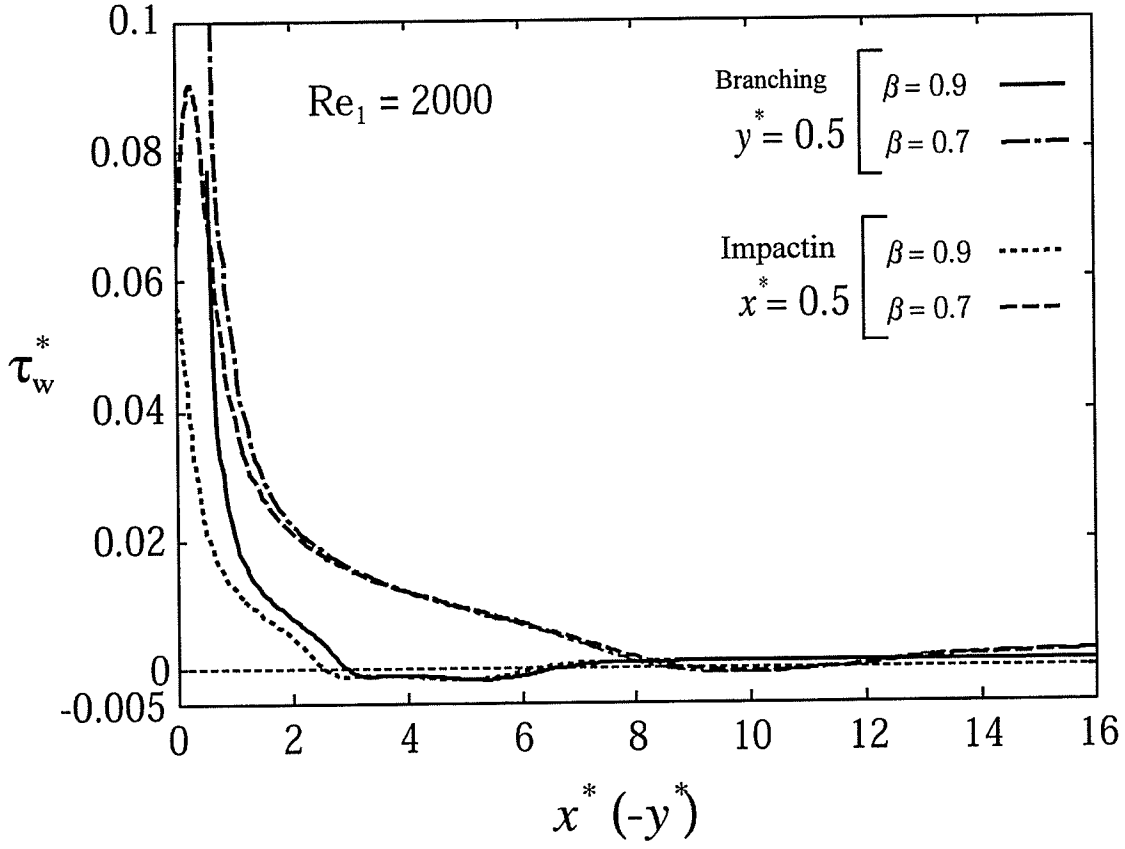

Figure E.10 Wall shear stress along one wall in outlet 2

E.4.2 Streamlines

For two-dimensional steady flow of an incompressible fluid, the stream function ψ is defined by

$$u = \frac{\partial \psi}{\partial y} \quad \text{and} \quad v = -\frac{\partial \psi}{\partial x} \tag{E.10}$$

Using the already computed velocity field, values of ψ were determined based on Equation (E.10) and the streamlines (lines of constant ψ) were plotted. A sample of

these results is shown in Figures E.11 and E.12. Values of ψ on the different walls of the junction are shown in Figure E.11(a) and arbitrary steps ($\Delta\psi$) were used between different streamlines in order to illustrate the main features of the flow field.

Figures E.11(a), (b), and (c) show the streamlines in an impacting tee junction for $Re_1 = 1000$ and $\beta = 0.5$, 0.8, and 0.9, respectively. Figure E.11(a) shows the symmetry of the streamlines around the junction centreline for the case of even mass split. Re-circulation zone B forming on the wall $x^* = -0.5$ can also be seen in the figure. Figure E.11(b) shows the streamlines for an 80/20 mass split. In the outlet carrying 80% of the inlet mass, re-circulation zone B forms on the wall $x^* = -0.5$, while re-circulation zone A does not appear. In the outlet carrying 20% of the inlet mass, a small re-circulation zone A appears as well as re-circulation zone B. It should also be noted that the separation point of re-circulation zone B exists near the end of the inlet region for the 20% outlet, while for the 80% outlet, this point is located on the outlet wall. Similar trends can be seen in Figure E.11(c) for the 90/10 mass split. All these results are consistent with the τ_w^*-results presented earlier.

Figure E.12 shows the streamlines in an impacting tee junction for $Re_1 = 2000$ and $\beta = 0.9$. These results, along with those in Figure E.11(c), demonstrate the effect of Re_1. Re-circulation zones A and B appear in both outlets for $Re_1 = 2000$. The size of re-circulation zone A in the 10% mass outlet increases as Re_1 increases. Also, the length required for the flow to reach full development in both outlets increases as Re_1 increases. Again, all these results are consistent with the τ_w^*-results presented earlier.

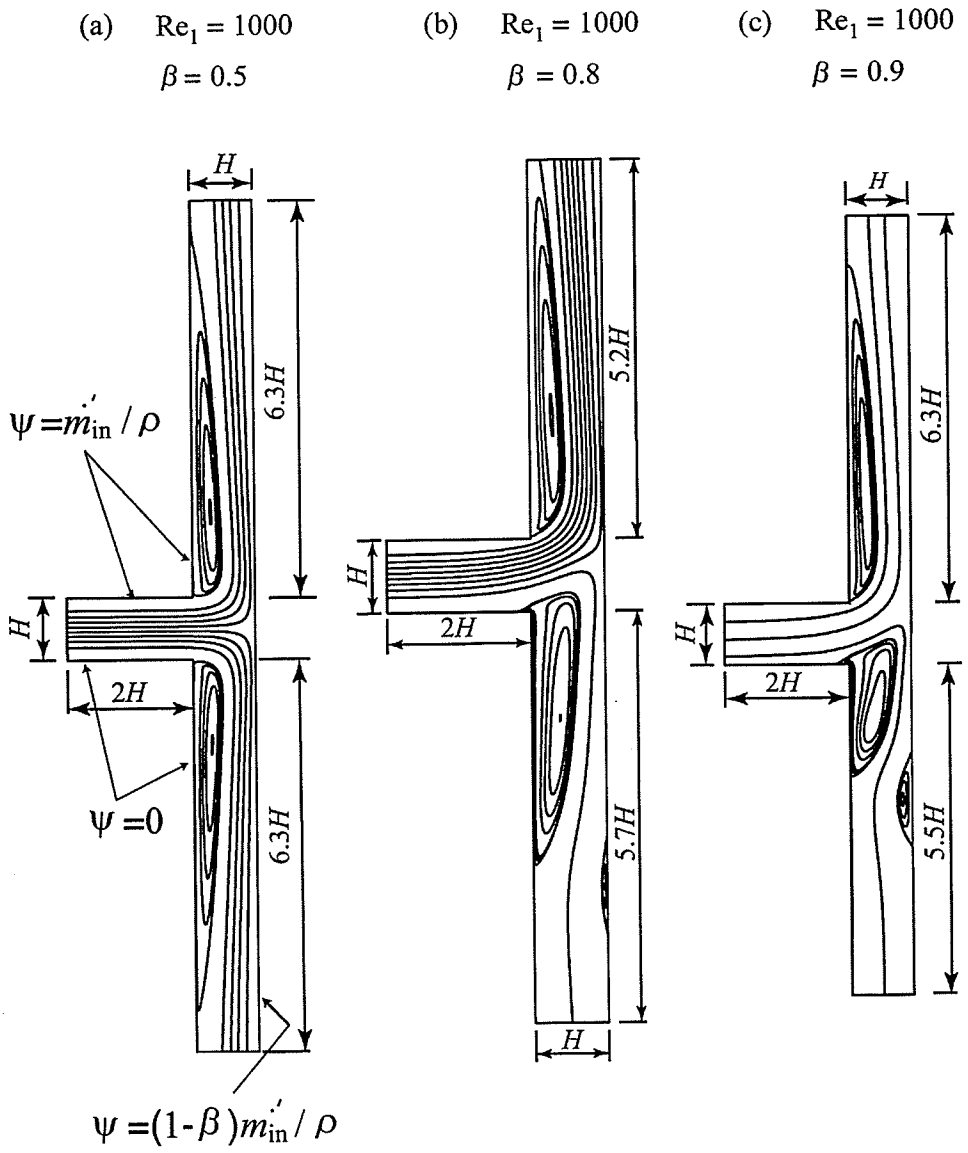

Figure E.11 Streamlines for $Re_1 = 1000$ and different β

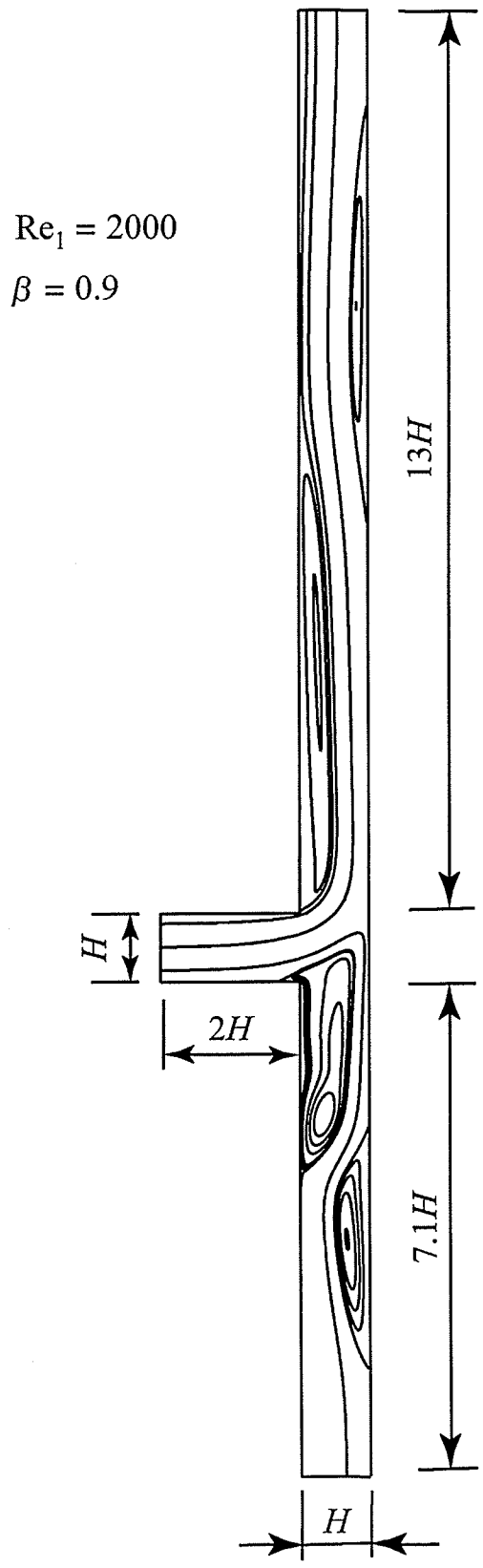

Figure E.12 Streamlines for $Re_1 = 2000$ and $\beta = 0.9$ in impacting tee junctions

Figure E.13 shows the streamlines in both configurations for the case of Re_1 = 2000 and $\beta = 0.9$. Surprisingly, the streamlines in both outlets are similar for the two types of the junctions. The size and the location of the four re-circulation zones formed on the walls are almost identical. The above observations are consistent with the results in Figures E.8, E.9, and E.10, where values of τ_w^* are almost identical on all the walls of the junction for the case of $\beta = 0.9$.

Figure E.14 shows the streamlines in both configurations for the case of Re_1 = 2000 and $\beta = 0.1$. It can be seen that the streamlines are similar only in outlet 3, which carries 10 % of the inlet mass flow rate. In the other outlet, the streamlines are completely different in shape. The above observations are consistent with the results in Figures E.8 and E.9, where values of τ_w^* in outlet 3 are very similar for the case of β = 0.1. These observations are also consistent with Figure E.10, where values of τ_w^* in outlet 2 were found to be similar only for high values of β.

E.4.3 Pumping Power

The pumping power E is defined as the rate of mechanical energy loss due to mass split at the junction. The value of E can be determined by applying an energy balance on a control volume surrounding the junction region (excluding the three arms of the junction). Accordingly, for both flow configurations, the value of E is given by,

$$E = \dot{m}'_{in}\left[\frac{P_1}{\rho} + \frac{V_1^2}{2}\right] - \dot{m}'_{in}(1-\beta)\left[\frac{P_2}{\rho} + \frac{V_2^2}{2}\right] - \dot{m}'_{in}\beta\left[\frac{P_3}{\rho} + \frac{V_3^2}{2}\right] \qquad \text{(E.11)}$$

where P_1, P_2, and P_3 are the average pressures at sides 1, 2, and 3 of the junction extrapolated from the fully developed regions of the inlet, outlet 2, and outlet 3 regions.

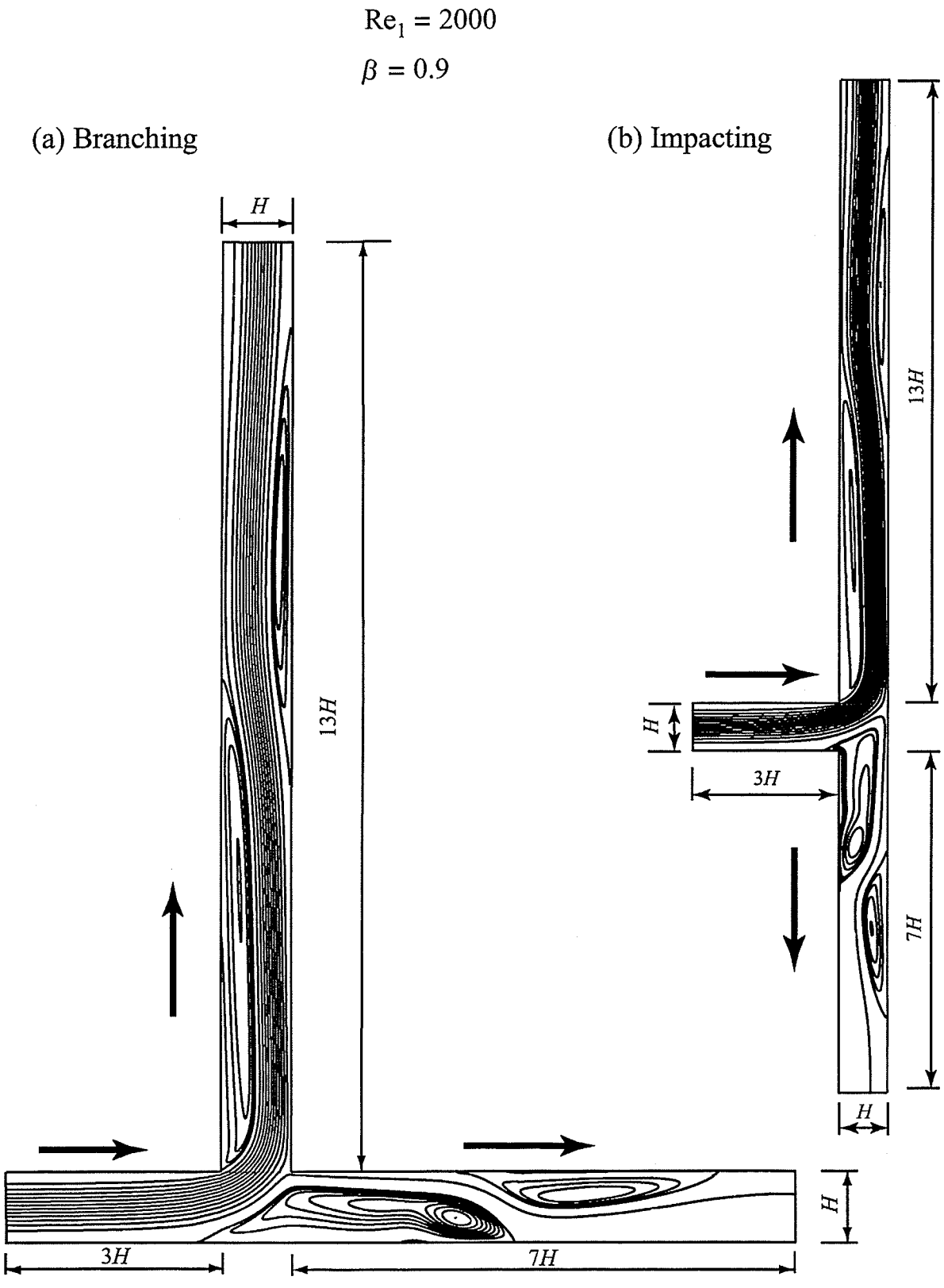

Figure E.13 Streamlines for $Re_1 = 2000$ and $\beta = 0.9$ in both configurations

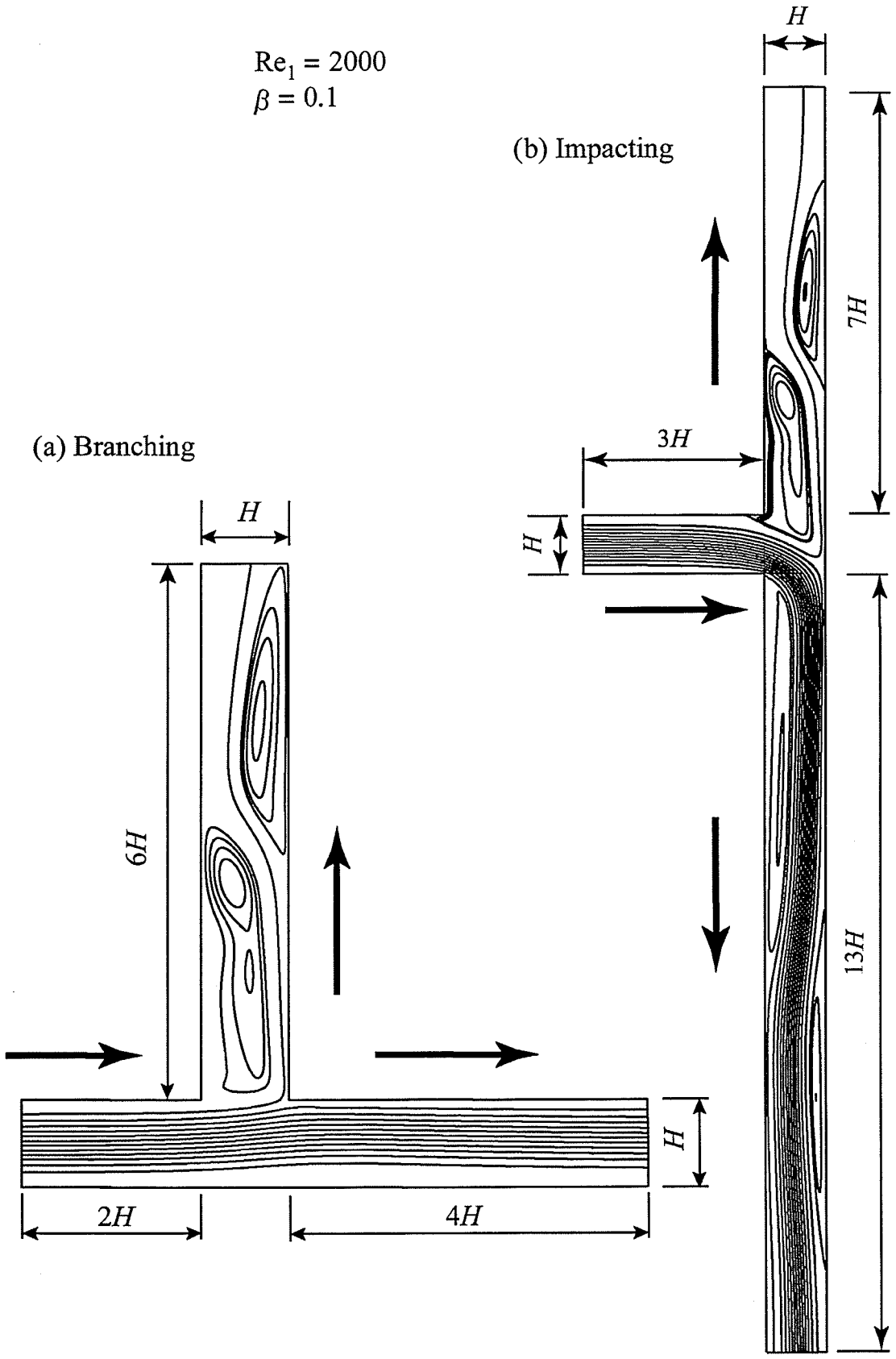

Figure E.14 Streamlines for $Re_1 = 2000$ and $\beta = 0.1$

In dimensionless form,

$$E^* = (1-\beta)\left[\left(P_1^* - P_2^*\right) + \beta\,(2-\beta)\right] + \beta\left[\left(P_1^* - P_3^*\right) + 1 - \beta^2\right] \qquad \text{(E.12)}$$

where $E^* = E/\left(\dot{m}'_{in} V_1^2 / 2\right)$.

The definition of P_1^*, P_2^*, and P_3^* is illustrated graphically in Figure E.15 for the case of branching junctions. For each combination of Re_1 and β, the fully-developed, linear profiles of P^* from the inlet, outlet 2, and outlet 3 regions were extrapolated to the centre of the junction ($x^* = y^* = 0$), as shown in Figure E.15, to obtain the values of P_1^*,

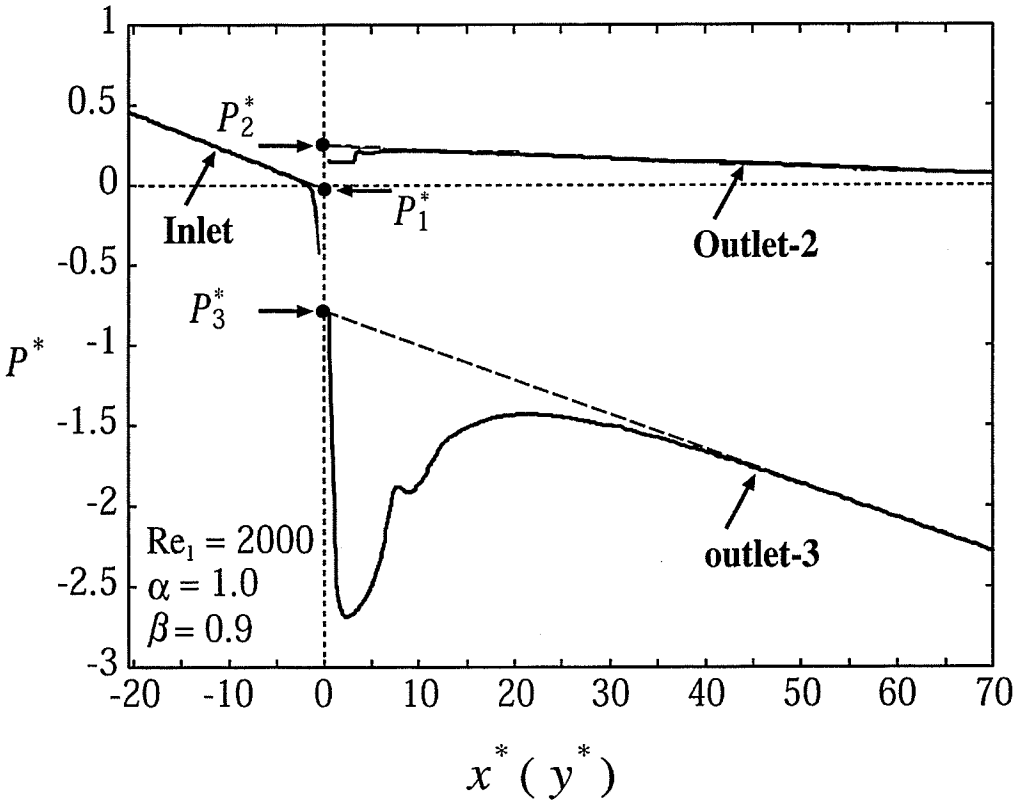

Figure E.15 Distribution of the cross-sectional average pressure in the branching junction

P_2^*, and P_3^*. Similar method was used for the case of impacting junctions to get the three mean pressures. These values were then substituted into Equation (E.12) to calculate E^*.

Figure E.16 shows the variation of E^* with β for Re_1 = 1000 and 2000. It is clear from Figure E.16 that Re_1 has insignificant effect on E^*. As well, for the impacting junction, values of E^* are symmetric around β = 0.5 where E^* reaches its minimum value. This symmetry in the results of impacting tees is expected due to geometrical symmetry whereby, for example, a 30/70 mass split is just a mirror image of a 70/30 split. For the case of branching junctions, Figure E.16 shows that the value of E^* starts

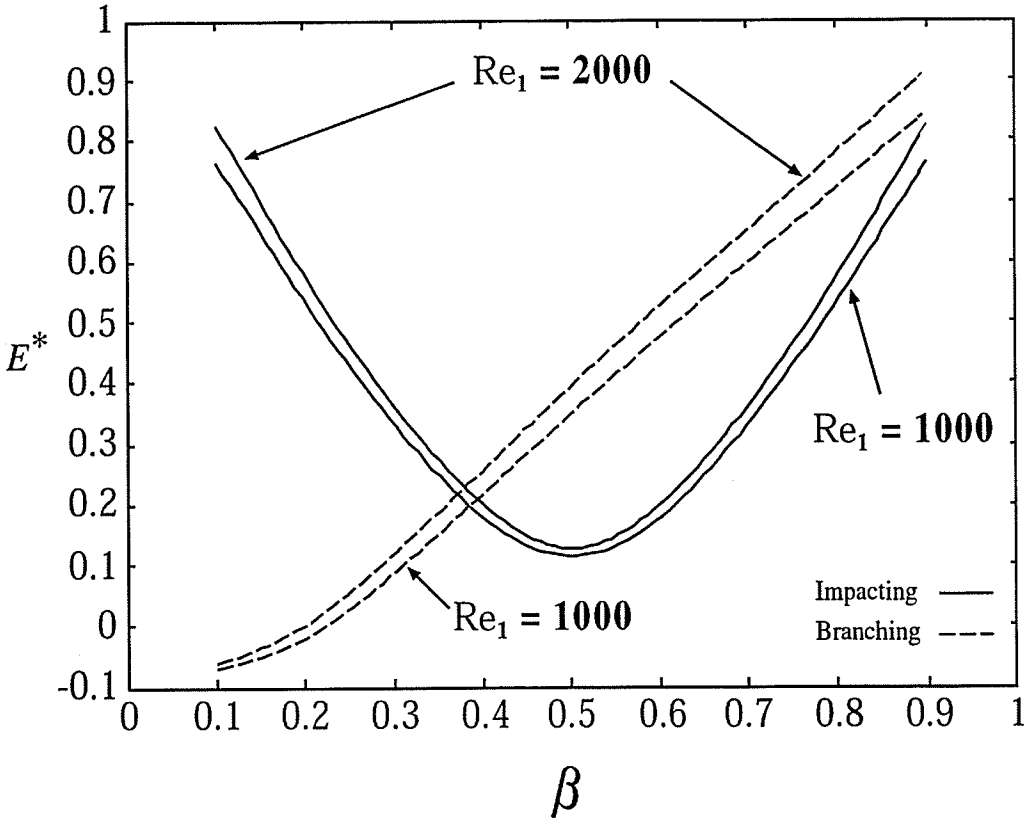

Figure E.16 Pumping power for both configurations

low at small β and then increases with increasing β up to a maximum at $\beta = 0.9$. From Figure E.16, it may be concluded that the branching junction requires less pumping power up to $\beta \cong 0.4$, while the impacting junction requires less pumping power for $\beta \geq 0.4$.

E.4.4 Isotherms

Figures E.17(a), (b), and (c) show the isotherms for three different cases, plotted using a uniform interval $\Delta T^* = 0.1$. By definition, $T^* = 1$ at all walls in the heat-transfer sections.

Figure E.17(a) shows the isotherms for $Re_1 = 1000$ and $\beta = 0.5$. As expected for this case of even mass split, the isotherms are symmetric around the junction centreline. The wall areas covered by re-circulation zone B are areas of poor heat flux, as can be inferred from the shape of the isotherms in those areas. As well, the location on the impacting wall corresponding to $x^* = 0.5$ and $y^* = 0$ appears to be the location of maximum heat flux in the domain.

Figure E.17(b) shows the isotherms for $Re_1 = 1000$ and $\beta = 0.9$. The portion of the flow with high T^* from the area adjacent to the wall $y^* = -0.5$ in the inlet region is diverted into outlet 2. As a result, poor heat transfer is expected in outlet 2. The wall $x^* = 0.5$ in outlet 3 appears to be experiencing high heat flux with a maximum located at $y^* \cong 0.5$. It can also be seen that the wall $y^* = 0.5$ in the inlet experiences high heat flux values near the junction region due to the large portion of the flow diverted into outlet 3.

The effect of increasing Re_1 from 1000 to 2000 on the isotherms for $\beta = 0.9$ can be assessed by comparing Figs. D.17(b) and D.17(c). For the isotherms in outlet 2, the

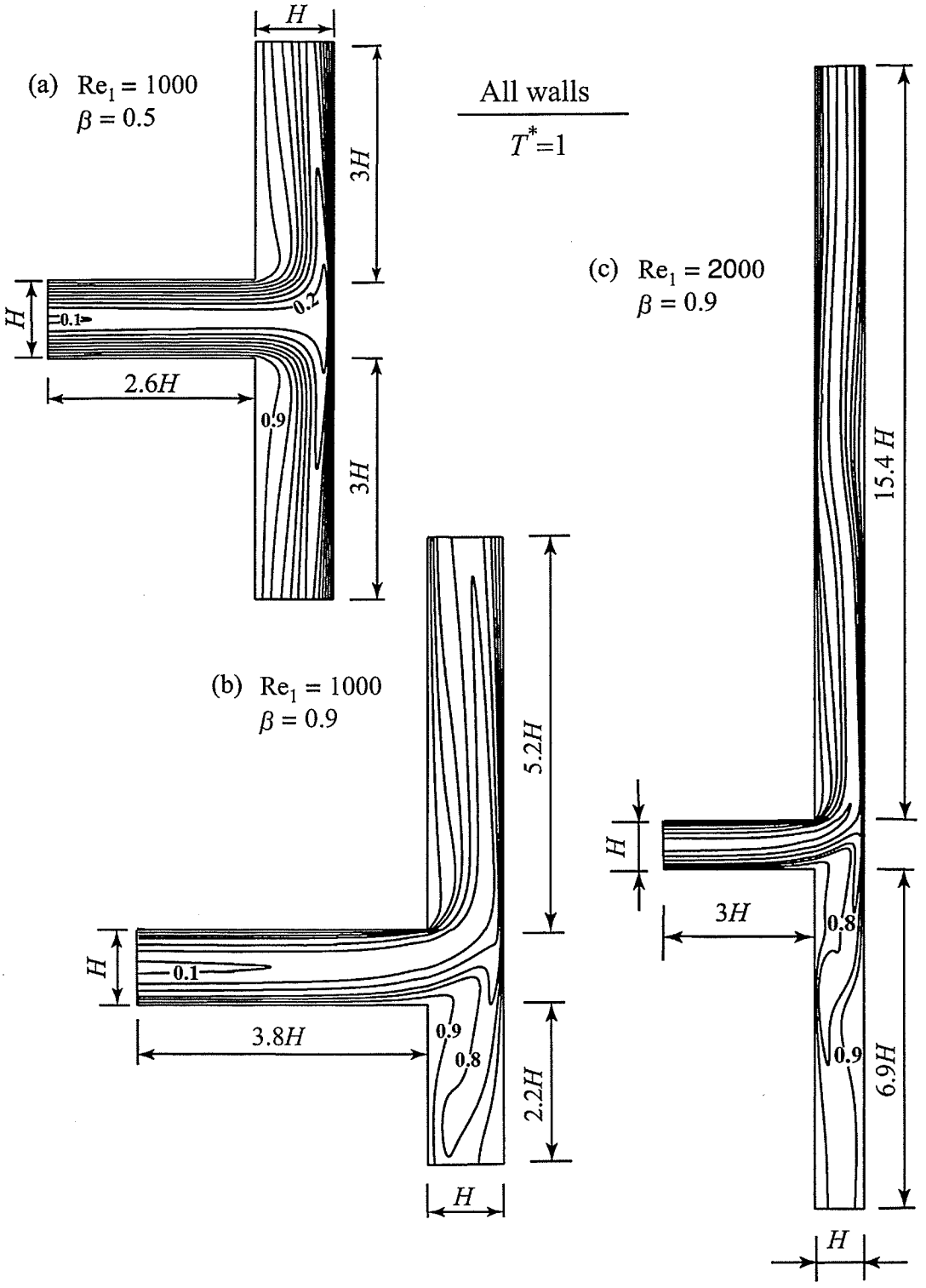

Figure E.17 Isotherms for different conditions

Re_1-effect appears to be fairly small. In outlet 3, the wall $x^* = 0.5$ experiences high heat fluxes in the initial part. The heat flux then decreases to a local minimum due to the existence of re-circulation zone A, followed by an increase around the reattachment point of this re-circulation zone, and finally decreases monotonically towards the fully developed value. On the other hand, the wall $x^* = -0.5$ experiences low heat fluxes in the initial part due to the existence of re-circulation zone B. The heat flux then increases around the reattachment point of this re-circulation zone, and finally decreases monotonically. It appears from these results that a re-circulation zone formed on a certain wall pushes the isotherms away from that wall causing them to get closer to the opposite wall.

Figure E.18 shows the isotherms in both configurations for the case of $Re_1 = 2000$ and $\beta = 0.9$. It can be seen that the isotherms in both outlets are similar for the two types of the junctions. The locations where the isotherms get close to each other and the locations where they get further apart are almost identical.

E.4.5 Wall Heat Flux

The distribution of wall heat flux along $y^* = 0.5$ in the inlet region is shown in Figure E.19 for $Re_1 = 2000$ and $0.1 \leq \beta \leq 0.9$. In the fully developed part of the inlet region, q_w^* decreases exponentially along x^* due to the decrease in $(T_w - T_b)$. This behaviour would appear as a straight line with a slight negative slope on the semi-log plot in Figure E.19. Close to the junction region, deviation from this behaviour occurs due to the disturbance caused by the flow split. It can be seen that for $\beta = 0.1$ and 0.3, q_w^* decreases sharply near the junction region. This decrease in q_w^* is due to the deceleration of the flow near the wall $y^* = 0.5$ as the flow enters the junction region.

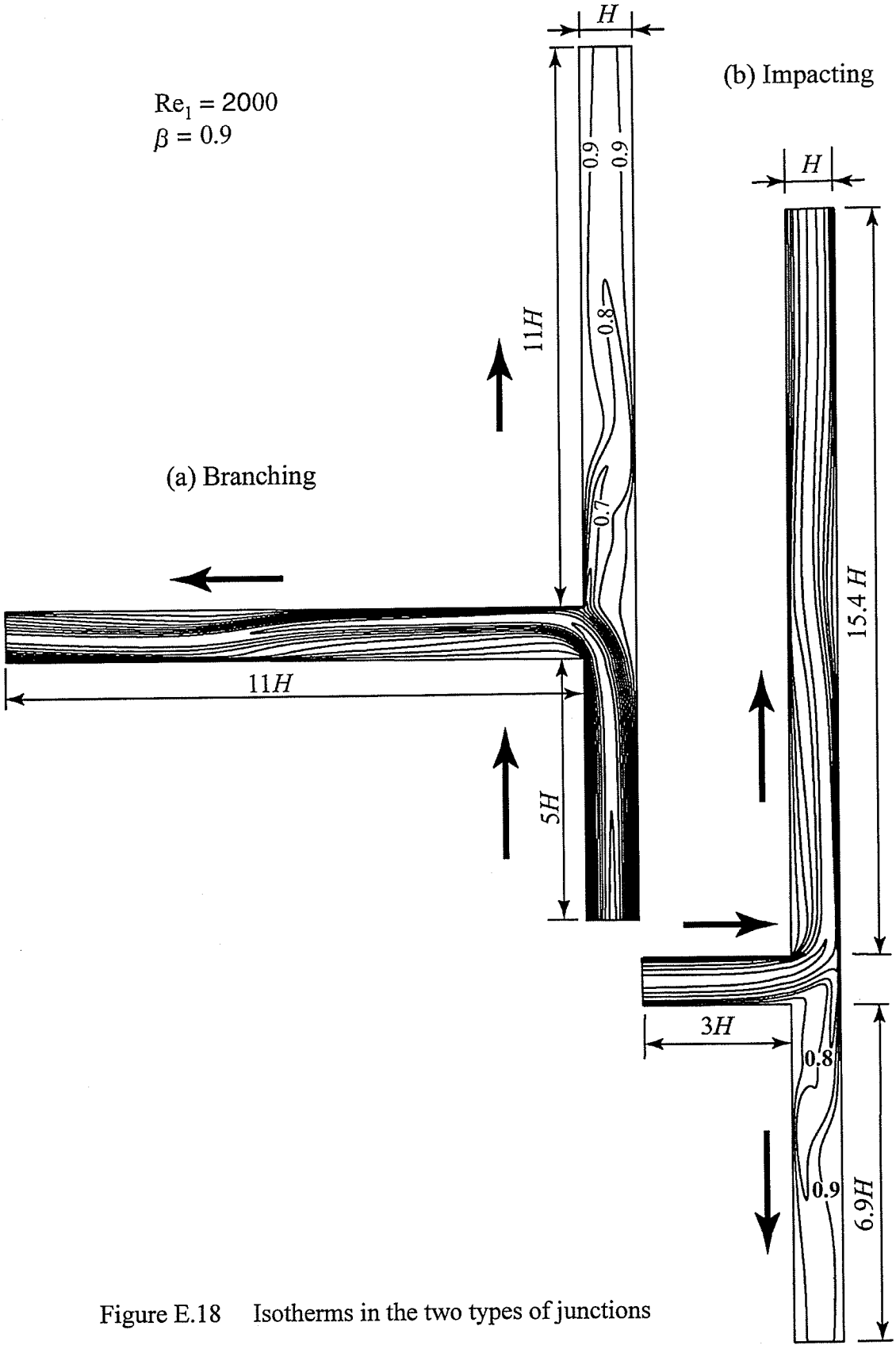

Figure E.18 Isotherms in the two types of junctions

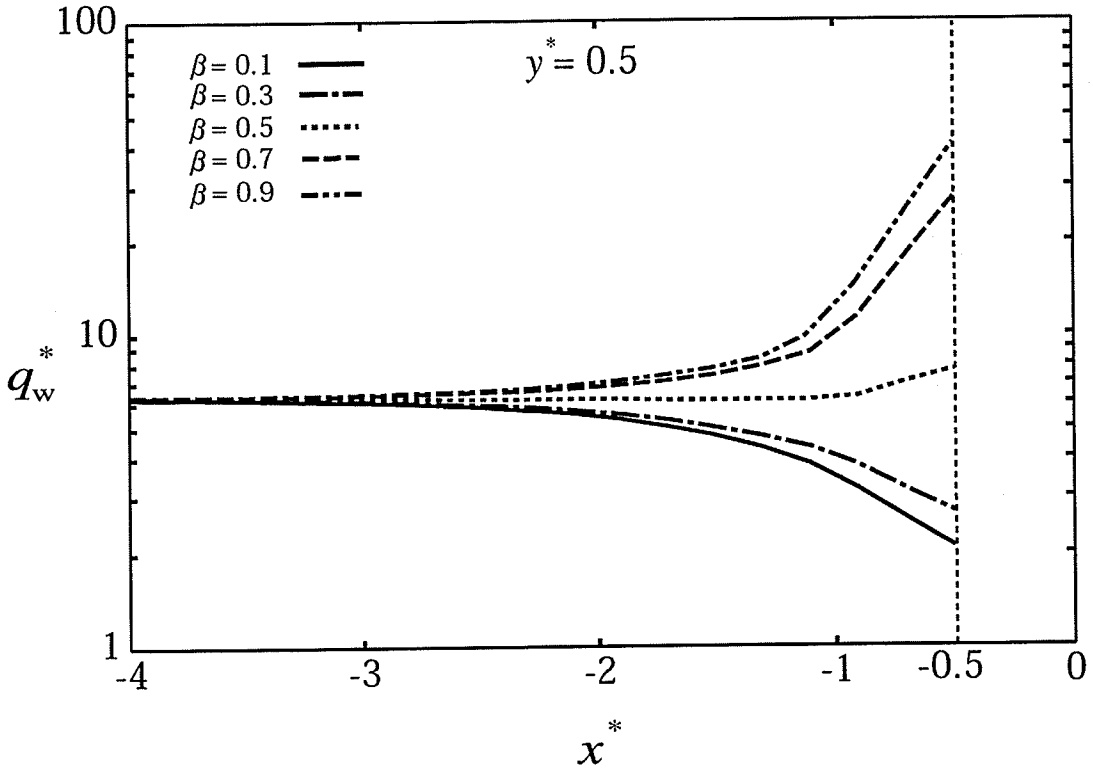

Figure E.19 Distribution of q_w^* along $y^* = 0.5$ for $Re_1 = 2000$

The reverse happens for $\beta \geq 0.5$, where q_w^* experiences an increase close to the junction, the magnitude of which depends on β, as shown in Figure E.19. At $Re_1 = 1000$, the q_w^*-distributions along $y^* = 0.5$ were found to be similar in trend to those shown in Figure E.19, except that the values of q_w^* were lower.

The distribution of wall heat flux along $x^* = 0.5$ in outlet 3 is shown in Figure E.20 for $Re_1 = 2000$ and $0.1 \leq \beta \leq 0.9$. There are two types of behaviors in this figure depending on whether or not re-circulation zone A exists. For $\beta = 0.5$ and 0.7, re-circulation zone A does not exist and as result, q_w^* decreases gradually from the high value close to $y^* = 0$ towards the fully-developed conditions. For $\beta = 0.1$, 0.3, and 0.9,

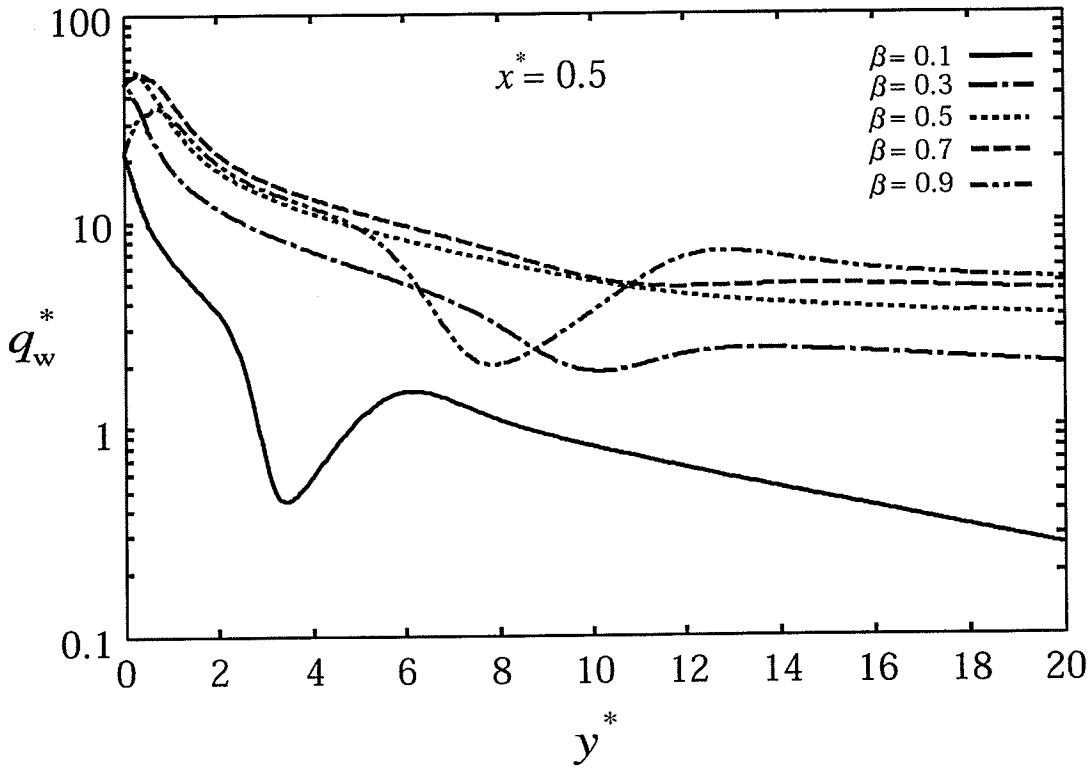

Figure E.20 Distribution of q_w^* along $x^* = 0.5$ for $Re_1 = 2000$

the heat flux starts with a high value at $y^* = 0.0$, decreases to a local minimum in the area occupied by re-circulation zone A, increases to a local maximum around the reattachment point, and finally decreases gradually towards the fully developed conditions. The trends in the results for $Re_1 = 1000$ were found to be consistent with those described for $Re_1 = 2000$ with lower magnitudes of q_w^*.

The distribution of wall heat flux along $x^* = -0.5$ in outlet 3 is shown in Figure E.21 for $Re_1 = 2000$ and $0.1 \leq \beta \leq 0.9$. For all β, the heat flux starts with a high value at $y^* = 0.5$, decreases to a local minimum due to re-circulation zone B, and then increases to a local maximum around the reattachment point of this re-circulation zone.

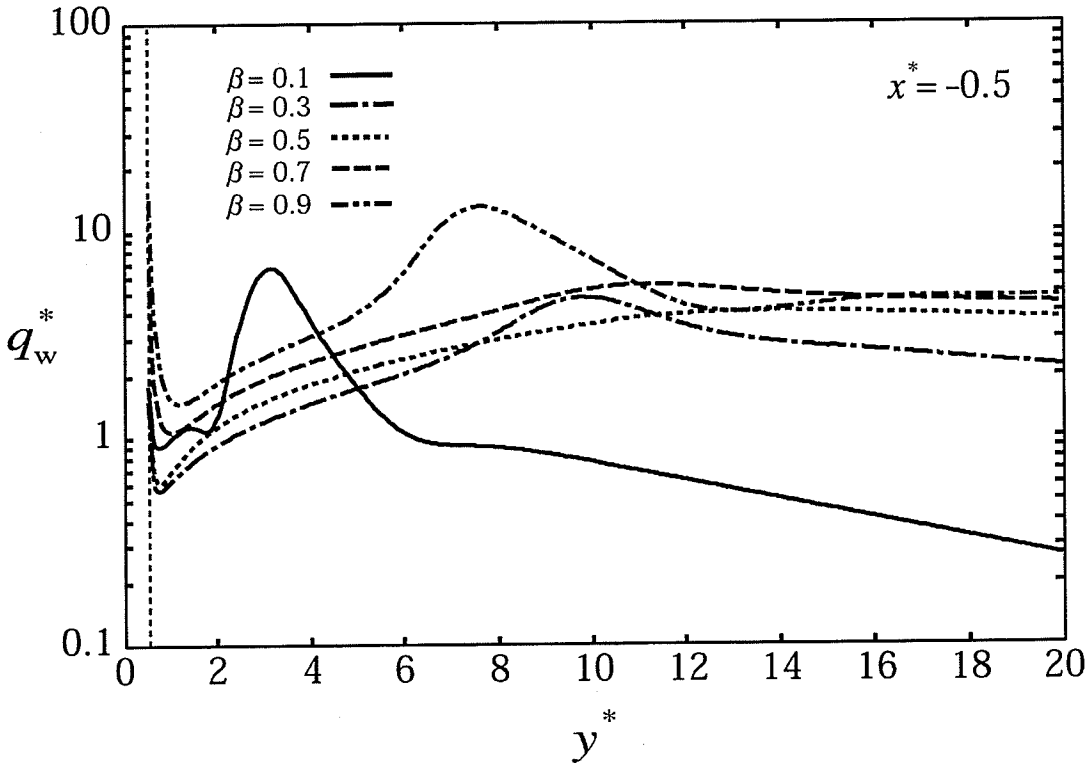

Figure E.21 Distribution of q_w^* along $x^* = -0.5$ for $Re_1 = 2000$

Downstream of re-circulation zone B, the behaviour depends on the existence of re-circulation zone A. For $\beta = 0.5$ and 0.7, q_w^* decreases gradually from the maximum reached around the reattachment point to the fully developed value. For $\beta = 0.1$ and 0.9, q_w^* decreases again to another local minimum due to re-circulation zone A formed on the opposite wall and then recovers around the reattachment point of this zone. It should be mentioned that re-circulation zone A exists also for $\beta = 0.3$; however, its size is so small that it does not affect values of q_w^*. Beyond the areas occupied by re-circulation zones A and B, the value of q_w^* decreases gradually approaching fully developed

conditions. Again, the results for q_w^* at $Re_1 = 1000$ were found to be consistent in trend with these results but the values of q_w^* were lower.

All the above results of heat-flux distributions are consistent with the plots of the isotherms shown earlier in Figures E.17(a), (b), and (c).

Figures E.22 and E.23 show the variation of q_w^* along both walls of outlet 3 of the two configurations for $Re_1 = 2000$, and $\beta = 0.1$ and 0.9. It is clear that for $\beta = 0.9$, the distribution of q_w^* is almost identical for the two junctions. For $\beta = 0.1$, the results have the same trend with a small difference in magnitude in the range $0 \leq y^* \leq 7$. These observations are consistent with those seen in Figures E.8, E.9, and E.10. This

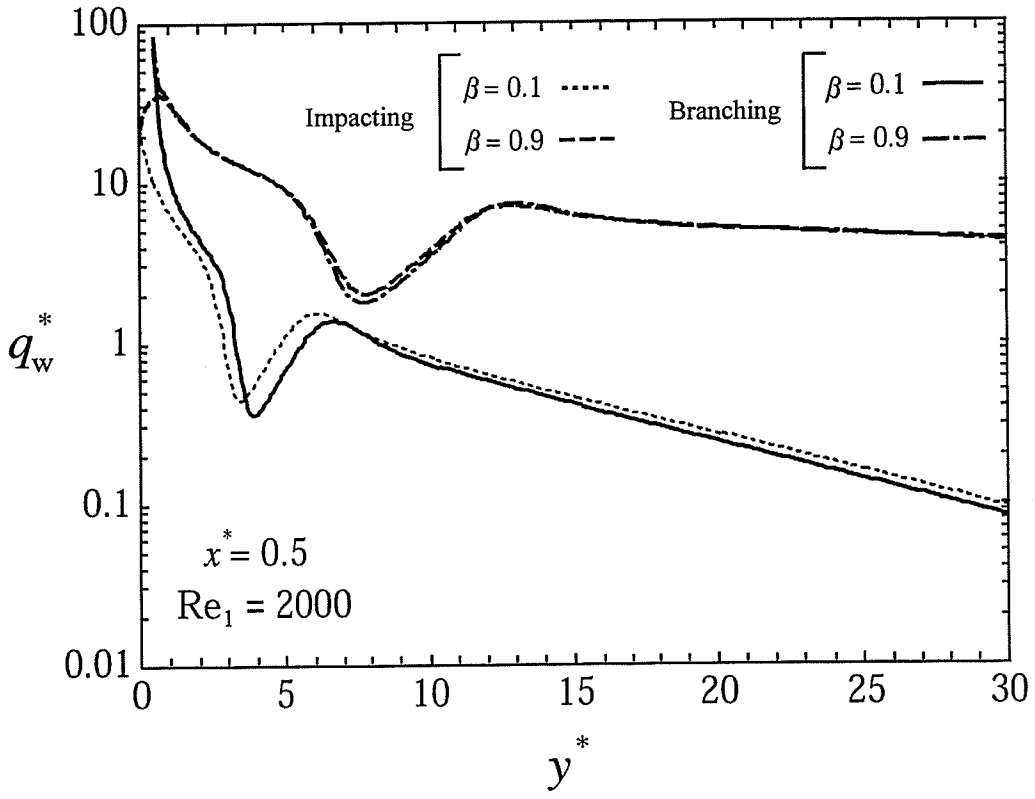

Figure E.22 Wall heat flux in outlet 3, $x^* = 0.5$

similarity in q_w^*-distribution at $\beta = 0.1$ and 0.9 was also found to be at $Re_1 = 1000$. However, for values of β between 0.1 and 0.9, this similarity was found to disappear, as was the case for τ_w^*.

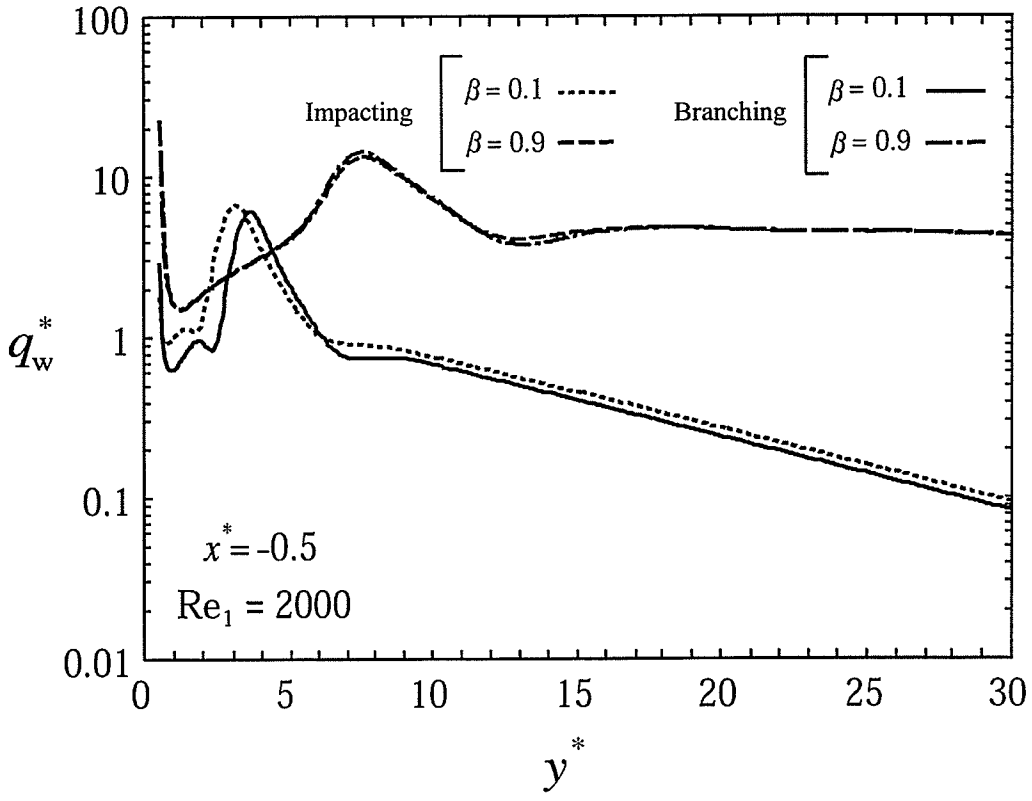

Figure E.23 Wall heat flux in outlet 3, $x^* = -0.5$

Figure E.24 shows the variation of q_w^* along one of the walls of outlet 2 for $Re_1 = 2000$, and $\beta = 0.7$ and 0.9. It can be seen that there is similarity in trend between the two junctions. In terms of magnitudes, there are small deviations only in the range $0 \leq y^* \leq 3$. It was also found that the similarities seen in Figure E.24 persisted at $\beta = 0.5$, but disappeared for $\beta < 0.5$. These exact trends were also found to be valid along the other

wall of outlet 2 at the same values of β. All these results are consistent with those seen earlier in Figures E.10 and E.13.

All the above observations (regarding the similarity -or lack of it- between the two types of junctions) made for $Re_1 = 2000$ were also found to be valid for $Re_1 = 1000$.

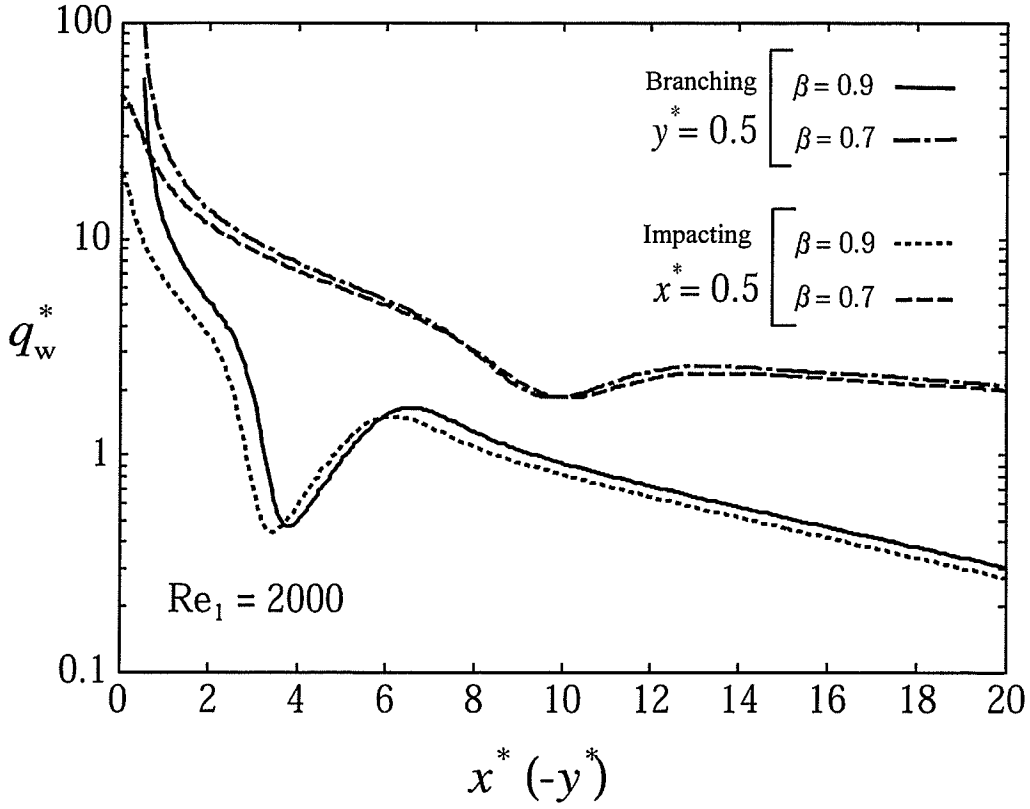

Figure E.24 Wall heat flux along one wall in outlet 2

E.4.6 Overall Heat Transfer

The overall rate of heat transfer from all walls of the junction, characterized by the dimensionless parameter Q^*, was calculated from Equation (E.9). The value of Q^* is dependent on the selected geometry of the junction (i.e., values of L_1, L_2, L_3, L_{21}, and

L_{31}, which were all fixed in the present study), as well as Re_1 and β. Effects of Re_1 and β on Q^* are shown in Figure E.25. For fixed Re_1, the value of Q^* increases with β up to a maximum at about $\beta = 0.5$. The value of Q^* then drops with a further increases in β. This pattern of Q^* variation with β is not surprising in view of earlier results. It may be recalled from previous results that high or low values of β result in poor heat transfer in outlet 2 or outlet 3, respectively. Figure E.25 also shows that Q^* increases considerably with an increase in Re_1, consistent with the observations made earlier on the Re_1-effect on q_w^*.

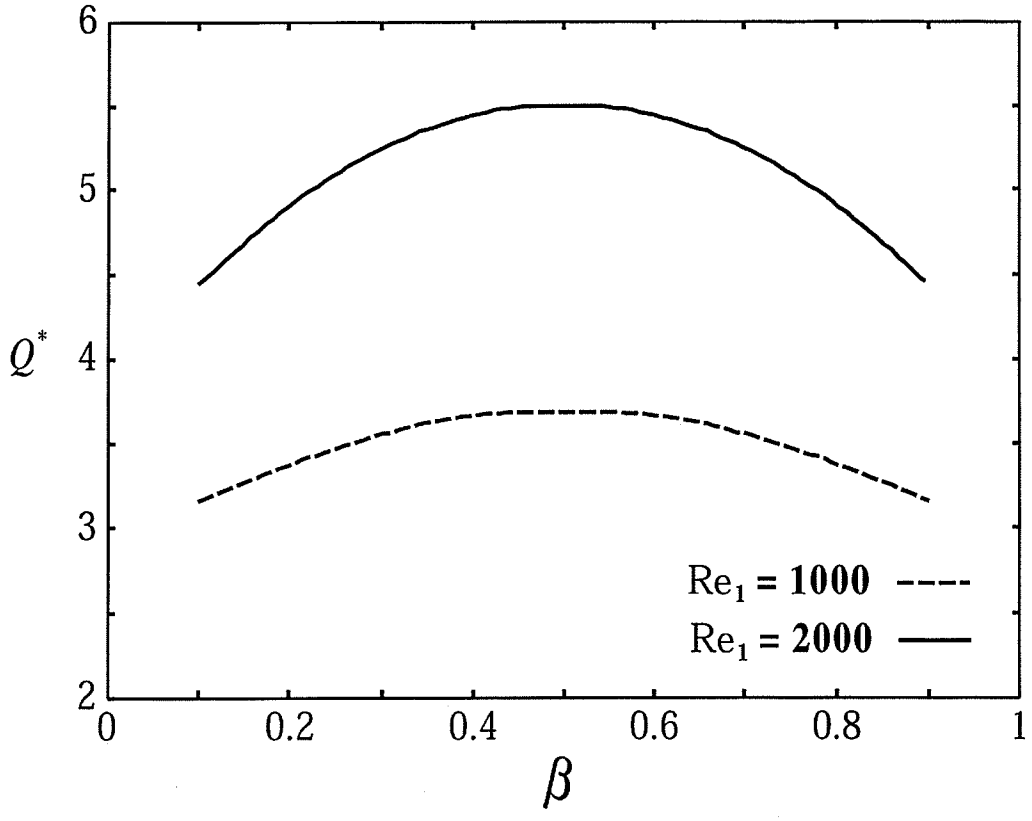

Figure E.25 Values of Q^*

E.4.7 Excess Heat Transfer

Another important parameter that can be used in evaluating the performance of the junction is the excess heat transfer Q_e defined as,

$$Q_e = Q - Q_{fd} \tag{E.13}$$

where Q is the total rate of heat transfer from all sides of the junction, and Q_{fd} is the total rate of heat transfer assuming fully-developed flow in all sides of the junction. Thus, Q_e reflects the effect of the junction on the rate of heat transfer. The value of Q_{fd} was calculated assuming fully-developed conditions over the lengths L_1, L_{21}, and L_{31} (see Figure E.1) with mass flow rates $\dot{m}'_{in}$, $(1-\beta)\dot{m}'_{in}$, and $\beta\,\dot{m}'_{in}$ in sides 1, 2, and 3 of the junction. Under these conditions, Nusselt number has a value of 7.5407 (Shah and London, 1978). The value of Q was calculated by integrating q_w over the whole surface area of the heat-transfer sections of the junction. Figure E.26 shows the variation of Q_e^* $\left(=Q/\left[k\left(L_1^*+L_{21}^*+L_{31}^*\right)\left(T_w-T_{in}\right)\right]\right)$ with β for Re_1 = 1000 and 2000. It can be seen that Q_e^* is positive over the whole range of β except for the branching junction with $\beta = 0.1$. The fact that Q_e^* is positive indicates that the junction enhances the rate of heat transfer over fully-developed conditions. The magnitude of this enhancement increases as Re_1 increases. The impacting junction produced the expected symmetrical behaviour with a maximum at $\beta = 0.5$. Finally, Figure E.26 shows that the impacting junction has higher values for Q_e^* in the range $0.1 \le \beta < 0.4$ while the opposite is true in the range $0.4 < \beta \le 0.9$.

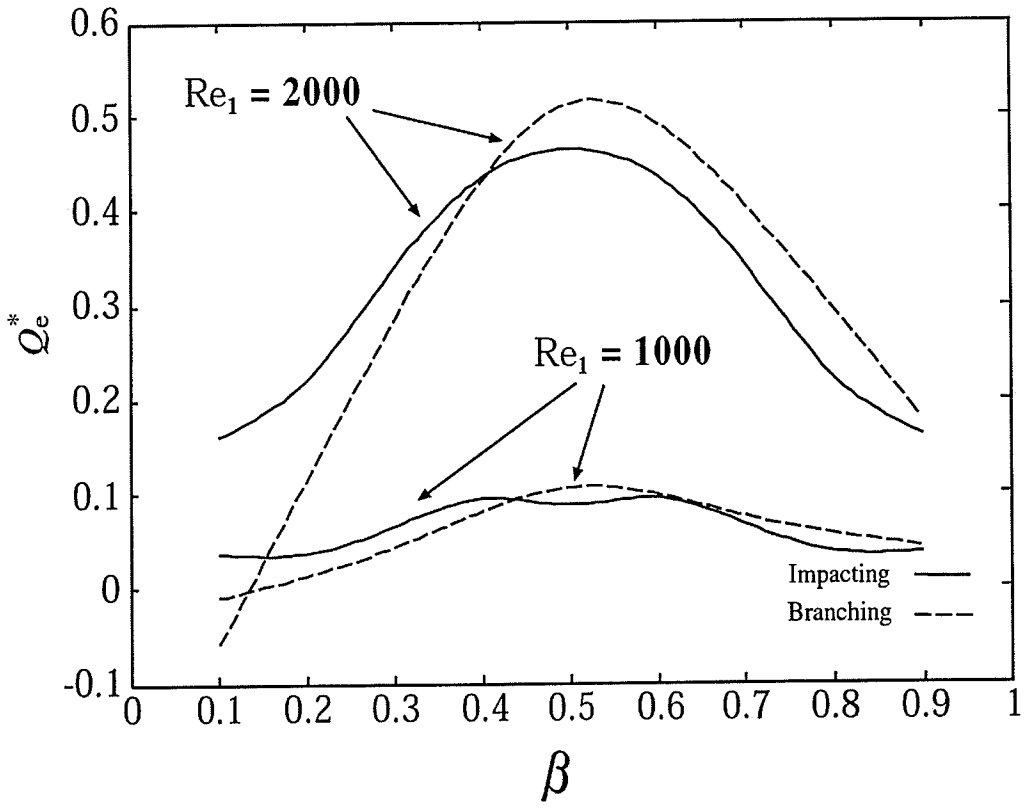

Figure E.26 Excess heat transfer for both configurations

Nomenclature for Appendix E

Symbol	Description	Units
A_w	Total surface area of the heat-transfer sections	m^2
c_p	Specific heat	J/kg.k
E	Pumping power	W
H	Duct size in the inlet, outlet-2, and outlet-3	m
k	Thermal conductivity	W/m.k
L	Duct length	m
$\dot{m}'$	Mass flow rate per unit depth	kg/m.s
p	Pressure	Pa
Pr	Prandtl number	-
Q	Total rate of heat transfer per unit depth	W/m
q	Local heat flux	W/m^2
Re	Reynolds number	-
T	Temperature	K
T_1	Inlet temperature	K
u	Velocity component in the x direction	m/s
V	Cross-sectional average velocity	m/s
v	Velocity component in the y direction	m/s
x, y	Cartesian co-ordinates	m
β	Ratio of outlet-3-to-inlet mass flow rates	-
ν	Kinematic viscosity	m^2/s
ρ	Density	kg/m^3

τ	Shear stress	N/m^2

Subscripts

1, 2, 3	Inlet, outlet-2, and outlet-3
21	Heat-transfer portion of outlet-2
22	Adiabatic portion of outlet-2
31	Heat-transfer portion of outlet-3
32	Adiabatic portion of outlet-3
in	Inlet face
w	At the wall

Superscript

*	Dimensionless quantity